

I

Stretchable Surface Electromyography Electrode Array Based on Liquid Metal and Conductive Polymer

Shuaijian Yang

Main Supervisors: Dr Samit Chakrabarty

Dr Jessica Kwok

Dr Xingyu Jiang

Submitted in accordance with the requirements
for the degree of Doctor of Philosophy

School of Biomedical Sciences, University of
Leeds

September 2023

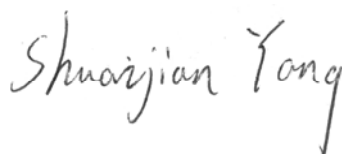
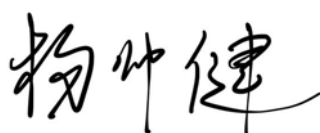
The candidate confirms that the work submitted is his own, except where work which has formed part of jointly authored publications has been included. The contribution of the candidate and the other authors to this work has been explicitly indicated below. The candidate confirms that appropriate credit has been given within the thesis where reference has been made to the work of others.

A part of this thesis has been accepted for publication in Nature Communications: 'Stretchable surface electromyography electrode array patch for tendon location and muscle injury prevention.' Shuaijian Yang, Jinhao Cheng, Jin Shang, Chen Hang, Jie Qi, Leni Zhong, Qingyan Rao, Lei He, Chenqi Liu, Li Ding, Mingming Zhang, Samit Chakrabarty, Xingyu Jiang. (First author).

This copy has been supplied on the understanding that it is copyright material and that no quotation from the thesis may be published without proper acknowledgement.

The right of Shuaijian Yang to be identified as Author of this work has been asserted by Shuaijian Yang in accordance with the Copyright, Designs and Patents Act 1988.

© 2023 The University of Leeds, Shuaijian Yang



Signed

Acknowledgements

I can not recall when it began, but it must have bewildered my younger self. Sharing my accomplishments with you, my beloved parents, Daqiang Yang and Yurong Ji, filled me with a greater joy and pride than the achievements alone. As I have grown, I now understand this profound emotion stems from our family's sincere love and aspirations. I am keenly aware that your boundless love far exceeds what I can return. I am immensely fortunate to be your son, appreciating everything you've done from the depths of my heart. Without your unwavering support, my pursuit of a PhD would have been unlikely. I wholeheartedly cherish and love you both.

I extend my deepest gratitude to my co-supervisor, Prof. Xingyu Jiang, for illuminating my path in the realm of science when I was uncertain how to navigate it. The pivotal moment when you generously offered me the opportunity to pursue a PhD is etched in my memory. Your steadfast guidance and unwavering support have been my constant sources of confidence and courage in exploring uncharted territories. The motto you have instilled in me, 'unparalleled advantage', will serve as my guiding light, and I am committed to passing on the torch in the future.

Prof. Lixue Tang, my senior, also provided me with substantial assistance in experiments and research. I am grateful for your guidance, which allowed me to explore the fascinating world of liquid metal.

Throughout my four-year PhD journey, I have been incredibly fortunate to receive the support and friendship of some truly exceptional individuals. I

am deeply grateful to my first-year roommates in the UK, who stood by my side during the challenging times with the pandemic, especially Yanran Li. Your phrase 'If uncertain of what you desire, at least figure out what you deny,' greatly bolstered my resolve to be a PhD candidate.

I would also like to extend my heartfelt appreciation to my best friends, Jinhao Cheng and Jin Shang, who were my steadfast companions during the middle two years of this journey. Your generous assistance and resolute companionship, both in life and in the laboratory, were invaluable in the publication of my work.

I also need to express my sincere appreciation to Zhuowei Feng, Leni Zhong, Chang Che, and Zeyang Pang. Your support and assistance during the final year of my PhD were a source of strength, dispelling the stress and anxiety that can often accompany this stage of academic pursuits.

To all my colleagues at the University of Leeds and the Southern University of Science and Technology, thank you for your kind assistance and support throughout my experiments and daily life.

Lastly but foremost, I want to express my most sincere gratitude to Dr. Samit Chakrabarty. Words can hardly capture the depth of my appreciation. Your unwavering support and guidance, evident in every meeting, every conversation, and every chat, have not only shaped me into a better researcher but also a better person. I hold you in the highest esteem, and it is a true honour to have been your PhD student. I will always treasure the time we have shared, the work we have accomplished together, and the friendship we have built.

Abstract

Electromyography (EMG), the science of detecting and interpreting muscle electrical activity, plays a crucial role in clinical diagnostics and research. It enables assessment of muscle function, detection of abnormalities, and monitoring of rehabilitation progress. However, the current use of EMG devices is primarily limited to clinical settings, preventing its potential to revolutionize personal health management. If surface electromyography (sEMG) electrodes are stretchable, arrayed, reusable and able to continuously record, their applications for personal health management are broadened. Existing electrodes lack these essential features, hampering their widespread adoption. This thesis addresses these limitations by designing an adhesive dry electrode using tannic acid, polyvinyl alcohol, and PEDOT:PSS (TPP). Through meticulous optimization, TPP electrodes offer superior stretchability and adhesiveness compared to conventional Ag/AgCl electrodes. This ensures stable and long-term skin contact for recording. Furthermore, a metal-polymer electrode array patch (MEAP) is introduced, featuring liquid metal (LM) circuits and TPP electrodes. MEAPs exhibit better conformability than current commercial arrays, resulting in higher signal quality and stable recordings, even during significant skin deformations caused by muscle movements. Manufactured using scalable screen-printing, MEAPs combine stretchable materials and array architecture for real-time monitoring of muscle stress, fatigue, and tendon displacement. They hold great promise in reducing muscle and tendon injuries and enhancing performance in both daily exercise and professional

sports. In addition, a pilot study compares MEAP performance in clinical electrodiagnostics with needle electrodes, demonstrating the non-invasive advantage of MEAP by successfully recording the signals from the same motor unit as the needle. These advancements position MEAP at the forefront of the EMG field, poised to drive breakthroughs in electrodiagnostics, personalized medicine, sports science, and rehabilitation.

Table of Contents

| | |
|---|-------|
| Stretchable Surface Electromyography Electrode Array Based on Liquid Metal and Conductive Polymer | I |
| Acknowledgements | III |
| Abstract | V |
| Table of Contents | VII |
| List of Tables | XII |
| List of Figures | XIII |
| List of Abbreviations | XVIII |
| Chapter 1 General Introduction | 1 |
| 1.1 Electromyography | 3 |
| 1.1.1 Rationale | 3 |
| 1.1.2 EMG signals parameter | 4 |
| 1.1.3 EMG electrode types | 7 |
| 1.1.4 Typical materials for sEMG electrode | 9 |
| 1.1.5 Key considerations for sEMG electrode materials | 13 |
| 1.1.6 Limitations of current sEMG electrodes | 21 |
| 1.1.7 EMG international standards for sEMG recording | 22 |
| 1.1.8 EMG signal processing | 23 |
| 1.1.9 Clinical diagnosis | 26 |
| 1.2 Liquid metal | 29 |
| 1.2.1 Fundamental properties of GLM | 29 |
| 1.2.2 Methods to fabricate and pattern GLM | 30 |
| 1.2.3 Metal-polymer conductors (MPC) | 34 |
| 1.2.4 Applications in biosensing | 34 |
| 1.3 Polymers | 44 |
| 1.3.1 PDMS | 45 |
| 1.3.2 Thermoplastic polyurethane (TPU) | 47 |
| 1.3.3 PEDOT:PSS | 49 |

VIII

| | | |
|-----------|--|----|
| 1.3.4 | Polyvinyl alcohol (PVA) and tannic acid (TA) | 51 |
| 1.4 | Aims..... | 54 |
| 1.4.1 | Creation of a new material for sEMG electrodes with conductive polymers and characterization of its properties | 54 |
| 1.4.2 | Integration of the new electrode and MPC to fabricate an sEMG electrode array and characterization of its properties | 55 |
| 1.4.3 | Utilization of the developed sEMG array for multiplexed muscle information to prevent muscle injury in daily life | 55 |
| 1.4.4 | Exploration of the clinical diagnosis potential of the developed sEMG array..... | 56 |
| Chapter 2 | General Methods..... | 57 |
| 2.1 | Materials and reagents | 57 |
| 2.2 | Instruments..... | 57 |
| 2.3 | Synthesis of conductive polymer | 58 |
| 2.3.1 | Synthesis of PEDOT-PVA electrodes..... | 58 |
| 2.3.2 | Synthesis of TPP electrodes..... | 59 |
| 2.4 | Array fabrication | 59 |
| 2.4.1 | PDMS substrate..... | 59 |
| 2.4.2 | TPU substrate..... | 61 |
| 2.5 | Materials characterizations methods | 62 |
| 2.6 | sEMG recording..... | 64 |
| 2.7 | Subject tasks | 64 |
| 2.7.1 | Comparison test between PEDOT-PVA and TPP electrodes..... | 64 |
| 2.7.2 | Long-term test..... | 65 |
| 2.7.3 | Conformability test on the forehead..... | 65 |
| 2.7.4 | Fatigue comparison tests..... | 65 |
| 2.7.5 | Muscle contraction task for muscle activity maps..... | 66 |
| 2.7.6 | Muscle contraction task for muscle-tendon junction location.. | 66 |
| 2.7.7 | Muscle contraction task for muscle injury prevention | 67 |
| 2.8 | Data collection and processing..... | 67 |
| 2.9 | Appendix..... | 68 |
| Chapter 3 | Characterizations of TPP electrodes..... | 69 |
| 3.1 | Introduction..... | 69 |

| | | |
|-----------|--|-----|
| 3.2 | Determination of the formula of TPP..... | 72 |
| 3.2.1 | Determination of the ratio between PVA and PEDOT:PSS | 72 |
| 3.2.2 | Determination of each constituent in TPP..... | 82 |
| 3.3 | Characterizations of 8% TPP..... | 89 |
| 3.3.1 | Electrical and mechanical properties | 89 |
| 3.3.2 | Repeatability of use | 94 |
| 3.3.3 | Long-term test..... | 97 |
| 3.4 | Comparing tests..... | 99 |
| 3.4.1 | TPP electrodes and dry electrodes in other literature..... | 99 |
| 3.4.2 | Comparison of conformability between TPP and Ag/AgCl electrodes | 102 |
| 3.4.3 | Comparison of muscle fatigue monitoring between TPP and Ag/AgCl electrodes | 105 |
| 3.5 | Impact of viscosity on TPP ink spray patterns | 107 |
| 3.6 | Conclusions | 111 |
| Chapter 4 | Characterizations of MEAPs..... | 113 |
| 4.1 | Introduction | 113 |
| 4.2 | Fabrication..... | 114 |
| 4.2.1 | MEAP with substrate of PDMS | 114 |
| 4.2.2 | MEAP with substrate of TPU | 116 |
| 4.3 | Characterizations of MEAPs..... | 118 |
| 4.3.1 | Topography and stretchability..... | 118 |
| 4.3.2 | Repeatability of use | 119 |
| 4.3.3 | Permeability | 120 |
| 4.4 | Comparing tests..... | 122 |
| 4.4.1 | Properties of MEAP and those of sEMG arrays in other literatures | 122 |
| 4.4.2 | sEMG recording performances of MEAP and CA on muscle..... | 123 |
| 4.4.3 | sEMG recording performances of MEAP and CA on muscle-tendon junction..... | 129 |
| 4.5 | Conclusions | 133 |
| Chapter 5 | Applications of MEAP..... | 135 |
| 5.1 | Introduction | 135 |

| | | |
|-----------|---|-----|
| 5.2 | MEAP for sEMG activation mapping | 136 |
| 5.2.1 | Muscle activity map on biceps brachii | 138 |
| 5.2.2 | Muscle activity map on abductor pollicis brevis | 141 |
| 5.3 | MEAP for muscle-tendon junction location..... | 145 |
| 5.3.1 | Location of muscle-tendon junction on distal biceps tendon | 145 |
| 5.3.2 | Location of muscle-tendon junction on Achilles tendon with 10 mm-IED MEAP | 152 |
| 5.3.3 | Location of muscle-tendon junction on Achilles tendon with 6 mm-IED MEAP | 157 |
| 5.4 | MEAP for muscle injury prevention | 160 |
| 5.4.1 | Muscle loading and fatigue of subject A | 163 |
| 5.4.2 | Location of muscle-tendon junction of subject A | 168 |
| 5.4.3 | Muscle injury index | 176 |
| 5.4.4 | Statistics across different subjects..... | 177 |
| 5.5 | Conclusions | 183 |
| Chapter 6 | Use of MEAP for electrodiagnostic..... | 184 |
| 6.1 | Introduction..... | 184 |
| 6.2 | Comparison of EMG signals recorded by needle and MEAP | 188 |
| 6.2.1 | Recording summary..... | 189 |
| 6.2.2 | Trial 1..... | 190 |
| 6.2.3 | Trial 5..... | 192 |
| 6.3 | Conclusions..... | 193 |
| Chapter 7 | General discussion..... | 195 |
| 7.1 | Material selection for developing dry electrode | 195 |
| 7.2 | Wireless recording for MEAP | 197 |
| 7.3 | Minimizing the influence of skin deformation on MEAP recordings | 198 |
| 7.4 | Unlocking new frontiers in prosthetics and exoskeletons with MEAP | 201 |
| 7.5 | Advancing electrodiagnostic and electrophysiological research with MEAP | 204 |
| Chapter 8 | Conclusions..... | 207 |
| 8.1 | Concluding remarks..... | 207 |

| | | |
|-----|--------------------|-----|
| 8.2 | Future works | 209 |
| | References | 212 |

List of Tables

| | |
|---|------------|
| Table 1.1.1 A comparison of cost of metals..... | 21 |
| Table 1.1.2 Fundamental information about disorders and the associated EMG tools. | 27 |
| Table 1.3.1 Comparison of Young’s modulus between common materials for wearable devices..... | 48 |
| Table 3.4.1 Comparisons between dry electrodes in other literatures and this work..... | 101 |
| Table 4.4.1 Comparisons between sEMG arrays in other literatures and this work..... | 123 |
| Table 6.2.1 The summary of parameters of MUAPs recorded by needle and MEAP..... | 190 |
| Table 7.3.1 IED between adjacent channels when biceps brachii is relaxed, fully extended and fully flexed..... | 199 |

List of Figures

| | |
|---|----|
| Figure 1.1.1 Recording by EMG electrodes. | 4 |
| Figure 1.1.2 Surface electrode types in experimental signals. | 9 |
| Figure 1.1.3 Chemical structure of PEDOT:PSS and core-shell structure of the film. | 11 |
| Figure 1.1.4 Chemical structure of PDMS. | 13 |
| Figure 1.1.5 Circuit models of non-conformal and conformal electrodes on skin folds. | 15 |
| Figure 1.2.1 MPC electronics for movement monitoring. | 37 |
| Figure 1.2.2 MPC-based electronics for ECG recording. | 39 |
| Figure 1.2.3 MPC-based electronics for EEG recording. | 40 |
| Figure 1.2.4 LM-based electronics for EMG recording. | 42 |
| Figure 1.2.5 MPC-based electronics for photoplethysmography and blood oxygen. | 44 |
| Figure 1.3.1 Transfer printing technique of GLM using PDMS. | 46 |
| Figure 1.3.2 Chemical structure of TPU. | 47 |
| Figure 1.3.3 Doping with other polymers to enhance the PEDOT:PSS film. | 51 |
| Figure 1.3.4 Chemical structure of gallol and catechol group. | 53 |
| Figure 1.3.5 Molecular structure of tannic acid. | 54 |
| Figure 3.1.1 TPP films. | 72 |
| Figure 3.2.1 Strain and conductivity of PEDOT-PVA electrodes with different PVA additions. | 74 |
| Figure 3.2.2 Abrasion-resistance of PEDOT-PVA electrodes. | 75 |
| Figure 3.2.3 Water-resistance of PEDOT-PVA electrodes. | 76 |
| Figure 3.2.4 The viscosities of PEDOT-PVA solutions. | 77 |
| Figure 3.2.5 The results of impedance of PEDOT-PVA electrodes. | 78 |
| Figure 3.2.6 The radar plot of characterization results with different PVA addition. | 79 |
| Figure 3.2.7 SEM images of the PEDOT:PSS film with or without PVA addition. | 80 |
| Figure 3.2.8 AFM images of the PEDOT:PSS film with or without PVA addition. | 81 |

| | |
|---|-----|
| Figure 3.2.9 Mechanical characterizations of TPP films with different TA loading. | 82 |
| Figure 3.2.10 Peeling force of TPP films on the skin. | 83 |
| Figure 3.2.11 The photograph of residue test of TPP films with different TA loading peeled off from the skin. | 84 |
| Figure 3.2.12 Conductivity of TPP films with different TA loading. | 85 |
| Figure 3.2.13 The cross-sectional SEM images of TPP films with different TA additions. | 87 |
| Figure 3.2.14 Schematic illustration of the working mechanism in PEDOT-PVA and TPP films and related chemical structures. | 88 |
| Figure 3.3.1 The changes of resistance, strain and peeling force with or without each component in TPP film. | 90 |
| Figure 3.3.2 Comparisons of impedance between different types of electrodes. | 90 |
| Figure 3.3.3 Recording performance by electrodes with or without adhesiveness during dynamic task. | 93 |
| Figure 3.3.4 Real-time monitoring of the TPP film by stretching the film from a strain of 0 to 20% for about 500 cycles. | 94 |
| Figure 3.3.5 The change in adherence and impedance of TPP electrodes on the skin. | 95 |
| Figure 3.3.6 SNR variation and baseline noise levels of TPP electrodes on the skin. | 96 |
| Figure 3.3.7 The repetitive test of TPP films on the skin. | 97 |
| Figure 3.3.8 Biocompatibility of TPP electrodes on skin. | 98 |
| Figure 3.3.9 Biocompatibility of TPP electrodes on skin. | 99 |
| Figure 3.4.1 Comparison of recording performances on frontalis muscle between Ag/AgCl and TPP electrodes. | 103 |
| Figure 3.4.2 Schematic illustrations and lateral photos of Ag/AgCl electrode and TPP electrode on skin folds. | 104 |
| Figure 3.4.3 Quantifications of recording performances by two electrodes on frontalis muscle. | 104 |
| Figure 3.4.4 Quantifications of recording performances by two electrodes on frontalis muscle. | 106 |
| Figure 3.4.5 sEMG signals and linear fit results of median frequency during flexion 1, 2 and 3 recorded by Ag/AgCl and TPP electrodes. | 107 |
| Figure 3.5.1 Results of spray patterning with different addition of xanthan gum in TPP ink and a simplified model for dewetting. .. | 109 |

| | |
|---|-----|
| Figure 3.5.2 The viscosities of TPP ink with different loadings of xanthan gum..... | 110 |
| Figure 4.2.1 sEMG signals and linear fit results of median frequency during flexion 1, 2 and 3 recorded by Ag/AgCl and TPP electrodes. | 116 |
| Figure 4.2.2 MEAP with substrate of TPU for electrodiagnostic recording on APB..... | 118 |
| Figure 4.3.1 Characterizations of MEAPs. | 119 |
| Figure 4.3.2 The reattachment test of 24-channel MEAP on the skin. | 120 |
| Figure 4.3.3 The permeability comparison test between MEAP, MEAP (punctures) and polyimide. | 121 |
| Figure 4.4.1 The configuration comparison between MEAP and CA. | 124 |
| Figure 4.4.2 The entire setup for connection between MEAP and EMG recording system. | 125 |
| Figure 4.4.3 The typical sEMG signals recorded using CA and MEAP on biceps brachii. | 126 |
| Figure 4.4.4 The spatial SNR performance map for each channel of CA and MEAP for the first and last muscle contraction on biceps brachii. | 127 |
| Figure 4.4.5 Statistical analysis of performances between CA and MEAP on biceps brachii..... | 128 |
| Figure 4.4.6 The typical sEMG signals recorded using CA and MEAP on muscle-tendon junction of biceps brachii. | 130 |
| Figure 4.4.7 The spatial SNR performance map for each channel of CA and MEAP for the first and last muscle contraction on muscle-tendon junction of biceps brachii..... | 131 |
| Figure 4.4.8 Statistical analysis of performances between CA and MEAP on muscle-tendon junction of biceps brachii..... | 132 |
| Figure 5.2.1 Comparison of surface areas of Ag/AgCl electrodes and TPP electrodes. | 137 |
| Figure 5.2.2 Experimental setup for sEMG activation mapping on BB. | 138 |
| Figure 5.2.3 sEMG recorded by each channel of MEAP on BB. | 139 |
| Figure 5.2.4 Muscle activity maps of sEMG recorded from BB, showing the process of graded recruitment during contractions. | 141 |
| Figure 5.2.5 Experimental setup for sEMG activation mapping on APB. | 142 |
| Figure 5.2.6 sEMG recorded by each channel of MEAP on BB. | 143 |

| | |
|---|------------|
| Figure 5.2.7 Muscle activity maps of sEMG recorded from APB, showing the process of graded recruitment during contractions..... | 144 |
| Figure 5.3.1 Location of distal biceps tendon by MEAP and ultrasound image. | 147 |
| Figure 5.3.2 The selection of column of the MEAP on the biceps brachii of subject A. | 148 |
| Figure 5.3.3 Location of distal biceps tendon in isometric task. | 151 |
| Figure 5.3.4 Location of distal biceps tendon in dynamic task..... | 152 |
| Figure 5.3.5 Location of Achilles tendon by MEAP with IED of 10 mm. | 154 |
| Figure 5.3.6 Location of Achille tendon by MEAP with IED of 10 mm in isometric task..... | 155 |
| Figure 5.3.7 Location of Achille tendon by MEAP with IED of 10 mm in dynamic task..... | 156 |
| Figure 5.3.8 Location of Achilles tendon by MEAP with IED of 6 mm. | 157 |
| Figure 5.3.9 Location of Achille tendon by MEAP with IED of 6 mm in isometric task..... | 158 |
| Figure 5.3.10 Location of Achille tendon by MEAP with IED of 6 mm in dynamic task..... | 159 |
| Figure 5.4.1 High-density sEMG recording by MEAP for muscle injury prevention. | 161 |
| Figure 5.4.2 Experiment design for injury prevention..... | 162 |
| Figure 5.4.3 sEMG signals of biceps brachii of subject A with five different loads recorded by MEAP..... | 164 |
| Figure 5.4.4 RMS values of sEMG signals of subject A. | 166 |
| Figure 5.4.5 Median frequency details of sEMG signals recorded by MEAPs of subject A..... | 167 |
| Figure 5.4.6 Summary of RMS and fatigue information of subject A. | 168 |
| Figure 5.4.7 Muscle-tendon junction location of subject A in isometric task..... | 169 |
| Figure 5.4.8 Muscle-tendon junction location of subject A in dynamic task..... | 170 |
| Figure 5.4.9 Mean frequencies of sEMG signals of subject A with load of 5 kg recorded by MEAP and their normalised values..... | 171 |
| Figure 5.4.10 Scatter plot matrix of mean frequencies recorded in the 6 channels of column 1 of subject A during the isometric task..... | 173 |

| | |
|---|------------|
| Figure 5.4.11 Scatter plot matrix of mean frequencies recorded in 6 channels of column 1 of subject A during the dynamic task. | 174 |
| Figure 5.4.12 Statistical analysis of the differences in mean frequencies among different channels during full flexions by subject A..... | 175 |
| Figure 5.4.13 Statistical analysis of the differences in mean frequencies among different channels during full extensions by subject A... | 176 |
| Figure 5.4.14 A visual representation of the potential for muscle injury index, generated based on the assessments made using the MEAP. | 177 |
| Figure 5.4.15 The Gardner-Altman of sEMG signals recorded by MEAP on different subjects..... | 179 |
| Figure 5.4.16 Results of muscle information recorded by MEAP of the task carried by subject B..... | 181 |
| Figure 5.4.17 Results of muscle information recorded by MEAP of the task carried by subject C..... | 182 |
| Figure 6.1.1 Possible localizations determined from the electrodiagnostic study..... | 185 |
| Figure 6.1.2 Cross-section anatomy and abductor pollicis brevis insertion point. | 187 |
| Figure 6.2.1 Recording configuration of MEAP and needle on APB.. | 189 |
| Figure 6.2.2 MUAP from motor unit 1 in trial 1. | 192 |
| Figure 6.2.3 MUAP from motor unit 1 in trial 5. | 193 |

List of Abbreviations

| | |
|--------------|--|
| Ag | Silver |
| AgCl | Silver chloride |
| APB | Abductor pollicis brevis |
| ATP | Adenosine triphosphate |
| Au | Gold |
| BB | Biceps brachii |
| BO | Blood oxygen |
| BP | Blood pressure |
| CA | Commercial array |
| Cd | Cadmium |
| CEDE | The Consensus for Experimental Design in Electromyography projects |
| CNS | Central nervous system |
| CNTs | Carbon nanotubes |
| DoF | Degrees of freedom |
| ECG | Electrocardiogram |
| EEG | Electroencephalography |
| EGaIn | Eutectic gallium-indium |
| EMG | Electromyography |

| | |
|------------------|---|
| FCU | Flexor carpi ulnaris |
| FPC | Flexible printed circuit |
| GLM | Gallium-based liquid metals |
| IED | Inter-electrode distance |
| In | Indium |
| LM | Liquid metal |
| LMNPs | Liquid metal nanoparticles |
| MEAP | Metal-polymer electrode array patch |
| MDF | Median frequency |
| MNF | Mean frequency |
| MPC | Metal-polymer conductor |
| MU | Motor unit |
| MUAP | Motor unit action potential |
| NCS | Nerve conduction studies |
| NMJ | Neuromuscular junction |
| Pb | Lead |
| PDMS | Polydimethylsiloxane |
| PEDOT:PSS | Poly(3,4-ethylenedioxythiophene)- poly(styrenesulfonate) |
| PEG | Polyethylene glycol |
| PET | Polyethylene terephthalate |

| | |
|---------------|---|
| PI | Polyimide |
| PPA | Polyethylene glycol blended polydimethylsiloxane-based adhesive |
| PPG | Photoplethysmography |
| Pt | Platinum |
| PTFE | Polytetrafluoroethylene |
| PVA | Polyvinyl alcohol |
| PVP | Polyvinylpyrrolidone |
| RMS | Root mean square |
| sEMG | Surface Electromyography |
| SENIAM | Surface Electromyography for the Non-Invasive Assessment of Muscles |
| Sn | Tin |
| SNR | Signal-to-noise ratio |
| TA | Tannic acid |
| Ti | Titanium |
| TPP | Tannic acid, PEDOT:PSS & PVA blend |
| TPU | Thermoplastic polyurethane |
| WPU | Waterborne polyurethane |
| Zn | Zinc |

Chapter 1

General Introduction

Electrophysiology, the study of electrical activity in the body, plays a vital role in modern healthcare. It provides crucial insights into our health and well-being by monitoring various physiological processes, from the beating of our hearts to the activity of our muscles and nerves. With the rapid advancement of technology, we are on the brink of a transformative future where everyone could have a wearable electrophysiological recording device, revolutionizing the way we monitor our health. Among these technologies, the seamless integration of electromyography (EMG) recording devices into our everyday routines holds promise of a healthier and more interconnected world.

Imagine a future where every individual possesses a wearable EMG recording device seamlessly integrated into their daily routine offering them personalised care. Picture a world where athletes and fitness enthusiasts utilize wearable EMG monitors to optimize their training regimens, preventing injuries and enhancing performance. Envision a healthcare landscape where clinicians remotely monitor the vital signs of patients with neuromuscular disorders, enabling timely interventions and reducing hospitalizations. These unobtrusive, user-friendly devices would continuously track muscle activity, providing real-time data on our physical condition. Whether it is monitoring muscle fatigue during exercise,

assessing the impact of daily activities on muscle health, or detecting early signs of neuromuscular disorders, these wearables would empower individuals to proactively manage their well-being.

This future is not as far-fetched as it may seem. Wearable EMG recording devices have the potential to empower individuals to take control of their health, providing real-time data that can lead to better decision-making, personalized treatments, and improved overall well-being. The journey toward this future is already underway, with ongoing research and innovation pushing the boundaries of what these devices can achieve.

In this context, the primary objective of this thesis centres around the advancement and potential replacement of existing non-invasive EMG activity recording tools with newly developed devices, aimed at enhancing functionality and improving user experiences. To achieve this, the study indeed has an interdisciplinary nature, drawing from various domains, including materials science, engineering, electrophysiology, and clinical applications. Considerable effort has been made to systematically introduce the distinct components that form the foundation of this research.

The general introduction covers three critical elements: EMG, liquid metal (LM), and conductive polymers. It provides an overview of the current state of tools in this integrated field and highlights the existing gaps. The aim is to provide the research context most comprehensively possible.

1.1 Electromyography

1.1.1 Rationale

Electromyography (EMG) is a technique used to measure and record the electrical activity produced by muscles. When a muscle fibre is relaxed, the resting membrane potential is maintained by the intrinsic ionic equilibrium mechanisms. The cell maintains a greater negative potential within compared to the outside. When the muscle contracts in response to a neurotransmitter released at the motor endplate¹, the membrane depolarizes, resulting in a potential difference between the inner and outer regions of the cell. Each muscle cell (fibre) consists of multiple myofibrils, and within each myofibril, numerous sarcomeres can be found. When an action potential is generated, the release of calcium ions by the sarcoplasmic reticulum triggers the interaction between the two key proteins, actin and myosin, within sarcomeres. The conformational change in actin enables myosin to attach, and with the help of ATP, myosin pulls the actin strands together, leading to muscle contraction. Since a muscle is made of many fibres, the ionic movements across all of them lead to the generation of an electrical field that is detected by the EMG electrodes. The whole process is shown in Figure 1.1.1.

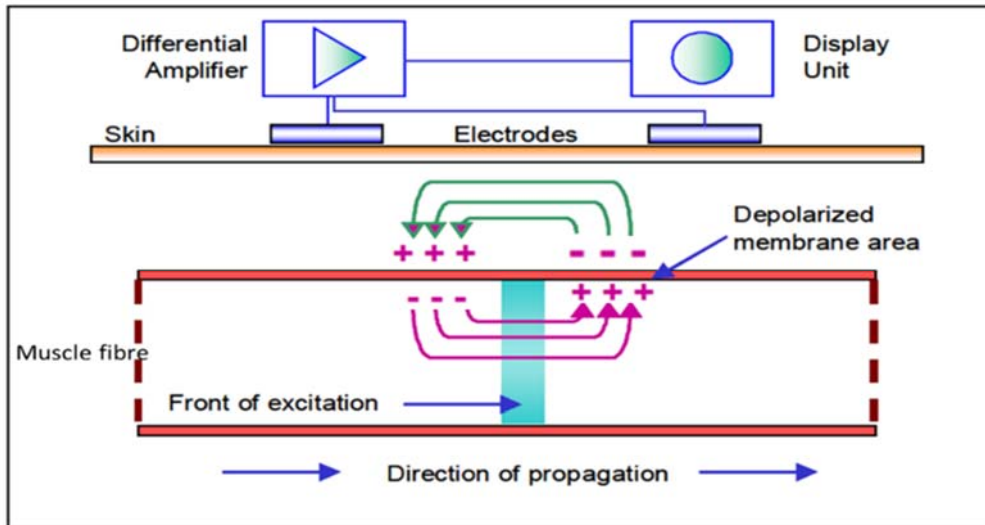


Figure 1.1.1 Recording by EMG electrodes. Electricity will propagate in both directions along the muscle fibre and be recorded by surface EMG electrodes. The amplitude of the signal is typically quite small, necessitating the use of a differential amplifier in the EMG recording system to amplify the signal. Adapted from *A practical introduction to kinesiological electromyography*, 1(2005), 30-5¹.

1.1.2 EMG signals parameter

1.1.2.1 Amplitude and root mean square (RMS)

The raw surface EMG (sEMG) signals can have amplitudes ranging from ± 5000 microvolts, which directly indicates the extent of muscle contraction. However, due to the presence of multiple muscle fibres, the amplitudes can vary significantly. In cases where the overall muscle loading state needs to be represented, the root mean square (RMS) is a more standardized and appropriate measure. This measure can be used to assess muscle activation levels and quantify muscle activity during different tasks or exercises. The RMS is calculated as below²:

$$RMS = \sqrt{\frac{1}{N} \sum_{i=1}^N x_i^2} \quad (1)$$

where x_i is voltage amplitude of EMG signal at the data point i ; N is the number of data points.

1.1.2.2 Median frequency (MDF)

One motor unit (MU) consists of one motor neuron and the muscle fibres it innervates. During muscle contractions, multiple motor units within the muscle are recruited, each with its own unique firing frequency. When all these motor units work together, their electrical signals combine to create a complex and varying signal. As a result, the sEMG signals can be transformed from the time-domain to the frequency-domain using a Fourier transform to display the MU recruitment pattern changes during muscle contraction. Besides, the bin width in Fourier transform is crucial as it determines the frequency range captured. A larger bin width provides lower frequency resolution and a broader range, whereas a smaller bin width offers higher frequency resolution and a narrower range. Typically, a decrease in median frequency (MDF) indicates muscle fatigue, as longer muscle contractions lead to the recruitment of fewer muscle fibres. This decrease in median frequency can also have significant implications in clinical diagnosis. For instance, if the decrease is observed at the beginning of a test, it may suggest a pathological change in the muscle, resulting in the recruitment of only a few muscle fibres for the contraction^{3,4}.

The MDF is calculated as below⁵:

$$\sum_{j=1}^{MDF} P_j = \sum_{j=MDF}^M P_j = \frac{1}{2} \sum_{j=1}^M P_j \quad (2)$$

where P_j is the EMG power spectrum at the frequency bin j ; and M is the

length of frequency bin.

1.1.2.3 Mean frequency (MNF)

MNF is generally slightly higher than MDF due to the skewed shape of the EMG signal power spectrum⁶. Despite this difference, the behaviour of MDF and MNF is often similar, making MNF another suitable measure for muscle fatigue assessments. However, it is worth noting that the variance of MNF is typically lower than that of MDF, and in certain research scenarios, MNF may exhibit distinct performance characteristics compared to MDF⁵. Consequently, the choice between these two measures should be guided by the specific research objectives. The MNF is calculated as below⁵:

$$MNF = \frac{\sum_{j=1}^M f_j P_j}{\sum_{j=1}^M P_j} \quad (3)$$

Where f_j is the frequency value of EMG power spectrum at the frequency bin j ; P_j is the EMG power spectrum at the frequency bin j ; and M is the length of frequency bin.

1.1.2.4 Time duration

The time duration of motor unit action potential (MUAP), compound muscle action potentials, or sensory nerve action potential plays a significant role in clinical diagnosis, particularly the duration of MUAP. A typical MUAP duration ranges between 5 and 15 ms, defined as the time from the initial deflection from baseline to the final return of the MUAP to baseline⁷. The duration of MUAP increases with the number of fibres and the cross-sectional area of a motor unit, and it is directly influenced by individual age and inversely by temperature⁸. In pathological cases, the number of

phases, duration, and amplitude of the MUAP may be abnormal, making duration changes valuable in distinguishing neuropathic or myopathic conditions. Longer MUAP duration is often associated with neuropathic disorders, such as chronic neuropathic lesions resulting from reinnervation. In contrast, myopathies typically involve a decrease in the number of functional muscle fibres within the motor unit, leading to shorter-duration MUAPs. Thus, the duration of MUAP is a critical aspect of clinical diagnosis. It is worth noting that although MUAPs can be reliably captured using needle electrodes, their detection with sEMG electrodes is more challenging.

1.1.3 EMG electrode types

There are two types of EMG electrodes: intramuscular and surface electrodes. Intramuscular electrodes can obtain more accurate signals directly from muscle fibres as they are inserted into the muscle, minimizing interference from other muscle fibres. In comparison with that, surface electrodes can only record muscle activity from the skin surface. While surface electrodes offer limited assessment compared to intramuscular electrodes, their non-invasive nature makes them more popular and widely used.

1.1.3.1 Needle electrodes

The earliest recorded EMG electrode in history was a knife touching the body of a frog, demonstrated by Luigi Galvani in 1790⁹. In 1825, Sarlandiere invented needle electrodes to directly receive signals of

muscle contraction from muscle bellies¹⁰. Monopolar and concentric needle electrodes are commonly used in clinics for disease diagnosis due to their ability to detect clearer signals from single fibre activity and provide a high signal-to-noise ratio compared to sEMG electrodes^{11–13}. However, the invasive nature of needle electrodes caused significant pain and tissue necrosis, despite providing more detailed information. Moreover, factors such as the risk of infection require these electrodes to be disposable, leading to increased experimental costs. As a result, intramuscular electrodes are less acceptable and popular for use in non-clinical settings and are not favoured by most researchers.

1.1.3.2 Surface electrodes

To address the challenges posed by needle electrodes, Guillaume Benjamin Duchenne introduced the use of electrodes on the skin in 1833⁹, which marked the beginning of sEMG. Since then, sEMG electrodes have gained increasing attention and undergone rapid advancements. They are commonly employed in a bipolar mode to record muscle activity, offering a simple and widely used method for monitoring muscle activity during sports and rehabilitation of function^{14–16}. However, some issues remain to be resolved, such as how to obtain stable and high-resolution signals using sEMG. Additionally, when monitoring single-fibre or single motor unit activity, sEMG may encounter interference from other muscle fibres, which presents a challenge in obtaining precise measurements. Continual efforts are being made to enhance the stability and resolution of sEMG signals, aiming to overcome these limitations in the precise monitoring of individual

muscle units. One promising approach involves the implementation of sEMG electrode arrays to augment the spatial resolution of recording. Presently, both one-dimensional (1D) and two-dimensional (2D) electrode arrays are extensively utilized for this purpose (Figure 1.1.2).



Figure 1.1.2 Surface electrode types in experimental signals. a Bipolar electrodes. **b** 1D electrode array. **c** 2D electrode array. Adapted from *Journal of Electromyography and Kinesiology* **49**, 102363 (2019)¹⁷.

1.1.4 Typical materials for sEMG electrode

Traditional noble metals like platinum (Pt) and silver (Ag) have widely been used for EMG electrodes before in the light of low impedance and high chemical stability. However, their high cost and short service life have led to scientists identifying new conductors. Most of them are softer than normal metals allowing them to maintain function for longer. These novel materials hold a promise for being commercially viable but are still fraught with issues like being harsh on the skin. Instead, if they were as flexible and stretchable like the skin, it would be a lot more acceptable for use.

1.1.4.1 Traditional metals

Pt can be used as a needle or sEMG electrode because of its remarkable chemical stability and resistance to corrosion^{18,19}. Pt is preferred as an

electrode for electrochemical analysis but not for EMG, as noble metals get polarised forming an electrical double layer when in contact with an electrolyte or even the skin. This double layer acts as a capacitor affecting charge transfer and thus introducing noise²⁰. Moreover, Pt is a ductile metal and survives less than a day due to the normal motion of a vertebrate limb²¹. Gold (Au), another popular electrode material, shares similar issues.

To address these challenges, Ag was used for sEMG electrodes fabrications. Unlike pure Pt, the Ag electrodes contains the main body of Ag and an AgCl film over it. This Ag/AgCl electrode is close to a nonpolarizable electrode allowing current to pass through electrode-tissue interface²². Since AgCl is insoluble in aqueous solutions, some conductive gels can be used at the interface to reduce the contact impedance. However, this typical wet electrode may not be suitable for long-term test, because of the desiccation of gels. Ag/AgCl electrodes also have limitations in terms of robustness, as the AgCl film can chip away after repeated use. Moreover, these electrodes might release highly toxic metal ions into the tissue, posing a risk of infection²³. As a result, researchers have been focused on developing robust, non-toxic, and dry electrode (using without gel) alternatives.

1.1.4.2 PEDOT:PSS

Poly(3,4-ethylenedioxythiophene)-poly(styrenesulfonate) (PEDOT:PSS) was widely used for chronically recording from neurones due to their low impedance and high charge density²⁴⁻²⁶. The interpenetrating network of conductive PEDOT domains and insulating PSS domains results in the

deposition of gel particles in a core-shell morphology (Figure 1.1.3).

It is favored as a material for in-vivo implanted electrodes due to its high biocompatibility²⁷ and low Young's modulus²⁸. However, pure PEDOT:PSS is not flexible enough to meet the requirements of sEMG applications on the skin, especially with large deformations²⁹. As a result, various strategies are being explored to enhance this material, such as polymer doping. More details will be discussed in chapter 1.3.3.

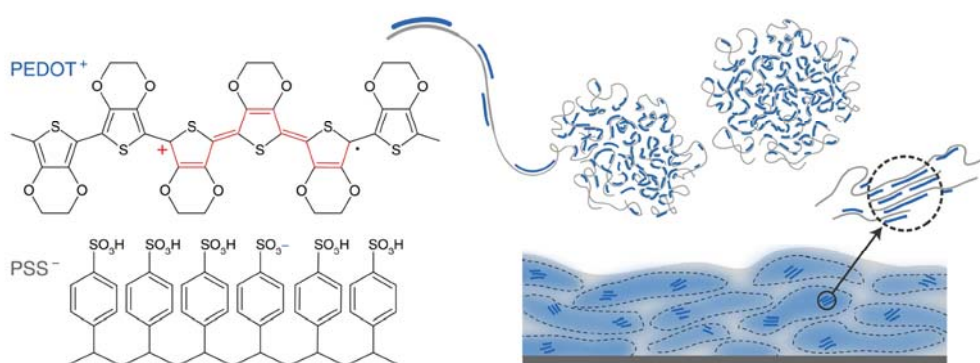


Figure 1.1.3 Chemical structure of PEDOT:PSS and core-shell structure of the film. Adapted from *Nat Commun* 7, 11287 (2016).

1.1.4.3 Carbon nanotubes

Carbon nanotubes (CNTs) is a popular material for a scaffold in tissue engineering because of its great biocompatibility with cells³⁰. CNTs also show various favourable electrical attributes like high conductivity and high charge density. These make CNTs good candidate material for bioelectrical interface³¹. Another reason for CNTs being popular with neuroscientists, for electrodes, is their high compatibility with biomolecules^{32,33}. They have been reported to be good performers as EMG

electrodes³⁴; however, CNTs have a relatively high Young's modulus, which hinders their conformal attachment to the skin, thus limiting their application in this field.

1.1.4.4 PDMS-based conductive composites

Polydimethylsiloxane (PDMS) is an organic polymer which is famous for its unusual flow properties (Figure 1.1.4). A simple fabrication requiring just the mixing of a base and curing agent has made PDMS the most popular material for various laboratory-based experiments, e.g., microfluidics^{35,36}. Moreover, PDMS is transparent, non-toxic, and biologically inert. The Young's modulus of PDMS, which can be around hundreds of kilopascals, makes it a suitable substrate for sEMG electrodes, considering that the Young's modulus of skin is approximately several megapascals³⁵. PDMS can be doped with metal or conductive particles to create good conductive composites. Many of the materials explored above, for instance CNTs³⁷, Ag or Ag nanowires are used with PDMS to make dry and portable EMG electrodes replacing Ag/AgCl electrodes³⁸. Another way to take advantage of PDMS is to coat a conductive layer of a ductile metal on it. Since the electrode can be thin the device then possesses great flexibility. Au and Titanium (Ti) have been with PDMS for EMG recording³⁹. While in this case, cracks on the surface are easily generated due to the modulus mismatch between PDMS and metals.

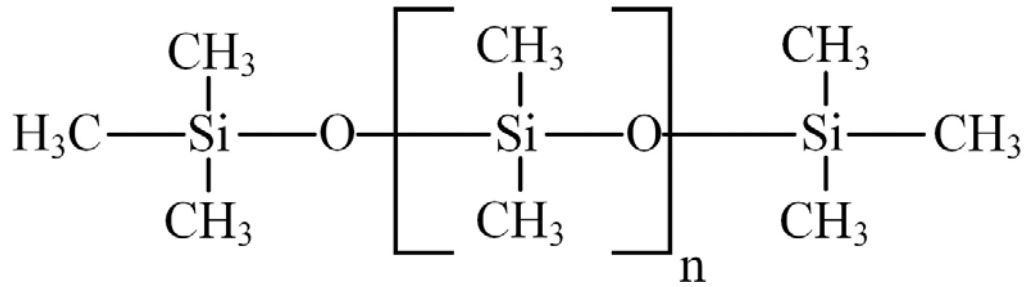


Figure 1.1.4 Chemical structure of PDMS. Adapted from *PLoS One* **16**, e0251092 (2021)

1.1.4.5 Gallium-based liquid metals (GLM)

Flexibility in EMG electrodes is highly desirable, and some designs incorporate a combination of materials to achieve this, using metals for contact points, elastomers for the main body, and metal wires between contact points and connectors. However, using traditional metals like Pt, Ag, or Au can still limit the overall flexibility of the device⁴⁰. GLM electrodes offer a promising solution to this issue, as they exhibit remarkable flexibility and stretchability, making them ideal for EMG applications. An easy fabrication process has been developed, which involves coating elastomeric substrates like PDMS with GLM patterns, thereby enhancing their commercial potential⁴¹, enhancing their commercial potential.

1.1.5 Key considerations for sEMG electrode materials

To make a good electrode, the selection of material is crucial; many factors need to be considered simultaneously towards this choice. The ideal material used for sEMG electrodes should have low impedance, be effective for long-term use, be bio-safe and have low fabrication cost.

1.1.5.1 Mechanical properties

To improve electrode performance, there is typically a strong focus on enhancing mechanical properties such as flexibility, stretchability, and durability. Flexibility and stretchability play a crucial role in extending the usage life of EMG electrodes, especially in prosthetics for growing children. This attribute also enables the fabrication of more portable and affordable devices, making them suitable not only for research purposes but also for everyday applications. Durability directly impacts the reusability of electrodes. By employing a robust design, fabrication costs can be reduced, and biosafety can be improved, thus expanding the potential applications of EMG electrodes to various fields.

1.1.5.1.1 Flexibility and stretchability

Flexibility of Pt and Ag/AgCl electrodes (Young's modulus for Pt – 168 GPa and Ag – 83 GPa) are much inferior to PDMS-based (Young's modulus – 360-870 KPa) electrodes. Pt and Ag are ductile and malleable metals, lacking elasticity, which often leads to permanent deformation after movement. In contrast, PDMS-based electrodes offer a significant advantage as they can conform to the contours of human skin and even adapt to regions within the body. This conformal nature allows the devices to maintain the same position and shape over extended periods of activity. As a result, PDMS-based electrodes are considered conformal electrodes, adhering closely to the skin. This characteristic brings several benefits, such as longer service life, reduced need for replacement, and higher signal-to-noise ratio (SNR). Figure 1.1.5 illustrates the issue where a non-conformal electrode creates a gap between itself and the skin. With the

volume of 1 mm^3 , the impedance of epidermis is about $157 \text{ M}\Omega$, while the impedance of air gap is about $170 \times 10^3 \text{ M}\Omega$, which has 3 order-of-magnitude differences⁴². When muscle contracts, the air gap created by non-conformal electrode provides extra resistance and capacitance to increase impedance of the whole circuit, which decreases signal quality. It also might cause motion artefact during the muscle movements. In addition, the circuit model illustrates how conformal electrodes keep the stable impedance of the whole circuit between skin and electrodes, which help conformal electrodes maintain the signal quality during recording. Therefore, the lack of conformability is the primary challenge faced by noble metal electrodes.

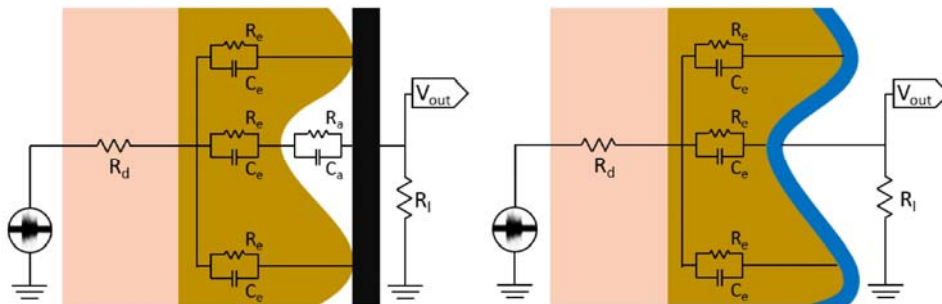


Figure 1.1.5 Circuit models of non-conformal and conformal electrodes on skin folds. In the circuit model of non-conformal electrodes, dermis resistance (R_d), epidermis resistance (R_e) and capacitance (C_e), air gap resistance (R_a) and capacitance (C_a) are considered.

1.1.5.1.2 Durability

To discuss the durability of electrodes, three factors should be considered generally: whether electrodes will (1), deform; (2), need reset; (3), lose signal quality after long-time using. For the first factor, muscle movements usually lead to deformation or motion of Pt electrode attached to the skin.

This makes Pt electrode hardly suitable for sEMG recording electrode for long-term wearable devices. With the second and third, dry electrodes, particularly those utilizing an elastic substrate like PDMS-based electrodes, demonstrate superior durability compared to Ag/AgCl electrodes. Wet electrodes can suffer from the issue of gel desiccation, which leads to a significant reduction in signal quality during recording while dry electrodes do not encounter this problem. In summary, dry electrodes with elastic substrates typically exhibit robustness and longevity, making them a favourable choice for various applications.

1.1.5.2 Electrical properties

There are two issues usually attracting major attention in EMG recording, impedance, and corrosion.

1.1.5.2.1 Impedance

Impedance is an electrical property of material to oppose alternating current flow. Impedance depends not only on the material itself but also effective contact area of electrode that smaller area means higher impedance. Because impedance also varies with the frequency of measurement current, the value measured by current with a frequency of 1 kHz is mostly used to characterize the resistance ability of electrodes. A desirable impedance level is dependent on the specific program or experiment. Lower than 10 k Ω impedance of electrode tested by 1 kHz current is roughly considered as satisfying in sEMG. However, a layer of dead skin cells covering outside human body will provide a high skin-

electrode impedance⁴³. Thus, many preparations on the skin need to be done to reduce impedance before measurement like shaving the test position, cleaning with alcohol or using conductive gel between skin and electrodes⁴⁴. In addition, the stability of impedance between skin and electrodes also counts for obtaining low noise signals⁴⁵. This problem existing in the whole measuring process, again attracts the attention back to mechanical properties of electrodes to avoid relative motion between skin and electrodes. This correlation highlights the need to consider multiple factors simultaneously when fabricating a high-quality EMG electrode.

1.1.5.2.2 Corrosion

Another electrical problem for electrode failures is corrosion. There are many causes for corrosion, and they mostly have tight relations with the material selection. Galvanic corrosion usually happens in metals. This chemical change should be avoided if possible, considering the importance of stability in signal recording. Other than voltaic cell reactions, metals are also likely dissolved in solutions, resulting in toxicity release or electrode disappearance. For example, in sEMG where sweat is the most popular environment, any tiny change in pH or ion concentration of sweat probably causes corrosion of metal electrodes. Noble metal electrodes will form an oxide layer on the surface to resist corrosion, like Pt and stainless steel²¹. Ag also forms oxide layer on the surface, but it will be eroded slowly by chloride ions which poison surrounding tissues. The corrosion problem will be intensified in stimulation because the current flow is greater. Au and Ag

will rapidly dissolve with chelating chloride ions, and stainless steel is likely to have rust corrosion. Compared to metal electrodes, Ag/AgCl or PDMS-based conductive composite electrodes have much better performance in corrosion resistance. The AgCl layer outside is insoluble in most aqueous environments, and PDMS is also an inert material, contributing to the formation of robust electrodes.

1.1.5.3 Biological properties

It is important to ensure the electrode products are safe to human. sEMG electrodes are considered biologically safe if the material is non-toxic, and the skin is not irritated on contact. In fact, biocompatibility is mostly discussed for implanted device in-vivo because stricter criteria need to be satisfied. Some materials for implanted, in-vivo neural recording electrodes will be discussed based on previous research providing a more detailed assessment of biocompatibility of electrodes.

Pt shows a really good performance in biocompatibility. Many researches have been done to prove the safety of this metal. For example, Pt wire was employed as a reference electrode chronically for over four years in Macaque cortex⁴⁶. Food and Drug Administration also conducted study suggesting there is no evidence that Pt is toxic to in-vivo tissue⁴⁷. Au, like Pt, has been proven to be biocompatible⁴⁸. However, both metals are too expensive for the fabrication of devices.

Ag salts are toxic to the tissue making Ag not suited for implanted electrodes. Although Ag/AgCl electrodes are widely used in sEMG, they probably irritate the skin³⁷. During the movement of muscles, AgCl layer

might be damaged to give a direct contact between skin and Ag. In view of safety, Ag/AgCl electrodes need to be optimized in many aspects. This also prompts novel materials to be studied in the field like PEDOT:PSS, CNTs or LMs. Fortunately, none of them shows harm to cell growth which means good biocompatibility^{30,41,49}. Another advantage for using these new conductors is their substrates like PDMS or thermoplastic polyurethane (TPU) also have high biocompatibility which ensures the electrodes could be used in-vivo or on the skin.

1.1.5.4 Commercial properties

The most popular and successful commercial electrodes for EMG recording is Ag/AgCl electrodes. Although most electrodes are still being explored in laboratories, it is valuable to discuss their commercial properties like the difficulty of fabrication or cost. These factors can be important for the electrodes to be on future market.

1.1.5.4.1 Fabrication process

Difficulty, speed and scale are common factors to consider in fabrication process. Electrodes which can be fabricated easily, and quickly can be scaled-up thus having potential to occupy a position in the future market. However, according to most articles about metal electrodes, the difficulty of fabrication becomes the primary issue. To provide flexibility to their electrodes, researchers often choose to combine polymers with metals such as Pt, Au, or Ag, or modify the metals to have specific physical features. Thus, this results in many complicated steps like evaporation, deposition, sputtering or plasma etching. For example, there are five steps

to deposit Pt on silicon substrates and then finally remove from particular positions to make contact sites¹⁹. To coat Au on polymers, magnetron sputtering or RF sputtering are usually utilized with Ti as attachment layer³⁹. There is no doubt that difficulty of fabrication is increased in the circumstance of dealing with so many layers of different materials. However, when comes to novel conductors, fabrication is much simplified. For instance, in a CNTs/PDMS electrode fabrication, a few hours of PDMS curing is the only step, after the dispersion of CNTs in PDMS which needs 5 - 15 hours³⁷. Though the operation is much easier, too long time of production still restrains the commercial potential of this type of electrodes. The time consumption can be even reduced greatly if conductors are coated instead of being embedded. GLMs possess this advantage exactly that they can be screen-printed or inkjet-printed which available for massive production⁵⁰. The whole process can be done in 2 hours, which has a quite high efficiency of fabricating. This impressive method has huge potential in commercial manufacture.

1.1.5.4.2 Cost

A price comparison between materials was made to show the difference, in Table 1.1.1.

| Material | Price per gram (£) |
|--------------------|--------------------|
| Pt - 204013 | 285.0 |
| Au - 265772 | 297.2 |
| CNTs - 901002 | 174.0 |
| PEDOT:PSS - 483095 | 61.2 |
| Ag - 796042 | 32.0 |
| EGaIn - 495425 | 13.9 |

Table 1.1.1 A comparison of cost of metals. The prices at 2023 are from website of sigmaaldrich.com.

In view of cost of material, Pt, Au and CNTs are not suitable materials for EMG electrodes. PEDOT:PSS, Ag and eutectic gallium-indium (EGaIn) are far more preferred for an affordable device. Currently, both PEDOT:PSS and EGaIn are under research for potential applications in EMG^{51,52}.

1.1.6 Limitations of current sEMG electrodes

In the case of wet electrodes, the gel plays a crucial role in ensuring high-quality recordings. However, this component also introduces certain limitations. Desiccation, or drying, poses a significant challenge as it leads to a decline in both gel adhesiveness and conductance over time. As the gel dries, the impedance of the interface increases, resulting in elevated baseline noise. This phenomenon can negatively impact signal quality during extended recording sessions. Notably, studies indicate that the RMS of noise triples in value after 24 hours of drying⁵¹. Furthermore, the conformability of such electrodes on the skin is not good enough, often leading to detachment when the subject sweats. This issue is significant as poor contact can result in position shifts, thereby affecting both signal

quality and stability.

Usually, to lower the crosstalk from other muscles, an optimal electrode should be lower than 5 mm in size and the inter-electrode distance (IED) should be lower than 10 mm¹⁷. However, the spatial resolution of these electrodes is limiting, owing to their surface areas when recording activity of both small and the large muscles. Taking the forearm as an example, obtaining signals from a specific muscle using sEMG electrodes can be challenging due to crosstalk from adjacent muscles beneath the skin.

To address this issue, high-density electrode arrays have been developed and used in laboratory settings⁵³. Upon meeting the electrode size and IED requirements mentioned above, these arrays can offer more precise recordings. While the material for the most popular sEMG commercial array currently available is polyimide, which has the Young's modulus of 3 GPa. Due to its characteristics, without the incorporation of specific design elements like a serpentine pattern, achieving complete conformal contact with the human skin (with a Young's modulus of 10 kPa) is challenging. Thus, the choice of materials for such electrode arrays would once again raise the issue of conformability.

1.1.7 EMG international standards for sEMG recording

About the international standards for sEMG recording, the Surface Electromyography for the Non-Invasive Assessment of Muscles (SENIAM) and The Consensus for Experimental Design in Electromyography (CEDE) projects stand as influential cornerstones. SENIAM, a comprehensive compilation of guidelines and recommendations, establishes a

standardized approach encompassing various facets of electromyographic operations. Covering crucial aspects including electrode shape and size, IED, electrode orientation, placement of working and reference electrodes, fixation methods on the skin, and signal acquisition techniques, SENIAM ensures a uniform and dependable framework for conducting muscle activity studies. On the other hand, CEDE introduces a new paradigm by emphasizing dynamic electrode designs, fostering advancements in flexibility, comfort, and wearability for improved electromyographic applications. Furthermore, emerging guidelines dedicated to high-density electrode arrays are in the process of development. These encompass a range of facets, including array configuration, optimal muscle attachment sites, and tailored protocols for sEMG recording^{17,54}. These guidelines collectively shape the future of muscle activity assessment, bridging scientific rigor with innovative electrode technologies. Anyone engaged in sEMG recording or the development of novel electrodes should make reference to these evolving guidelines.

1.1.8 EMG signal processing

In EMG, the signal processing assumes a paramount role in unravelling intricate information concealed within muscle activity. A systematic sequence of steps constitutes this processing endeavour, with each step encompassing distinct objectives and methodologies.

1.1.8.1 Preprocessing stage

During this stage, various filters are employed to mitigate noise and motion

artifacts. In most scenarios, the implementation of a notch filter is essential to effectively attenuate powerline noise, often at frequencies of 50 or 60 Hz. Another common practice in sEMG recording involves the use of a 20 Hz high-pass filter to eliminate low-frequency noise resulting from cable oscillations or body motions. Through the strategic use of various filters, researchers can concentrate on EMG signals within specific power spectrum bands. However, it is important to acknowledge that employing fewer filters always preserves a greater portion of information within the EMG signals.

1.1.8.2 Feature extraction

After preprocessing, the feature extraction stage unfolds, including the quantitative parameters such as RMS, MDF, MNF or temporal attributes. These extracted features encapsulate the fundamental characteristics of muscle behaviour. For instance, the RMS is linked to muscle loading and MDF is related to muscle fatigue. Many of these parameters form the foundation for subsequent classification processes.

1.1.8.3 Temporal-frequency analysis

Temporal-frequency analysis in EMG serves as a powerful tool to reveal the dynamic patterns and variations of muscle activity over time. By combining time-domain and frequency-domain information, this approach demonstrates how muscle contractions evolve temporally and how their frequency components change. Such identifications of specific muscle activation patterns, modulation of frequency content during fatigue, and the

detection of transient events within the EMG signal can characterize the communication between the central nervous system and muscles. This method facilitates a deeper understanding of motor control, neural pathways, and the neural-muscular interface, contributing to the advancement of neurophysiological research and clinical applications in spinal cord and brain-related EMG studies.

1.1.8.4 Machine learning classification

Machine learning has emerged as a powerful tool in many fields, including EMG. EMG signals are highly complex and contain rich information about muscle contractions, fatigue, and other physiological processes. Machine learning algorithms can be trained to recognize specific patterns and features within EMG signals, allowing for the identification of different muscle movements or gestures. This has significant implications for prosthetics and assistive devices, as machine learning can enable precise control based on EMG signals, enhancing the interaction between humans and technology. It has also been employed to study the dynamics of muscle coordination and motor unit recruitment, providing a deeper understanding of the mechanisms of motor control.

In fact, machine learning can also be employed in all the above steps to enhance the accuracy and efficiency of EMG signal processing. Traditional methods for noise reduction, feature extraction, and temporal-frequency analysis can be time-consuming and require extensive manual tuning. By utilizing machine learning algorithms, the unique characteristics of individual EMG signals can be learned and adapted, resulting in more

accurate and consistent results.

1.1.9 Clinical diagnosis

Many myopathic disorders have a high mortality rate due to their frequent impact on other organs, such as the lungs, joints, heart, and skin. The ten-year mortality rate from idiopathic inflammatory myopathies alone was reported to be 31%⁵⁵. While most myopathic disorders are treatable, the presence of neurogenic disorders with similar symptoms can complicate precise diagnosis and specific treatments. In such scenarios, EMG emerges as a crucial tool for patient examination. Additionally, EMG plays a significant role in assessing and guiding the rehabilitation of certain cerebrovascular diseases, such as stroke, often in conjunction with electroencephalography (EEG)⁵⁶.

1.1.9.1 Diagnosis standards

As a pivotal technique for diagnosing and facilitating the recovery of nerve or muscle dysfunction, EMG is anticipated to gain broader application in clinical diagnosis, scientific research, and even daily monitoring. However, a disconnect between the needs of clinicians and the offerings of technicians, stemming from diverse research directions, has hindered the development of highly effective tools. There is an urgent need for a criterion that accurately reflects requirements of clinicians. In an effort to bridge this gap, fundamental information about the most common neuropathic and myopathic disorders and the functions of EMG tools have been compiled in Table 1.1.2.

| Disorders | Symptoms | EMG functions | Electrode |
|------------------------------------|---|--|--------------|
| Idiopathic inflammatory myopathies | Muscle weakness, joint pain and general tiredness ⁵⁷ . | Muscle-fibre conduction velocity for diagnosis ⁵⁸ . | Needle sEMG. |
| Stroke | Inability to move or feel on one side of the body, problems understanding or speaking ⁵⁹ . | EMG, neuromuscular electrical stimulation (NMES) for rehabilitation ^{56,60,61} . | sEMG, EEG. |
| Multiple sclerosis | muscle weakness, trouble with sensation, trouble with coordination ⁶² . | Evoked potentials, nerve conduction velocity (NCV) for diagnosis ⁶³ . | sEMG. |
| Myasthenia gravis | Varying degrees muscle weakness, drooping eyelids, trouble talking or walking ⁶⁴ . | Repetitive nerve stimulation (RNS), single-Fibre EMG (SFEMG) for diagnosis ⁶⁵ . | Needle. |
| Parkinson's disease | Shaking, rigidity, difficulty walking ⁶⁶ . | Feature extraction, reduce pathological tremor for rehabilitation ⁶⁷ . | sEMG. |
| Huntington's disease | Problems with coordination, jerky body movements ⁶⁸ . | Feature extraction, reduce pathological tremor for diagnosis ⁶⁹ . | sEMG. |
| Spasticity | Intermittent or sustained involuntary activation of muscles ⁷⁰ . | Feature extraction, reduce pathological tremor for diagnosis ⁷¹ . | sEMG. |
| Clonus | A rhythmic, oscillating, stretch reflex mostly in ankle ⁷² . | Feature extraction, reduce pathological tremor for rehabilitation ^{72,73} . | Needle sEMG. |
| Epileptic seizures | Including shaking of the limbs and loss of consciousness ⁷⁴ . | Real-time monitoring for diagnosis or rehabilitation ⁷⁵ . | sEMG. |
| Diabetic peripheral neuropathy | Burning and knife-like pain, numbness ⁷⁶ . | Detection of sensorial and motor defects in nerves for diagnosis ⁷⁷ . | sEMG. |

Table 1.1.2 Fundamental information about disorders and the associated EMG tools.

1.1.9.2 Current tools and limitations

Currently, needle electrodes are the primary clinical diagnostic tools for EMG. While these electrodes offer exceptional signal quality and recording precision, especially for capturing MUAPs, they also come with certain

drawbacks. The invasive nature of needle EMG, involving the insertion of fine electrodes into muscles, can lead to discomfort and pain. This discomfort is further exacerbated by the repetitive insertion process required to locate specific motor units.

In the context of children, these disadvantages become even more pronounced. Children may experience difficulties in cooperating during the procedure due to factors such as fear, discomfort, or an inability to remain still. Their lower pain tolerance can present challenges and potential distress, making the procedure more challenging to perform. Additionally, the muscles targeted for needle EMG in children may be smaller compared to those in adults. This size difference can impact the ease of electrode insertion and affect the overall quality of the recorded signals.

In summary, needle EMG electrodes offer valuable insights into muscle function and neuromuscular disorders, but their invasive nature and potential discomfort should be weighed against the benefits in each clinical or research scenario. If a novel non-invasive tool can achieve accurate recording and recognition of MUAPs, akin to needle electrodes, it could significantly enhance patient comfort while upholding the precision and reliability of the diagnostic process. This innovation can have the potential to revolutionize EMG clinical diagnosis by substituting invasive tools with non-invasive alternatives.

1.2 Liquid metal

Gallium-based liquid metal (GLM) showcases remarkable attributes, including high conductivity and biocompatibility, making it a valuable asset in the advancement of conformal bio-electronics. Through its synergy with polymers, metal-polymer conductors (MPC) present a versatile framework for creating conformal cyborg devices. These devices empower capabilities like sensing, restoration, and augmentation within the human body, promising a range of transformative applications. This section delves into the foundational characteristics of this innovative material and its synergistic applications in biosensing alongside other polymers.

1.2.1 Fundamental properties of GLM

The unique physical properties of Ga have positioned it at the forefront of flexible electronics, leading to its widespread utilization. The inclusion of Ga dimer imparts covalent characteristics and reduces the melting point to 29.8 °C (1 atm). This element has the ability to create alloys with other metals like In, Sn, Zn, Cd, and Pb, resulting in even lower melting points which can retain their liquid state at room temperature. Furthermore, the extremely low vapor pressure of Ga (approximately 0.001 Pa at room temperature) ensures this metal can be handled openly without the risk of inhalation. This quality makes it a notably safer substitute for mercury, given that the vapor pressure of mercury is approximately 1.26 kPa at room temperature.

The liquid nature of GLM makes it remarkably stretchable and well-suited for a range of fabrication techniques. GLM also demonstrates impressive conductivity, with examples like Galinstan and EGaln having a comparable conductivity of approximately $3.4 \times 10^6 \text{ S}\cdot\text{m}^{-1}$ at 20 °C, which is roughly 30 times that of conductive polymers. This heightened conductivity is crucial for electrical applications, such as electrophysiology, reconfigurable antennas or wearable stimulators.

Furthermore, Ga possesses distinct chemical and biological attributes that render it exceptionally well-suited for the construction of conformal devices. When exposed to air, it develops a dense oxide skin that can be manipulated by techniques such as lasers or electrochemical reactions^{78,79}. Additionally, GLM shows low toxicity to cells⁸⁰, making it a viable choice for implantable devices and various bio-applications.

1.2.2 Methods to fabricate and pattern GLM

To create a functioning device, it is necessary to pattern GLM in order to establish electrical circuits that can support a range of versatile functions. However, the high surface tension of GLM precludes its direct printing like traditional inks. Two primary approaches are pursued in this context: 1. patterning of bulk GLM; 2. patterning of liquid metal nanoparticles (LMNPs).

1.2.2.1 Methods to pattern bulk GLM

GLM patterning can be achieved through the utilization of a stencil, allowing the GLM to create patterns on the substrate⁸¹. This process

requires optimal wettability of the GLM on the substrate. Various methods, such as a sprayer, a roller or a blade can be employed to facilitate the passage of the GLM through the stencil. Extrusion printing is another viable method for GLM patterning, akin to a painting process⁸². Notably, the GLM droplet can assume a three-dimensional structure when utilizing gallium oxide to stabilize its shape. This technique can also be employed for constructing dangling connections in electronics. GLM can also be injected into microfluidic channels to create specific patterns⁸³. The wettability of the GLM against the microfluidic channel is a critical consideration in this approach, as inadequate wettability can result in increased injection resistance.

In addition to the aforementioned direct printing methods, GLM can also be patterned using selective adhesion techniques. Initially, a pattern is designed with a high affinity for GLM, in contrast to the untreated portion of the substrate. Subsequently, the process of patterning GLM can be likened to a stamping procedure. This affinity can be classified into two categories: metal-metal and metal-polymer interactions. With regard to metal-metal interaction, specific metals such as Au and Cu display a tendency to create alloys with Ga once the Ga oxide layer is eliminated, resulting in selective binding⁸⁴. Further enhancement of this interaction can be achieved by modifying surface morphology through adjustments in surface tension. With regard to polymer-metal interaction, the oxide skin of GLM tends to establish hydrogen bonds with diverse chemical groups like -OH and -NH₂⁸⁵. Consequently, polymers abundant in these groups, such as polyvinyl alcohol (PVA) and TPU, are commonly employed for the initial

fabrication of specific patterns.

1.2.2.2 Methods to pattern LMNPs

Reducing the size of GLM droplets is a good strategy to uniformly distribute liquid metal within a solution or ink, thereby aiding in simplified patterning. Utilizing various physical methodologies, GLM can be transformed into LMNPs. For instance, the utilization of mechanical mixing or sonication has successfully generated LMNPs on a large scale^{41,50}. Tuning the size of these droplets within the nano to micro range can be achieved by manipulating power and time of processing. To further enhance droplet size uniformity, the adoption of microfluidics or laser beams techniques has been explored for the creation of LMNPs, although scalability can be limited by the available capabilities of equipment^{86,87}. Moreover, alternative approaches have been investigated for generating LMNPs through a bottom-up process. By employing physical vapor deposition, the condensation of GLM vapor leads to the production of LMNPs⁸⁸. An additional technique involves the reduction of gallium ions within a solution to synthesize gallium nanoparticles, akin to traditional nanomaterial synthesis, ensuring a heightened level of consistency in particle size⁸⁹.

By dispersing LMNPs in a specific solvent, they can function as a conductive ink for fabricating flexible electronics. Screen-printing is a viable method for large-scale production with simplicity and scalability, although it achieves a moderate resolution (50 μm)⁴¹. Conversely, the microfluidic channel technique can be applied to achieve higher-resolution patterning of LMNPs, reaching a resolution of 5 μm ⁹⁰. However, this approach may

suffer from efficiency limitations. Alternatively, the utilization of a stencil and sprayer enables the patterning of LMNPs onto diverse surface morphologies, albeit with a constrained resolution (100 μm)⁹¹. Introducing magnetic metals into the LMNPs allows for the utilization of a magnetic field to achieve precise patterning. The magnetic LMNPs can be manipulated within a flexible polymer matrix, aligning with the direction of the magnetic field⁹².

The subsequent critical step in the fabrication of LMNP-based electronics involves the sintering of the LMNPs. Due to the insulating nature of the oxide layer present on GLM, it becomes crucial to rupture this layer and establish conductive pathways between the GLM components within the LMNPs. The primary mechanism for achieving this rupture involves the application of external energy to the oxide layers, with common strategies including mechanical force, laser irradiation, heat, and acoustic methods. In the context of mechanical force, localized pressure, peeling, stretching, or subjecting the circuits to humidity can all achieve sintering^{41,50,93,94}. In the case of laser irradiation, application of a high-energy laser leads to extensive rupture of the oxide skin, facilitating complete sintering of the LMNPs⁹⁵. With regard to heat, thermal expansion microspheres have been introduced into LMNPs to induce oxide layer breakage through squeezing at elevated temperatures⁹⁶. Sound-based sintering has also been explored, where the acoustic field is employed to sinter LMNPs within the polymer matrix⁹⁷. Ultrasound is utilized to convey microscopic force, enabling relatively microscale sintering of LMNPs within the polymer framework, thus achieving sintering without the risk of LM leakage.

1.2.3 Metal-polymer conductors (MPC)

A substrate for liquid metal is essential in devices based on GLM, as GLM remains in a liquid state at room temperature and lacks a fixed shape. Polymers serve as a crucial solution to bestow GLM-based devices with structural stability and expanded potential such as stretchability and flexibility. This synergistic combination of GLM and polymers is commonly referred to as MPC.

Various types of polymers can serve as substrates or matrices for GLM-based devices. LMNPs can be directly printed or transferred onto elastic hydrogels^{98,99}, electro-spun films⁹⁹ or conventional elastomers such as silicone⁴¹, polyacrylics⁵¹, block co-polymers¹⁰⁰. In the case of 3D devices, LM can be integrated into polymer sponges, expanding the range of potential applications¹⁰¹.

PDMS stands out as a formidable candidate for substrate material due to its optical clarity, inertness, non-toxicity, and crucially, its elasticity, as detailed in previous sections (Chapter 1.1.4~1.1.5). By integrating PDMS with GLM, researchers have created a printable MPC with exceptional attributes: high stretchability and flexibility (up to 500% strain), impressive conductivity (8×10^3 S/cm), and biocompatibility⁴¹. This pioneering material has found widespread application across various domains, catalysing advancements in the realm of bio-devices.

1.2.4 Applications in biosensing

The emergence of unforeseen acute illnesses and a rising population

vulnerable to such conditions have heightened the need for real-time biosensing. Consequently, wearable devices are gaining remarkable traction in the market. Wearable sensors have assumed pivotal roles in diverse scenarios, encompassing breath sensors for divers, motion sensors for athletes, and electrocardiogram sensors for fitness enthusiasts. MPC stands out as a highly competitive material in the realm of wearable biosensing device advancements, primarily owing to its exceptional stretchability. This attribute empowers highly flexible electronics to achieve superior conformability on the human body. As a result, these remarkably pliable electronics enhance user experiences, enable expanded functionality, and ensure heightened recording precision.

1.2.4.1 Movements

With the expansion of the metaverse and virtual reality devices, the demand for precise motion monitoring of hands and limbs is in a rapid growth. The essential objective for developments of such devices is to enhance immersive encounters of users within the virtual realm. Despite the maturity of motion capture techniques, which normally use recording optical markers affixed to body parts, several limitations persist. For instance, optical markers on fingers and other hand components can occlude each other, leading to challenges in tracking intricate finger movements through video-based methods. Such constraints are unacceptable in human-machine interactions. Fortunately, the stretching of skin over joints can approximate joint angles, and strain sensors prove

effective in this context. The underlying principle is that alterations in resistance correspond to conductor elongation. In such scenarios, MPC emerges as an exceptional option for a strain sensor due to its remarkable capacity to withstand elongation.

Researchers used the screen-printing technique to pattern GLM as strain sensors onto latex gloves⁴¹ (Figure 1.2.1a). This innovative approach enables the development of a wearable keyboard that accelerates the translation of ideas into written text by recording the deformation of each finger. However, a solitary layer of GLM circuits might not suffice for comprehensive hand motion tracking, considering the intricate joints present in the hand. To address this challenge, researchers have devised a multilayered electronic tattoo technique¹⁰⁰ (Figure 1.2.1b). Through this advancement, the simultaneous measurement of hand movements in 15 degrees of freedom can be achieved. The wireless real-time tracking of finger motions is enabled via Bluetooth transmission. Such hand movement monitoring bears potential applications in diverse realms such as game control and remote surgery. Furthermore, the versatility of MPC strain sensors extends across various substrates. Such novel GLM printing inks are capable of being applied to Polyethylene terephthalate (PET), PDMS, TPU, latex, and textiles⁵⁰ (Figure 1.2.1c). Leveraging this innovation, a multifunctional intelligent T-shirt was designed to capture the chest expansion movements of the wearer. Additionally, a novel wet-adhesive elastomer, PPA (Polyethylene glycol blended polydimethylsiloxane-based adhesive), was introduced by infusing Polyethylene glycol (PEG) into PDMS¹⁰² (Figure 1.2.1d). This adhesive

substrate supports the stable operation of GLM strain sensors for over two days, even in instances of excessive sweating. This type of MPC, substantiated by these prolonged tests, underscores its stability and reliability.

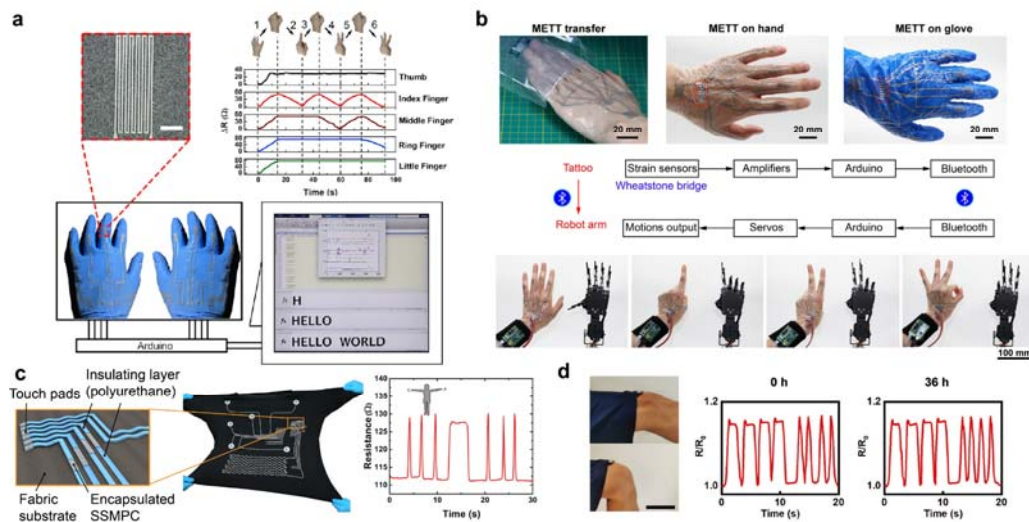


Figure 1.2.1 MPC electronics for movement monitoring. **a** An MPC strain sensor on a wearable glove keyboard through finger motion monitoring. **b** The application of a multilayered electronic tattoo facilitating remote control of a robotic hand. **c** MPC integrated strain sensors on a wearable T-shirt, designed to monitor chest expansions. **d** Utilization of an MPC strain sensor affixed to a wet-adhesive elastomer, enabling prolonged recording on the knee. Adapted from *iScience* **4**, 302–311 (2018); *Sci Adv* **7**, eabe3778 (2021); *ACS Appl Mater Interfaces* **11**, 7138–7147 (2019); *Adv Funct Mater* 2200444 (2022).

1.2.4.2 Electrophysiology

ECG The electrocardiogram (ECG) serves as a crucial diagnostic tool for assessing the cardiac characteristics of individuals through quantitative measurements. The reliability and accuracy of diagnoses heavily depend on the quality of ECG signal recording. Furthermore, the ability to capture anomalies that may occur sporadically necessitates long-term recording in

ECG assessments. Both these aspects underscore the importance of ECG electrodes capable of recording high-quality signals over long-term periods. However, existing commercial electrodes encounter challenges in achieving consistent, long-term recording due to issues like gel desiccation, non-conforming electrode detachment during skin deformation, and the loss of adhesive effectiveness in the presence of moisture or sweat. To address these challenges, various strategies employing GLM devices have been explored to enhance ECG electrodes. Researchers developed a direct method involving spraying skin-adhesive liquid metal particles directly onto the skin to create ECG electrodes⁹¹ (Figure 1.2.2a). The resulting pattern of these particles ensures conformal contact even in skin folds, significantly reducing impedance within the ECG frequency range. This low impedance leads to an improved signal-to-noise ratio for electrodes made from skin-adhesive liquid metal particles. Consequently, these electrodes outperform commercial electrodes in capturing clear P waves even after 24 hours of application. For sustained long-term recording, a wet-adhesive elastomer is employed as the substrate for MPC electrodes, ensuring enhanced conformal and stable adhesion¹⁰² (Figure 1.2.2b). After 48 hours, MPC electrodes on wet-adhesive elastomer continue to exhibit clear P, QRS, and T wave recordings, whereas commercial electrodes exhibit more noise due to hydrogel water loss and irreversible deformation on the skin. Researchers have also introduced a novel material, EGaln-SBS, by incorporating GLM circuits into electro-spun elastomeric fibre mats⁹⁹ (Figure 1.2.2c). This material offers high permeability, stretchability, conductivity, and electrical stability. The EGaln-

SBS electrode consistently captures high-quality ECG signals, irrespective of whether the skin is relaxed or under compression.

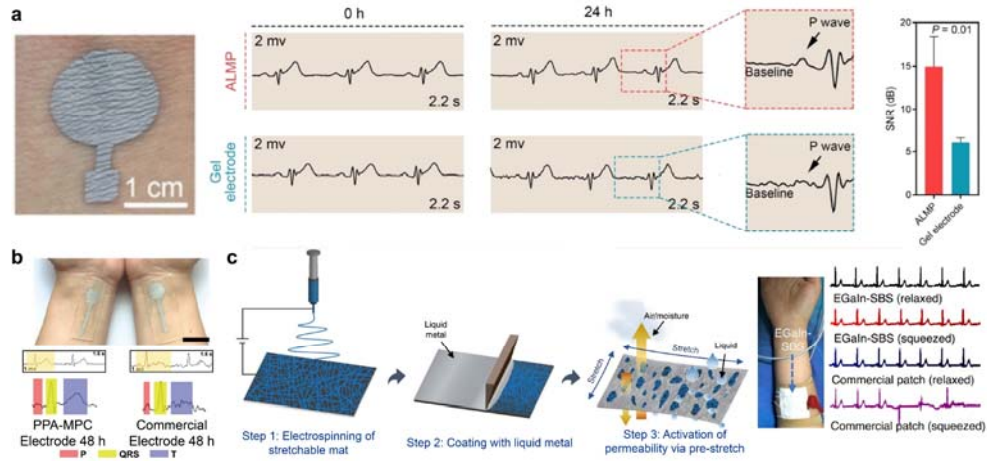


Figure 1.2.2 MPC-based electronics for ECG recording. **a** Electrodes created from skin-adhesive liquid metal particles demonstrate stable ECG recording even after 24 hours. **b** MPC electrode patches utilizing wet-adhesive elastomer maintain high-quality ECG monitoring for up to 48 hours. **c** ECG signals recorded by the EGaln-SBS electrode on elastomeric electro-spun mat. Adapted from *Nano Lett* **22**, 4482–4490 (2022); *Adv Funct Mater* 2200444 (2022); *Nature Materials* 2021 20:6 **20**, 859–868 (2021).

EEG EEG offers a remarkable advantage in terms of speed due to its exceptional ability to provide extremely high temporal resolution, enabling the revelation of brain information in milliseconds. This technology is invaluable for monitoring human and animal brain development, investigating epilepsy, pinpointing seizure origins, testing physiological pathways, and many other applications. However, a common challenge lies in the mechanical disparity between biological tissues and traditional neural interfaces. For example, Utar or Michigan electrode arrays, which incorporate high Young's modulus stainless steel, can pose a risk of damaging brain tissue upon insertion. To address this challenge,

researchers have introduced a highly stretchable electrode array based on MPC¹⁰³ (Figure 1.2.3a). By incorporating MPC, this array maintains stable electrical properties and compliant mechanical performance even under a strain of 100%. This innovative array enables real-time monitoring of epileptiform activities in rats. In human EEG recording, EEG caps are commonly employed. However, a drawback of EEG caps is the time-consuming gel injection process. This issue can be resolved by using an integrated EEG patch. Researchers have also utilized a bi-phasic Ag-EGaIn composite to create a wearable EEG recording patch¹⁰⁴ (Figure 1.2.3b). This device remains unaffected by daily activities like physical exercise or bathing. Successfully capturing the suppression of the Alpha rhythm, this patch holds potential applications in sleep monitoring and human-brain interfaces.

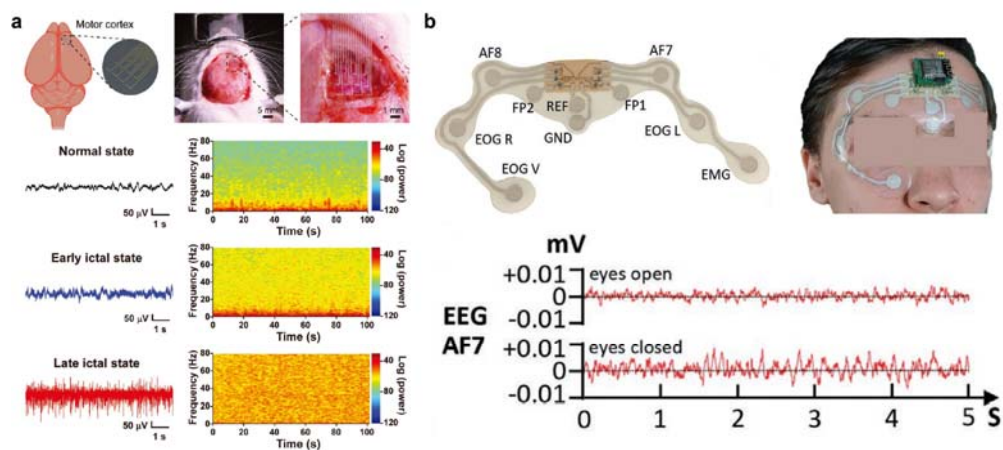


Figure 1.2.3 MPC-based electronics for EEG recording. **a** In vivo EEG signal recording using MPC neural electrode arrays. **b** EEG patch featuring MPC electrodes. Adapted from *Small* **17**, 2006612 (2021); *Adv Funct Mater* **32**, 2205956 (2022)

EMG In the context of sEMG, two critical electrode-related issues hinder the effectiveness of this technique. Firstly, a common challenge with most

sEMG electrodes is their susceptibility to detaching when exposed to sweat, as their adhesives tend to fail in wet environments. This problem can significantly compromise the accuracy and durability of sEMG recordings, particularly during vigorous physical activities. Secondly, many sEMG electrodes lack the ability to conform well to soft skin, leading to the formation of air gaps between the electrodes and the skin. This can introduce more noise during recordings and increase the likelihood of electrode detachment. To tackle the initial concern, the wet-adhesive elastomer has proven effective in enabling sEMG signal recording for a duration of up to 24 hours, even following the subject being exposed to water, such as taking a shower¹⁰² (Figure 1.2.4a). Furthermore, researchers have effectively employed skin-adhesive liquid metal particles to capture the flexion of the flexor carpi ulnaris⁹¹ (Figure 1.2.4b). This approach has yielded a high SNR of 23.34 dB due to the seamless conformability to skin folds of the pattern, eradicating air gaps and lowering interface impedance. To further enhance interface contact, sticky MPC are introduced⁵¹. By incorporating a pressure-sensitive adhesive coating layer onto the substrate with GLM circuits on the same side, conductive circuits have been endowed with adhesiveness, ensuring the device remains securely attached to the skin even during deformation (Figure 1.2.4c). Electrodes fabricated from this sticky MPC have successfully recorded clear sEMG signals from the biceps brachii. With regard to forearm sEMG recording, electrode arrays have proven capable of capturing more information compared to standard commercial electrodes due to their higher density within a relatively smaller area. Researchers have

developed an GLM micromesh carried by an elastomer sponge with permeability similar to textiles, achieving a comfortable fit¹⁰⁵. By attaching this array to the forearm, diverse sEMG signals are recorded for distinct hand gestures (Figure 1.2.4d). This innovation holds promise as a reliable interface between humans and machines.

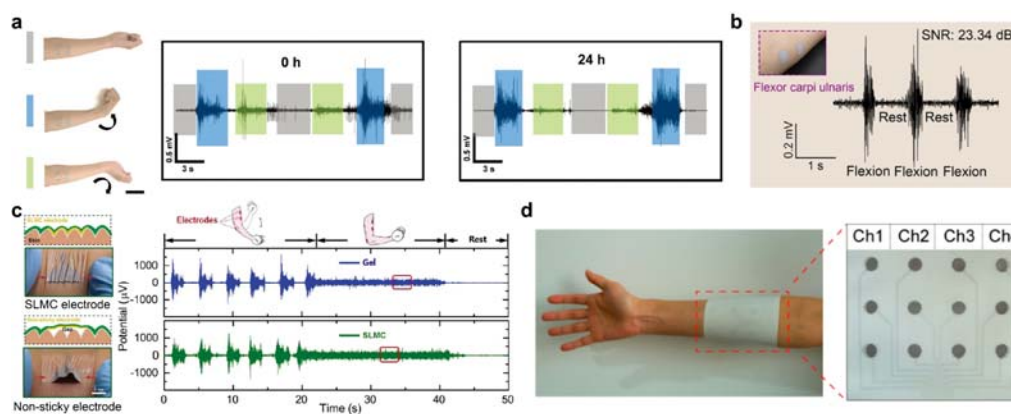


Figure 1.2.4 LM-based electronics for EMG recording. **a** Long-term EMG recording for 24 hours using MPC adhesive electrodes. **b** EMG signal from flexor carpi ulnaris captured using skin-adhesive GLM particles. **c** EMG recording on the arm facilitated by sticky MPC electrodes. **d** Human-machine interface created with an integrated GLM micromesh epidermal sensing sleeve. Adapted from *Adv Funct Mater* 2200444 (2022); *Nano Lett* **22**, 4482–4490 (2022); *Advanced Science* **9**, 2202043 (2022); *ACS Appl Mater Interfaces* **14**, 13713–13721 (2022).

1.2.4.3 Blood PPG & blood oxygen

Blood pressure (BP) serves as a critical determinant of cardiovascular health. In the realm of health monitoring, the assessment of blood pressure through long-term or ambulatory monitoring provides valuable insights into daily activity and sleep-induced BP fluctuations. However, existing ambulatory BP monitoring tools often give rise to discomfort issues. Repeated cuff inflation can lead to soreness, while prolonged usage may

trigger skin irritation. Similarly, measuring blood oxygen (BO) levels can also be discomforting. Thus, the development of a comfortable tool for extended BP and BO measurement is imperative. MPC-based devices present a preferable solution due to their excellent skin conformability, ensuring user comfort without causing inflammation. Employing MPC, a flexible PCB incorporating a BO measurement module has been developed, facilitating continuous photoplethysmography (PPG) signal recording from the wrist⁹⁴. This recording enables the computation of blood pressure and blood oxygen data (Figure 1.2.5a). To tackle the challenge of prolonged recording, researchers have invented a device that harnesses power directly from the human body via a stretchable biofuel cell¹⁰⁶. This cell, comprising carbon electrodes and MPC circuits, captures glucose and lactate from sweat as reactants, generating power for LED illumination and supplying energy to oximeters, temperature sensors, and other detectors (Figure 1.2.5b). Similarly, a wearable health monitoring system, leveraging MPC circuits and PPG sensors, is developed, ensuring conformal contact with the skin on the neck¹⁰⁷ (Figure 1.2.5c). This device exhibits remarkable functionality even under a strain of 150%. Physical pressure sensors, including a micro-bump amplifying GLM resistance change, are employed for blood pressure measurement¹⁰⁸ (Figure 1.2.5d). This innovation successfully captures pulse information from the wrist and facilitates cuffless BP monitoring.

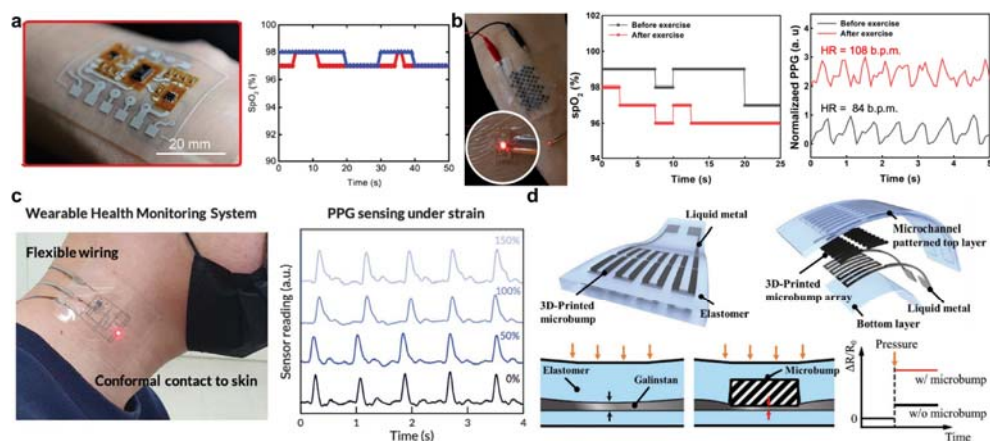


Figure 1.2.5 MPC-based electronics for photoplethysmography and blood oxygen. **a** MPC-based PPG and BO detection system on the wrist. **b** Biofuel cells using MPC technology for wearable device energy supply. **c** MPC-based PPG sensor for health monitoring on human neck. **d** 3D-printed rigid microbump-integrated MPC-based pressure sensor can detect BP. Adapted from *Mater Horiz* 7, 1186–1194 (2020); *Anal Chem* 94, 16738–16745 (2022); *Science* (1979) 378, 637–641 (2022); *Adv Healthc Mater* 8, (2019).

1.3 Polymers

Within the realm of MPC, the role of polymers emerges as another pivotal aspect. Polymers can fulfil a dual role as both substrates and encapsulation layers, offering protection to GLM against potential issues such as leakage, oxidation, and undesired reactions. When GLM functions as interconnects within a device, the application of insulating elastomers, such as PDMS and TPU emerges as a preferable option. This configuration guarantees the stretchability or flexibility of the entire device while simultaneously preventing any unwanted short circuits. On the other hand, in instances where GLM assumes the role of electrodes, the integration of conductive polymers such as PEDOT:PSS proves to be an effective strategy. Such polymers not only safeguard the active GLM electrode but also preserve

its inherent conductive properties, ensuring the desired functionality is maintained.

1.3.1 PDMS

Thanks to the transformation from GLM to LMNPs, those tiny particles can be uniformly dispersed in the solutions or inks, enabling a range of printing techniques. Subsequently, two distinct approaches to printing are employed: 1. Printing onto initial substrates and then transferring onto elastomeric substrates to create MPCs; 2. Direct printing onto elastomeric substrates to form MPCs. When considering transfer printing, PDMS presents an ideal option. Its liquid state before curing allows it to permeate and fill the spaces between LMNPs on the initial substrate. Upon curing, PDMS solidifies, facilitating the transfer of the GLM pattern from the primary substrate to the PDMS (Figure 1.3.1). In terms of wearable devices, this strategy offers several advantages. Encapsulation by the primary substrate and PDMS films permits extended storage before utilization. The auto-sintering process during peeling simplifies the application of MPC circuits. GLM becomes embedded within PDMS, affording some degree of circuit protection. The thickness of the PDMS film can be adjusted through spin-coating parameters.

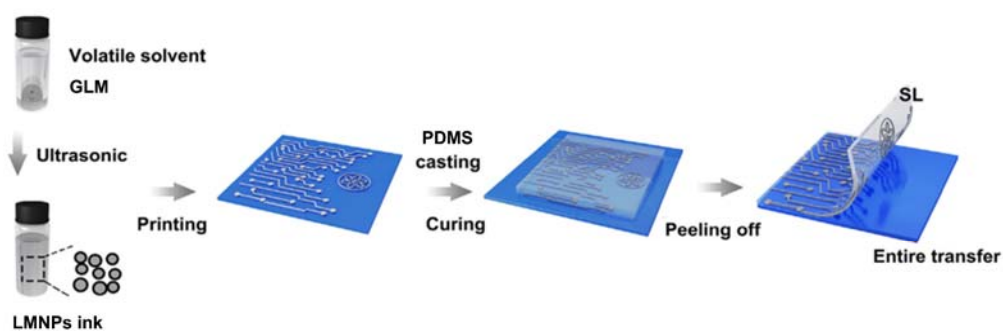


Figure 1.3.1 Transfer printing technique of GLM using PDMS. Adapted from *iScience* **4**, 302–311 (2018).

It is worth to mention a critical surface modification technique about PDMS: plasma treatment. In a nearly vacuum environment with high voltage, the surface undergoes oxidation, resulting in the formation of a thin, wettable, brittle silica-like layer. Utilizing a mould, it becomes possible to generate a specific pattern on the PDMS with favourable hydrophilicity, thereby enabling the subsequent patterning of aqueous ink. In addition to surface modification, the bulk properties of PDMS can be adjusted by altering the quantity of curing agent or introducing other polymers through doping. For instance, when the elastomer base to curing agent ratio is 10:1, the Young's modulus of cured PDMS measures 2.61 ± 0.021 MPa; whereas this ratio shifts to 33:1, the modulus changes to 0.56 ± 0.021 MPa¹⁰⁹. Ordinarily, PDMS is non-adhesive because the vinyl groups react with the hydrosiloxane due to the catalytic influence of a platinum catalyst present in the curing agent, creating a highly cross-linked network. Nevertheless, researchers have discovered that the addition of a specific amount of PEG oligomer to the PDMS precursor, followed by thorough mixing, results in the oligomer adhering to and enveloping the platinum catalyst¹⁰². This

process diminishes the contact between the PDMS precursor and the Pt catalyst, considerably retarding the hydrosilylation process. Consequently, PDMS-PEG acquires a network with lower levels of cross-linking. The elongated and softer side chains extending from the backbone bestow this material with a reduced modulus and increased adhesiveness. The ability to adjust its mechanical properties through straightforward recipe modifications grants PDMS a versatile range of applications across various contexts.

1.3.2 Thermoplastic polyurethane (TPU)

TPU stands out as a highly versatile engineering thermoplastic endowed with elastomeric properties. Its adaptability to various industrial processes allows them to be shaped and formed upon heating (Figure 1.3.2). TPU also exhibits excellent resistance to abrasion and solvents such as oils. Lots of advantages position them as crucial materials in engineering applications.

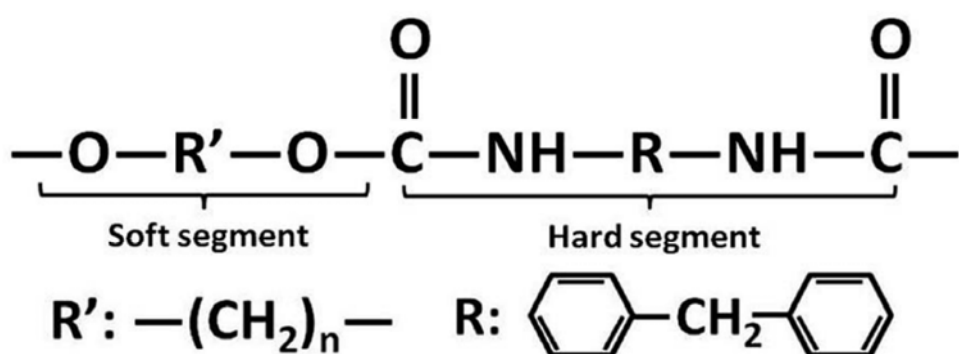


Figure 1.3.2 Chemical structure of TPU. Adapted from *RSC Adv* 8, 42337–42345 (2018)

Similar to PDMS, TPU is an elastomeric material with an impressive

maximum elongation of over 1000%. Its excellent resilience enables TPU to endure repeated stretching. Moreover, the Young's modulus of TPU is comparable to that of PDMS (Table 1.3.1). It is noteworthy that both TPU and PDMS share a modulus similar to that of human skin. Given this similarity, the utilization of these two materials is particularly advantageous for epidermal applications.

| | Young's modulus (MPa) |
|----------------------------------|-----------------------|
| Human skin | 4.6 |
| PDMS | 1.0 |
| TPU | 6.0 |
| Polyethylene terephthalate (PET) | $2.95 \cdot 10^3$ |
| Parylene C | $3.2 \cdot 10^3$ |
| Polyimide (Kapton from DuPont) | $4.0 \cdot 10^3$ |

Table 1.3.1 Comparison of Young's modulus between common materials for wearable devices.

As a well-established commercial product, TPU serves as an ideal substrate for the direct printing process discussed earlier. Following the printing step, stretching becomes essential to sintering MPC circuits. Impressively, even under extreme deformations, this MPC maintains its conductivity remarkably well, registering 380,000 S/m at a strain of 1000%⁵⁰. An added advantage of employing TPU as the MPC matrix is its straightforward integration through hot-pressing. The typical parameters for hot-pressing to combine two TPU layers at 150°C for 10 seconds. This simple encapsulation technique greatly facilitates the industrial-scale production of MPC-based wearable devices. For specific pattern creation on TPU, laser engraving is a commonly employed method, offering resolutions as fine as 50 µm, thereby enabling refined circuit and electrode designs. The established biocompatibility of TPU, evident in numerous

medical applications like medical infusion stickers, underscores its suitability for wearable device incorporation. This material, prevalent in everyday life, is increasingly favoured for integration into wearable technologies.

1.3.3 PEDOT:PSS

This polymer consists of two main components: cationic part PEDOT⁺ and anionic part PSS⁻. PEDOT possesses excellent conductivity, yet its insolubility in water limits its practical application. In this context, PSS serves a dual role: firstly, as a counterion to stabilize the doped PEDOT, and secondly, as a matrix for creating an aqueous dispersion of PEDOT. The prevailing structural model in solution involves small PEDOT segments closely interacting with bundles of PSS, generating colloidal gel particles within the aqueous medium¹¹⁰. These particles exhibit higher PEDOT density at their core and greater hydrophilic PSS density at their periphery. Deposition and drying processes of PEDOT:PSS yield a unique pancake-like grain morphology, featuring a PEDOT-rich core enveloped by a PSS-rich shell. With its commendable conductivity, user-friendly properties, and favourable biocompatibility, PEDOT:PSS finds applications across diverse fields encompassing energy, electronics, and biology. A variety of techniques are available for fabricating PEDOT films, such as thermal treatment, spin-coating, and electrodeposition.

Furthermore, ongoing researches explore composite materials involving PEDOT. The combination of PEDOT:PSS and graphene has demonstrated remarkable characteristics, including a high conductivity

about 4142 S/cm, high transparency, and exceptional mechano-electrical stability¹¹¹ (Figure 1.3.3a). This innovative amalgamation, characterized by its ultra-thin profile, has resulted in a dry epidermal electrode capable of precise monitoring of electrophysiological signals, such as those originating from facial skin and brain activity. Nonetheless, it is worth noting that this material does have a limitation in terms of adhesiveness. When affixed to the skin during rigorous exercises, there is still a possibility of motion artifacts. To address this issue, PEDOT:PSS holds certain advantages due to its aqueous nature, allowing for the incorporation of various water-soluble polymers through doping. This flexibility in combinations can confer distinct properties to the resulting film. For instance, the researchers has blended PEDOT:PSS, waterborne polyurethane (WPU), and D-sorbitol¹¹². This blend exhibits adhesion capabilities under both dry and wet skin conditions because the addition of D-sorbitol introduce abundant hydrogen bonds into the film. The electrodes made by this material can obtain high-quality epidermal biopotential signals, encompassing ECG, EMG, and EEG measurements (Figure 1.3.3b). An alternative approach to enhance adhesiveness involves reducing the modulus of the film to reinforce physical crosslinking on the interface, thereby promoting better adhesion. Researchers have successfully developed this innovative material by introducing a supramolecular solvent (β -cyclodextrin and citric acid) into PEDOT:PSS (Figure 1.3.3c). With an abundance of hydroxyl functional groups and charged molecules, this material displays robust interface adhesion on substrates. This strength in adhesion is attributed to the synergistic effects of multiple weak interactions

occurring at the interface⁵².

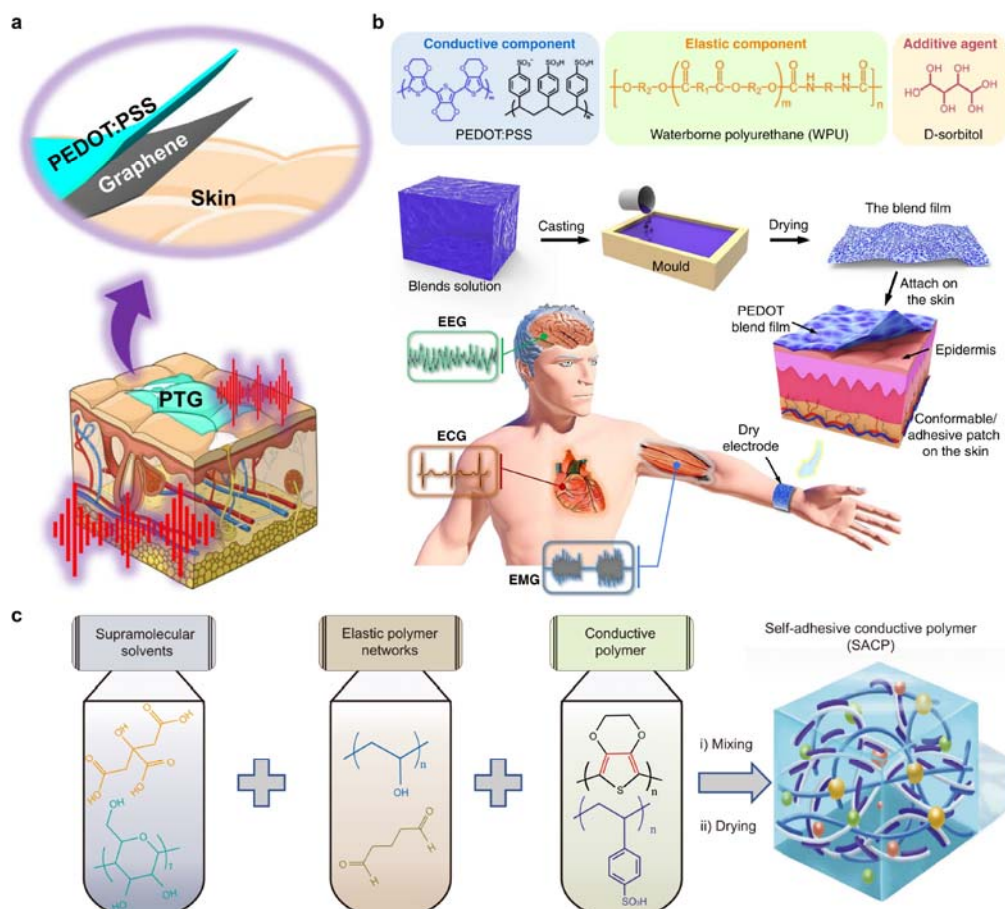


Figure 1.3.3 Doping with other polymers to enhance the PEDOT:PSS film. **a** The interaction with graphene imparts the PEDOT:PSS film with high conductivity mechano-electrical stability. **b** A self-adhesive, stretchable, and conductive polymer film achieved by incorporating D-sorbitol into the PEDOT:PSS blend. **c** Lower modulus and enhanced interfacial adhesion and stretchability in a PEDOT:PSS film through the introduction of supramolecular solvents. Adapted from *Nat Commun* **12**, 1–12 (2021); *Nat Commun* **11**, 4683 (2020); *Nat Commun* **13**, 358 (2022).

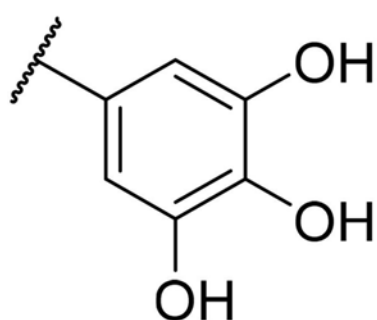
1.3.4 Polyvinyl alcohol (PVA) and tannic acid (TA)

PVA stands out as a semi-crystalline polymer boasting a range of appealing characteristics, including hydrophilicity, biodegradability, and exceptional film-forming capabilities. Its advantageous chain mobility contributes to greater flexibility compared to amorphous polymer films.

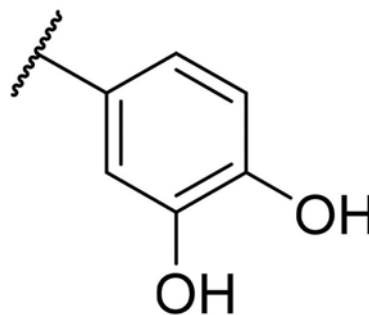
PVA is replete with hydroxyl groups, making it readily soluble in water. Consequently, PVA frequently finds its place in water-based film systems to fine-tune mechanical properties. For instance, the addition of PVA to PEDOT: PSS solutions can elevate the ultimate elongation of the film from 2% to 55%¹¹³. Moreover, PVA is a favoured choice for hydrogel formation. The ample hydroxyl groups in PVA engage in hydrogen bonding with water, facilitating substantial water absorption and retention, leading to a gel-like structure. Hydrogels form through cross-linking, where polymer chains interconnect to establish a three-dimensional network that entraps water. PVA cross-linking can occur through diverse methods, encompassing chemical cross-linking or physical entanglement of polymer chains. Chemical cross-linking involves forging covalent bonds between PVA chains, enhancing gel stability and water retention.

The remarkable water interaction of PVA owing to hydroxyl groups also enables its collaboration with various small molecules to serve diverse functions. For instance, the introduction of glycerol heightens polymer chain mobility, enhancing flexibility by reducing intermolecular forces and mitigating inherent polymeric material brittleness¹¹⁴. Adhesiveness stands as another highly desired attribute of films. The remarkable adhesiveness observed in the plaque-substrate interface proteins of mussels is attributed to their notably high content of 3,4-dihydroxy-L-phenylalanine (DOPA) and lysine amino acids^{115,116}. Based on the literature concerning bioadhesion¹¹⁷⁻¹²⁰, it has been observed that the interactions between phenolic hydroxyl and proteins can generate adhesiveness. The most famous ones are catechol and gallol groups (Figure 1.3.4). Gallol groups,

also known as galloyl groups, are chemical moieties derived from gallic acid, which is a type of phenolic compound found in plants. Gallol groups contain multiple hydroxyl functional groups, which can interact with the amino acid residues in proteins, collectively creating a strong and adhesive force.



Gallol group



Catechol group

Figure 1.3.4 Chemical structure of gallol and catechol group. Adapted from *Journal of Macromolecular Science, Part A* **59**, 625–645 (2022)

In this context, the presence of TA, coupled with PVA, confers adhesiveness to the surface of the film, attributed to abundant gallol groups of TA (Figure 1.3.5). Researchers have identified that a straightforward blend of PVA and TA yields an underwater adhesive, showcasing reusable adhesion¹²¹.

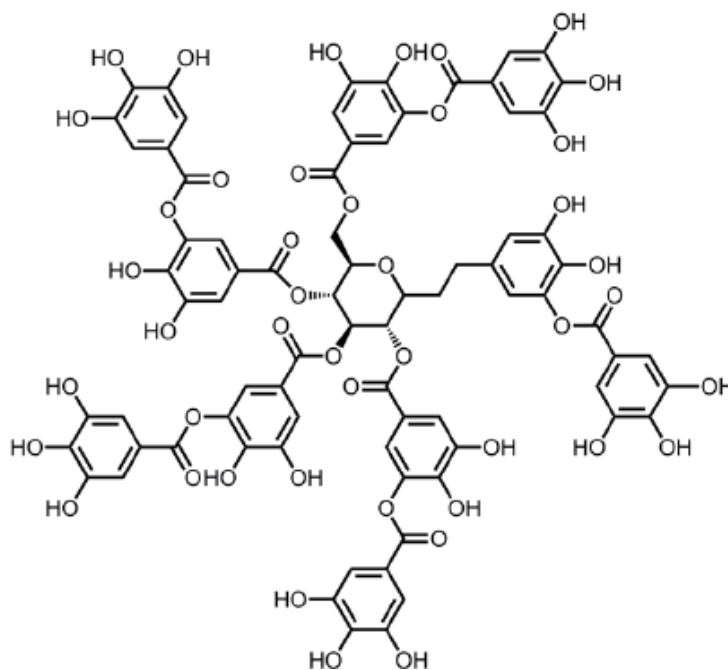


Figure 1.3.5 Molecular structure of tannic acid. Adapted from *RSC Adv* 5, 16112–16115 (2015)

1.4 Aims

The main objective of this study is to overcome the limitations of existing sEMG electrodes through the development of a stretchable sEMG electrode array using MPC and conductive polymers. This innovation shall provide significant advancements that not only broadens the range of applications in everyday life but also enhances the potential of sEMG electrode utilization in clinical settings, which can significantly amplify the impact of sEMG. To attain this objective, the following approaches are pursued.

1.4.1 Creation of a new material for sEMG electrodes with conductive polymers and characterization of its properties

Given the aforementioned limitations of current sEMG electrodes, the imperative is to create a new material which is adhesive, durable and conformal for a dry electrode. This is essential because existing materials often fall short in meeting all the requisite criteria. Characterizations of this new material is imperative, to unravel the underlying mechanisms and verify the viability of this material for sEMG electrodes.

1.4.2 Integration of the new electrode and MPC to fabricate an sEMG electrode array and characterization of its properties

The subsequent stage involves the amalgamation of the newly developed electrodes with MPC circuits, culminating in the creation of an sEMG array. This array should possess enhanced stretchability and hold the promise of commercialization due to the incorporation of MPC. Characterizing this array becomes necessary to validate its capability for accurate sEMG signal recording. Moreover, a comparison should be drawn with a commercially available array to showcase the distinctive advantages offered by this innovative approach.

1.4.3 Utilization of the developed sEMG array for multiplexed muscle information to prevent muscle injury in daily life

The array will be utilized to capture sEMG signals from diverse muscles, extracting various parameters from these signals to reveal the muscular condition. These derived factors hold substantial potential for enhancing

muscle injury prevention in everyday activities, fostering the advancement and adoption of sEMG techniques.

1.4.4 Exploration of the clinical diagnosis potential of the developed sEMG array

In theory, employing a high-resolution sEMG array can enable the recording of motor unit signals from superficial muscles, thereby achieving a similar function as needle electrodes. In light of this, it is meaningful to conduct a comparative analysis between signals obtained from the new sEMG array and those captured using needle electrodes. This comparison aims to uncover the clinical diagnostic potential inherent in the developed sEMG array.

Chapter 2

General Methods

2.1 Materials and reagents

Deionized water was prepared by a laboratory water purifier (Milipore Milli-Q). All organic solvents, salts and reagents are purchased from Sigma-Aldrich except for the following: PEDOT:PSS (Clevios PH 1000, 1.0~1.3 wt%) aqueous solution was purchased from **Heraeus Co.**, Germany. Polyvinyl alcohol 1799 (PVA), n-Decyl alcohol (98%), xanthan gum were from **Macklin Inc.**, China. Polydimethylsiloxane (PDMS, Sylgard184) were purchased from **Dow Corning Co**, USA. Polyethylene terephthalate and thermoplastic polyurethane films were purchased from **Tunsing**, China. Silicone film (0.2 mm) were purchased from **Shengyuwujin**, China. PTFE syringe driven filter (0.45 μm) was purchased from **Jet Bio-Filtration Co., Ltd**, China. Ag/AgCl electrodes (Red Dot 2223 and Foam Monitoring Electrode 2228) were purchased from **3M**, USA. The 64-channel sEMG array was purchased from **Neuracle**, China. The conductive gel g.GAMMAgel was purchased from **G.tec**, Austria. Medical infusion stickers were purchased from **Hongsheng**, China. Front-end connectors were designed and fabricated from **EasyEDA**, China.

2.2 Instruments

The sonicator (Branson SFX 550) and water bath of a sonicator (Branson CPX5800H) were from **Emerson Electric Co.**, USA. The spin coater (RC-

150) was from **Suzhou MEMStools Semiconductor Technology Co., LTD**. The plasma cleaner (PDC-MG) was from **Chengdu Mingheng Science & Technology**. The spray machine (AC-108N) was from **YEHONG AIR TOOLS**. The motion controller (AMC4030) for repetitive strain was from **CHENGDU FUYU TECHNOLOGY CO., LTD**. Hot-pressing machine (G311) was from **Freamc**, China. Laminating machine (WD-V480) was from **HANGZHOU CAIDE OFFICE EQUIPMENT CO., LTD**, China. Laser graving machine (T1 pro) was from **Shanghai Diaotu Industrial co., LTD**, China. RCA abrasion wear tester was from **Norman Tool Inc.**, USA. HR 10 Discovery Hybrid Rheometer was from **TA Instruments**, USA. Scanning electron microscope (SU8220) was from **Hitachi**, Japan. Atomic force microscope (MFP-3D) was from **Asylum Research**, USA. Universal testing system (Instron 68TM-5) was from **Illinois Tool Works Inc.**, USA. Multi Autolab/M204 potentiostat was from **Metrohm**, Switzerland. Programmable temperature and humidity tester (QHP-360BE) was from **LICHEN**, China. Confocal microscope was from **Nikon**, Japan. G.Hiamp multi-channel amplifier was from **G.tec**, Austria. Nicolet EDX System was from **Natus Medical Incorporated.**, USA. Mindray L14-6NE probe (Mindray DC-40 Ultrasound System) was from **Lysis Healthcare GmbH**, Austria.

2.3 Synthesis of conductive polymer

2.3.1 Synthesis of PEDOT-PVA electrodes

PEDOT:PSS solution was filtered by a PTFE syringe driven filter before

use. The PEDOT-PVA solutions were made by each adding 0, 0.01927, 0.0288, 0.0575, 0.115, 0.1725 g PVA into 5 ml PEDOT:PSS solutions with 250 μ l DMSO, whose weight fractions of PVA were 0, 25, 33.3, 50, 66.7 and 75 wt%, respectively. The solutions were stirred at 80 °C for 4 hours to be prepared. Solutions were cast onto a specific substrate and electrodes were finalized through a 20-minute heating process.

2.3.2 Synthesis of TPP electrodes

For TPP electrodes, PEDOT-PVA solution was made by controlling the ratio between PVA and PEDOT as 2:1. A three-fold dilution was made to the PEDOT-PVA solution. The TPP solutions were made by each adding 0, 0.024, 0.048, 0.096, 0.144, 0.192, 0.24, 0.288, 0.336, 0.384 g TA into 3 ml diluted PEDOT-PVA solution with 150 μ l DMSO totally included, whose weight fractions of TA were 0, 0.8, 1.6, 3.2, 4.8, 6.4, 8, 9.6, 11.2, 12.8 wt%, respectively. The TPP solutions were stirred for 5 min to be prepared. Solutions were cast onto a specific substrate and electrodes were finalized through a 20-minute heating process. For TPU-based MEAP, 0.4% xanthan gum was added into TPP solution to increase the viscosity.

2.4 Array fabrication

2.4.1 PDMS substrate

3 g EGIn and 1 mL n-Decyl alcohol were added into a 5 mL centrifuge tube and sonicated by a sonicator. For screen printing, the EGIn was sonicated for 1 min with the power of 300 W. Printing equipment and masks

were bought online to print required circuit patterns on polyethylene terephthalate (PET) substrates. The PDMS (base: curing agent ratio of 10:1) was spin coated on the PET substrate with 1000 rpm, 30s. The PDMS films were peeled off from PET films after curing in 80 °C for 20 min. An electrode mask made by silicone film was attached to the circuit side of PDMS film. After the plasma treatment, the mask was removed, and 66.7 % TPP solution was introduced on the electrode location. Because only the areas that were to become the electrodes were plasma-treated to become hydrophilic, TPP solution would only cover these areas to form the electrodes according to the shape of the design. After heating in 80 °C for 10 min, the flexible electrode film was made. The adhesive PPA¹⁰² were spin-coated on PDMS for encapsulation of the liquid metal circuits to prevent leakage. Note that electrode sites and connection pads were protected by silicone films during the encapsulation to allow the electrodes and connection pads to be exposed. After curing in 80 °C for 20 min, the soft electrodes were completed. The thickness of PDMS-MEAPs was lower than 100 µm, typically with the substrate of 65 µm, the encapsulation layer of 25 µm and the TPP electrode of 30 µm. For comparison between commercial array, the diameters and inter-distances of TPP electrodes were 4 mm and 8 mm. For biceps brachii recording, the diameters and inter-distances of TPP electrodes were 5 mm and 15 mm, respectively. For abductor pollicis brevis recording, the diameters and inter-distances of TPP electrodes were 1 mm and 5 mm, respectively. For the Achilles tendon location, the MEAP #1 with IED of 10 mm had electrode surface area of 20 mm² and the MEAP #2 with IED of 6 mm had electrode surface area of 30

mm². The front-end connectors were made by polyimide flexible printed circuit (FPC) for connecting specific MEAPs. The FPC and MEAP were hot-pressed together with force of 50 N and temperature of 140 °C for 30 s by a hot-pressing machine. With a customized back-end connector, every channel of MEAP can be independently connected to EMG recording system.

2.4.2 TPU substrate

0.83 g Polyvinylpyrrolidone (PVP) was added into 20 ml n-Decyl alcohol to make 5% PVP-Decanol solution by mixing in 60 °C for overnight. 3 g EGaIn and 1 mL PVP-Decanol were added into a 5 mL centrifuge tube and sonicated by a sonicator. For screen printing, the EGaIn was sonicated for 2 min with the power of 300 W. Printing equipment and masks were bought online to print required circuit patterns on TPU substrates. A TPU electrode mask with back layer was affixed to the circuit side of TPU substrate using the laminating machine with 110 °C. TPP solution with 8% of TA containing xanthan gum was sprayed onto the electrode location, and after 10 minutes of heating in 80 °C, the back layer of the electrode mask was peeled off, resulting in the formation of the electrode pattern. A medical infusion sticker with patterns for electrode sites was hot-pressed onto the TPU substrate with 140 °C for 10 s, serving as the encapsulation layer and providing adhesiveness to the substrate. All electrode patterns on TPU or medical infusion stickers were made by laser graving machine with power of 100% and speed of 7%. Before use, the 50% strain was applied to the MEAP to sinter MPC circuits. The thickness of TPU-MEAPs was around 100 μm,

typically with the substrate of 40 μm , the encapsulation layer of 25 μm and the medical infusion sticker of 40 μm . For APB recording, the diameters and inter-distances of TPP electrodes were 1 mm and 3 mm, respectively. The front-end connectors were made by polyimide FPC for connecting MEAPs to clinical recording machine. The FPC and MEAP were hot-pressed together with force of 50 N and temperature of 140 $^{\circ}\text{C}$ for 30 s by a hot-pressing machine.

2.5 Materials characterizations methods

The abrasion test was performed by an RCA abrasion wear tester. A paper ribbon was imposing a consistent rubbing force of 1.715 N on the electrode. The resistance of PEDOT-PVA strip was monitored during the abrasion test by connecting two ends of the strip to electrochemical workstation. When the resistance had more than a hundredfold change, the PEDOT-PVA was regarded as damaged by the paper ribbon. All electrode strips of 50 x 5 mm kept being rubbed until they cracked. The water resistance test was conducted in a water bath of a sonicator. For viscosity test, different PEDOT-PVA solutions were tested using HR 10 Discovery Hybrid Rheometer at 25 $^{\circ}\text{C}$, 1% of the strain and 1 Hz frequency. The topography of PEDOT-PVA film was characterized by SEM and AFM. For the cross-sectional SEM images, TPP films were freeze-dried overnight followed by quenching in liquid nitrogen. The tensile testing was performed by a universal testing system, size of PEDOT-PVA and TPP films was 30 mm long and 10 mm wide. The stroke speed of the measurement was 0.5 mm

min⁻¹. The peeling force measurement was conducted on the forearm. Before the measurement, the forearm skin was cleaned with a mixed solution of deionized water and ethanol. The TPP films were made 20 mm wide and 20 mm long. During the test, the stroke speed was kept at 15 mm s⁻¹. The stroke speed in repetitive stretch test was kept at 6 mm min⁻¹. Electrode-skin impedance measurement was performed with 10 frequencies per decade within a frequency range from 10 Hz to 10 kHz considering that most of the sEMG responses are in the 20 Hz to 500 Hz range. A sinusoid stimulation voltage, with RMS amplitude of 10 mV and no direct current offset, was applied to obtain the impedance curve. For both PEDOT-PVA and TPP electrodes, two working electrodes were attached over flexor carpi ulnaris (FCU) muscle with an IED of 20 mm, on the internal part of the forearm, and reference electrode was attached on the elbow, on the external part of the forearm. To compare, Ag/AgCl electrodes were used to achieve impedance results using the same process. Both types of electrodes had the surface contact area of 20 mm². The permeability test was done with three beakers, each filled with 100 ml of deionized water, covered by MEAP, MEAP (punctures), and polyimide, respectively. Each beaker was secured with a rubber band to ensure that water only passed through the cover. The three beakers were placed in an environment with a temperature of 33 °C and a humidity of 30%, simulating the conditions on human skin.

2.6 sEMG recording

For non-clinical tests, the electrodes were connected to g.Hiamp multi-channel amplifier for sEMG signal acquisition with a sampling frequency of 1200 Hz and an analogue notch filter at 48 ~ 52 Hz. The skin was cleaned with alcohol before recording. Foam Monitoring 2228 electrodes were used for long-term test, conformability test on the forehead, and Red Dot 2223 electrodes were used for fatigue comparison tests. 2228 and 2223 electrodes have the surface contact area of 2 and 2.4 cm². The TPP electrodes in each comparison test have the same surface contact area with 2228 or 2223 electrodes correspondingly. All interelectrode distance for bipolar recording is 20 mm. Bipolar recording was used for single-channel TPP electrode and monopolar recording was used for MEAP to obtain sEMG signals. The commercial array has 64 channels Ag/AgCl electrodes on a polyimide substrate with thickness of 100 μm. The conductive gel was used between commercial array and the skin. For comparison with the needle electrode, the MEAP was affixed to the abductor pollicis brevis and connected to the Nicolet EDX System to collect data, with bipolar recording. For all sEMG recording, no skin treatment was used, including shaving, rubbing or cleaning of the skin. All sEMG signals were filtered with a 20 Hz Butterworth infinite impulse response high-pass filter, which is recommended for general use¹²².

2.7 Subject tasks

2.7.1 Comparison test between PEDOT-PVA and TPP

electrodes

During the biceps brachii muscle recordings, a comparative test between PEDOT-PVA and TPP electrodes was performed. The subject was instructed to keep the curl speed between flexion and extension at 4.5 rad/s. Five contractions of each electrode were tested for RMS alterations.

2.7.2 Long-term test

Both TPP and Ag/AgCl electrodes were attached on FCU and sEMG bipolar recording was done every noon to monitor performances of electrodes. The subject was asked to behave the same as daily life, including work, exercise and taking shower regularly. The subject was asked to pull a 4 kg dumbbell with his wrist for recording. Three contractions were recorded each day to provide statistical RMS and SNR values.

2.7.3 Conformability test on the forehead

The TPP and Ag/AgCl electrodes were attached on the left and right frontalis muscle, respectively. Monopolar recording was used and the subject was asked to raise the eyebrow (frontalis contraction) for 5 min, making each contraction for 5 seconds. Each contraction was analysed to give RMS of noise and SNR values.

2.7.4 Fatigue comparison tests

Electrodes were attached on the most prominent bulge of the muscle belly of FCU, and different types of electrodes were attached exactly on the

same position. The subject was asked to curl the wrist 60 s for three times for each type of electrodes.

2.7.5 Muscle contraction task for muscle activity maps

For biceps brachii recording, the subject performed a biceps curl (concentric and eccentric activity) starting from a full extension of the elbow to a full flexion, with a 4 kg dumbbell while sEMG signals were recorded from the muscle with all 24 sites. The task performed lasted for 10 seconds, and then the subject released the dumbbell to the starting position. For APB recording, the task was moving thumb to the proximal end of little finger and moved back. The RMS values of the recorded sEMG were calculated for timesteps of 0.25 s and 0.083 s for BB and APB, respectively. Muscle activity maps were generated to help visualize the change in activity during the task.

2.7.6 Muscle contraction task for muscle-tendon junction location

Five male subjects, with average age of 23.4 ± 1.9 (mean \pm SD), were recruited for the task. The isometric task for biceps brachii was holding the 5 kg dumbbell for 30 seconds, with forearm paralleled to the ground and the arm with a right angle to the forearm. The dynamic task was making a biceps curl with the 5 kg dumbbell including bending and extending. The isometric task for the Achilles tendon recorded by MEAP #1 was maintaining three lower leg positions in Fig. 5.3.5, with the gastrocnemius naturally contracting. The isometric task for the Achilles tendon recorded

by MEAP #2 was maintaining four lower leg positions, with the gastrocnemius making voluntary contraction. The dynamic task for both MEAPs were the same that the subject did plantarflexion to dorsiflexion with their tiptoe on the step.

2.7.7 Muscle contraction task for muscle injury prevention

The same five subjects mentioned earlier used their non-dominant hand to perform one-arm concentration curls to record sEMG signal generated from biceps brachii muscle by MEAP. The MEAP had 4 columns and 6 rows; column 1- 4 and row 1- 6 were from left to right and bottom to top, respectively. The isometric task started at 10 s and kept for 30 s; after 1 min rest, 10 curls in dynamic task were performed to complete one session. The subjects were asked to control curl speed around 4.5 rad/s for 5 total sessions by the order of 1- 5 kg loadings. For the location of muscle-tendon junction, when $0.45 \leq \text{frequency}_{\text{mean}} \leq 0.55$, the channel was considered on muscle-tendon junction. The tendon strain was calculated based on the average distal biceps tendon length¹²³. All human experiments were conducted with the approval from the Medical Ethics Committee of Southern University of Science and Technology (approval no. 2021SYG049).

2.8 Data collection and processing

Impedances were collected and analysed by NOVA (Metrohm Autolab,

V2.1.4). sEMG data were collected by g.Recorder (g.tec, V5.16.01) and analysed by OT BioLab+ (V1.5.9) and Origin Pro 2021. All RMS, median frequency, and mean frequency values of the recorded sEMG signals were computed for time steps of 0.125 seconds, unless specified otherwise. For dynamic tasks in muscle-tendon junction location section, the mean frequency values of sEMG data were initially smoothed using a Savitzky–Golay filter (with a frame length of 21 and an order of 1) in Matlab R2020a; for real-time monitoring of dynamic tasks in the same section, each set of values were determined first and then the means were generated and plotted as mean \pm SD. In the section of injury prevention, the Gardner–Altman plot was generated with a confidence level of 0.95 and a total of 5000 bootstrap samples. For statistical analysis, data are presented with mean values \pm SD, unless otherwise noted in the figure caption. Significance was defined as *P < 0.05; **P < 0.01; ***P < 0.001; ****P < 0.0001. Statistical analysis was performed using Origin Pro 2021.

2.9 Appendix

The needle electrode recordings were carried out by a clinician, Dr Taimour Alam, at Leeds General Infirmary as part of a pilot study involving one healthy subject. The data obtained from the clinical recording by the clinician was subsequently analysed by the author. All testing procedures adhered to the ethical guidelines of Leeds General Infirmary.

Chapter 3

Characterizations of TPP electrodes

3.1 Introduction

Electrophysiology involves either recording of electrical signals or the delivery of electrical charges as stimuli. The electrode in electrophysiology, as an interface between humans and devices, is crucial for both of the aforementioned techniques. For a long time, the field of EMG has been grappling with electrode-related challenges. EMG, a technique that can provide multiplexed information about muscles for diagnosis, rehabilitation, exercise improvement, and injury prevention, should be as common and useful in our daily lives as ECG. However, existing needle electrodes are invasive, and existing surface electrodes cannot achieve high-quality recording for a long term, severely limiting the widespread adoption of EMG.

To obtain accurate data from muscles, sEMG electrodes must meet numerous requirements, including low impedance for signal quality¹²⁴, good stretchability and adhesiveness for signal stability¹²⁵, small size (diameter ≤ 5 mm) for high-density recording¹⁷, and good biocompatibility and durability for wearable devices. Among these challenges, the most significant is the rigidity of most electrodes, which prevents them from conforming well to human skin. This often leads to position shifts that affect signal reception or electrode failure due to prolonged strain on the electrode itself²¹.

Currently, existing sEMG electrodes have several limitations.

Nonpolarizable Ag/AgCl electrodes have replaced traditional electrodes like platinum or gold and are the most commonly used type in clinics and research. Using conductive gel between the electrode and skin yields a high SNR. However, signal quality typically decreases as the gels dry out, and in this case, the lack of electrode conformability on the skin can further worsen signal quality¹²⁶. Additionally, Ag/AgCl electrodes often lack a robust structure, with AgCl film chipping away after repeated use and releasing highly toxic metal ions into the tissue, posing a risk of infection²³. Devices based on gold or platinum can have flexibility and fatigue issues that limit their performance on soft skin, and a lack of adhesiveness at the electrode site can cause motion artifacts in sEMG signals^{38,127–131}. There have been reports of novel sEMG electrode providing muscle information for clinical use and human-machine interfacing. However, these electrodes are usually made of solid metals, which are non-conformal to the skin, reducing signal quality and resulting in short recording timespans^{40,132,133}. Some electrodes are made of inorganic compounds or conductive polymers with limited flexibility on non-stretchable substrates, causing contact issues between the device and the skin^{134,135}. Thus, developing an adhesive, conformal, and non-toxic dry electrode is still a goal of many researchers. Dry electrodes force the material to be classified into three types: metal, carbon materials, and conductive polymers. Conventional metals and carbon materials have exceedingly high Young's moduli, requiring complex procedures to fabricate micro-/nano-structures for flexible bioelectronics. In comparison, employing conductive polymers that can be variably tuned offers a more advantageous approach, as

researchers can tailor them to specific functionalities depending on the application scenarios.

In this context, PEDOT:PSS is a suitable conductive polymer due to its good biocompatibility, high conductivity, and high electrochemical stability^{110,136,137}. However, pure PEDOT:PSS film only exhibits a strain of ~5%, which is insufficient for accommodating most skin deformations²⁹. Its water-soluble properties limit its use in the presence of sweat, and its poor resistance to rubbing affects durability when in contact with the skin¹³⁸. The non-adhesive nature of pure PEDOT:PSS film also poses contact issues, reducing the quality of electrophysiological signals.

Based on the literature concerning the interaction between gallol groups and proteins on the skin, it has been observed that these interactions can generate adhesiveness. Additionally, certain polymers have been found to enhance the stretchability of PEDOT:PSS, e.g. PVA. In this section, it is aimed to address the challenge of sEMG electrodes using PEDOT:PSS by incorporating TA and PVA. This new polymer blend is called TPP. Each component in this system contributes uniquely to the final properties of the electrode film (Figure 3.1.1a). It is found that this film shows excellent stretchability and adhesiveness on the skin (Figure 3.1.1b and c). To demonstrate and confirm the novelty of these sEMG electrodes, various characterizations are essential.

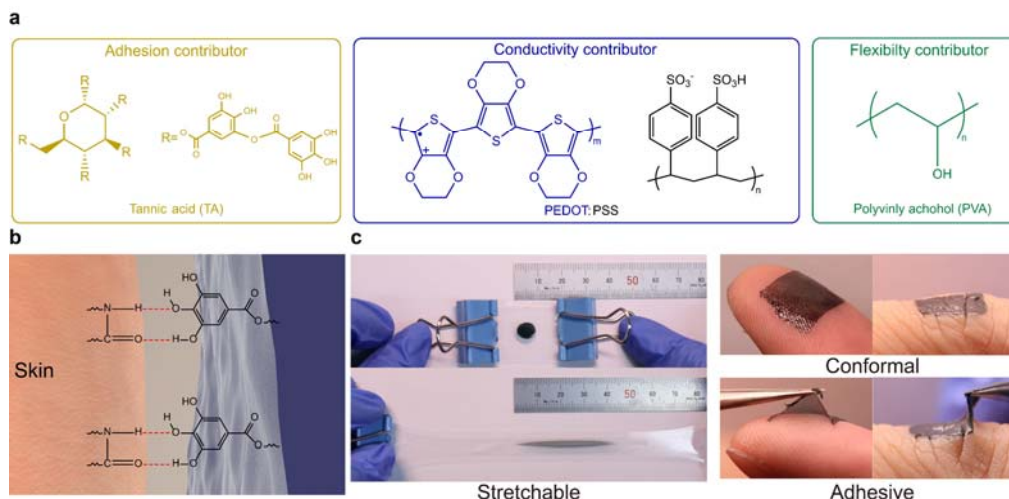


Figure 3.1.1 TPP films. **a** Different constituents and their functions in TPP electrode. **b** Schematic diagram of adhesion between TPP electrode and skin. **c** Photographs of the performance of TPP electrodes during stretching and on skin.

3.2 Determination of the formula of TPP

The common approach for determining the optimal ingredient proportions in a ternary system involves first establishing the ratios in a binary system and subsequently considering the third component. In this study, to ascertain the ideal concentration of each constituent in the TPP solution, the focus was initially on optimizing the PVA loading in the PEDOT:PSS solution.

3.2.1 Determination of the ratio between PVA and PEDOT:PSS

The establishment of optimal ratio between PVA and PEDOT:PSS depends on various properties of the PEDOT:PSS film measured in relation to varying PVA doping concentrations. Weight fractions of PVA at 0%, 25%, 33.3%, 50%, 66.7%, and 75% were investigated.

Considering the need for conformability of sEMG electrode on the skin, my primary focus is to evaluate the stretchability of the film. Since it is well known that the addition of PVA can enhance the stretchability of the film, but also introduces insulation which theoretically affects its conductivity, finding a balance becomes imperative. In this context, it is aimed to establish a viable range of ratios between PEDOT:PSS and PVA for a film suitable for sEMG electrodes. It is found that as the concentration of PVA increases, the stretchability of the PEDOT-PVA film improves. Notably, the highest conductivity is achieved at a PVA content of 25% (Figure 3.2.1). Researchers have observed that a small quantity of PVA can significantly enhance the electrical conductivity of PEDOT:PSS, primarily attributed to the interaction between the hydroxyl functional group of the polymer and PEDOT:PSS¹³⁹. However, as the concentration of PVA continues to increase, the insulated portion become more pronounced, leading to a subsequent decrease in conductivity. It is also found the a PVA concentration of at least 66.7 wt%, gives a stretchability of over 30% which is similar to that of the human skin¹¹². Considering stretchability as a priority, if the loss of conductivity does not significantly impact signal quality of sEMG recording, it is advisable to explore PVA concentrations exceeding 66.7 wt% in further research.

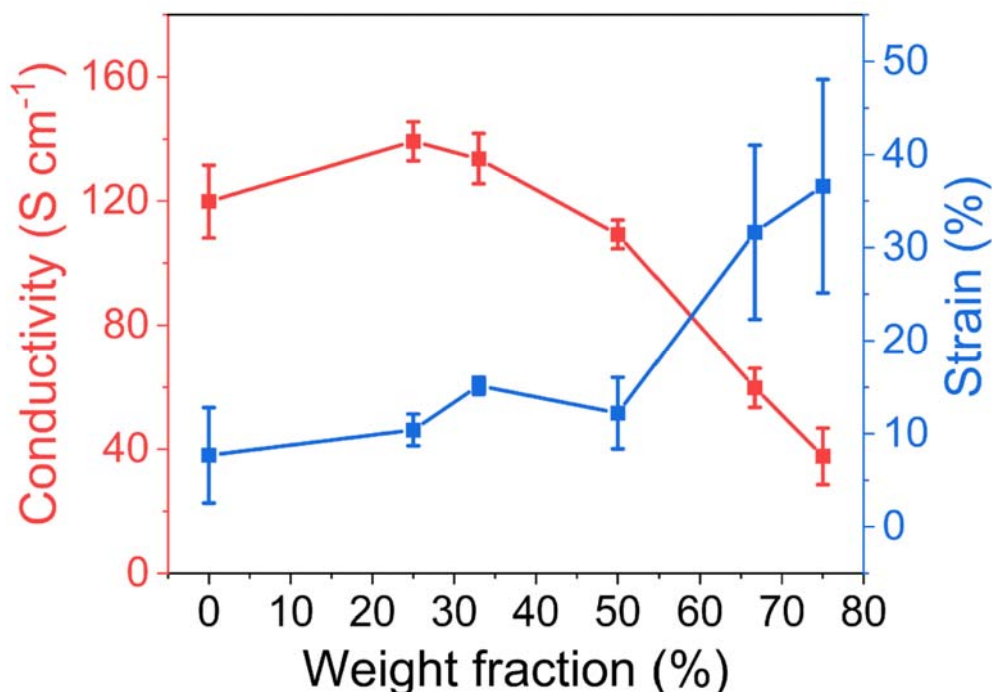


Figure 3.2.1 Strain and conductivity of PEDOT-PVA electrodes with different PVA additions.

When considering the application on the skin, it becomes necessary for sEMG electrodes to exhibit robust abrasion resistance. The results demonstrate a substantial enhancement in the abrasion resistance of PEDOT-PVA film with the addition of PVA. This improvement can be attributed to the strong interlock between PEDOT:PSS and PVA, with tenacious PVA part contributing to the protection. This observation provides additional evidence of the good miscibility between PEDOT:PSS and PVA from a different perspective. In the absence of such miscibility, the film would probably exhibit a gradual resistance change instead of the sudden change observed, as the PEDOT:PSS part would continuously strip off from the film during the abrasion (Figure 3.2.2a). To quantify the impact, the time-to-abrasion data with an exponential model was fitted,

revealing that the addition of PVA for improved abrasion resistance may offer more significant benefits than other properties that exhibit proportional relations (Figure 3.2.2b). This principle should be taken into account when determining the optimal ratio between PEDOT:PSS and PVA.

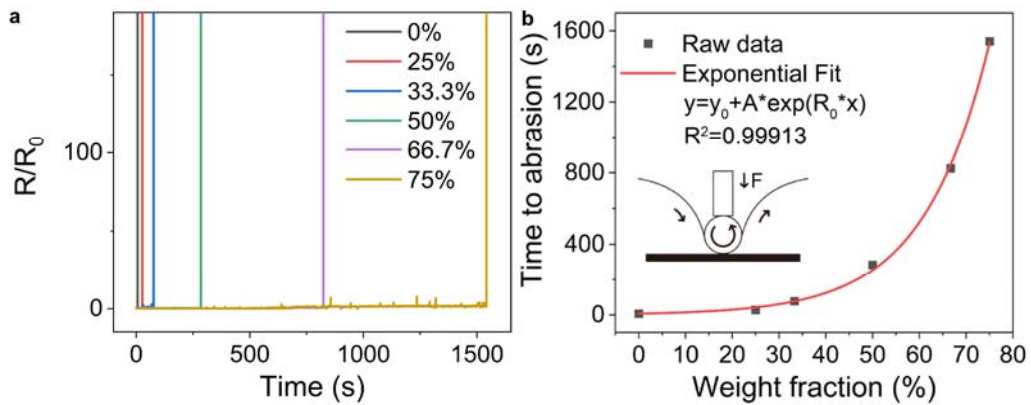


Figure 3.2.2 Abrasion-resistance of PEDOT-PVA electrodes. **a** Real-time monitoring of resistance change across different PEDOT-PVA electrodes. R is the real-time resistance of the film; R_0 is the initial resistance of the film. **b** Comparison between final time to abrasion across different PEDOT-PVA electrodes.

Because of the aqueous base of PEDOT-PVA, it becomes essential to investigate the durability of this binary system in an aqueous environment, especially given the potential effect of sweat on the skin when used as an sEMG electrode. The results showcase that the addition of PVA leads to a linear increase in the water resistance of the film (Figure 3.2.3). From this perspective, a higher PVA concentration is preferable.

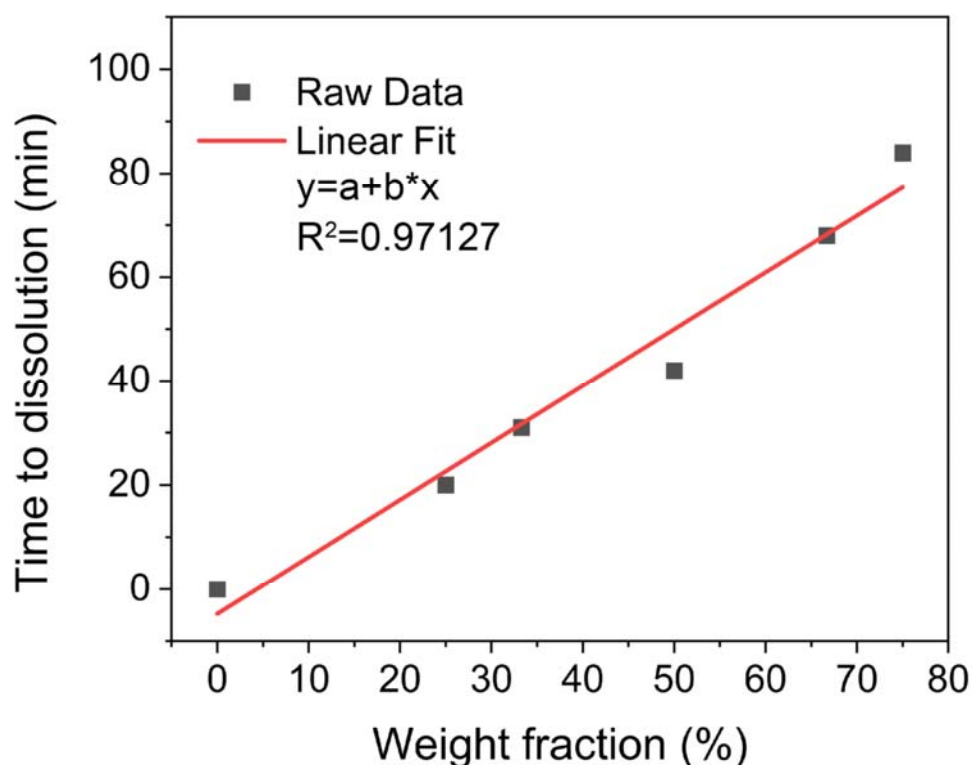


Figure 3.2.3 Water resistance of PEDOT-PVA electrodes.

Viscosity measurements of PEDOT-PVA solutions with varying PVA concentrations were also conducted. It is worth noting that, from a processing perspective, a lower viscosity solution is preferred due to ease of transfer, reduced consumption per square, and the generation of a more uniform film during evaporation. The results demonstrate that the addition of PVA increases the viscosity of the solution, with a more significant impact observed when the concentration exceeds 75 wt% (Figure 3.2.4). This observation implies that the addition of PVA should be carefully controlled within a reasonable range to facilitate ease of processing.

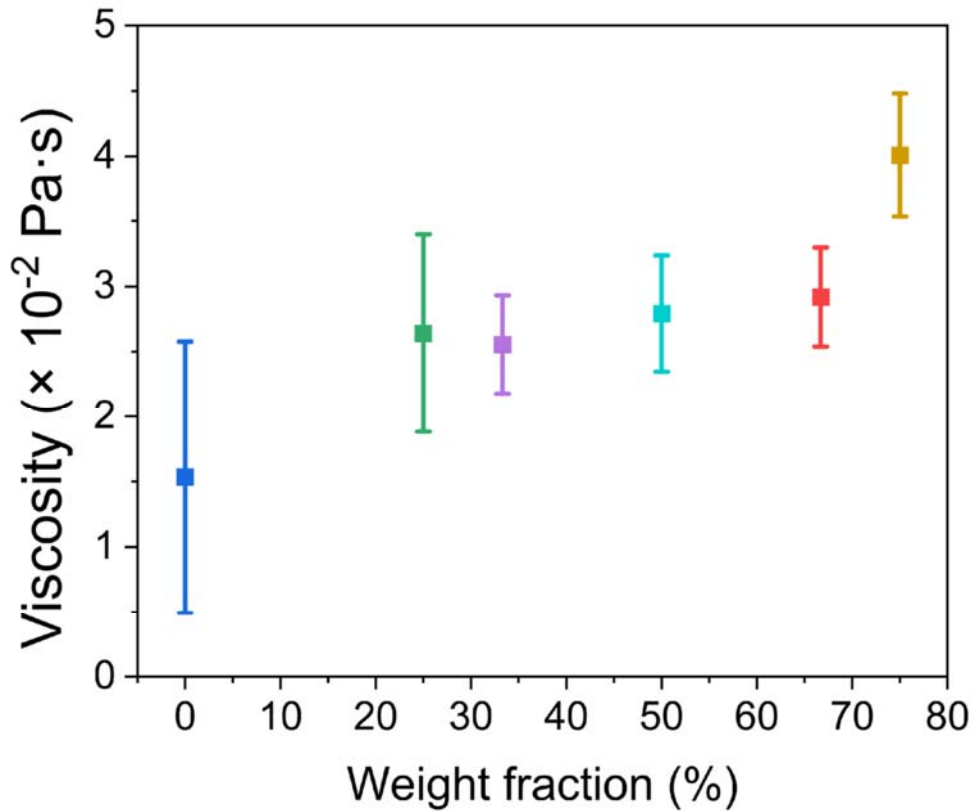


Figure 3.2.4 The viscosities of PEDOT-PVA solutions.

The impedance of sEMG electrodes plays a critical role in signal quality. Lower impedance leads to higher signal amplitudes compared to baseline noise, resulting in an improved SNR. To assess the performance of PEDOT-PVA electrodes, commercial Ag/AgCl sEMG electrodes were included as a reference. The results indicate that all PEDOT-PVA electrodes exhibit similar impedances to the Ag/AgCl electrode, with values falling within the same order of magnitude (Figure 3.2.5a). Impedances were measured at 100 Hz, a commonly used frequency for comparing muscle activity (Figure 3.2.5b). Notably, the impedance results align with the conductivity findings, showing optimal electrical performance when the PVA concentration is 25%. These findings should be considered in the final

determination of the binary system.

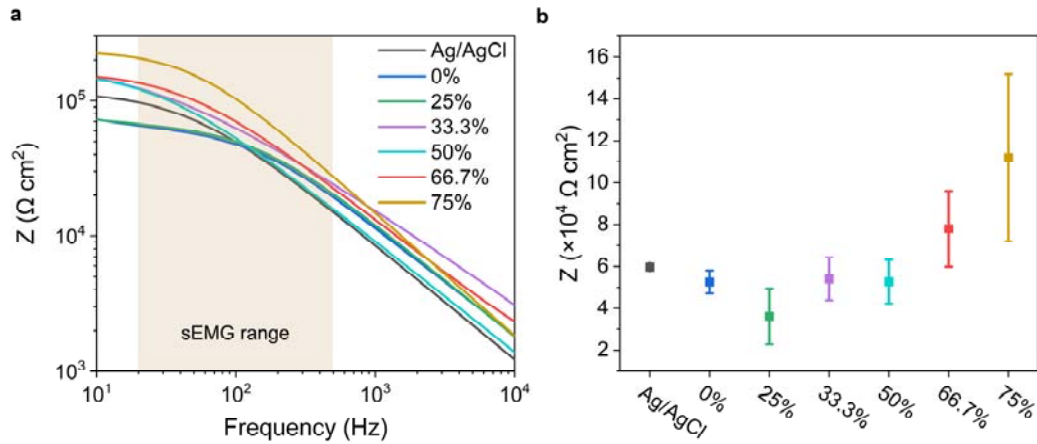


Figure 3.2.5 The results of impedance of PEDOT-PVA electrodes. a The impedances of the Ag/AgCl electrode and PEDOT-PVA electrodes in frequency domain. **b** The impedances of the Ag/AgCl electrode and PEDOT-PVA electrodes measured at 100 Hz.

All the aforementioned results were summarized in a radar plot, with each scale normalized to its respective maximum value for ease of comparison. It is challenging to definitively determine the best choice because blending polymers often presents a dilemma, where improving one property may lead to a decline in another. This trade-off will be further discussed in Chapter 7. Yet, when prioritizing conformability, which is a primary issue with current sEMG electrodes, the conclusion is the optimal weight fraction of 66.7 wt%, equivalent to a weight ratio of 2:1, represents the ideal concentration of PVA and PEDOT:PSS. This ratio provides higher stretchability and durability, making it well-suited for sEMG applications on the skin (Figure 3.2.6).

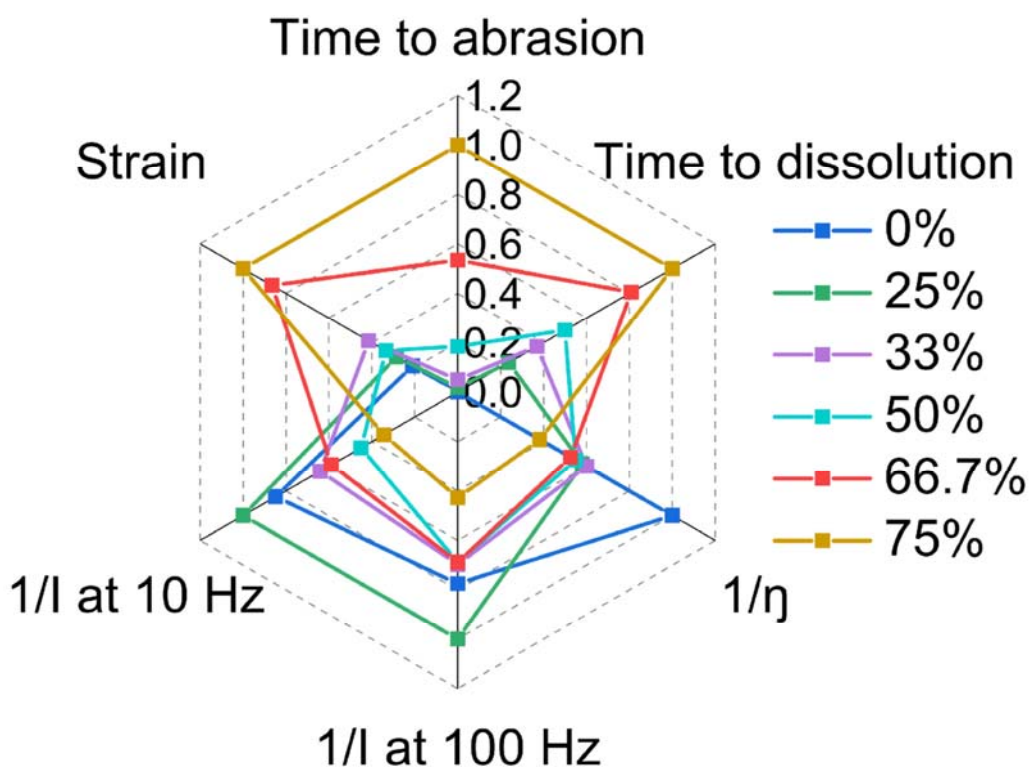


Figure 3.2.6 The radar plot of characterization results with different PVA addition.

Based on this, two types of electrode films: 1) pure PEDOT:PSS, 2) PEDOT:PSS with 66.7 wt% of PVA were chosen for further topographic characterizations using microscopy.

In the SEM results, both films exhibit the typical topography of dense polymer films (Figure 3.2.7). Upon closer examination and comparison between Figure 3.2.7b and 3.2.7d, it can be found that the inclusion of PVA within PEDOT:PSS results in the formation of a significantly more uniform film compared to pure PEDOT:PSS films. This enhanced miscibility can be attributed to the robust interaction between PVA and PEDOT:PSS facilitated by hydrogen bonds¹¹³.

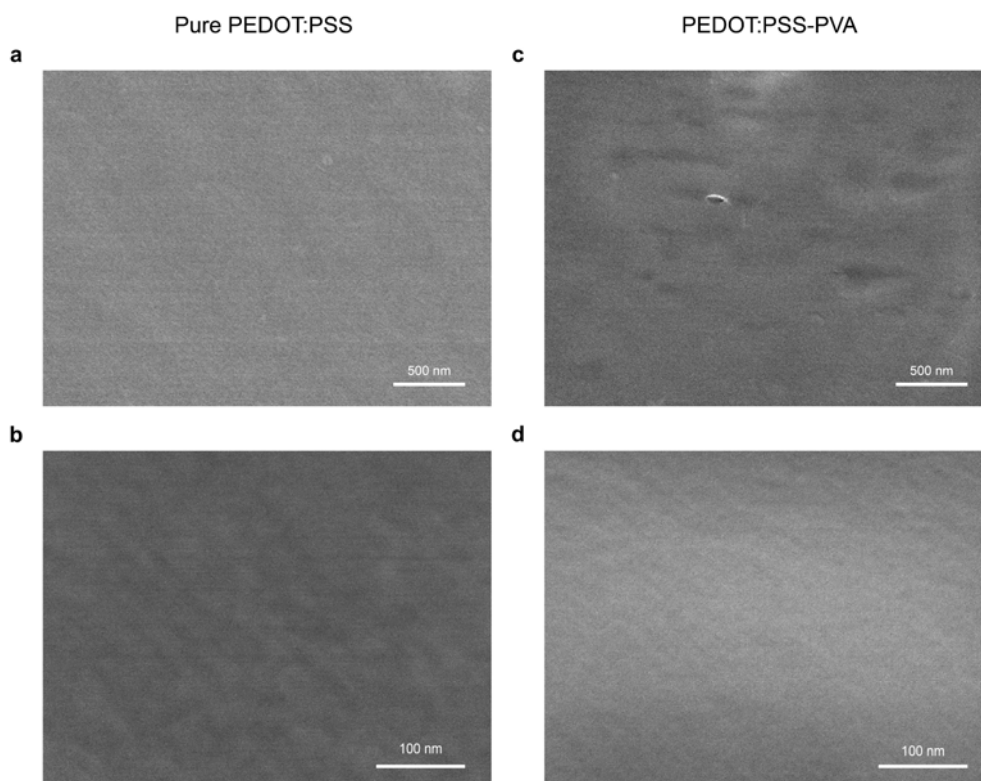


Figure 3.2.7 SEM images of the PEDOT:PSS film with or without PVA addition. a, b SEM images of the electrode film made by pure PEDOT:PSS. **c, d** SEM images of the electrode film made by PEDOT:PSS with 66.7 wt% of PVA and 5 vol% DMSO.

Analysis of the topography through AFM microscopy reveals a notable effect of PVA addition on smoothing the electrode films (Figure 3.2.8). The results from phase images further highlight the impact of PVA addition, introducing a new phase into the film when compared to the pure PEDOT:PSS film. Importantly, these phases exhibited excellent miscibility within the film. This outcome once again underscores the positive interaction between PEDOT:PSS and PVA when viewed at a microscopic level. It is also worth noting that the increased flexibility of the PEDOT-PVA film may be attributed to its composition of smaller grains and a smoother surface compared to the pure PEDOT:PSS film, when the blending

appears to reduce some structural flaws within the film.

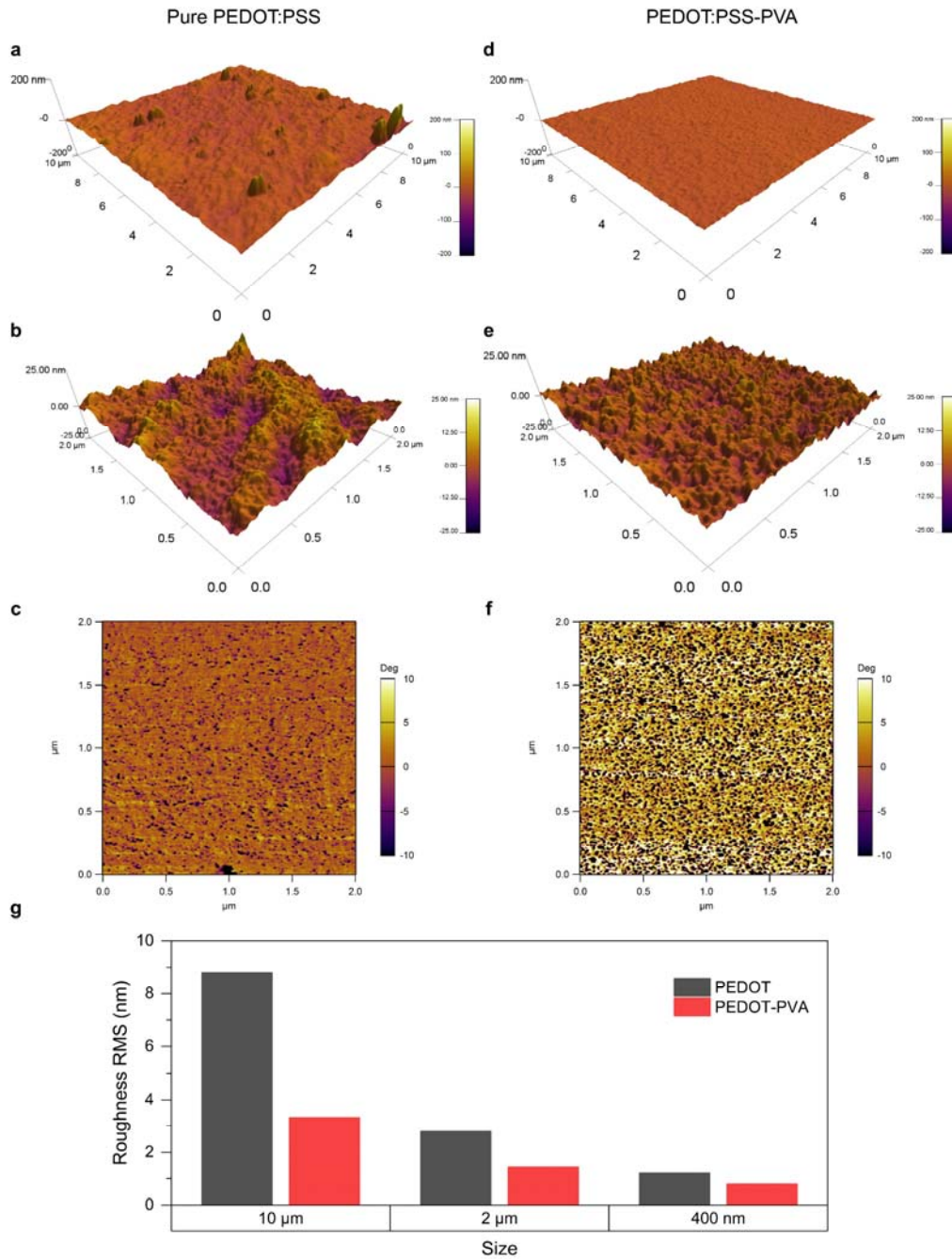


Figure 3.2.8 AFM images of the PEDOT:PSS film with or without PVA addition. a-c AFM images and phase image of the electrode film made by pure PEDOT:PSS. **d-f** AFM images and phase image of the electrode film made by PEDOT:PSS with 66.7 wt% of PVA and 5 vol% DMSO. **g** Surface roughness of two types of PEDOT:PSS films measured using AFM. PEDOT and PEDOT-PVA are abbreviations of pure PEDOT:PSS and PEDOT:PSS with 66.7 wt% of PVA, respectively.

3.2.2 Determination of each constituent in TPP

After the ratio between PEDOT:PSS and PVA was determined, different TPP films were made to identify the optimal TA concentration. Weight fractions of TA at 0%, 0.8%, 1.6%, 3.2%, 4.8%, 6.4%, 8%, 9.6%, 11.2%, and 12.8% were investigated.

The assessment was initially conducted on the mechanical performance of TPP films, focusing on conformability as it is the primary objective in this polymer blending study. The results indicate that the addition of TA further increases the elongation at break of the film (Figure 3.2.9). Additionally, the Young's modulus of the film decreases with increasing TA loading. Based on these findings, it can be inferred that a higher TA addition is more favourable for enhancing the conformability of TPP films when applied to the skin.

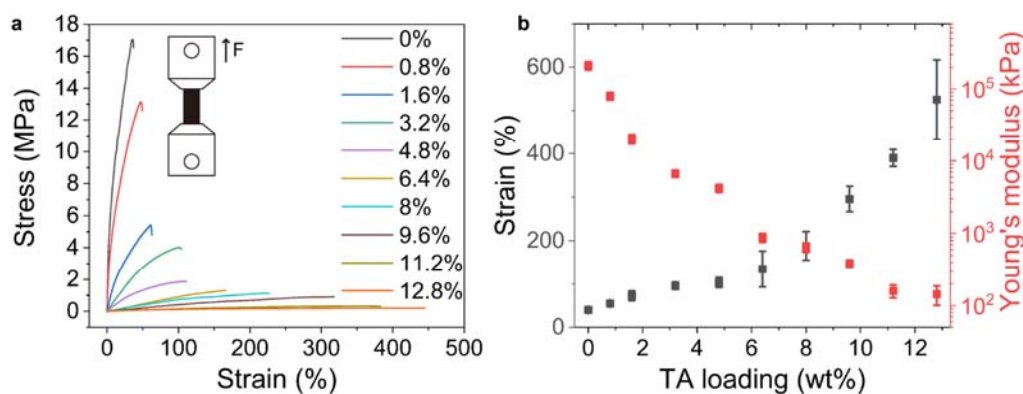


Figure 3.2.9 Mechanical characterizations of TPP films with different TA loading. a Tensile stress–strain curves. **b** Strain and Young's modulus of TPP films.

Another crucial property essential for high-quality recordings is the adhesiveness of the electrode. Therefore, a thorough evaluation of the

adhesiveness of the TPP film was conducted. The findings indicate that the peeling force required to remove the TPP film from the skin exhibits an increasing trend with higher TA loading (Figure 3.2.10). When considering both conformability and adhesiveness, it becomes evident that a higher TA loading is favourable.

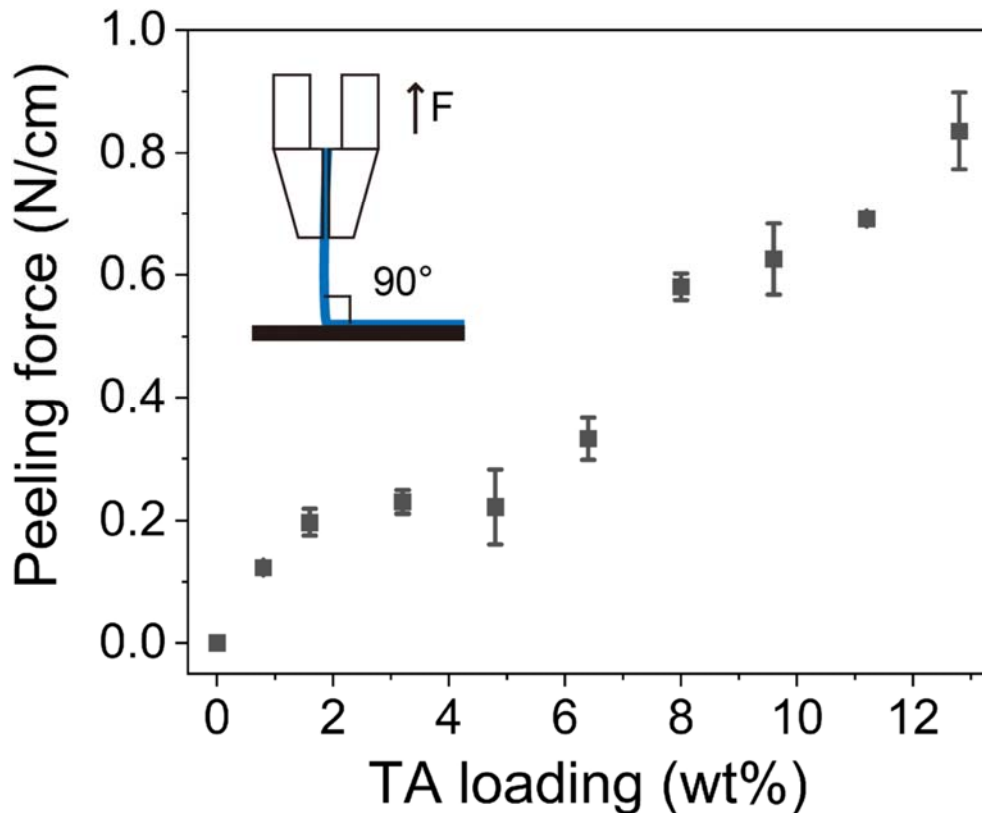


Figure 3.2.10 Peeling force of TPP films on the skin.

However, during the peeling test, it was observed that some TPP films with high TA loading could leave residue or even break during the peeling-off process. Consequently, it appears that the TA loading cannot be increased without limits. To establish a reasonable range, a residue test on TPP films with varying TA loading was conducted. The outcome showed that when the TA loading exceeds 9.6%, noticeable residue remained on the skin

after peeling (Figure 3.2.11). This experiment underscores the importance of controlling TA loading, as excessively high levels can compromise the integrity of the electrode, making it challenging not only for easy removal but also for potential repetitive use.

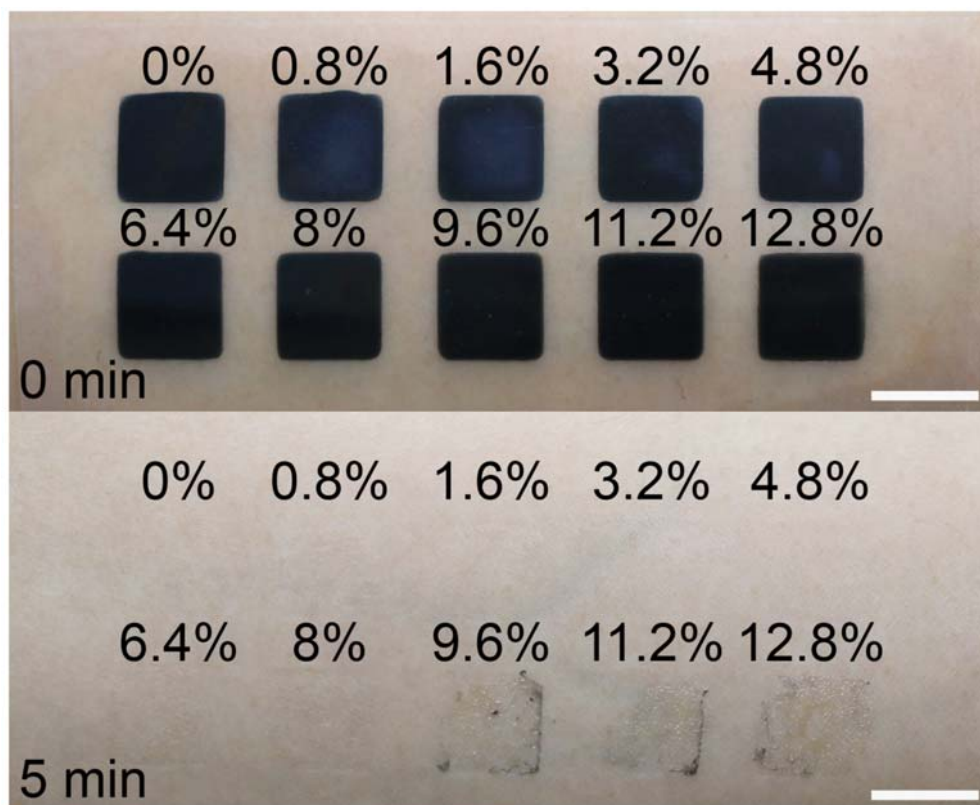


Figure 3.2.11 The photograph of residue test of TPP films with different TA loading peeled off from the skin. The films were attached to the skin for 5 min. Scale bar: 1 cm.

The conductivity of TPP films with varying TA loading was measured. The results indicate that the addition of TA leads to a reduction in conductivity (Figure 3.2.12). However, when TA loading exceeds 0.8%, there were no significant changes observed in conductivity. This suggests that the impact of TA loading on conductivity can be disregarded when prioritizing conformability and stretchability. This represents another compromise

encountered in the development of a new polymer film, a topic which will be explored further in Chapter 3.3.

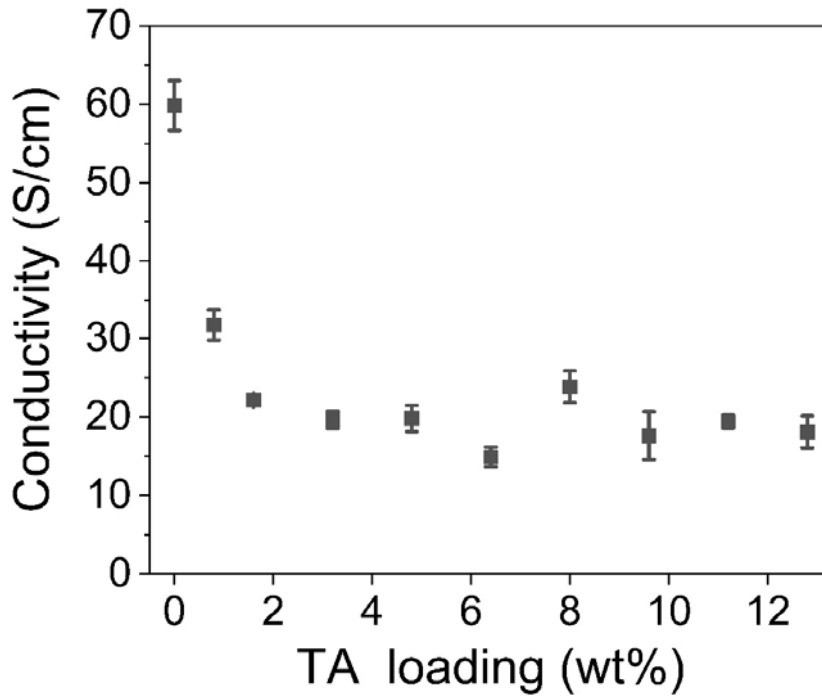


Figure 3.2.12 Conductivity of TPP films with different TA loading.

To elucidate the substantial impact of TA loading on the mechanical properties of the film, SEM was used to examine the microstructure of TPP films. Cross-sectional SEM images revealed the presence of porous structures in the TPP film with added TA, with the average pore size increasing when TA loading was higher (Figure 3.2.13). These pores range in size from hundreds of nanometres to several micrometres. While these porous structures borne some resemblance to hydrogel matrices, they fell short of being considered typical hydrogels, as most hydrogels typically possess pore sizes in the range of 10-500 μm and high content of water

(typically 70–99%)¹⁴⁰. These characteristics were not observed in the TPP film. In this context, it is supposed that the TPP film occupies an intermediate state between a pure polymer film and a hydrogel. This hypothesis finds support in the cross-sectional SEM images, where the film underwent a transition from a dense structure to a porous one as TA loading increases, representing a gradual transformation towards a hydrogel-like state. The presence of these porous structures in this intermediate state results in reduced cohesive energy and Young's modulus. The decreased cohesive energy in the adhesive electrode can lead to cohesive rupture (damage to the electrode) rather than adhesive rupture (occurring on the surface), potentially leaving undesirable residue upon peeling from the skin. This has been confirmed by previous tests (Figure 3.2.11). The lower Young's modulus imparts better compliance and stretchability to the film, which are crucial for achieving conformal adhesion between the electrodes and the skin¹⁴¹. This has also been confirmed by the results of tensile and peeling tests on TPP films with increasing concentrations of TA (Figure 3.2.9 and 3.2.10).

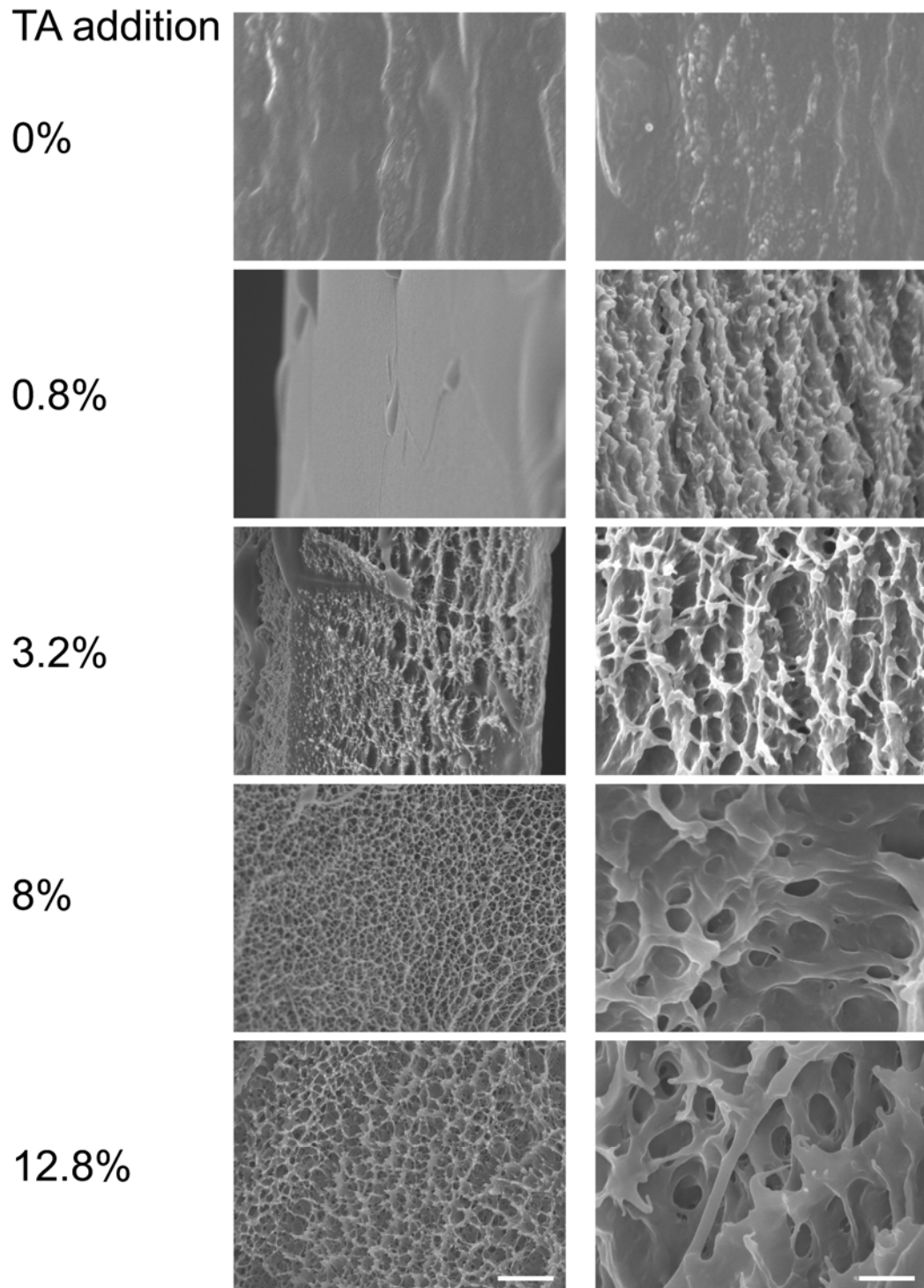


Figure 3.2.13 The cross-sectional SEM images of TPP films with different TA additions. The scale bars in images are 4 and 1 μm , respectively.

In an effort to further comprehend the mechanism behind the alteration of

the microstructure in the TPP film following TA addition, a simple model was built to visualize the process. Several studies have reported that the introduction of a certain amount of TA into hydrophilic polymer solutions can lead to the formation of tacky and elastic supramolecular complexes. These complexes are characterized by TA acting as a binder between polymer chains^{121,142,143}. TA contains gallol groups capable of forming various interactions, including hydrogen bonds, electrostatic interactions, hydrophobic interactions, and cation- π interactions with different adherends. These tacky complexes also enhance wetting behaviour on various surfaces and establish strong adhesion through Van der Waals forces and mechanical interlocks. Based on these findings, it is proposed that the addition of TA results in increased cross-linking of the PVA chains at specific positions mediated by TA. This cross-linking process expands the space between polymer chains and ultimately gives rise to the observed porous structure (Figure 3.2.14).

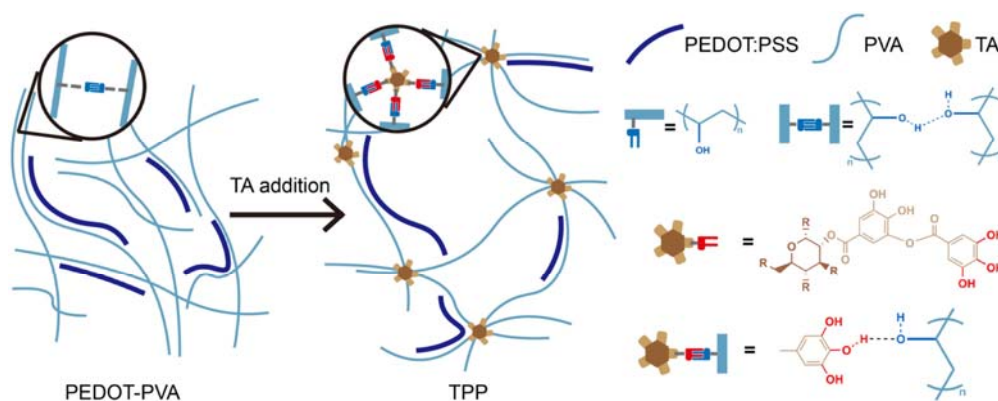


Figure 3.2.14 Schematic illustration of the working mechanism in PEDOT-PVA and TPP films and related chemical structures.

After considering all of these observations, it was determined that a final

weight concentration of TA at 8% strikes a balance, rendering the film soft and adhesive without being prone to tearing. This TPP film exhibited an elongation at break of 188%, a Young's modulus of 644 kPa, and adhesive forces of 0.58 N/cm on the skin.

3.3 Characterizations of 8% TPP

3.3.1 Electrical and mechanical properties

After determining the concentration of each constituent in the TPP solution, we proceeded to verify the indispensability of each component by examining their impact on the conductivity, stretchability, and adhesiveness of the electrode. In terms of conductivity, the absence of PEDOT:PSS resulted in a significant increase in resistance (Figure 3.3.1). Concerning stretchability, the absence of PVA reduced the elongation at break from 175% to 15.5%. Regarding adhesiveness, the absence of TA rendered the film non-adhesive. Each of these results serves to confirm the essential role of each constituent in the TPP film, providing a deeper understanding of the formation of this ternary system.

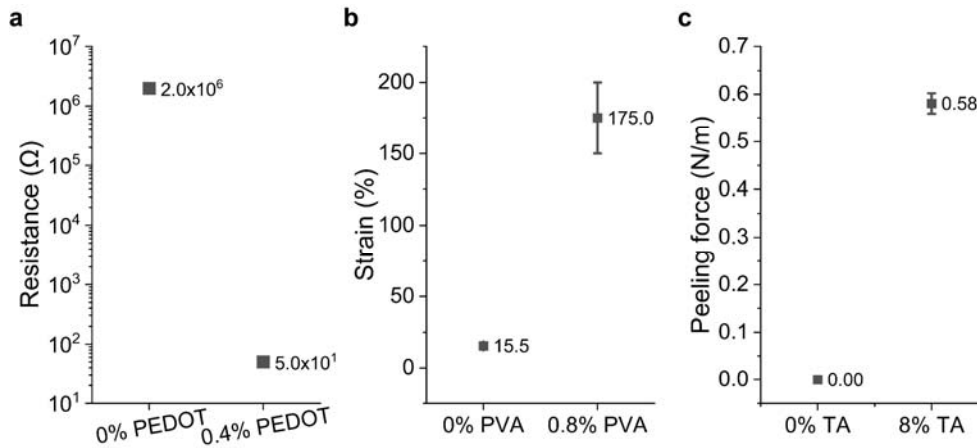


Figure 3.3.1 The changes of resistance, strain and peeling force with or without each component in TPP film.

We examined the electrode-skin impedance of the TPP film and compared it with that of Ag/AgCl and PEDOT-PVA electrodes. The results reveal that the impedance performance of the TPP film closely resembled that of the PEDOT-PVA film and is slightly superior to that of the Ag/AgCl electrode within the sEMG frequency range (Figure 3.3.2).

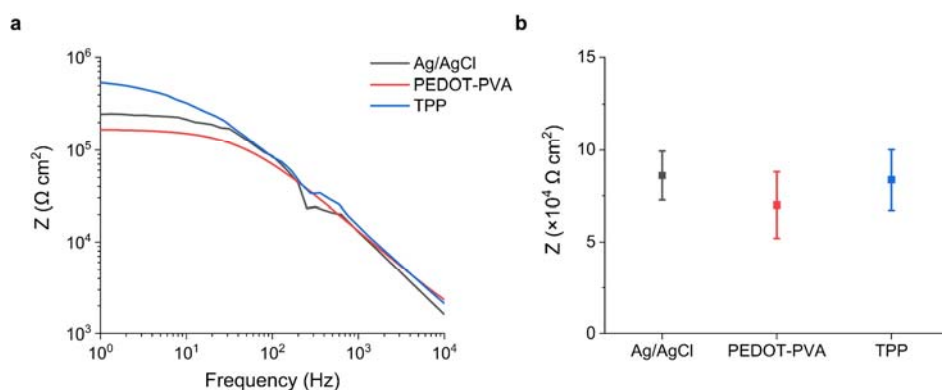


Figure 3.3.2 Comparisons of impedance between different types of electrodes. **a** Bode plots of three electrodes tested on the skin. Specially for sEMG, the impedances from 20 – 200 Hz should be focused on. **b** The impedances of three electrodes measured at 100 Hz.

It is clear that TPP electrodes, in comparison to PEDOT-PVA electrodes, do compromise certain electrical properties in favour of achieving exceptional stretchability and adhesiveness. Thus, it becomes imperative to assess the impact of this compromise on sEMG recording. Two electrode pairs using PEDOT-PVA and TPP electrodes were fabricated, and each pair is labelled as electrodes 1 and 2. These electrode pairs were then applied to the biceps brachii for recording during biceps curls. sEMG signals filtered using two different low cutoffs were compared to evaluate electrode performance. The signals recorded by PEDOT-PVA electrodes exhibited significant instability when subjected to a 1 Hz high-pass filter. This instability stems from non-adhesiveness, causing relative movement between the electrodes and the skin, resulting in motion artifacts within the low-frequency domain. In contrast, the adhesive TPP electrodes yielded much more stable recordings under similar conditions (Figure 3.3.3a). Further analysis through spectrograms revealed that the activation of EMG signals at 40 Hz was clearly discernible in results recorded by TPP electrodes, while it remained challenging to distinguish with PEDOT-PVA electrodes (Figure 3.3.3b). These findings highlight the advantage of using adhesive TPP electrodes. Additionally, the quantification of the RMS changes was done between EMG signals filtered using two different low cutoffs. The results indicate that adhesive TPP electrodes exhibit greater stability and are capable of effectively recording lower frequencies even during dynamic tasks (Figure 3.3.3c). This is advantageous as it reduces the need for extensive post-processing before analysis, allowing for more comprehensive data analysis while preserving valuable information. Based

on these test results, it becomes evident that the trade-off of electrical performance for enhanced stretchability and adhesiveness holds significant value, particularly in dynamic tasks. Therefore, TPP emerge as a preferred choice for sEMG electrodes over PEDOT-PVA.

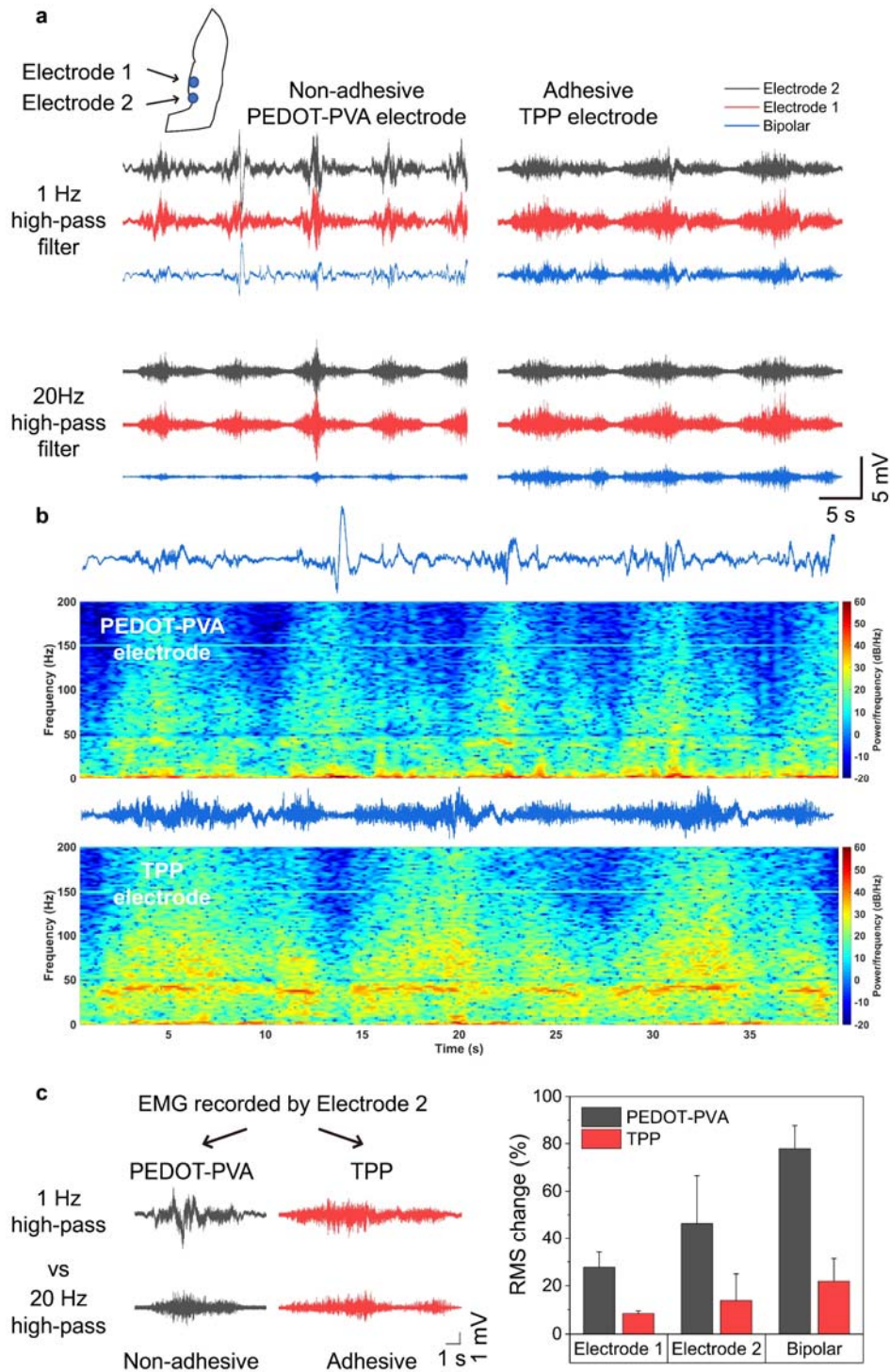


Figure 3.3.3 Recording performance by electrodes with or without adhesiveness during dynamic task. **a** sEMG results filtered by 1 Hz and 20 Hz high-pass filter. **b** Spectrogram comparison between results recorded by two types of electrodes. **c** EMG signals recorded by PEDOT-PVA and TPP electrodes. The raw data was filtered by 1 Hz and 20 Hz high-pass filter; RMS change between two filtered signals showed the extent of discrepancy. $RMS\ change = \frac{RMS_{1Hz} - RMS_{20Hz}}{RMS_{1Hz}}$.

3.3.2 Repeatability of use

Furthermore, the TPP film demonstrates excellent repeatability even after being stretched to a strain of 20% for 1000 cycles (Figure 3.3.4). This property is invaluable in ensuring the durability of the electrode, especially considering the continuous deformations of the skin during muscle movements. It is worth noting that the MPC can also endure strains of up to 80% for 1000 cycles while maintaining a stable resistance⁵⁰. The exceptional durability of both materials ensures the overall long-lasting performance of the device.

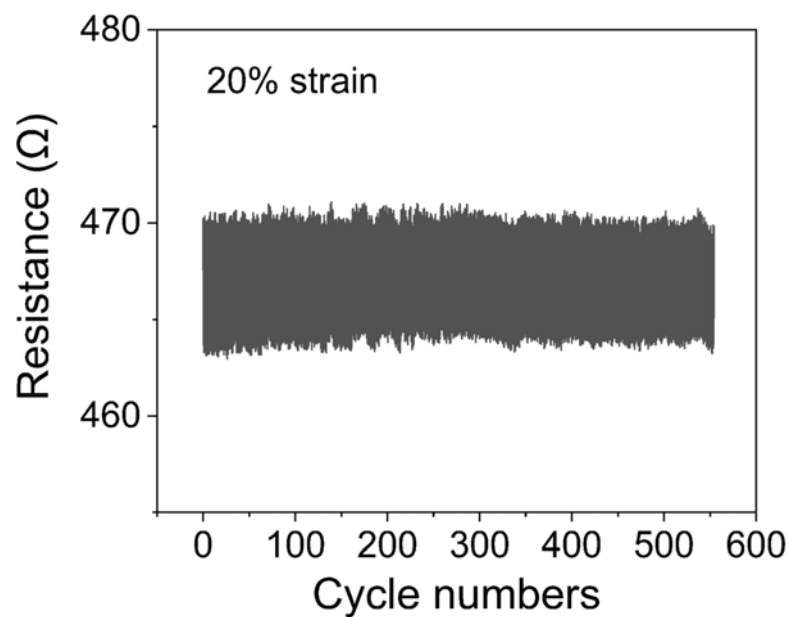


Figure 3.3.4 Real-time monitoring of the TPP film by stretching the film from a strain of 0 to 20% for about 500 cycles.

To assess the consistency of electrical and mechanical properties of electrodes on the skin, the evaluation was conducted after subjecting them to 200 cycles of skin compression and stretching. These evaluations involved physically squeezing and stretching the skin using fingertips to test the

stability of the electrodes. The results reveal that TPP electrodes exhibit remarkable stability in terms of adhesion and skin-electrode impedance (Figure 3.3.5).

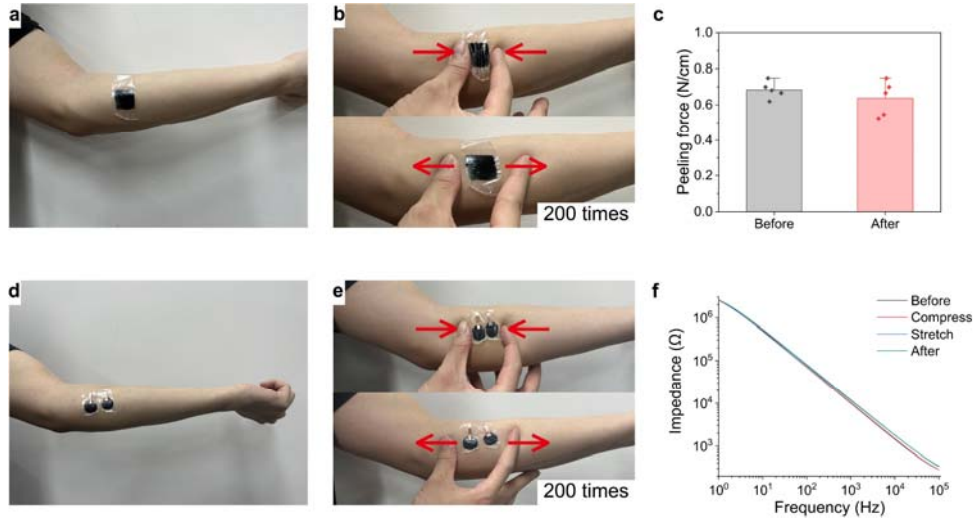


Figure 3.3.5 The change in adherence and impedance of TPP electrodes on the skin. a, b images of the electrode applied to the skin and the motions made during the adhesion test. **c** The peeling force of TPP electrodes off the skin before and after motions (n=5). **d, e** Images of the electrode applied on the skin and the process of movements during impedance test. **f** The impedance of TPP electrodes on the skin before, after motions and in the state of compressing and stretching.

Furthermore, the change in SNR was employed as a direct measure to assess the stability of TPP electrodes on the skin. Despite subjecting them to 200 cycles of compression and stretching, the SNR of sEMG signals recorded by TPP electrodes remained consistently stable. The baseline noise level reduced from 1.22 μV to 1.04 μV and remained stable even after the motions. Consequently, there was minimal change in the SNR of signals, demonstrating the remarkable stability of TPP electrodes on the skin, even after undergoing compression and stretching (Figure 3.3.6).

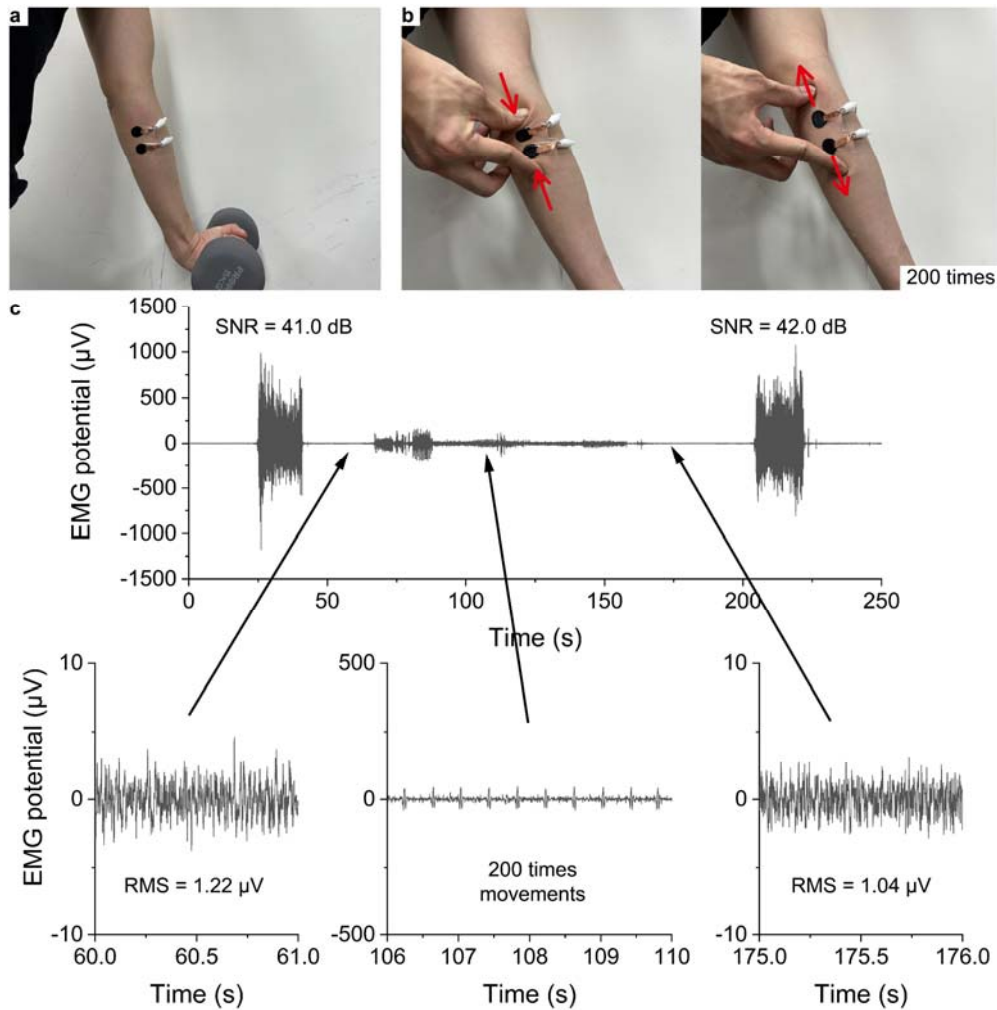


Figure 3.3.6 SNR variation and baseline noise levels of TPP electrodes on the skin. a, b Images showing the electrode applied to the skin and the motions made to compare SNR. **c** Demonstration of the entire process of recording using the TPP electrodes applied on skin before and after motions.

The repeatability of the TPP electrode was evaluated by repeatedly peeling the electrode off and reattaching it to the skin while measuring the RMS of noise. The results consistently showed an RMS noise level of approximately 1.5 μV over 10 reattachments (Figure 3.3.7). This test confirms that TPP electrodes can be used repetitively without compromising recording performance.

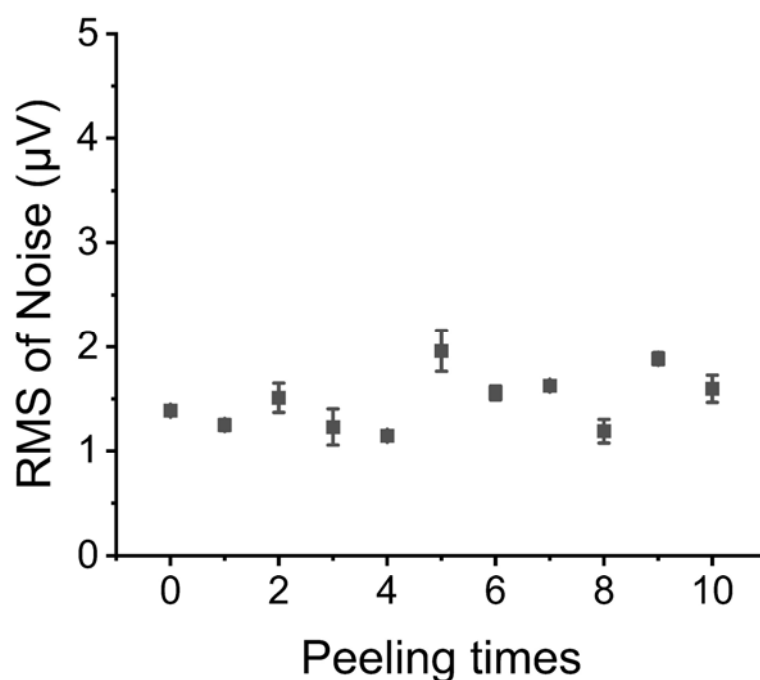


Figure 3.3.7 The repetitive test of TPP films on the skin. Noise levels were recorded after the reattachment of TPP film, with measurement repeated three times (n=3).

The tests presented in Figures 3.3.5-3.3.7 provide strong evidence of the durability of TPP electrodes on the skin. These encouraging results serve as a fundamental step in demonstrating the potential for the commercialization of TPP electrodes. Further testing on the repeatability of the MEAP will be conducted in Chapter 4.

3.3.3 Long-term test

The biocompatibility of TPP electrodes was assessed on the skin and compared them with Ag/AgCl electrodes. Both electrode types were found to be skin-friendly, allowing for 24-hour wear without causing any itchiness or inflammation (Figure 3.3.8). However, a notable difference emerges. After 6 hours of attachment, the adhesive from Ag/AgCl electrodes

detached and adhered tightly to the skin, proving difficult to remove. In contrast, TPP electrodes left very little residual adhesive on the skin even after 24 hours of adhesion.

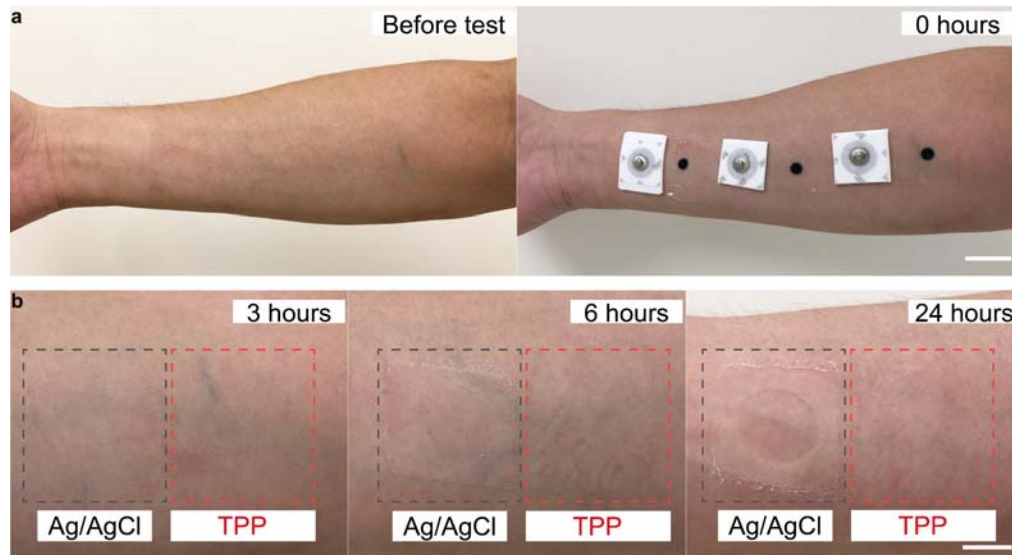


Figure 3.3.8 Biocompatibility of TPP electrodes on skin. **a** Photographs of arm skin of the subject for the biocompatibility test. Scale bar: 2 cm. **b** Skin condition after wearing of 3, 6, and 24 hours. Scale bar: 1 cm.

Based on the favourable outcomes of the biocompatibility test, we proceeded with a long-term assessment to explore the potential of the electrodes for use in wearables. TPP electrodes were applied to the muscle belly of the FCU of a subject. The results demonstrated that TPP electrodes performed exceptionally well, maintaining an SNR level above 30 dB for 3 days and above 20 dB for nearly 5 days, while Ag/AgCl electrodes dropped to 20 dB within 6 hours (Figure 3.3.9). The total wear-time for the long-term test exceeded 10 days, during which TPP electrodes caused no itchiness or inflammation. Regarding the increase in baseline noise, it is hypothesized that normal perspiration might gradually affect the

effective contact area and conductivity of the TPP film. Sweat components like fats and salts may accumulate slowly on the TPP film, resulting in increased noise intensity¹⁴⁴. Additionally, the natural thickening of the stratum corneum due to normal metabolic processes may raise impedance between the electrodes and skin during extended measurements.

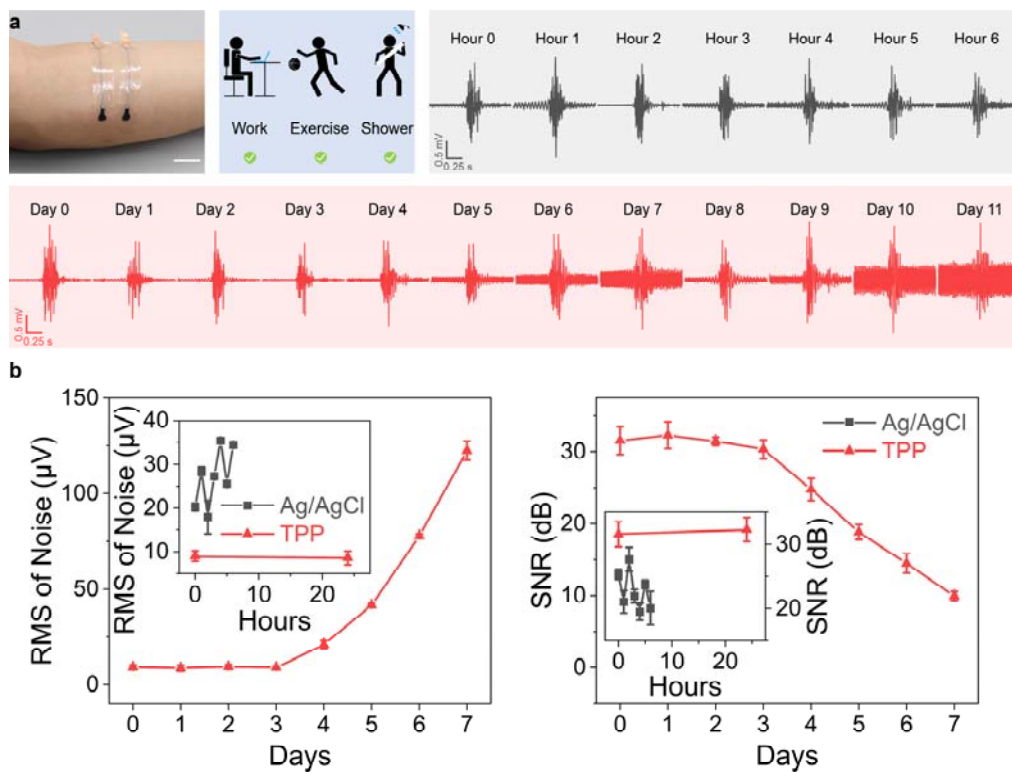


Figure 3.3.9 Biocompatibility of TPP electrodes on skin. **a** A photograph of the electrodes for long-term test, and a schematic diagram to illustrate activities of the subject during the test. sEMG signals recorded by TPP and Ag/AgCl electrodes during the long-term test. Scale bar: 2 cm. **b** Comparisons of baseline noise and SNR of sEMG signals recorded by TPP and Ag/AgCl electrodes during the long-term test.

3.4 Comparing tests

3.4.1 TPP electrodes and dry electrodes in other literature.

When comparing TPP electrodes with dry electrodes reported in the literature, TPP electrodes excelled in terms of durability and signal quality. All information was summarized in Table 3.4.1. Among these studies, one was published in 2020, nine in 2021, and three in 2022. This selection allows for a comprehensive comparison that accurately represents the current state of sEMG electrode technology. It is noteworthy that among 13 studies, only 6 discussed sticky electrodes, and TPP electrodes outperform others in terms of adhesiveness, contributing to their superior SNR compared to all dry electrodes. The inherent stretchability of TPP electrodes ensures a high elongation at break, placing them at the forefront in comparative evaluations. Additionally, TPP electrodes boast the smallest electrode area, which can be reduced to as little as 0.8 mm². This feature holds significant potential for future high-density array fabrication, allowing for the incorporation of more channels within the same substrate area comparing to other reported dry electrodes. However, it is important to highlight that none of the electrodes in these studies could be used to create a stretchable array, limiting their applicability in the sEMG sector. This comparison indicates that TPP electrodes are at the forefront of the field.

| Materials for electrodes | Materials for substrates | Intrinsically stretchable? | Strain | The adhesioness (N/cm) | The smallest area of the electrode (mm ²) | Electrode-skin impedance at 100 Hz (K Ω ·cm ²) | Long-term test (Hours) | RMS of Noise (μ V) | SNR (dB) |
|--|--------------------------|----------------------------|-------------|------------------------|---|---|------------------------|-------------------------|--------------------------------|
| Ag ¹⁴⁵ | Polyimide | No | 80% | 0 | 16.0 | 12.8 | 11 | N/A | N/A |
| Ag-filled epoxy ¹⁴⁶ | Epoxy | No | N/A | 0 | 100.0 | 80.0 | 24 | ~43.0 | 16.0 |
| Ag flakes/PDMS ¹⁴⁷ | PDMS | Yes | 480% | 0 | 100.0 | 34.0 | 10 | ~540.0 | N/A |
| Ag-polytetrafluoroethylene ¹⁴⁸ | Polyurethane | Yes | 20% | 0 | 600.0 | N/A | N/A | ~74.0 | N/A |
| Au nanoparticles ¹⁴⁹ | Polyimide | No | N/A | 0 | 80.0 | N/A | 24 | ~60.0 | ~21.0 |
| PEDOT:PSS/Glycerol ¹⁵⁰ | Silk fibre | Yes | 250% | N/A | 314.0 | ~157.0 | N/A | N/A | N/A |
| PEDOT:PSS/Glycerol/Polysorbate ¹⁵¹ | N/A | Yes | 100% | 0.013 | 100.0 | 200.0 | 12 | N/A | 35.2 |
| PEDOT:PSS/Poly(lactic acid) ¹⁵² | N/A | No | 34% | ~0.467 | 176.6 | ~35.3 | N/A | ~47.0 | 22.8 |
| PEDOT:PSS/Poly(poly(ethylene glycol) methyl ether acrylate) ¹⁵³ | N/A | Yes | 75% | 0.005 | 400.0 | N/A | N/A | ~60.6 | 4.5 |
| PEDOT:PSS/Polyvinyl alcohol/Borax ¹⁵⁴ | N/A | Yes | 400% | N/A | 254.3 | 101.7 | N/A | N/A | 29.5 \pm 1.3 |
| WPU/Deep eutectic solvent/Tannic acid ¹⁵⁵ | N/A | Yes | 178% | 0.125 | 1256.0 | 25 | N/A | 50.0 | ~14.0 |
| PEDOT:PSS / Waterborne polyurethane/D-sorbitol ¹¹² | N/A | Yes | 43% | 0.43 | 400 | 15 | 16 | ~25 | ~20 |
| PEDOT:PSS / Polyvinyl alcohol/Tannic Acid ¹⁵⁶ | N/A | Yes | 54% | 0.28 | 16 | 100 | N/A | 11.8 | 34.96 |
| This work: PEDOT:PSS / Polyvinyl alcohol/Tannic Acid/Liquid metal | PDMS/TPU | Yes | 188% | 0.58 | 0.8 | 80 | 120 | 1.0 | 42.3\pm0.7 |

Table 3.4.1 Comparisons between dry electrodes in other literatures and this work.

3.4.2 Comparison of conformability between TPP and Ag/AgCl electrodes

Ensuring a stable and high-quality signal is crucial, particularly when recording from areas with skin folds. To validate this aspect, sEMG signal recordings were conducted on the frontalis muscle using both Ag/AgCl and TPP electrodes. Frontalis muscle sEMG is essential for research and treatment in areas such as sleep disorders, anxiety, headaches, and facial recognition¹⁵⁷. However, the presence of skin folds on the frontalis muscle can pose challenges for non-conformal electrodes during sEMG signal recording. Thanks to the exceptional conformability and adhesiveness of the electrode and substrate, TPP electrodes consistently achieved perfect skin attachment, regardless of skin compression or stretching (Figure 3.4.1a). During recording, TPP electrodes seamlessly adapted to skin folds, ensuring stable signals even when the frontalis muscle contracts. In contrast, Ag/AgCl electrodes failed after only four contractions. In this context, the noise levels which is even higher than signal levels, render them unsuitable for sEMG recording (Figure 3.4.1b).

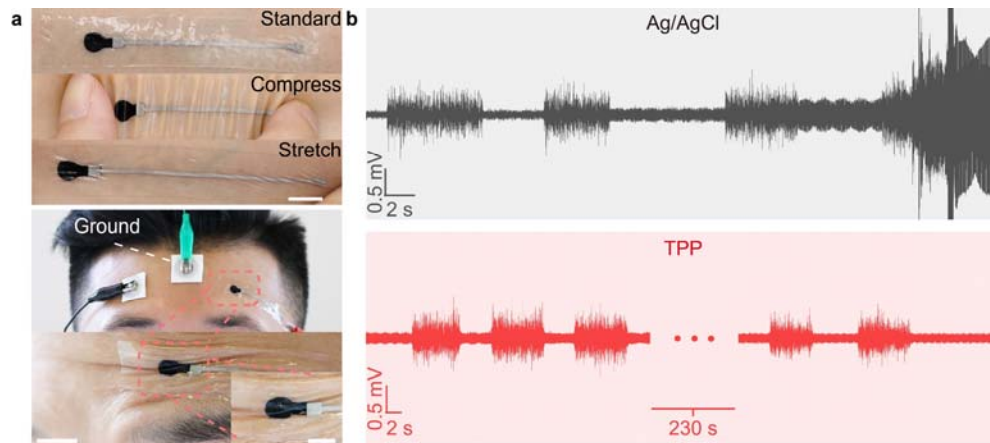


Figure 3.4.1 Comparison of recording performances on frontalis muscle between Ag/AgCl and TPP electrodes. **a** Top, standard, compressing and stretching TPP electrodes on the skin. Scale bar: 1 cm; bottom, photographs of Ag/AgCl and TPP electrodes when recording sEMG of frontalis and the TPP electrode in the skin folds. Scale bar of photograph at the bottom: 1 cm; bottom inset: 0.5 cm. **b** sEMG signals recorded by Ag/AgCl and TPP electrodes, respectively.

Based on lateral photos of both types of electrodes on the frontalis muscle, a schematic diagram to illustrate the differences has been created. In the case of non-conformal electrodes, such as Ag/AgCl electrode, skin folds appear when the frontalis muscle contracts, resulting in air gaps forming between the electrodes and the skin (Figure 3.4.2a). These air gaps reduce the adhesion force between the electrode and the skin, making the electrodes prone to detachment. In contrast, the TPP electrode maintains its shape and conforms to the skin folds, ensuring stable contact even during muscle contraction (Figure 3.4.2b).

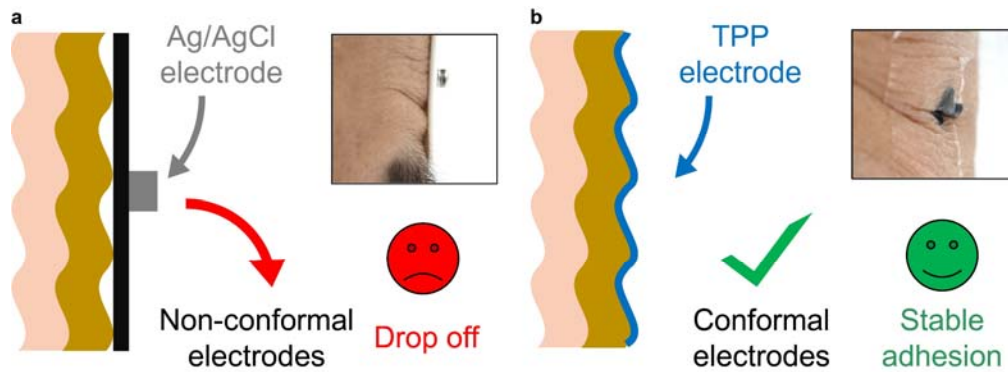


Figure 3.4.2 Schematic illustrations and lateral photos of Ag/AgCl electrode and TPP electrode on skin folds.

Finally, the quantification was conducted to compare the performance of both electrodes. The findings indicate that the TPP electrode exhibit significantly greater stability than the Ag/AgCl electrode for sEMG recording over skin folds, as demonstrated by the RMS of noise levels and SNR (Figure 3.4.3).

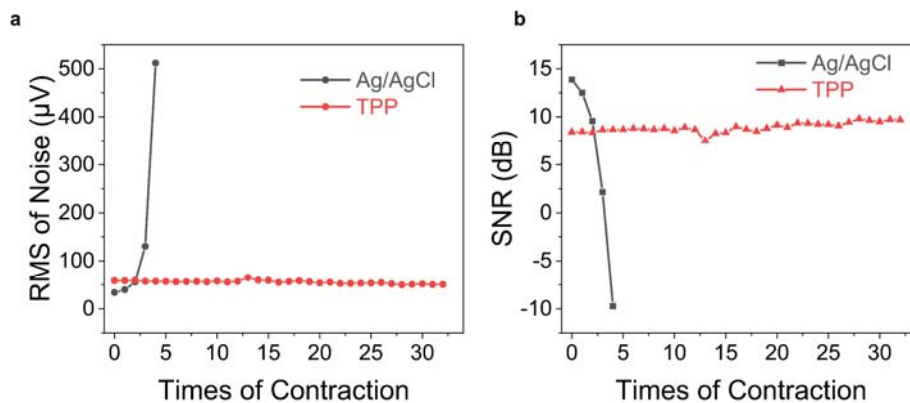


Figure 3.4.3 Quantifications of recording performances by two electrodes on frontalis muscle. a Noise level and b SNR recorded by two electrodes during contractions.

In comparison with commercial Ag/AgCl electrodes, this section confirms

the exceptional conformability and performance of TPP electrodes in sEMG recording.

3.4.3 Comparison of muscle fatigue monitoring between TPP and Ag/AgCl electrodes

Another critical application of sEMG in clinical diagnosis is to assess muscle function based on the median frequency of the signal^{4,5}. Typically, a decrease in median frequency indicates muscle fatigue. However, if this decrease occurs at the beginning of the test, it may signify pathological changes in the muscle, where only a few muscle fibres are recruited for contraction³. To evaluate the ability of TPP electrodes to capture frequency information in the signal, we compared them with Ag/AgCl electrodes placed at the same location on the FCU muscle (Figure 3.4.4a). Two pairs of electrodes were affixed to the forearm at the same position. The subject was instructed to curl the wrist while holding a 5 kg dumbbell for three sessions to activate the FCU. The TPP electrodes exhibited slightly better SNR than the Ag/AgCl electrodes, with values of 39.2, 37.5, and 40.5 dB for the three contractions recorded by TPP electrodes compared to 38.9, 37.5, and 38.6 dB for the Ag/AgCl electrodes. Spectrograms from TPP electrodes clearly displayed frequency information, similar to Ag/AgCl electrodes. Moreover, the spectrograms revealed a decreasing trend of frequency in the sEMG signal, which is a direct indicator of muscle fatigue (Figure 3.4.4b).

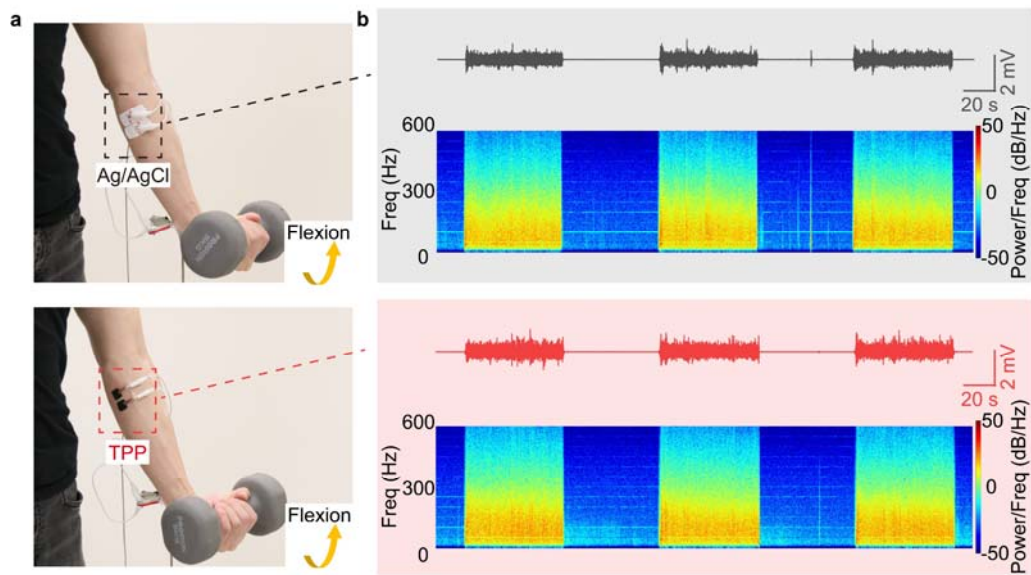


Figure 3.4.4 Quantifications of recording performances by two electrodes on frontalis muscle. a Photographs of electrode configuration on FCU and contraction task. **b** sEMG signals and spectrograms recorded by Ag/AgCl and TPP electrodes, respectively.

The tasks were designated as flexion 1, 2, and 3 for the calculation of median frequency during each task (Figure 3.4.5). To mitigate errors arising from fatigue, we performed a linear fit for the initial 25 seconds of each contraction to quantify the change, following a reported approach¹⁵⁸. The slopes obtained with both types of electrodes display negative values, indicating muscle fatigue. These quantified results validate that TPP electrodes can measure muscle fatigue similarly to Ag/AgCl electrodes.

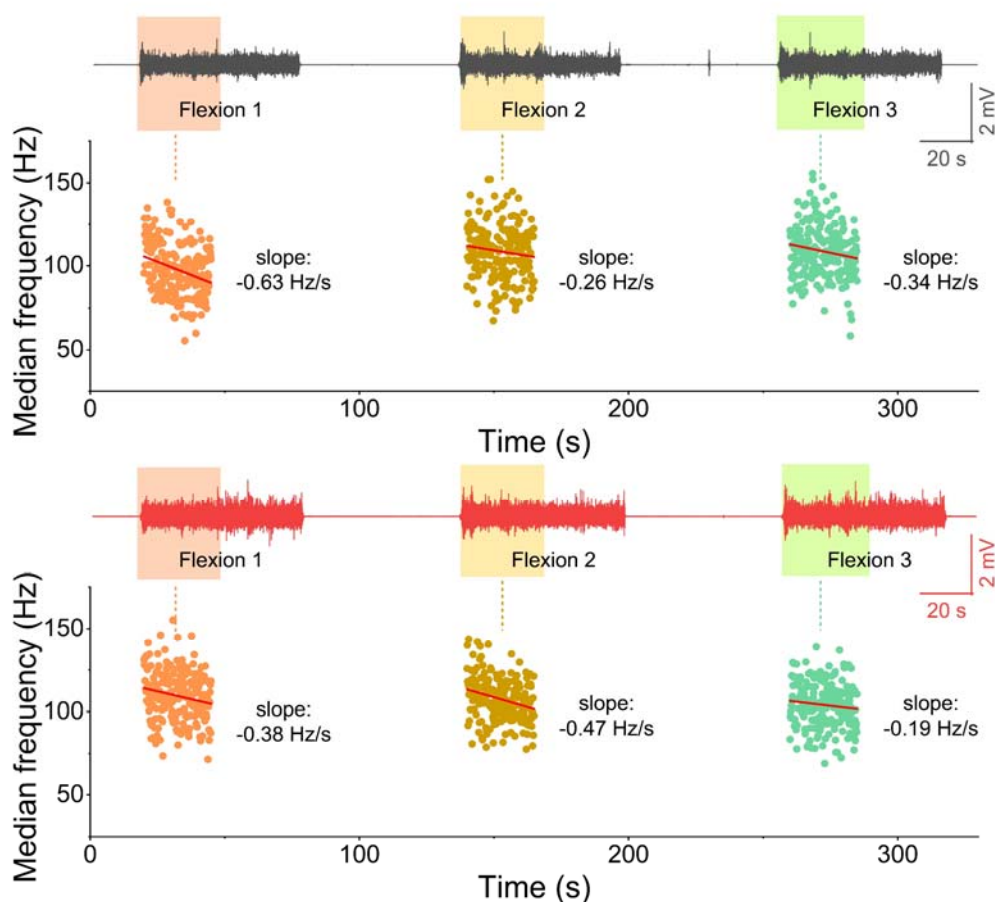


Figure 3.4.5 sEMG signals and linear fit results of median frequency during flexion 1, 2 and 3 recorded by Ag/AgCl and TPP electrodes. Decreasing median frequencies indicated fatigue of the muscle.

3.5 Impact of viscosity on TPP ink spray patterns

When recording from small muscles, the size of the electrode must be proportionally reduced, imposing specific requirements on the patterning method. This method should be both stable and highly efficient, allowing for the smallest possible electrode size while retaining scalability for potential high-density structures within an array. In this regard, the application of TPP via moulds to create specific patterns emerges as a

practical solution. However, initial observations revealed that the spraying pattern of the original TPP ink resulted in an island-like structure on the substrate, failing to form a uniform film suitable for an sEMG electrode (Figure 3.5.1a). Notably, significant improvement in film uniformity was observed after the addition of xanthan gum to the TPP ink (Figure 3.5.1b). This intriguing phenomenon prompted an exploration of its underlying causes, with the aid of a simplified dewetting model.

Dewetting, in this context, refers to the spontaneous withdrawal of a liquid film from an adverse surface, akin to water beading on a hydrophobic solid surface¹⁵⁹. In our spraying scenario, it is assumed that dewetting continually occurs due to defects on the substrates or airflow during spraying (Figure 3.5.1c). Either of these factors can create dry zones within the film. The initial assumption is that a uniform film is initially formed, but subsequent dewetting disrupts its continuity. In this scenario, the dewetting velocity becomes a critical factor. Given the continuous nature of spraying, a new droplet is deposited on the film at specific intervals. During this interval, the outcome depends on the relative rates of dewetting and droplet deposition. If dewetting occurs rapidly, creating a dry zone larger than the new droplet, dewetting persists. However, if dewetting is slow, the dry zone shrinks to a size smaller than the new droplet, causing the droplet to fully cover and terminate the dewetting process. These two assumptions are pivotal in the model, with dewetting velocity inversely related to viscosity. Consequently, an increase in the viscosity of the TPP ink is expected to yield improved uniformity in spray patterning.

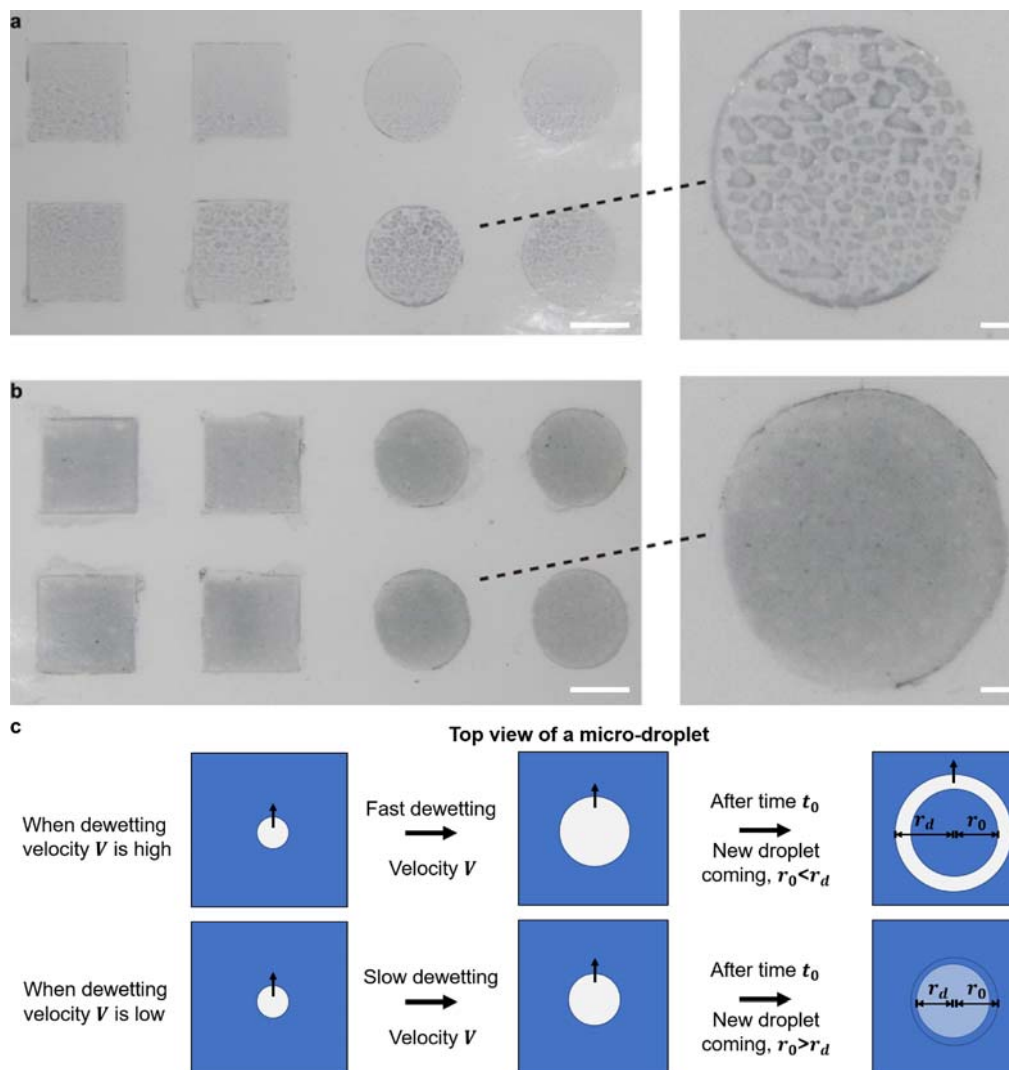


Figure 3.5.1 Results of spray patterning with different addition of xanthan gum in TPP ink and a simplified model for dewetting. a 0% addition of xanthan gum. **b** 0.4% addition of xanthan gum. **c** Dewetting model for spray patterning. V : dewetting velocity of droplets on the substrate; t_0 : time for droplets to be resprayed per unit area; r_0 : radius of spray droplets; r_d : radius of droplet dewetted after t_0 . Scale bar in **a** and **b**: 1 cm on left panels; 2 mm on right panels.

The final step in validating this model involved examining the viscosity of TPP ink with varying concentrations of xanthan gum. It was observed that viscosity increased with the addition of xanthan gum (Figure 3.5.2). In some patterning cases, 0.1% surfactant (Captone FS-31) was introduced

to improve the contact between the pattern and substrate. Consequently, the viscosity of TPP ink with 0.1% surfactant was also assessed, revealing that the presence of surfactant led to higher viscosity compared to ink without surfactant. This outcome may be attributed to the surfactant in reducing droplet or particle size within the TPP ink, ultimately resulting in higher viscosity. This phenomenon occurs because more of the continuous phase becomes bound within the interfacial layers¹⁶⁰.

However, it is worth noting that higher viscosity does not always translate to better performance. Excessively high viscosity can impede the ink to spray effectively from the nozzle. Consequently, after careful consideration, a concentration of 0.4 wt% xanthan gum was determined to be the optimal addition to the TPP ink for spray patterning.

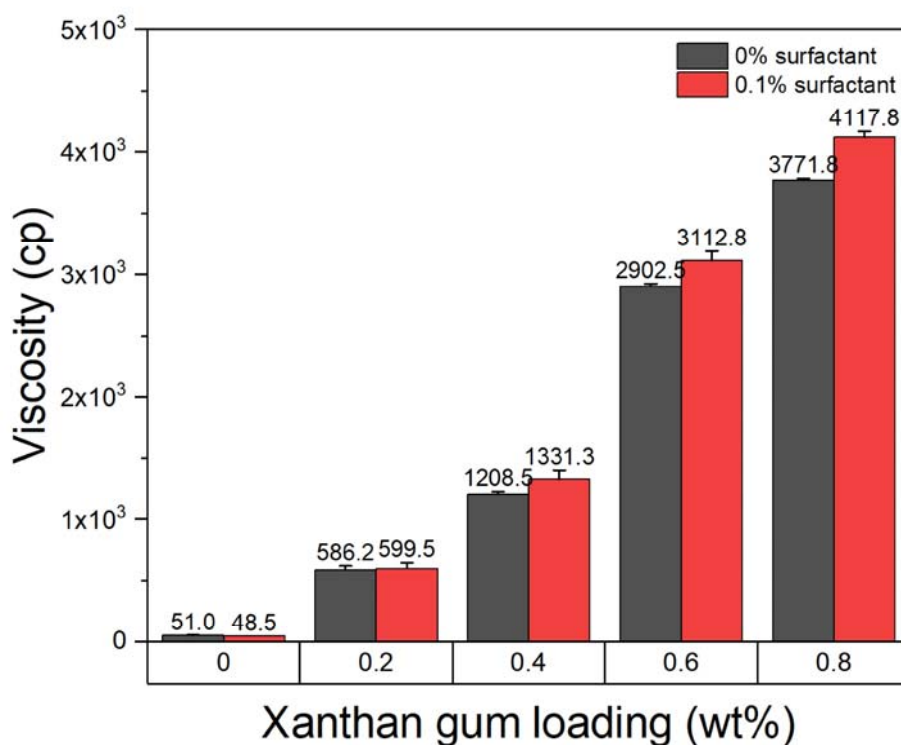


Figure 3.5.2 The viscosities of TPP ink with different loadings of xanthan gum.

In fact, in the TPP system, each component has its specific function in the whole system, just like PEDOT:PSS is for conductivity and tannic acid is more for adhesiveness. In this case, xanthan gum is added as a thickening agent to increase the viscosity of the ink. There are many substitutes to achieve the same function; for example, carboxymethyl cellulose, gelatine, or chitosan can also be used to increase the viscosity.

3.6 Conclusions

In the pursuit of the optimal TPP electrode, this section first meticulously delved into the ratios of two components: PVA and PEDOT:PSS. The investigation uncovered a delicate equilibrium between PVA content and electrode properties. Elevated PVA levels bolstered stretchability while maintaining electrical conductivity. Notably, a PVA concentration of approximately 66.7 wt% mirrored the stretchability of human skin. This increase in PVA content also correlated with improved abrasion resistance and linear enhancements in water resistance. However, excessive PVA addition resulted in heightened viscosity and impedance, affecting ease of processing. Finally, a radar plot identified the ideal balance at 66.7 wt% PVA, harmonizing stretchability, abrasion resistance, water resistance, viscosity, and impedance.

The exploration extended to the incorporation of TA into TPP films, amplifying conformability and adhesiveness. Microstructural analysis unveiled porous configurations in TPP films, with pore size scaling

proportionally to TA content. This intermediate state, bridging pure polymer films and hydrogels, translated into reduced cohesive energy, fostering compliance and stretchability. Striking equilibrium at 8% TA loading yielded an adhesive, supple, and robust TPP film, albeit with slight electrical trade-offs. This compromise between specific electrical properties in favour of enhanced stretchability and adhesiveness proved invaluable, especially during dynamic tasks.

Furthermore, TPP electrodes displayed remarkable stability in recording lower frequencies, curbing the need for extensive post-processing and preserving critical data. Their durability and biocompatibility were evident, enduring long-term test, repeated deformation and reattachment cycles with minimal performance impact. These results rendered TPP a superior choice for wearables compared to traditional Ag/AgCl electrodes.

The relationship between spray patterning and the viscosity of TPP ink was also explored, and it was found that a proper increase in viscosity can improve the patterning performance. The discovery of this new patterning method opens up more application potentials for various types of electrode or array fabrications based on TPP.

In conclusion, TPP electrodes offer an enticing solution for sEMG electrodes. Their amalgamation of electrical performance, flexibility, adhesiveness, and durability ushers in innovative possibilities in this domain.

Chapter 4

Characterizations of MEAPs

4.1 Introduction

Considering the numerous demands on electrophysiological electrodes, materials with excellent flexibility and stretchability, such as liquid metals, hold a significant advantage in this field^{51,161–169}. In previous work by Prof. Jiang's group, the MPC, made from EGaln, exhibited high stretchability and flexibility (strain of 500%), conductivity (8×10^3 S/cm), and biocompatibility. This material has found applications in flexible circuits, strain sensors, and electroporation electrodes^{41,100,170–173}. While some literature has reported the use of GLM as EMG electrodes, it is worth noting that using liquid metal as the contact electrodes directly on the skin can lead to issues like leakage and abrasion, which can severely reduce the working time of the device. However, this material performs exceptionally well when encapsulated in an elastomer, providing repeatability for over 100,000 stretches⁴¹. This makes it a highly suitable material for creating high-density sEMG recording configurations when used in conjunction with TPP electrodes.

The essence of high-density recording of sEMG electrodes lies in capturing a more detailed and precise representation of muscle activity. High-density recording involves placing a greater number of electrodes over a specific muscle or muscle group compared to traditional setups. This approach offers several key advantages: 1) spatial resolution: High-density electrode arrays provide finer spatial resolution, allowing for a more accurate

localization of muscle activity. This is particularly valuable for applications such as muscle localization, biofeedback training, and the study of complex muscle interactions; 2) enhanced signal information: With more electrodes, multiple regions within a muscle can be recorded simultaneously. This enables a deeper understanding of muscle behaviour, including variations in muscle activation patterns and the timing of muscle contractions; 3) improved signal separation: high-density recording can help distinguish between adjacent muscles that may have crosstalk. This is crucial for applications where precise muscle isolation is required, such as in clinical assessments and prosthesis control; 4) clinical applications: high-density sEMG is valuable in clinical settings for diagnosing neuromuscular disorders, monitoring rehabilitation progress, and optimizing treatments. It provides clinicians with a richer dataset for making informed decisions.

Based on TPP and MPC, the MEAP was fabricated to realize high-density sEMG recording. It is necessary to evaluate the durability and recording quality of this new device. A sEMG commercial array (CA) made of PI will be compared in this section to demonstrate the advantage of MEAP conformability on the skin. Noted that MEAP with substrate of PDMS is examined in chapter 4.3 and 4.4.

4.2 Fabrication

4.2.1 MEAP with substrate of PDMS

The MEAP consists of two main components: the circuit and the electrode.

The circuit part is made of MPC, known for its excellent stretchability and conductivity, ensuring both device durability and signal quality. However, MPC is not suitable for use as contact electrodes due to its vulnerability to abrasion and potential leakage when applied to the skin. Therefore, the electrode part employs TPP. Fabricating a MEAP is a straightforward process, achievable within 30 minutes using simple instruments such as screen printers and ovens (Figure 4.2.1a). The liquid metal circuit is protected by encapsulating it with PPA¹⁰², as developed in previous work by Prof. Jiang's group. This configuration ensures that only the TPP electrodes make contact with the skin. Thanks to scalable screen-printing fabrication, the MEAP can be easily customized for different muscle groups as needed. The MEAP can be stored on a release film to protect the device, and its user-friendly design, combined with remarkable stretchability, allows for direct attachment to the skin for sEMG signal recording (Figure 4.2.1b).

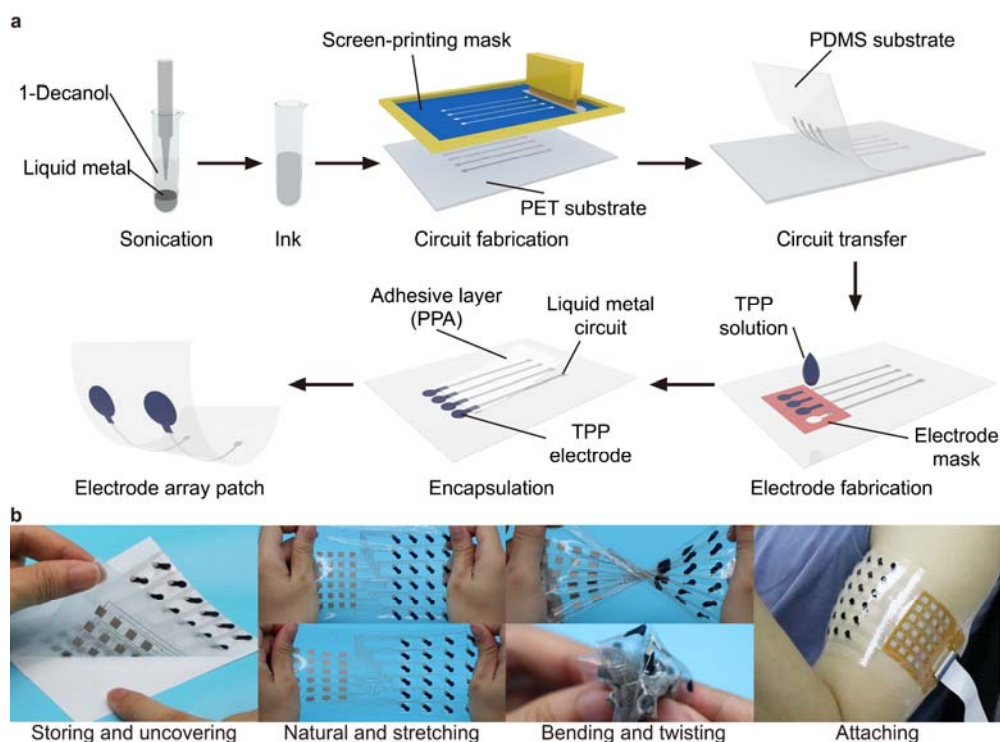


Figure 4.2.1 sEMG signals and linear fit results of median frequency during flexion 1, 2 and 3 recorded by Ag/AgCl and TPP electrodes. Decreasing median frequencies indicated fatigue of the muscle.

4.2.2 MEAP with substrate of TPU

When recording small muscles like the abductor pollicis brevis (APB), it is crucial to have a high-resolution MEAP to minimize crosstalk, especially for clinical applications discussed in Chapter 6. Clinical EMG signal needs to focus on MUAPs, which should originate from specific motor units within the APB. This requires both a fine surface area for TPP electrodes and IED to achieve the necessary resolution. Such a level of resolution can only be attained through an effective and stable patterning technique. Unfortunately, the hydrophilicity adjustment and patterning method used on PDMS are no longer suitable for the tiny electrode areas required for APB. Hot pressing between PDMS and FPC is also unstable due to PDMS

not being a thermoplastic material. These limitations render PDMS unsuitable for MEAPs to satisfy clinical needs. Consequently, we turned to TPU due to its stretchability, biocompatibility, and thermoplastic properties.

The stretchability and biocompatibility of TPU ensure that MEAP with a TPU substrate maintains excellent conformability on the skin, making it suitable for long-term sEMG applications. Additionally, the thermoplastic nature of TPU allows for a stable and secure connection with FPC after hot pressing, further enhancing signal quality for potential clinical diagnosis.

The MEAP for electrodiagnostic purposes consists of three layers: a TPP substrate with an MPC layer, a TPP electrode pattern layer, and a TPU encapsulation layer (Figure 4.2.2a). The TPP electrode pattern layer is formed by spraying TPP ink onto the TPP substrate, guided by a TPU mask layer to generate specific TPP patterns, eliminating the spacing issues between channels. The TPU encapsulation layer utilizes a medical infusion sticker with strong adhesiveness to establish a firm contact between MEAP and the skin. The final shape of the electrode site in contact with the skin is determined by the encapsulation layer, provided that the intermediate TPP electrode pattern maintains good alignment in practical use (Figure 4.2.2b-d).

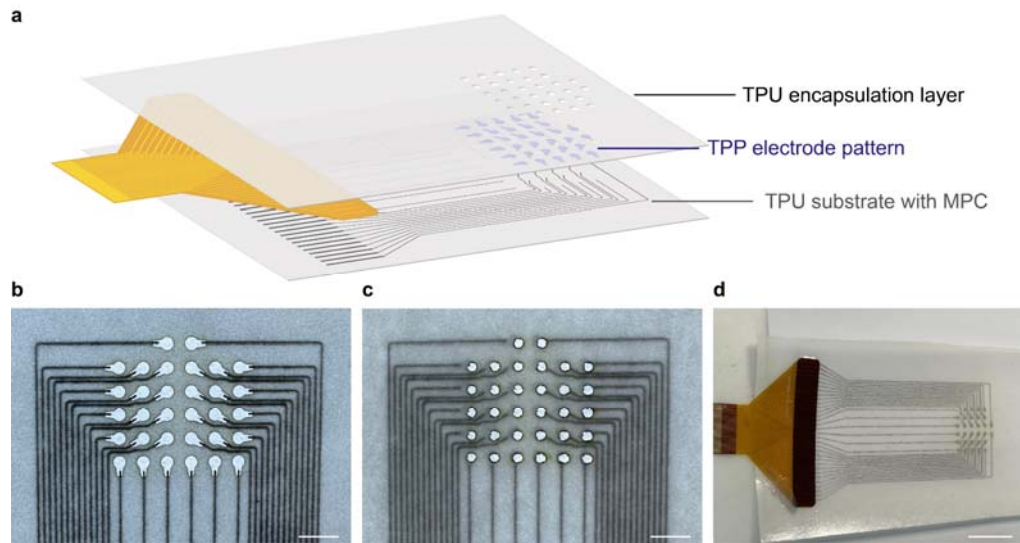


Figure 4.2.2 MEAP with substrate of TPU for electrodiagnostic recording on APB. **a** Schematic diagram of MEAP. **b** TPP electrode pattern mask. Scale bar: 5 mm. **c** TPU encapsulation layer. Scale bar: 5 mm. **d** Photograph of the final MEAP. Scale bar: 2 cm.

4.3 Characterizations of MEAPs

4.3.1 Topography and stretchability

The state of the LMNPs within the PDMS matrix was examined using SEM. The SEM images clearly revealed that the GLM nanoparticles were embedded in the PDMS (Figure 4.3.1a). On the peeling surface, the LMNPs exhibited isolated topography, but within the PDMS, they made contact with each other, forming conductive paths. The exposed parts created perfect connection pads for linking with the TPP electrode sites. In addition, the substrate of the MEAP can withstand elongation of over 200%, showcasing its exceptional stretchability (Figure 4.3.1b). This property ensures the MEAP can be applied to the skin while maintaining conformability.

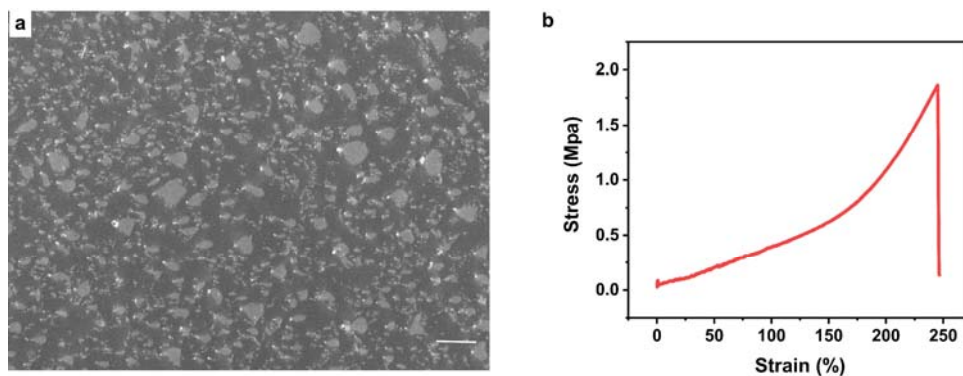


Figure 4.3.1 Characterizations of MEAPs. **a** SEM micrograph of the MPC circuit. Scale bar: 10 μm . **b** Stress-strain curves of the substrate of MEAP.

4.3.2 Repeatability of use

Similar to the TPP electrodes, assessments on the reattachment performance of the MEAP were conducted. A 24-channel MEAP was created, and it underwent over 20 reattachments on the biceps brachii (Figure 4.3.2a). Remarkably, the baseline noise consistently maintained an amplitude of approximately 50 μV across all channels, even after 28 reattachments (Figure 4.3.2b, c). Moreover, the SNR remained stable at 20 dB across all channels following 28 reattachments. Statistical plots were employed to demonstrate the stable performance of all MEAP channels (Figure 4.3.2d, e). These results strongly suggest that the MEAP can be used repetitively.

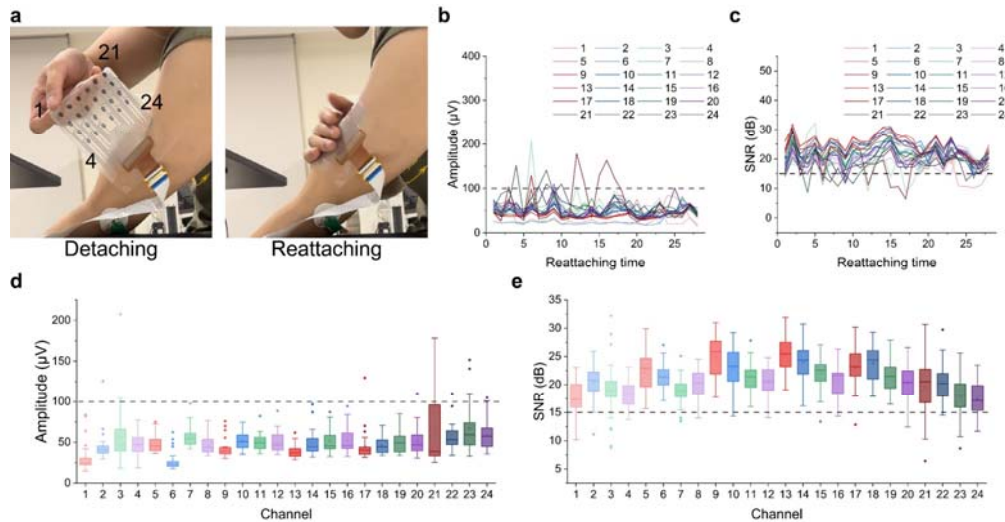


Figure 4.3.2 The reattachment test of 24-channel MEAP on the skin. a Images showing the process of detachment and reattachment of MEAP on biceps brachii. **b, c** The baseline noise of each channel and the SNR of each channel plotted for each reattachment. **d, e** Whisker plots of statistical verification of b and c for the 28 reattachments. Statistical analysis was conducted to assess the baseline noise and SNR of each channel throughout the reattachment test. 28 reattachments, per channel, were included in the analysis. The box plots depict the mean (centre square), median (centre line), 25th to 75th percentiles (box), and the lower and upper whiskers representing the smallest and largest values that are ≤ 1.5 times the interquartile range, respectively. Outliers are also shown.

4.3.3 Permeability

The permeability of a material attached to the skin is crucial for ensuring comfortable wear for subjects over extended periods. To assess this, we examined the permeability performance of MEAP for daily long-term use (Figure 4.3.3a-c). It was observed that the MEAP with punctures exhibited higher water loss compared to the intact MEAP, indicating that the permeability of MEAP can be adjusted by modifying the physical structure of the substrate (Figure 4.3.3d). This adjustability can be customized based on individual experiments and subject requirements, allowing us to create a comfortable wearing experience for daily use. This is particularly valuable

as the permeability can be increased to a level that promotes adequate airflow. The results of comparison indicate that the permeability of MEAP is sufficient to provide a comfortable wearing experience for daily use, taking into consideration that the insensible sweat rate of individuals ranges from 12 to 42 $\text{g}\cdot\text{m}^{-2}\cdot\text{h}^{-1}$ ¹⁷⁴. However, it is important to note that in comparison to PDMS, polyimide exhibited significantly lower permeability, suggesting limitations for long-term use (Figure 4.3.3e). The results clearly indicate that the permeability of MEAP is well-suited for extended usage, as it does not impede the normal evaporation of sweat from the skin.

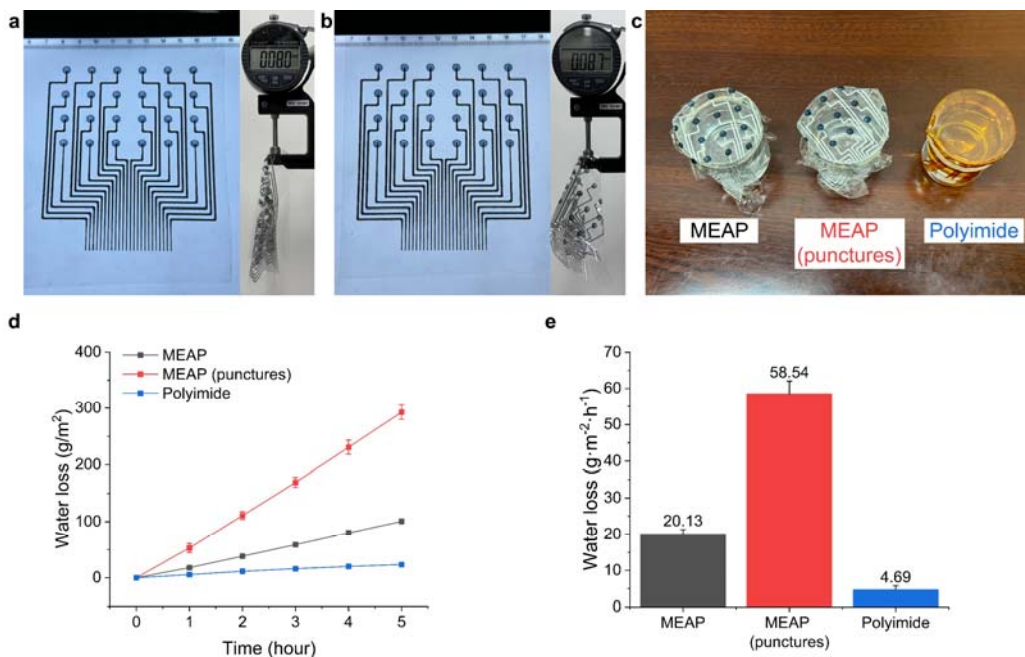


Figure 4.3.3 The permeability comparison test between MEAP, MEAP (punctures) and polyimide. **a, b** Images showing the MEAP and MEAP (punctures) with thicknesses of 80 and 87 μm , respectively. The MEAP (punctures) features 24 punctures (1 mm in diameter), corresponding to the number of TPP electrodes on the patch. **c** The experimental setup for the permeability test. **d, e** The water loss rates in the three beakers. Measurements were recorded for each beaker every hour, with $n = 3$ samples for each recording. **e** The water loss rate of each cover.

4.4 Comparing tests

4.4.1 Properties of MEAP and those of sEMG arrays in other literatures

To provide an objective assessment of MEAP, the properties of MEAP to other sEMG arrays were compared (Table 4.4.1). Among these studies, one was published in 2020, nine in 2021, and three in 2022. It is evident that MEAPs are the only ones with adhesiveness. This is primarily due to the fact that most electrode materials are metals, which struggle to achieve both adhesiveness and conductivity simultaneously. In such cases, conductive polymers have a distinct advantage. Additionally, the impressive 188% strain of MEAP surpasses that of the majority of previous works, ensuring conformal contact with the skin. Notably, the TPP electrodes integrated into MEAP are the only adhesive electrodes among all these works. The combination of stretchability and adhesiveness in MEAP contributes to its remarkable features, including the lowest noise RMS and the highest SNR for sEMG recording. Furthermore, the straightforward construction and reliable operation of MEAP make it suitable for various muscles and situations, enhancing signal capture. Considering these factors, MEAP should be considered state-of-the-art in the sEMG array sector.

| Materials for electrodes | Materials for substrates | Is it intrinsically stretchable? | Strain | The adhesiveness of electrode (N/cm) | The number of channels | Success rate of channels | The smallest area of the electrode (mm ²) | Long-term test (Hour) | RMS of Noise (μ V) | Signal-to-noise ratio (dB) |
|--|----------------------------|----------------------------------|-------------|--------------------------------------|----------------------------|--------------------------|---|-----------------------|-------------------------|--------------------------------|
| Ag/AgCl ink | Polypropylene | No | N/A | 0 | 16 | N/A | 5.1 | N/A | N/A | ~24.0 |
| Ag/AgCl ink | Polyethylene terephthalate | No | N/A | 0 | 64 | 100% | 14.5 | 2 | N/A | ~20.0 |
| Ag flakes/PDMS | PDMS | Yes | 30% | 0 | 8 | 100% | 26.4 | N/A | N/A | 29.5 |
| Ag nanowires | PDMS | Yes | 50% | 0 | 18 | 94.4% | 9.6 | N/A | N/A | N/A |
| Ag nanowires | Thermoplastic polyurethane | Yes | 600% | 0 | 4 | 100% | 201.0 | N/A | ~34.0 | 26.6 |
| Al | Polyethylene terephthalate | No | 51% | 0 | 16 | 100% | 84.0 | N/A | ~130.0 | N/A |
| Au | Polyimide | No | 40% | 0 | 20 | N/A | N/A | N/A | ~300.0 | ~20.0 |
| Au | Polyimide | No | 37% | 0 | 64 | N/A | 0.8 | N/A | ~10.0 | 40.0 \pm 8.0 |
| Au | Polyimide | No | N/A | 0 | 64 | N/A | 3.1 | N/A | N/A | 26.0 \pm 6.0 |
| Carbon/Silicone rubber | Textile | N/A | N/A | 0 | 14 | 100% | 400.0 | N/A | ~100.0 | 12.8 \pm 0.9 |
| MXene | PDMS | No | N/A | 0 | 40 | 100% | 7.1 | N/A | ~34.0 | N/A |
| Mxene | Parylene-C | No | N/A | 0 | 16 | 81.25% | 2.6 | N/A | ~118.0 | 24.4 \pm 1.7 |
| PEDOT:PSS/Cholinium lactate | Kapton | No | N/A | 0 | 16 | 100% | 2.6 | N/A | ~40.0 | 15.6 |
| Stainless steel | Textile | No | N/A | 0 | 150 | 90.6% | 113.0 | N/A | 50.6 \pm 14.8 | 30.8 \pm 2.4 |
| PEDOT/ Polyvinyl alcohol/ Tannic acid/ Liquid metal | PDMS | Yes | 188% | 0.58 | \geq64 | 100% | 0.8 | 120 | 1.0 | 42.3\pm0.7 |

Table 4.4.1 Comparisons between sEMG arrays in other literatures and this work.

4.4.2 sEMG recording performances of MEAP and CA on muscle

Electrode arrays adhering to the skin have been in development and use

since the 1990s. The most popular material for the currently available sEMG CA is PI, which has a Young's modulus of 3 GPa. However, due to its characteristics, it has been observed that a PI substrate-based array, unless designed with specific features like a serpentine design⁴⁰, cannot achieve full conformal contact with human skin, which has a much lower Young's modulus of 10 kPa. In order to address this issue, MEAP presents a highly promising solution. But it is crucial to showcase the advantages of MEAP by comparing it to the CA fairly. To ensure a fair comparison of contact performance on the skin, a 64-channel MEAP with the same configuration as the CA was fabricated (Figure 4.4.1). It is worth noting that the thickness of both arrays is 100 μm .

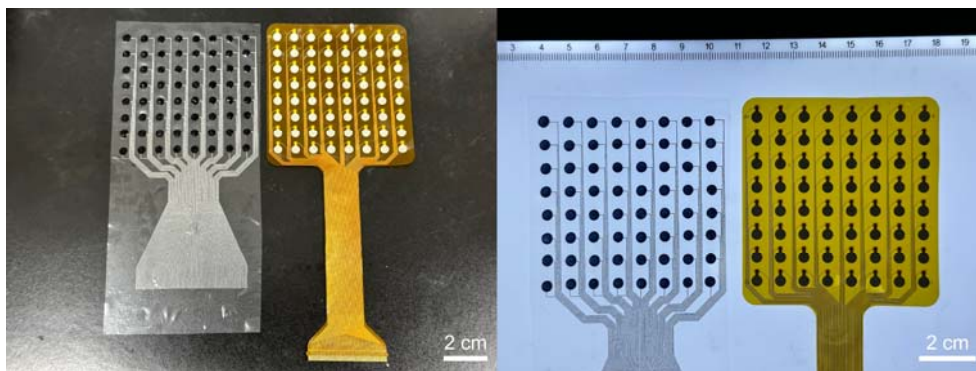


Figure 4.4.1 The configuration comparison between MEAP and CA. Both arrays have electrode diameter of 4 mm and IED of 8 mm.

Hot-pressing was used to merge the flexible printed circuit (FPC) with the MEAP. Employing a customized back-end connector, it was ensured that each channel of the MEAP could be independently connected to the sEMG recording system, enabling the analysis of the performance of each channel separately (Figure 4.4.2).

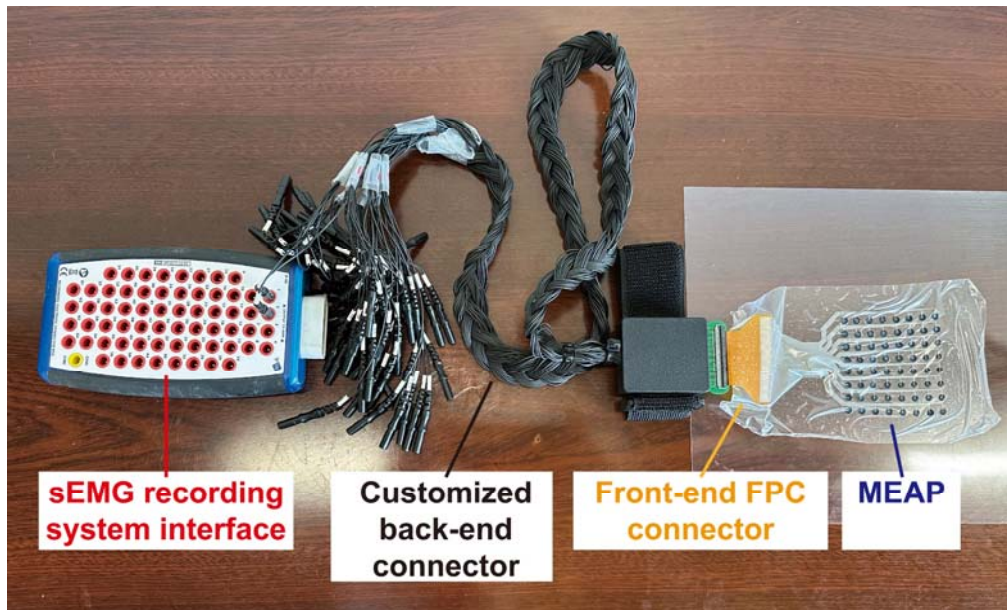


Figure 4.4.2 The entire setup for connection between MEAP and EMG recording system.

Both arrays were affixed to the right biceps brachii of the subject, with channels 1 to 64 arranged from the bottom left to the top right in a column-by-column fashion. The subject was instructed to flex their biceps to assess the attachment and recording performance of both arrays. It was observed that gaps were formed between CA and skin when the muscle contracted, whereas the MEAP remained securely adhered to the skin. These differences in attachment performance were also evident in the sEMG signals. While the signals recorded by the CA initially appeared sufficient for distinguishing sEMG patterns, the gaps caused by poor electrode-skin attachment resulted in increased baseline noise after only one muscle contraction (Figure 4.4.3). This would significantly lower the SNR level in future recordings. On the other hand, the recordings obtained with the MEAP demonstrated consistently high signal quality, with no increase in baseline noise even after ten muscle contractions. This would certainly

provide a longer duration of valid recording time compared to the CA.

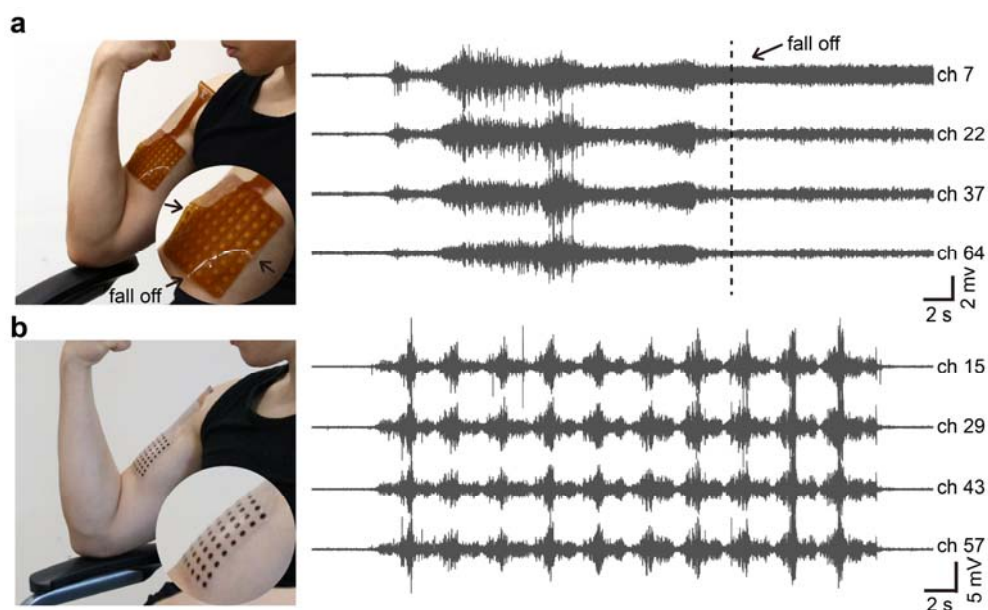


Figure 4.4.3 The typical sEMG signals recorded using CA and MEAP on biceps brachii. **a** Recording by CA. **b** Recording by MEAP.

To further underscore the impact of skin deformation on recording performance, an analysis of SNR was conducted for both the initial and final contractions. Additionally, an SNR map was constructed to visually depict the spatial variations in signal quality. In this map, SNRs were categorized into six distinct colours, enhancing the clarity of the illustration. The results revealed a striking contrast between the CA electrodes and the MEAP channels. None of the CA electrodes managed to attain an SNR exceeding 20 dB during the final contraction, while all MEAP channels consistently maintained an SNR above 20 dB for both the initial and final contractions (Figure 4.4.4). This discrepancy strongly suggests that the conformal attachment of electrodes plays a pivotal role in this distinction. Notably, the SNR of the first contraction recorded by the CA electrodes

appeared adequate initially but deteriorated significantly during the final contraction. This underscores the importance of secure and conformal electrode-skin contact in achieving reliable and consistent signal quality, especially under conditions of skin deformation.

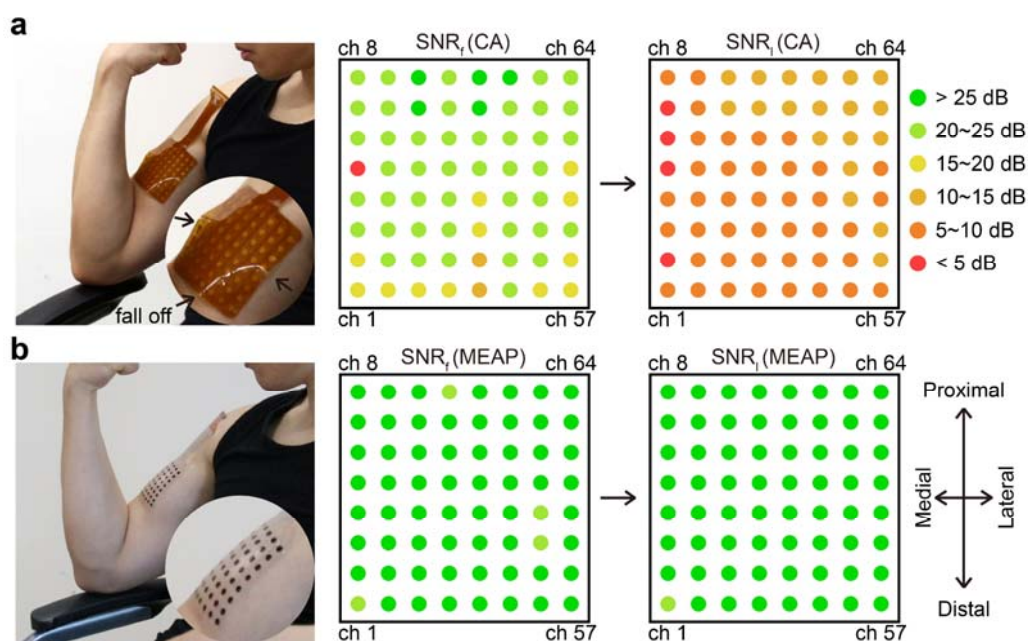


Figure 4.4.4 The spatial SNR performance map for each channel of CA and MEAP for the first and last muscle contraction on biceps brachii. **a** Recording by CA. **b** Recording by MEAP. SNR_1 : SNR of the first contraction; SNR_l : SNR of the last contraction.

These findings were further substantiated through rigorous statistical analysis. Due to the mismatch between the CA electrodes and the skin, a noticeable increase in baseline noise levels was observed across all CA electrodes after just one muscle contraction. Interestingly, after reattachment, the baseline noise levels decreased, underscoring once again that the gaps between the CA electrodes and the skin was the primary driver of this change (Figure 4.4.5a). When assessing the rates of

change in baseline noise, most CA channels exhibited a more than two-fold increase. In contrast, the MEAP consistently maintained a stable noise level even after ten muscle contractions (Figure 4.4.5b). This disparity in baseline noise levels was directly mirrored in the SNR results, with the MEAP demonstrating significantly higher SNR in its recordings compared to the CA electrodes.

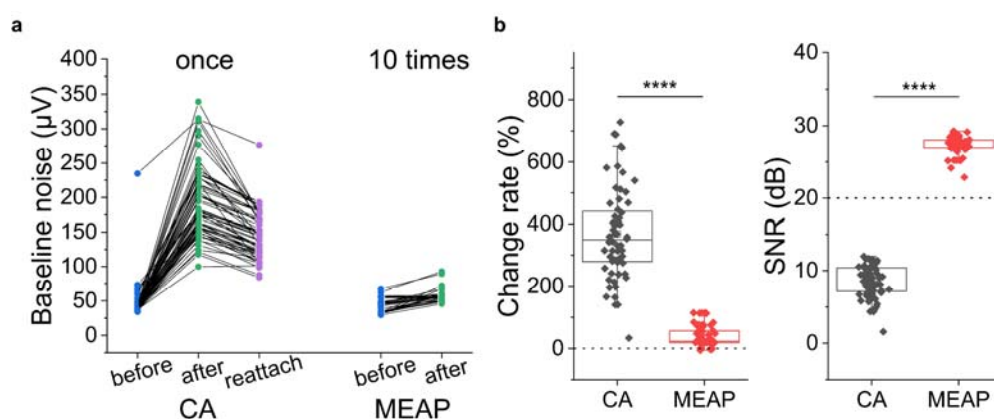


Figure 4.4.5 Statistical analysis of performances between CA and MEAP on biceps brachii. **a** Baseline noise level of CA before and after one muscle contraction, as well as after reattachment; baseline noise level of MEAP before and after ten muscle contractions; **b** Baseline noise change rates before and after muscle contractions; SNR performance of the last muscle contraction recorded by each of the CA and MEAP channels. Significance was determined by one sample t test (* $P < 0.05$; ** $P < 0.01$; *** $P < 0.001$; **** $P < 0.0001$).

This section compared CA and MEAP arrays on the biceps of the subject during muscle contraction. CA showed attachment gaps and increased noise upon contraction, while MEAP maintained secure skin adherence and high-quality signal recording even after multiple contractions. SNR analysis and statistics underscored the importance of conformal electrode-skin contact for superior signal quality.

4.4.3 sEMG recording performances of MEAP and CA on muscle-tendon junction

Recording spatial sEMG signals is crucial for a better understanding of muscle activation patterns, making it valuable for muscle condition assessments in clinical, neurophysiological, and sports-related scenarios. Typically, multiple sEMG electrodes are used simultaneously on a single muscle to gather comprehensive muscle information. While employing an array simplifies this process, there are instances where the array needs to be repositioned, such as over muscle-tendon junctions, to capture maximal spatial information. This necessitates a higher level of skin conformity for the array, as muscle-tendon junctions often involve significant skin deformation during muscle contractions.

To further evaluate the performance of the MEAP and conduct a comprehensive comparison with the CA, sEMG signals were recorded from muscle-tendon junctions, closer to the distal end of the biceps, using both arrays. In this context, the mismatch between the CA and the skin was even more pronounced than that observed over the main body of the biceps brachii (Figure 4.4.6a). This mismatch manifested in the sEMG signal recordings as a significant increase in baseline noise, sometimes surpassing the signal amplitude itself. Consequently, this made it impossible to extract meaningful muscle information. It is worth noting that the onset times of the increased noise varied across channels due to the spatial variability in skin deformation. Attempts were made to reattach the CA after signal dropout from certain channels, resulting in reduced noise

levels. This experiment reaffirmed that the primary cause of the elevated noise was the mismatch between the CA and the skin.

In contrast, the MEAP maintained perfect conformal contact with the skin, even under more substantial deformation (Figure 4.4.6b). This superior conformability ensured the preservation of high-quality sEMG signals across multiple channels even after ten contractions.

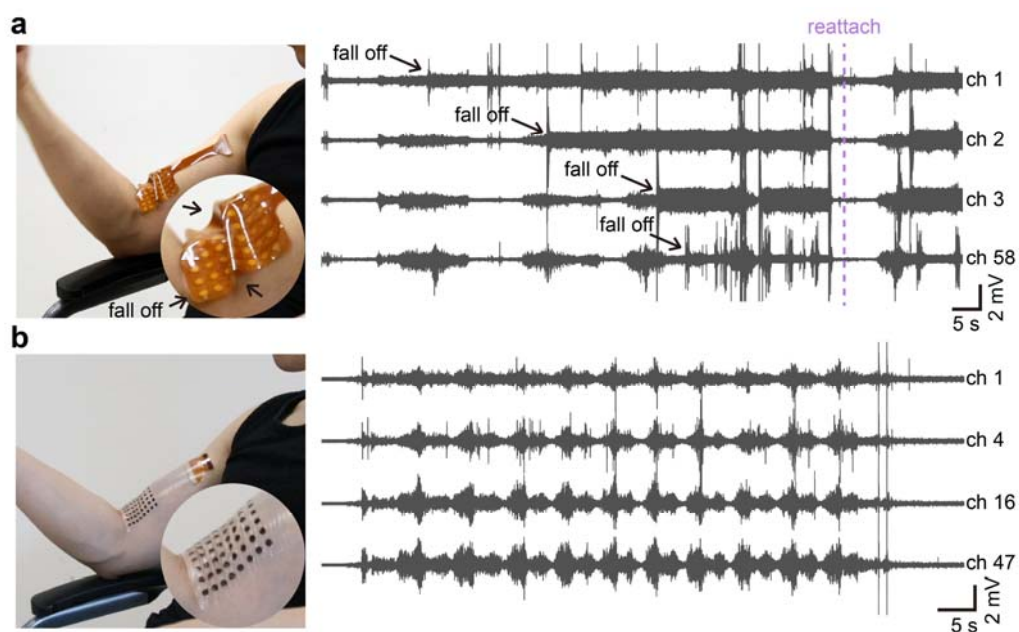


Figure 4.4.6 The typical sEMG signals recorded using CA and MEAP on muscle-tendon junction of biceps brachii. **a** Recording by CA. **b** Recording by MEAP.

Similarly, the spatial SNR performances were compared between the first and last contractions (Figure 4.4.7a). It was observed that the SNR of each channel universally decreased compared to the previous recordings on the muscle part. This is a natural outcome because spatial differences can lead to recording variations, which will be further elucidated and discussed in Chapter 5.

Recordings from the CA channels positioned over the muscle-tendon junction were notably affected by muscle contractions, as the SNR of most channels decreased from the first contraction to the last one. Once again, these observations underscored the detrimental impact of muscle contractions on the signal quality of sEMG recordings when a non-conformal array was employed. In contrast, MEAP consistently delivered stable recordings, with all channels maintaining an SNR greater than 15 dB, both during the initial and final contractions. These results highlight the robust recording stability achieved by MEAP.

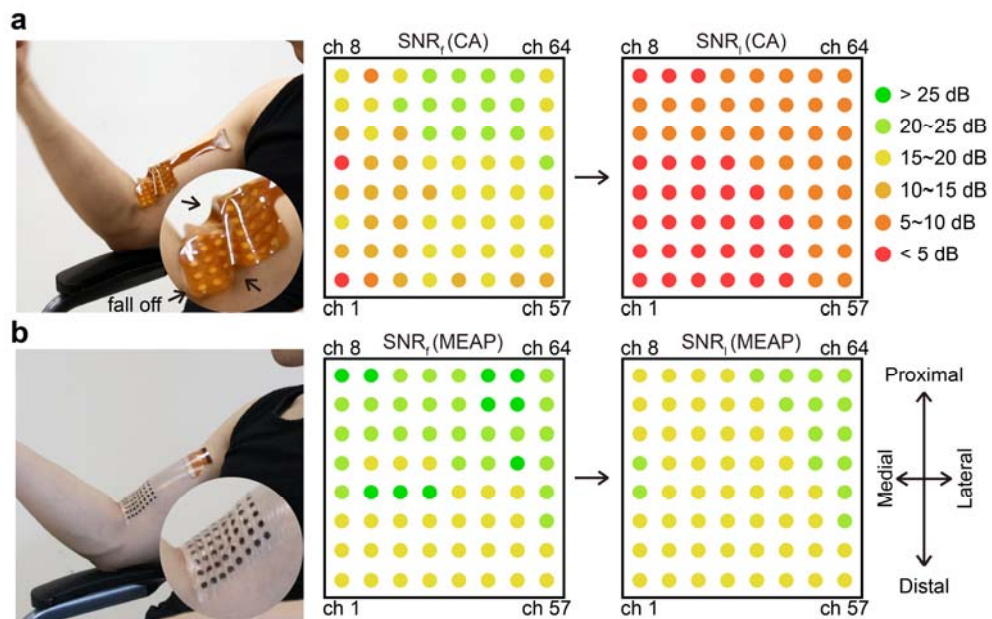


Figure 4.4.7 The spatial SNR performance map for each channel of CA and MEAP for the first and last muscle contraction on muscle-tendon junction of biceps brachii. **a** Recording by CA. **b** Recording by MEAP. SNR_f: SNR of the first contraction; SNR_i: SNR of the last contraction.

Statistical analysis of sEMG data from CA electrodes positioned at the distal end also yielded unsatisfactory results, with the baseline noise of each channel significantly increasing after three muscle contractions

(Figure 4.4.8a). However, it is important to highlight that MEAPs consistently maintained stable and excellent recordings even after ten muscle contractions. The final SNR comparison further demonstrated a significant difference between MEAP and CA (Figure 4.4.8b). These findings strongly indicate that MEAP is capable of recording superior sEMG signals compared to CA, primarily due to its superior contact performance, even when faced with substantial skin deformation.

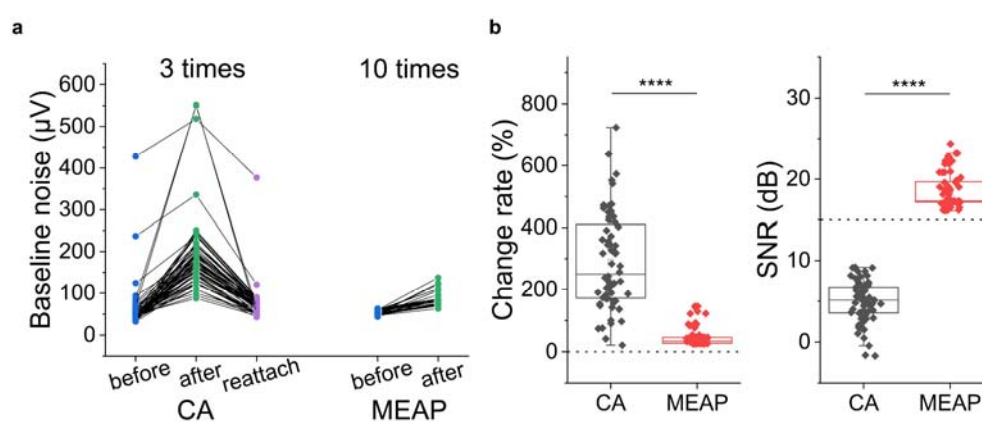


Figure 4.4.8 Statistical analysis of performances between CA and MEAP on muscle-tendon junction of biceps brachii. **a** Baseline noise level of CA before and after three muscle contractions, as well as after reattachment; baseline noise level of MEAP before and after ten muscle contractions; **b** Baseline noise change rates before and after muscle contractions; SNR performance of the last muscle contraction recorded by each of the CA and MEAP channels. Significance was determined by one sample t test (* $P < 0.05$; ** $P < 0.01$; *** $P < 0.001$; **** $P < 0.0001$).

This section compared the recording performance between MEAP and CA when targeting muscle-tendon junctions. The results indicated a more pronounced mismatch between CA and the skin, resulting in elevated baseline noise levels that made data extraction unfeasible. Conversely, MEAP maintained perfect conformal contact, preserving high-quality sEMG signals even after ten contractions. These results emphasize the

superior sEMG signal captured by MEAP, primarily attributed to its superior skin conformity, even under conditions of greater skin deformation compared to the muscle region.

4.5 Conclusions

In this chapter, MEAPs have been successfully developed by combining MPC and TPP electrodes, allowing for straightforward fabrication through scalable screen-printing techniques. Following a comprehensive examination, MEAPs have exhibited remarkable characteristics, including exceptional stretchability exceeding 200%, outstanding repeatability with over 28 reattachments, and favourable biocompatibility. Moreover, MEAPs have demonstrated adequate permeability when affixed to the skin, ensuring normal sweat evaporation and enhancing the overall comfort of wear. Importantly, we have discovered that the permeability of MEAPs can be tailored by adjusting the physical structure of the substrate, allowing for personalized settings to accommodate individual preferences. These combined attributes firmly establish MEAP as a dependable and long-lasting wearable device.

Furthermore, in a comparative analysis with other arrays documented in the literature, MEAP demonstrated superior adhesiveness and electrode site size, two critical factors for ensuring the stability and resolution of high-density recording. These findings firmly establish MEAP as a cutting-edge advancement in the current landscape of sEMG arrays. Comparisons between MEAP and CA, whether on muscle or muscle-tendon junction,

consistently showed superior and more stable sEMG signal recordings by MEAP than CA. Although they are both 100 μm , the higher stretchability of the materials used for MEAP gives the array better conformability on the skin, leading to its superior performances.

Chapter 5

Applications of MEAP

5.1 Introduction

Electrophysiological recordings, such as EEG, ECG and EMG, play a vital role in clinical diagnosis and the management of conditions affecting the brain, heart, nerves, and muscles^{175–178}. In recent years, sEMG has gained increasing importance in non-invasive diagnostics, treatment, daily health monitoring, and human-machine interfaces, including machine control^{179–183}. This technology also finds valuable applications in sports and training. Both amateur and professional athletes are susceptible to muscle strains and tendon injuries during exercises and training, which relate to three primary types of muscle contractions: isometric, concentric, and eccentric contractions^{184–187}. Isometric contractions occur when the muscle generates tension without changing its length, often used for tasks like maintaining posture. Concentric contractions involve muscle shortening as it generates force, typical in movements like lifting weights. Eccentric contractions, on the other hand, involve muscle lengthening while under tension, often occurring during controlled lowering of a weight. Eccentric contractions often pose a greater risk of causing muscle and tendon issues compared to isometric or concentric contractions^{186,187}. This heightened risk arises because eccentric contractions involve both force generation and muscle lengthening simultaneously. This combination places significant stress on both the muscle and the tendon, making them more

susceptible to strain and injury.

To prevent such injuries, sEMG is a valuable tool as it provides quantitative information such as RMS and median frequency, which are associated with muscle loading and fatigue¹⁸⁸. High-density sEMG has been used to study neuromuscular junctions, offering insights into muscle fatigue and pain^{189–193}. However, there is limited research on using sEMG techniques for identifying tendon displacement during exercise. Therefore, a tool capable of simultaneously assessing muscle loading, fatigue, and tendon displacement would be highly valuable for injury prevention. In this context, the MEAP holds significant promise in this regard, as it not only possesses the basic recording capabilities of conventional sEMG electrodes but also offers spatial information about muscles, potentially enabling the recording of RMS patterns and tendon displacement. This chapter aims to validate the ability of MEAP to capture RMS patterns and tendon displacement data. Subsequently, MEAP will be applied to different subjects to provide comprehensive muscle information for injury prevention.

5.2 MEAP for sEMG activation mapping

sEMG activation mapping is a powerful technique that enables the non-invasive and real-time visualization of muscle activity patterns in the human body. By strategically placing electrodes or array on the surface of the skin, sEMG signals can provide valuable insights into the timing, intensity, and coordination of muscle activation. This technology has wide-ranging applications, from clinical diagnostics and rehabilitation to sports

performance analysis and human-machine interface development. While in this field, electrode resolution is a recurring challenge, often limiting the ability to obtain high-resolution information. Traditional Ag/AgCl electrodes, with surface areas typically ranging from 1 to 2 cm², are commonly used to ensure signal quality but fall short in achieving the desired spatial resolution for recording activities in both small and large muscles. Ideal electrodes should have dimensions smaller than 5 mm and maintain an inter-electrode distance (IED) below 10 mm. TPP electrodes offer a solution to this limitation, as they can be tailored to meet these optimal design criteria. Furthermore, TPP technology allows for the fabrication of sEMG electrodes in various dimensions and specific shapes to align with specific recording requirements (Figure 5.2.1). This section focuses on evaluating the RMS mapping capabilities of MEAP with two distinct designs tailored for the biceps brachii (BB) and abductor pollicis brevis (APB) muscles, highlighting the potential to enhance spatial resolution in sEMG recordings.

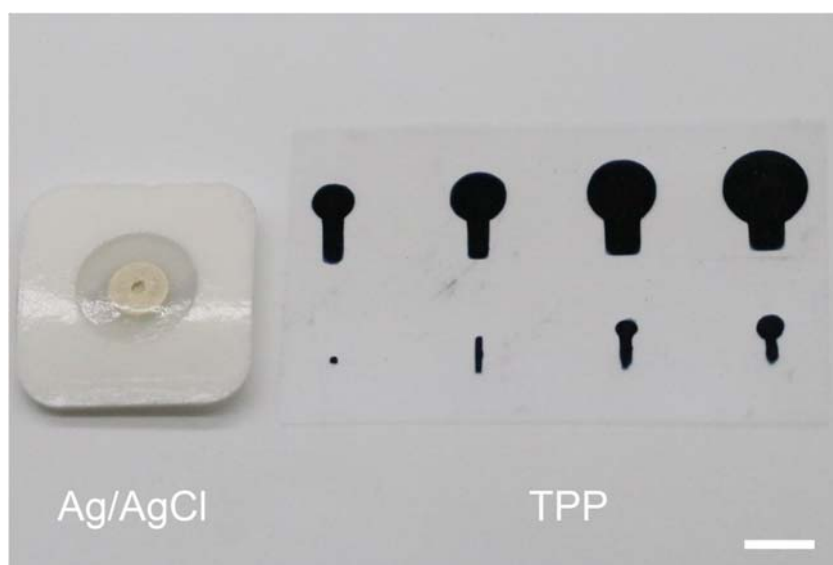


Figure 5.2.1 Comparison of surface areas of Ag/AgCl electrodes and TPP electrodes. Scale bar: 1 cm.

5.2.1 Muscle activity map on biceps brachii

For BB assessment, a 24-channel MEAP was customized with a diameter of 5 mm and an IED of 15 mm to ensure ample coverage of the BB muscle area (Figure 5.2.2a). Following attachment to the skin, a systematic labelling scheme employing alphabetical and numerical identifiers was implemented for both columns and rows to facilitate clear distinction between electrodes (Figure 5.2.2b). To activate the BB muscle, the subject was instructed to perform biceps curls using a 4 kg dumbbell. This standardized procedure allowed for consistent and targeted muscle activation during the evaluation (Figure 5.2.2c).

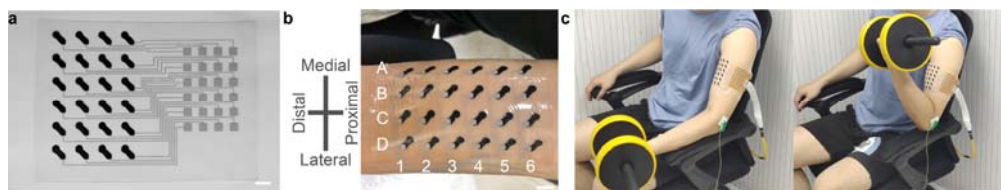


Figure 5.2.2 Experimental setup for sEMG activation mapping on BB. **a** A photograph of MEAP for BB. Scale bar: 1 cm. **b** Configuration of MEAP on BB. **c** Contraction task for BB activation.

The sEMG data captured during the entire biceps curl, encompassing both concentric and eccentric contractions, were visualized for each channel based on their spatial arrangement (Figure 5.2.3). Notably, distinct differences in the signals were readily discernible, confirming the absence of signal loss or deficiency among any channels. Additionally, it was evident that signals with higher amplitudes were concentrated in specific regions (close to C5). This concentration primarily stemmed from the proximity of these channels to the underlying muscle, as higher signal

amplitudes typically indicate closer electrode proximity to the muscle fibres.

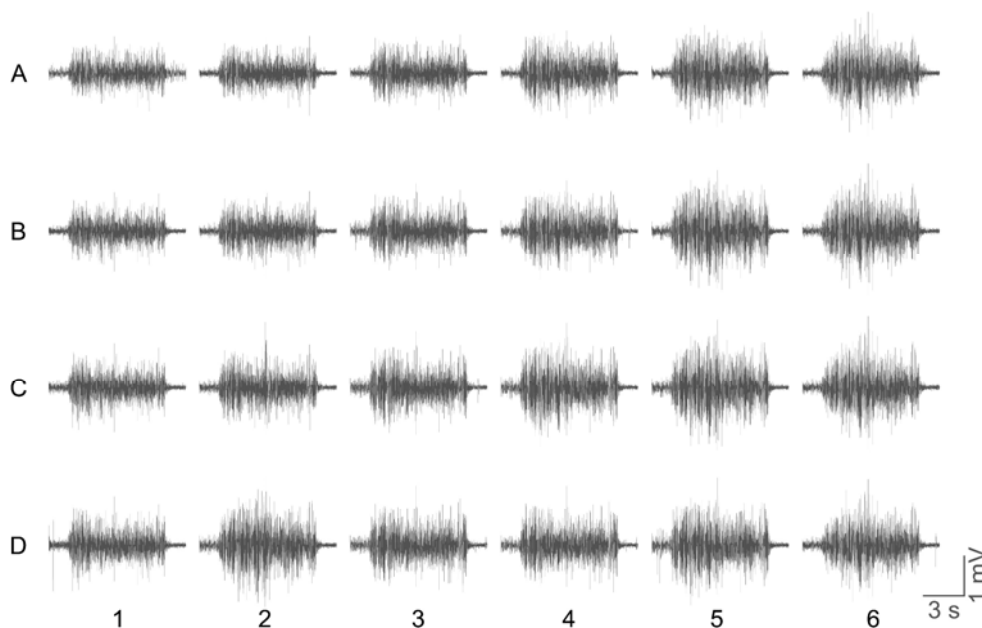


Figure 5.2.3 sEMG recorded by each channel of MEAP on BB.

Apart from directly comparing sEMG signals, we also calculated the RMS value for each channel at 0.125 s intervals to depict real-time changes in muscle activity. These RMS values were used to construct activation maps, revealing muscle activation patterns during a biceps curl, which we divided into four distinct phases: "before curling" corresponding to the rest phase, "curling beginning" and "full contraction" indicating concentric contraction, and "after releasing" representing eccentric contraction (Figure 5.2.4). Notably, no muscle activity was detected prior to the task. As the curling motion started, activity was recorded across all electrode sites, with the long head of the BB exhibiting greater activity compared to the short head. When BB reached full contraction, muscle fibres shortened, and the muscle belly shifted further from the distal end. This caused the active zone to shift to the right in the muscle activity maps, resulting in increased activity. This

phenomenon, where the muscle region exhibited higher activity while the tendon region showed lower activity, corresponds to the spatial variation in SNRs depicted in Figure 4.4.7. During eccentric contraction, as the subject lowered the dumbbell back to the resting position, muscle activity decreased compared to concentric contraction, and the active zone shifted back towards the middle. The reduction in amplitude during eccentric contraction aligns with observations in existing literature and can be attributed to a decrease in the recruitment of motor units and lower firing rate frequencies^{194–196}. Additionally, the presence of elastic tissue within the muscle plays a role. The resistance of the elastic component to stretching during eccentric contractions leads to reduced force actively generated by the contractile elements of muscle fibres, resulting in lower electrical activity compared to other contraction types. The unique design of our array allowed for effective monitoring of the entire muscle movement process underneath.

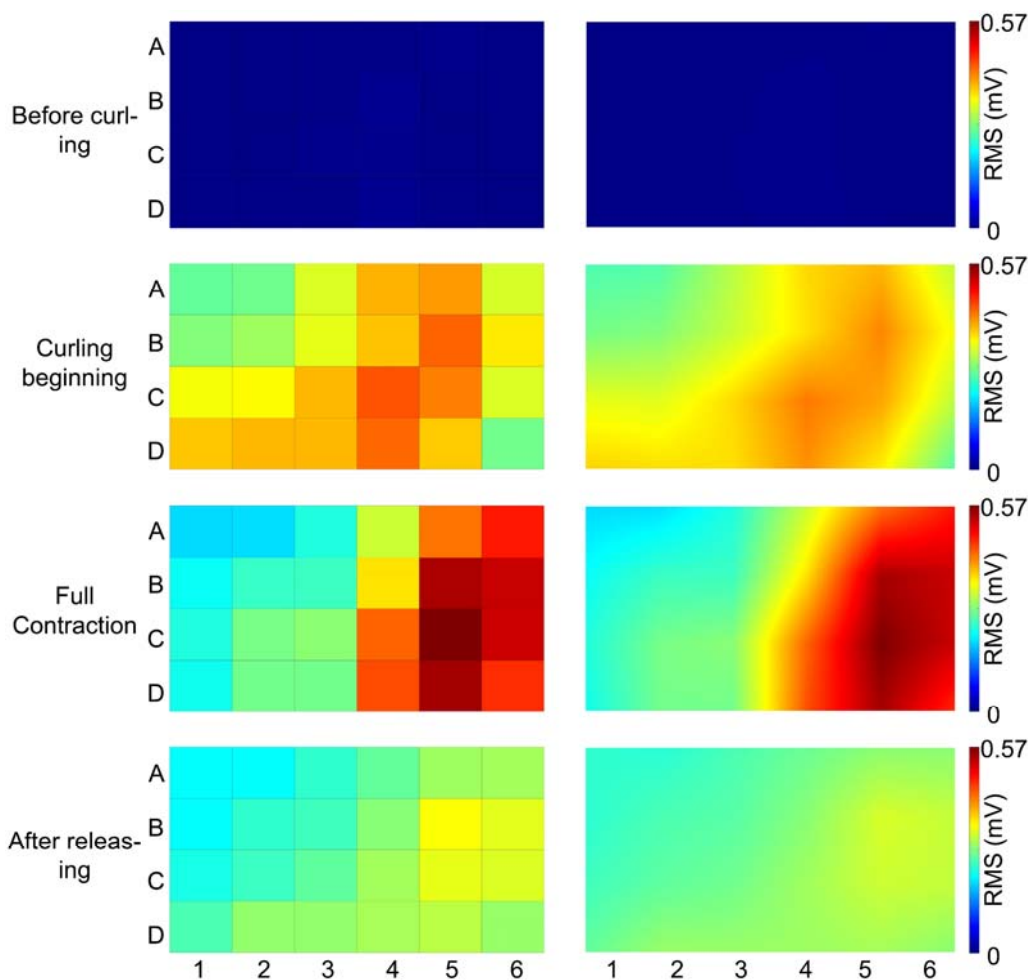


Figure 5.2.4 Muscle activity maps of sEMG recorded from BB, showing the process of graded recruitment during contractions. The left column is RMS values from each channel; the right column is 10th-order interpolated results of each channel.

5.2.2 Muscle activity map on abductor pollicis brevis

For APB assessment, a 24-channel MEAP was customized with a diameter of 1 mm and an IED of 5 mm to make a much finer recording configuration than that on BB, given the APB is a much smaller muscle compared to BB¹⁹⁷ (Figure 5.2.5a, b). Situated in the thenar eminence of the palm, APB is responsible for the crucial movement of abduction, enabling the thumb

to move away from the palm and oppose the other fingers. After attaching the MEAP to the skin, each channel was appropriately labelled, similar to the procedure for BB (Figure 5.2.5c). To activate the APB muscle, the subject was instructed to move their thumb towards the base of the little finger (Figure 5.2.5d).

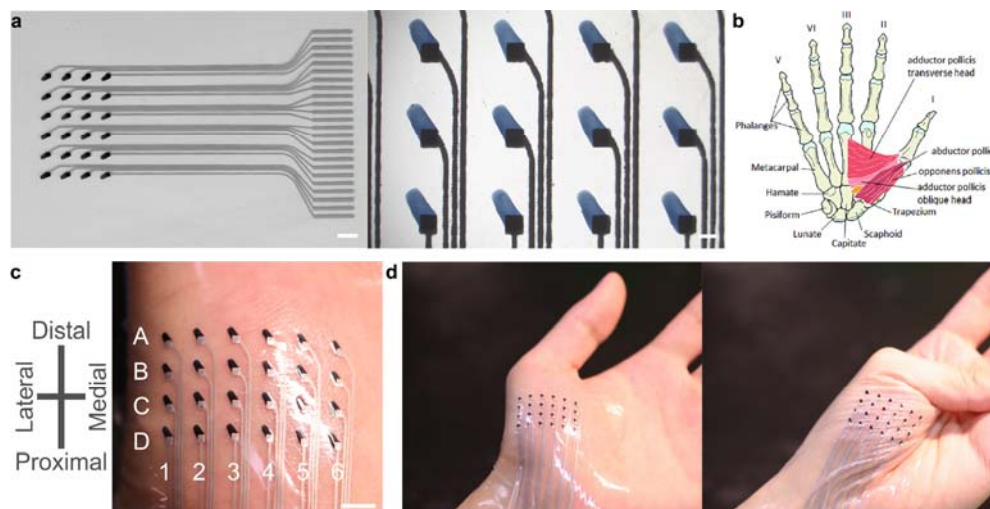


Figure 5.2.5 Experimental setup for sEMG activation mapping on APB. **a** Photographs of MEAP for APB. Scale bar: 5 mm and 1 mm. **b** Schematic drawings of the right hand, palmar view, with part of thenar muscles. Adapted from *PLoS One* **12**, (2017). **c** Configuration of MEAP on APB. **d** Contraction task for APB activation.

In terms of sEMG signals, each channel exhibited a satisfactory SNR that allowed for the differentiation of the activated portion from the baseline noise (Figure 5.2.6). However, it is apparent that most channels exhibited a lower SNR when compared to the recordings made by MEAP on BB. This decrease in SNR can be attributed to the smaller surface area of the electrodes, which results in higher impedance between the electrodes and the skin. Despite the SNR not being as optimal as in the previous BB recordings, it is still possible to discern that the diagonal pattern from the

top left to the bottom right displayed higher muscle activity.

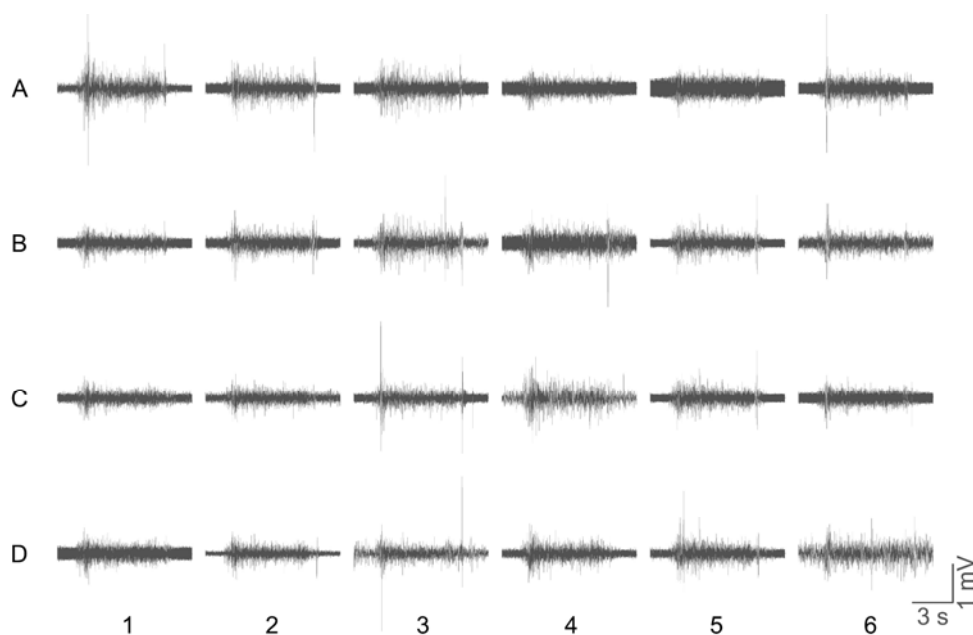


Figure 5.2.6 sEMG recorded by each channel of MEAP on BB.

In a similar manner, the entire task was segmented into four stages: pre-contraction, initiation of contraction, during contraction, and post-contraction. During recording on the APB, it becomes evident that the recruitment pattern follows the diagonal layout of the MEAP, which aligns with the physiological anatomical structure of the palm muscle (Figure 5.2.7). However, unlike the BB recordings, there was no observed shift in the activation zone of the APB. This can be attributed to the fact that the smaller muscle of the APB has limited spatial movement. It is also conceivable that with even higher resolution in the MEAP, these subtle positional changes in the muscle could be captured.

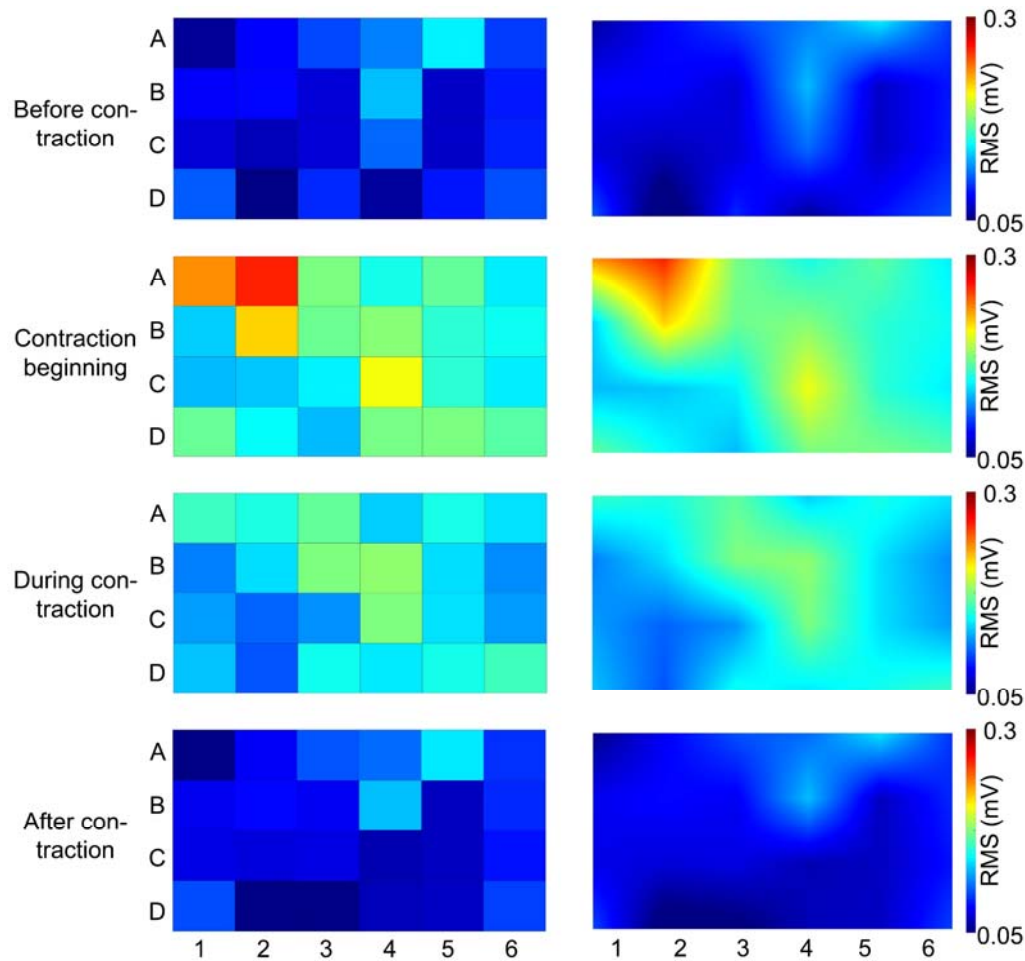


Figure 5.2.7 Muscle activity maps of sEMG recorded from APB, showing the process of graded recruitment during contractions. The left column is RMS values from each channel; the right column is 10th-order interpolated results of each channel.

In comparison to the BB recordings, the MEAP with smaller electrodes and a shorter IED yielded lower activity but finer recruitment patterns in the APB. These findings suggest that MEAPs with high spatial and time resolution can accurately capture the recruitment and length changes in muscles during contractions. Such tools hold significant potential for advancing clinical diagnosis, medical treatment, and sports sciences, offering substantial benefits in these domains.

5.3 MEAP for muscle-tendon junction location

Muscle injuries often occur during exercises that involve excessive stretching of the muscle and tendon. Currently, these injuries are typically confirmed after the fact using magnetic resonance imaging or ultrasound imaging to locate the muscle-tendon junction. Both of these instruments are heavy and cumbersome to use, making it impossible to provide an instant diagnosis, let alone real-time monitoring for injury prevention. In this context, the ability of a tool to offer real-time information to individuals during exercise, alerting them to excessive stretching and reducing the risk of injury, is a significant advantage not provided by the two imaging techniques mentioned above. Conventional Ag/AgCl electrodes lack the spatial resolution needed to provide information about tendon position. In contrast, high-density MEAP offers a clear distinction in mean frequencies recorded from different channels, allowing for the detection of tendon displacement and serving as a marker for actively monitoring tendon position. This section will verify the capability of MEAP to monitor the location of the muscle-tendon junction on the distal biceps tendon and Achilles tendon, where two common muscle-tendon injuries occur.

5.3.1 Location of muscle-tendon junction on distal biceps tendon

A distal biceps tendon tear is a relatively common musculoskeletal injury characterized by the partial or complete tearing of the tendon that connects the biceps muscle to the radius bone in the forearm. This injury typically occurs in the lower part of the biceps muscle near the elbow joint. It can be

caused by acute trauma, such as heavy lifting or a sudden force applied to the arm, which are scenarios commonly encountered by exercisers. Monitoring the condition of the distal biceps tendon in real-time could provide valuable guidance and information to individuals engaged in physical activities to help prevent injuries of this nature.

To monitor the location of the biceps distal tendon, the MEAP was employed with a diameter of 5 mm and an IED of 15 mm, as it provides sufficient coverage of the tendon (Figure 5.3.1a). To validate the capability of MEAP for tendon monitoring, ultrasound imaging was used as a gold standard reference. During this assessment, a representative subject (also subject A in following tests) performed an isometric task with a 5 kg load at a 90° angle in an isolated biceps curl, with the MEAP attached while undergoing ultrasound imaging. The ultrasound image clearly depicted the intersection of the two edges of the biceps brachii, extending to reveal the distal biceps tendon (Figure 5.3.1b). This junction was used as a marker for tendon movement. By analysing the ultrasound image, it was observed that the positional difference of the muscle-tendon junction was approximately 3.81 cm between flexion and extension (Figure 5.3.1b). Simultaneously, the relative location of the MEAP was recorded on the skin for further comparison.

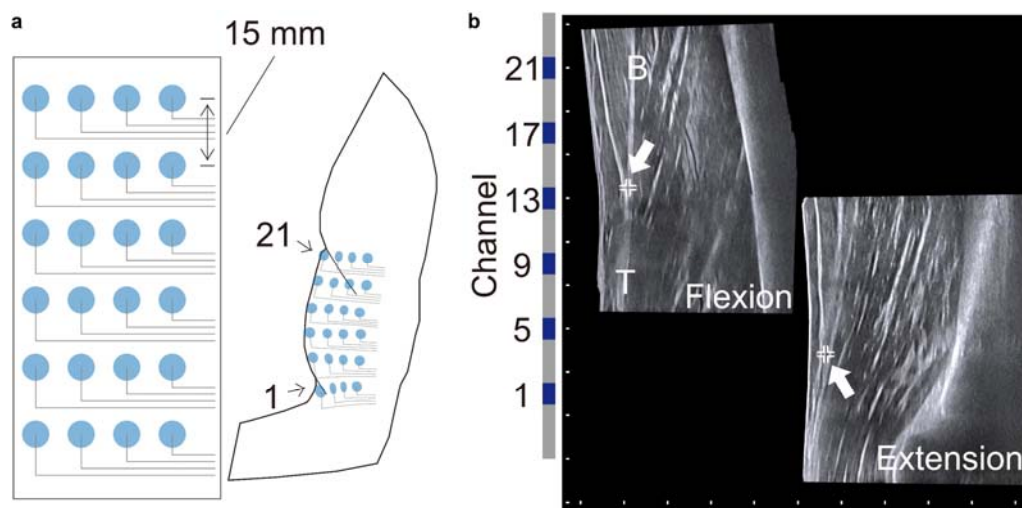


Figure 5.3.1 Location of distal biceps tendon by MEAP and ultrasound image. **a** Schematic diagram of a MEAP on the biceps. The IED was 15 mm. Channel numbers (1 – 24) were ordered from left to right and from bottom to top. **b** Ultrasound image of tendon displacement during the isometric task with load of 5 kg and MEAP relative position on the skin. Scale bar: 1 cm. B: biceps brachii; T: biceps distal tendon.

Before analysing the sEMG signals collected by MEAP, it is important to address the selection of columns for analysis. Given the interest in studying the longitudinal change of the tendon, the columns of MEAP were focused on, which run parallel to the tendon direction, for further processing. While distinguishing the ends close to the muscle and tendon is relatively straightforward in the longitudinal direction (row selection), the horizontal direction (column selection) presented a choice, as each MEAP had four columns of channels, usually with two middle columns both on the muscle. To make an informed decision, we relied on the RMS results obtained from each channel recorded by MEAPs (Figure 5.3.2). The results revealed that channels 17 and 21 consistently exhibited the highest RMS values across various tasks with different loads. This indicates that the first column is

closest to the muscle belly of the biceps brachii and, as such, was selected for monitoring the muscle-tendon junction location.

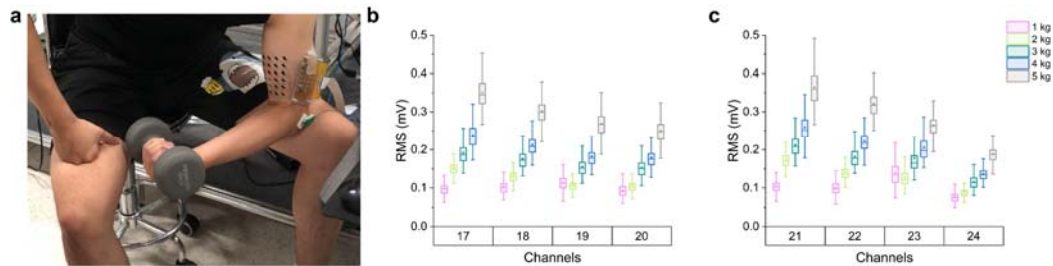


Figure 5.3.2 The selection of column of the MEAP on the biceps brachii of subject A. **a** A photograph of the subject A during the task. **b, c** The RMS values of each channel in the row 5 and 6, respectively, which are closest to the muscle belly of the biceps brachii.

When calculating the mean frequencies of sEMG signals recorded by each channel within the same column, a clear pattern emerged: the values ascended sequentially from the channel positioned near the muscle to the one near the tendon (Figure 5.3.3a). While this order remained consistent, the magnitude of the differences between each value changed during flexion and extension movements. To emphasize this difference, all channels were normalized based on the first and last channels, which were consistently positioned on the tendon and muscle, respectively. During the isometric task, the channels in between exhibited noticeable differences between flexion and extension (Figure 5.3.3b). Upon analysing the results of the ultrasound image, it was found that the junction location consistently approached a value of 0.5 after normalization. Therefore, we defined the channel with a value of 0.5 as the suitable marker for the muscle-tendon junction position, a finding further corroborated by palpation of the biceps brachii.

Here are the detailed calculations and standards, using the mean frequencies recorded by the first column as an example:

$$m_1, m_5, m_9, m_{13}, m_{17}, m_{21}.$$

According to the discussion with Figure 5.3.3b, it was found they were in descending order that

$$m_1 > m_5 > m_9 > m_{13} > m_{17} > m_{21}.$$

Then the normalization can be expressed as

$$n_1 = 1, n_5 = \frac{m_5 - m_{21}}{m_1 - m_{21}}, n_9 = \frac{m_9 - m_{21}}{m_1 - m_{21}},$$

$$n_{13} = \frac{m_{13} - m_{21}}{m_1 - m_{21}}, n_{17} = \frac{m_{17} - m_{21}}{m_1 - m_{21}}, n_{21} = 0,$$

When $n_i > 0.5$, the channel i was considered on tendon part; when $n_i = 0.5$, the channel i was considered on muscle-tendon junction; when $n_i < 0.5$, the channel i was considered on muscle part. Usually, 0.5 is between n_i and n_{i+1} , while a linear fitting is used to determine the junction location between the two certain channels.

To further validate the consistent recording capability of the MEAP in identifying junction positions, recordings were conducted on five different subjects using a total of 15 MEAPs (Figure 5.3.3c). Importantly, all MEAPs were fabricated following the same procedure but from distinct batches, and subjects were recruited randomly to ensure a randomized approach. Based on the previously established calculations and standards, it is essential to note that the focus of MEAP lies in determining the relative

position of the muscle-tendon junction under the array cover. Consequently, MEAPs were consistently positioned on the biceps brachii muscles of all subjects to ensure comparable junction locations. Several key observations reinforced our findings: 1. Mean frequencies recorded from channels 1 and 21 consistently reflected muscle and tendon regions, with channel 1 typically displaying the highest values and channel 21 the lowest across various subjects. 2. Mean frequencies consistently followed an ascending order from the channel positioned near the muscle to the one near the tendon, across different subjects. 3. Differences between each channel exhibited distinct patterns during both flexion and extension movements. These findings not only reaffirmed the calculations and standards established before but also demonstrated that they can be applied universally. Moreover, the mean frequency patterns for each channel consistently reflected the difference between flexion and extension, underscoring the reliable recording capabilities of MEAP in locating muscle-tendon junction positions. The calculation method was also refined to minimize the impact of skin deformation, a topic that will be discussed in greater detail in Chapter 7.

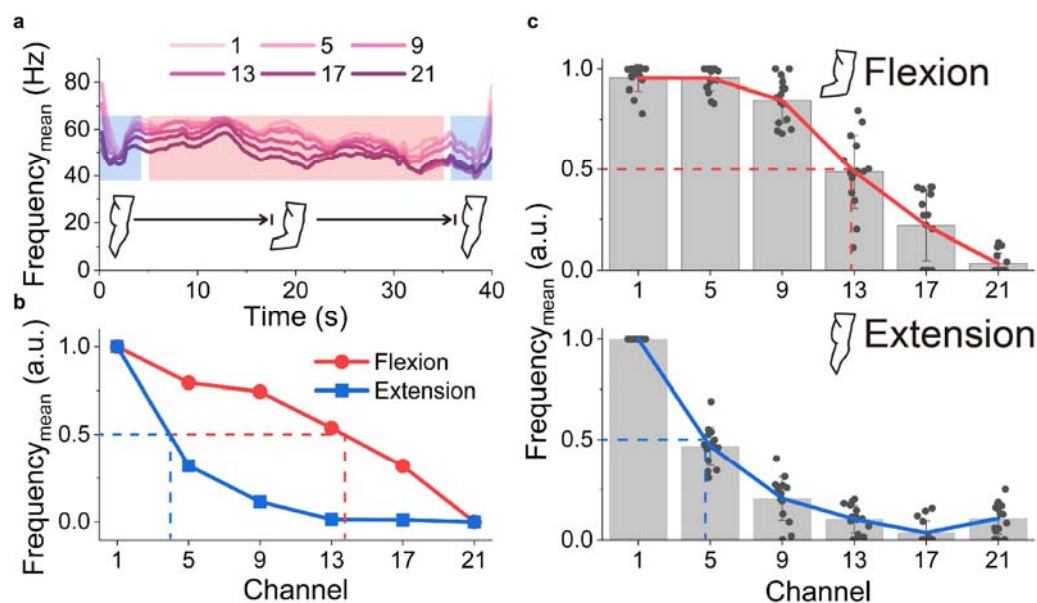


Figure 5.3.3 Location of distal biceps tendon in isometric task. a Mean frequencies of the sEMG signals from the biceps brachii of the representative subject during the isometric task. **b** The normalised mean frequencies for each channel during flexion and extension by the representative subject in isometric task. **c** The normalised mean frequency data in multiple subjects. All statistical experiments were conducted with the 3 repeated isometric or dynamic tasks performed by 5 subjects ($n=15$, different MEAPs used); data are presented as mean values \pm SD. a.u. = arbitrary units.

In addition to isometric tasks, real-time monitoring of tendons during dynamic tasks holds more significant value, as most muscle injuries occur in such situations. Following the rules and calculations established during isometric tasks, the mean frequencies of sEMG signals from each channel were normalized over a time domain (Figure 5.3.4a). It was evident that the normalized values of channels in between initially increased and then decreased over a 10-second duration, corresponding to a biceps curl with 5 seconds of concentric contraction followed by 5 seconds of eccentric contraction. By using 0.5 as the marker for the muscle-tendon junction, the displacement of the junction was continuously monitored throughout the

dynamic biceps curl task. Similarly, the results from different subjects were averaged to demonstrate the capability of MEAP to monitor tendon movement across different individuals (Figure 5.3.4b).

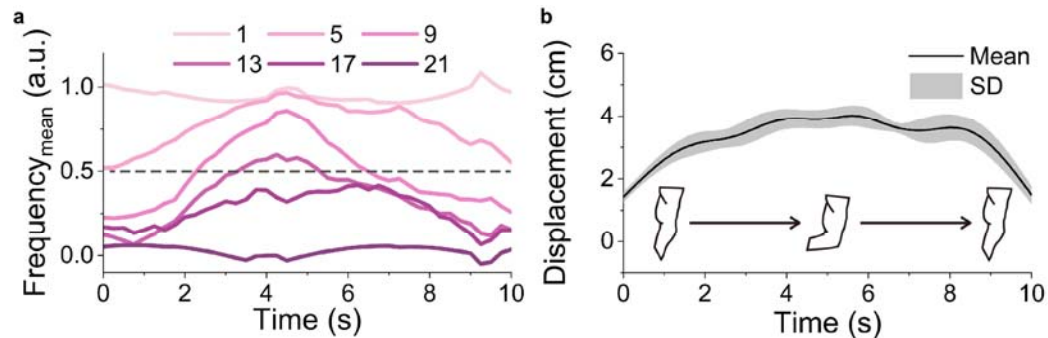


Figure 5.3.4 Location of distal biceps tendon in dynamic task. a Normalised values of mean frequencies of the EMG signals recorded from the biceps brachii of a representative subject during the dynamic task. **b** Real-time junction displacement in multiple subjects after calculation according to the rules founded in isometric task. All displacements represent the distance between the first channel position and the junction position; all statistical experiments were conducted with the 3 repeated isometric or dynamic tasks performed by 5 subjects ($n=15$, different MEAPs used); data are presented as mean values \pm SD. a.u. = arbitrary units.

This section has established the rule for locating the muscle-tendon junction by mean frequencies, with reference to ultrasound images. The MEAP has effectively monitored the muscle-tendon junction location during isometric tasks and tracked its movements during dynamic tasks, demonstrating its consistency across different subjects.

5.3.2 Location of muscle-tendon junction on Achilles tendon with 10 mm-IED MEAP

Achilles tendon tear refers to the partial or complete rupture of the Achilles

tendon, the largest and strongest tendon in the human body. This tendon, situated at the back of the lower leg, connects the calf muscles to the heel bone, enabling crucial functions like walking, running, and jumping. This injury frequently results from sudden and forceful movements, such as pushing off to sprint or making abrupt changes in direction, which are commonly encountered in sports like basketball, football, or tennis. Therefore, it is of great significance to investigate the feasibility of monitoring Achilles tendon movements using MEAP.

Initially, the movement range of the Achilles tendon was not well-defined. Therefore, a 24-row MEAP with an IED of 10 mm was utilized to establish a preliminary estimate of the movement range of the tendon. This particular MEAP configuration effectively covered a substantial area of the gastrocnemius and Achilles tendon (Figure 5.3.5a, b). During the experiment, the subject was instructed to isometrically contract the gastrocnemius muscle while positioned on a step, causing various degrees of tendon stretching. These states were categorized into three distinct phases: Flexion, Neutral, and Extension (Figure 5.3.5c).

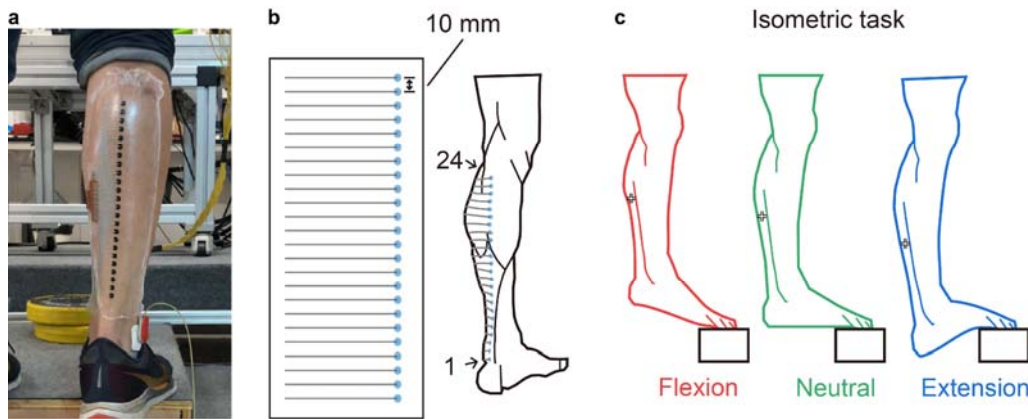


Figure 5.3.5 Location of Achilles tendon by MEAP with IED of 10 mm. **a** A photograph of the MEAP attached on the gastrocnemius and Achilles tendon. **b** Schematic diagram of configuration of MEAP on the gastrocnemius and Achilles tendon. Channel numbers (1 – 24) were ordered from bottom to top. **c** Isometric tasks on a step.

In contrast to the 6-channel design used for biceps monitoring with MEAP, the 24-channel configuration employed for Achilles tendon analysis provided higher resolution for identifying tendon movements. The fundamental rule established in the previous section remained applicable: channels positioned near the tendon exhibited high mean frequencies, while those near the muscle region displayed lower mean frequencies. This characteristic is clearly depicted in the plot of normalized values (Figure 5.3.6a). By maintaining 0.5 as the marker for the muscle-tendon junction, it became evident that the position of the junction differed across various isometric tasks. The junction displacements, which represent the distance between the junction and the first MEAP channel, were measured at 10.96, 8.74, and 7.53 cm for the Flexion, Neutral, and Extension, respectively (Figure 5.3.6b). These values closely matched the palpation results obtained from the representative subject. Once again, MEAPs were

attached to similar locations on the Achilles tendon in multiple subjects to determine junction locations. The results reaffirmed the consistent ability of the MEAP to monitor tendon movements, even across different individuals and muscle groups (Figure 5.3.6c).

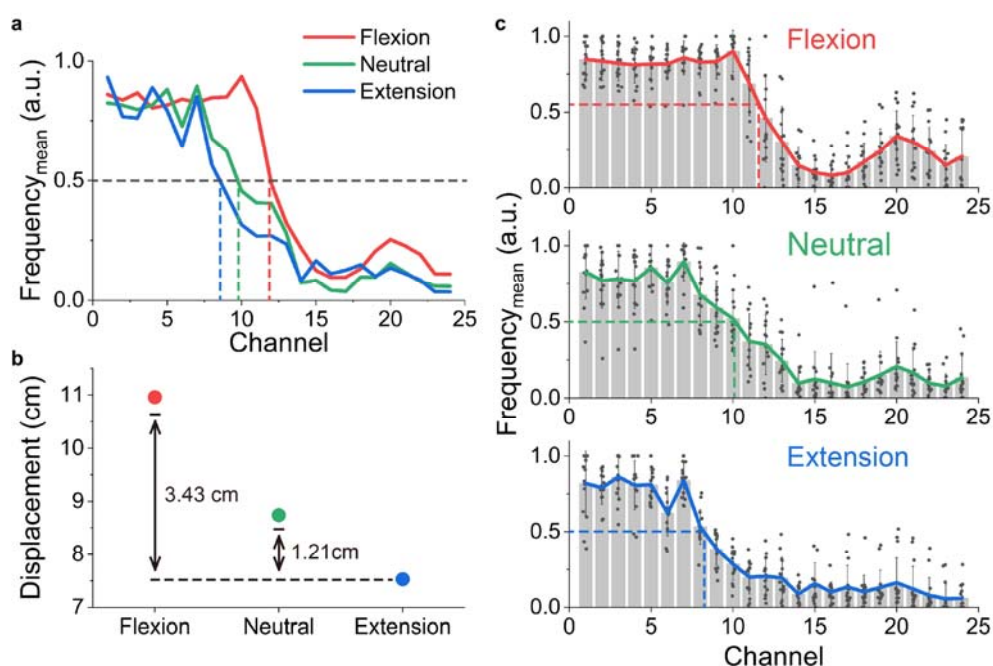


Figure 5.3.6 Location of Achille tendon by MEAP with IED of 10 mm in isometric task. **a** Normalised values of mean frequencies of the EMG signals from the gastrocnemius and Achilles tendon of a representative subject during different isometric tasks. **b** Corresponding displacements between different isometric tasks. **c** The normalised mean frequency data in multiple subjects. All displacements represent the distance between the first channel position and the junction position; all statistical experiments were conducted with the 3 repeated isometric or dynamic tasks performed by 5 subjects ($n=15$, different MEAPs used); data are presented as mean values \pm SD. a.u. = arbitrary units.

In the dynamic task involving the transition from Neutral to Flexion and then to Extension while on a step, multiple subjects participated. To enhance comprehension, the normalized values of mean frequencies in the time domain from a representative subject were presented. It was observed that

only 4 channels engaged in identifying the junction location because their values closely approximated 0.5 during some stages of the entire task (Figure 5.3.7a). Conversely, all other channels consistently exhibited normalized values either greater than or less than 0.5, and thus, they were not included in the calculation. These four channels effectively delineated the primary movement range of the muscle-tendon junction location in the lower leg. Once more, the MEAP effectively delivered real-time tendon monitoring results across different subjects (Figure 5.3.7b).

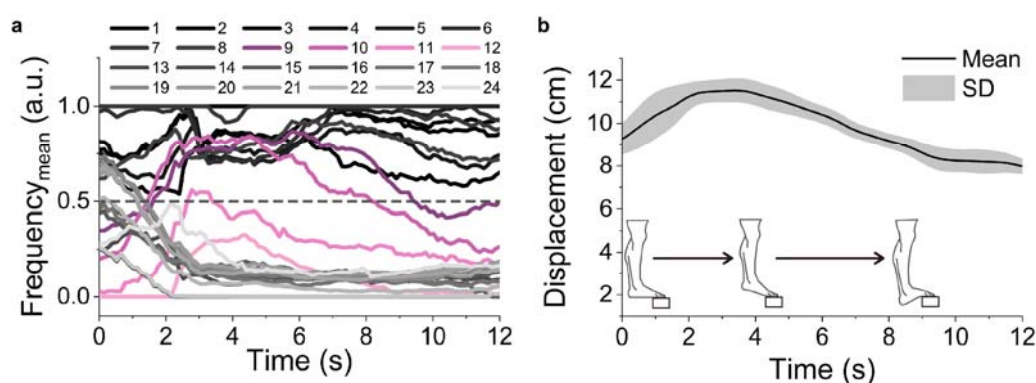


Figure 5.3.7 Location of Achilles tendon by MEAP with IED of 10 mm in dynamic task. **a** Normalised values of mean frequencies of the EMG signals recorded from the gastrocnemius and Achilles tendon of a representative subject during the dynamic task **b** Average results of real-time junction displacement in multiple subjects. All displacements represent the distance between the first channel position and the junction position; all statistical experiments were conducted with the 3 repeated isometric or dynamic tasks performed by 5 subjects ($n=15$, different MEAPs used); data are presented as mean values \pm SD. a.u. = arbitrary units.

This section utilized a 24-channel MEAP to monitor the Achilles tendon, confirming the rules established based on the distal biceps tendon location findings. The 24-channel MEAP column demonstrated greater resolution compared to the one used for the biceps brachii, effectively capturing real-

time information about tendon position.

5.3.3 Location of muscle-tendon junction on Achilles tendon with 6 mm-IED MEAP

Once the movement range of the junction was identified, a MEAP with a shorter IED of 6 mm was employed to enhance the precision of the location (Figure 5.3.8a, b). A smaller IED made it easier to distinguish the muscle-tendon junction between each pair of adjacent channels. In this round of isometric tasks, the exercises were conducted on the ground, and the Neutral phase was replaced with two new categories: Semi-flexion and Semi-extension (Figure 5.3.8c). Each posture involves a different degree of muscle contraction and, consequently, a distinct muscle-tendon junction position. This modification was made to evaluate whether the MEAP with a IED of 6 mm could effectively distinguish between these postures, even though they exhibit reduced variation.

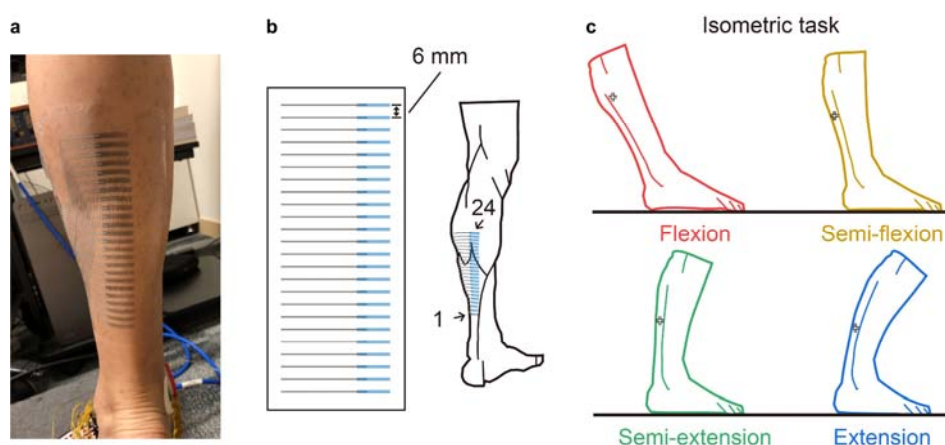


Figure 5.3.8 Location of Achilles tendon by MEAP with IED of 6 mm. **a** A photograph of the MEAP attached on the gastrocnemius and Achilles tendon. **b** Schematic diagram of configuration of MEAP on the gastrocnemius and Achilles tendon. Channel numbers (1 – 24) were ordered from bottom to top. **c** Isometric tasks on the ground.

Utilizing the smaller IED, tendon stretch was evaluated in four lower leg positions on flat ground during the isometric task. The outcomes revealed that the junction location in each isometric task could be discerned (Figure 5.3.9a). The displacements of tendon were 6.23, 5.82, 5.32 and 4.17 cm for four lower leg positions, respectively (Figure 5.3.9b). This demonstrates that MEAP is proficient in monitoring junction displacement across various tasks and scenarios. Once again, the results from different subjects confirmed the effectiveness of MEAP in locating tendons (Figure 5.3.9c).

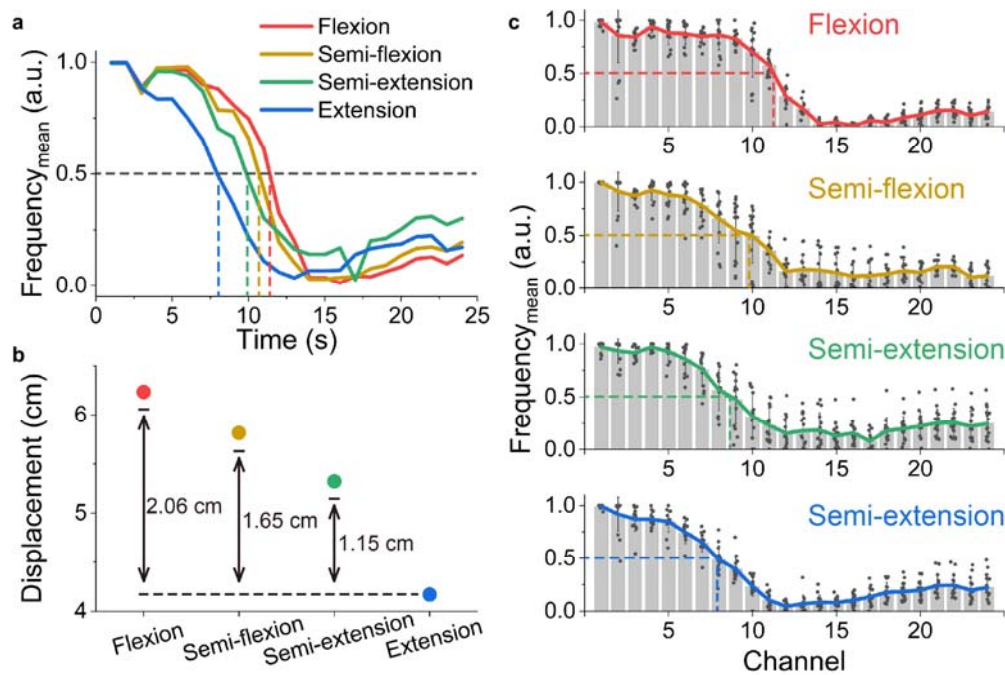


Figure 5.3.9 Location of Achilles tendon by MEAP with IED of 6 mm in isometric task. **a** Normalised values of mean frequencies of the EMG signals from the gastrocnemius and Achilles tendon of a representative subject during different isometric tasks. **b** Corresponding displacements between different isometric tasks. **c** The normalised mean frequency data in multiple subjects. All displacements represent the distance between the first channel position and the junction position; all statistical experiments were conducted with the 3 repeated isometric or dynamic tasks performed by 5 subjects ($n=15$, different MEAPs used); data are presented as mean values \pm SD. a.u. = arbitrary units.

During the dynamic task transitioning from plantarflexion to dorsiflexion on the step, the changes in normalized values of mean frequencies for each channel were displayed over time. It was observed that eight channels were involved in the junction location when using the MEAP with an IED of 6 mm, which was more than with the MEAP with an IED of 10 mm (Figure 5.3.10a). This aligns with the previously hypothesized idea that a MEAP with a lower IED can achieve higher resolution in tendon movements. This is because, for a similar distance of tendon movement, the smaller IED divides the distance into more segments, thus enhancing location precision. The entire process of the dynamic task transitioning from plantarflexion to dorsiflexion was monitored, with the final tendon movement being approximately 3 cm (Figure 5.3.10b).

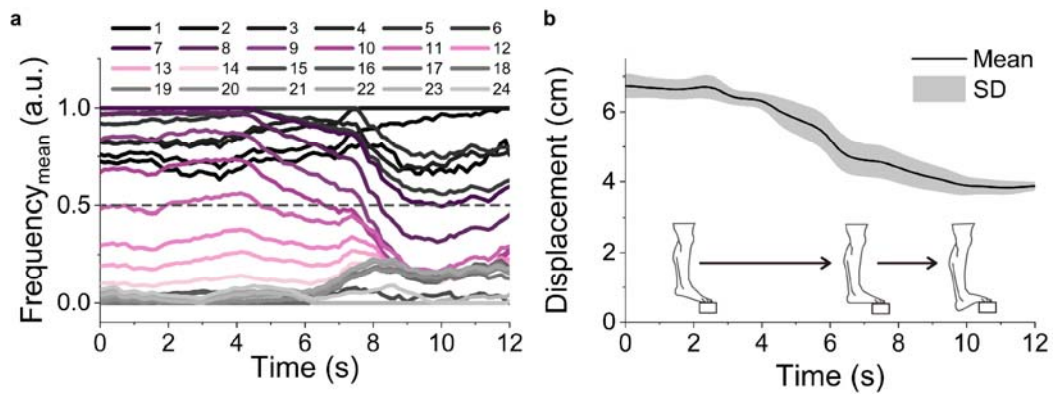


Figure 5.3.10 Location of Achilles tendon by MEAP with IED of 6 mm in dynamic task. **a** Normalised values of mean frequencies of the EMG signals recorded from the gastrocnemius and Achilles tendon of a representative subject during the dynamic task **b** Average results of real-time junction displacement in multiple subjects. All displacements represent the distance between the first channel position and the junction position; all statistical experiments were conducted with the 3 repeated isometric or dynamic tasks performed by 5 subjects ($n=15$, different MEAPs used); data are presented as mean values \pm SD. a.u. = arbitrary units.

This section demonstrates that the precision of tendon location can be enhanced by adjusting the resolution of the MEAP. This opens up the potential for improved monitoring of tendons and muscles, which is crucial for personalized monitoring and diagnostics.

5.4 MEAP for muscle injury prevention

The dumbbell biceps curl is a widely practiced exercise for strengthening the biceps brachii muscle, but it carries the potential risk of muscle injuries if done with incorrect loading or excessive training (Figure 5.4.1a, b). In such cases, MEAP emerges as the most suitable tool to offer professional guidance to exercisers. MEAP utilizes sEMG signals to derive key parameters such as RMS, median frequencies, and mean frequencies, which correspond to muscle loading, muscle fatigue, and tendon displacement, respectively. All these information provide comprehensive insights into muscle activity, aiding in injury prevention and exercise optimization¹⁹⁸. This injury prevention system utilizing MEAP is depicted in a diagram, highlighting its foundation on objective quantitative analysis of sEMG signals. This analysis allows for the creation of customized approaches tailored to the specific needs of individuals, encompassing both injury prevention and exercise enhancement strategies (Figure 5.4.1c).

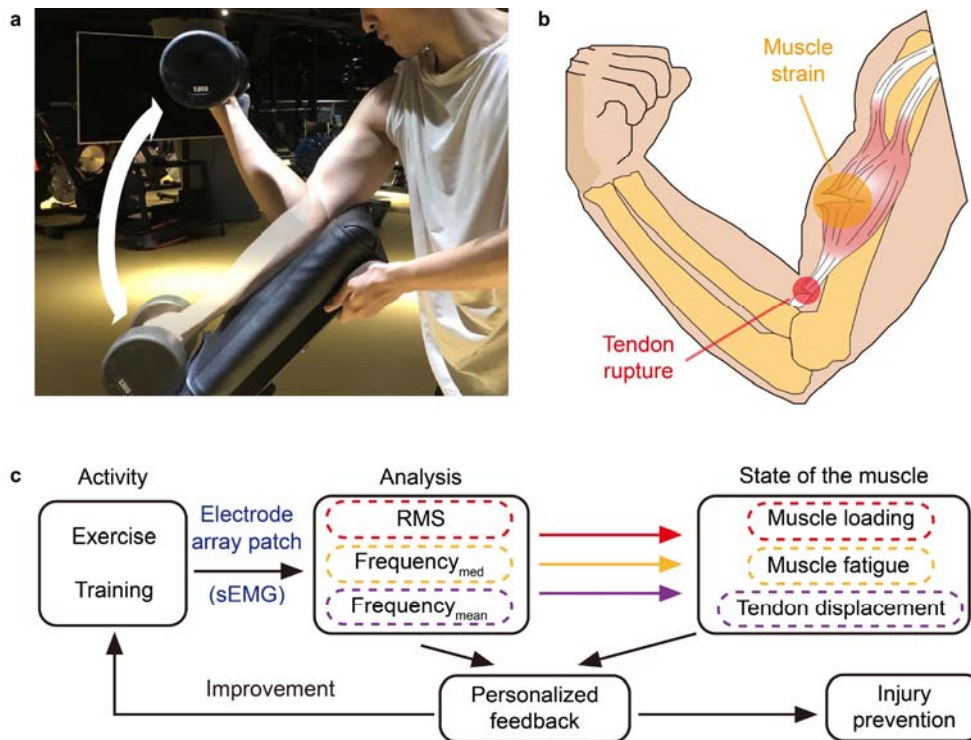


Figure 5.4.1 High-density sEMG recording by MEAP for muscle injury prevention. **a** A photograph of a biceps curl. **b** A risk schematic of biceps curl. **c** Diagram of the injury prevention system components.

To evaluate the capability of MEAP to provide multiplexed information, sEMG recordings were conducted on the biceps muscles of five subjects in five different sessions, with loads ranging from 1 kg to 5 kg (Figure 5.4.2a, b). Each session comprised three phases: an isometric task, a resting period, and a dynamic task involving 10 biceps curls, all aimed at acquiring comprehensive muscle-related data. As an illustrative example using subject A, the analysis focused on nine channels selected based on RMS results, with Channel 21 exhibiting the highest RMS value, indicating its proximity to the muscle (Figure 5.4.2c). The row and column corresponding to this channel were chosen for further analysis. The data from subject A will be analysed first in this section as a representative example, and

statistics across multiple subjects will be presented to verify the stability and reliability of MEAP for different individuals.

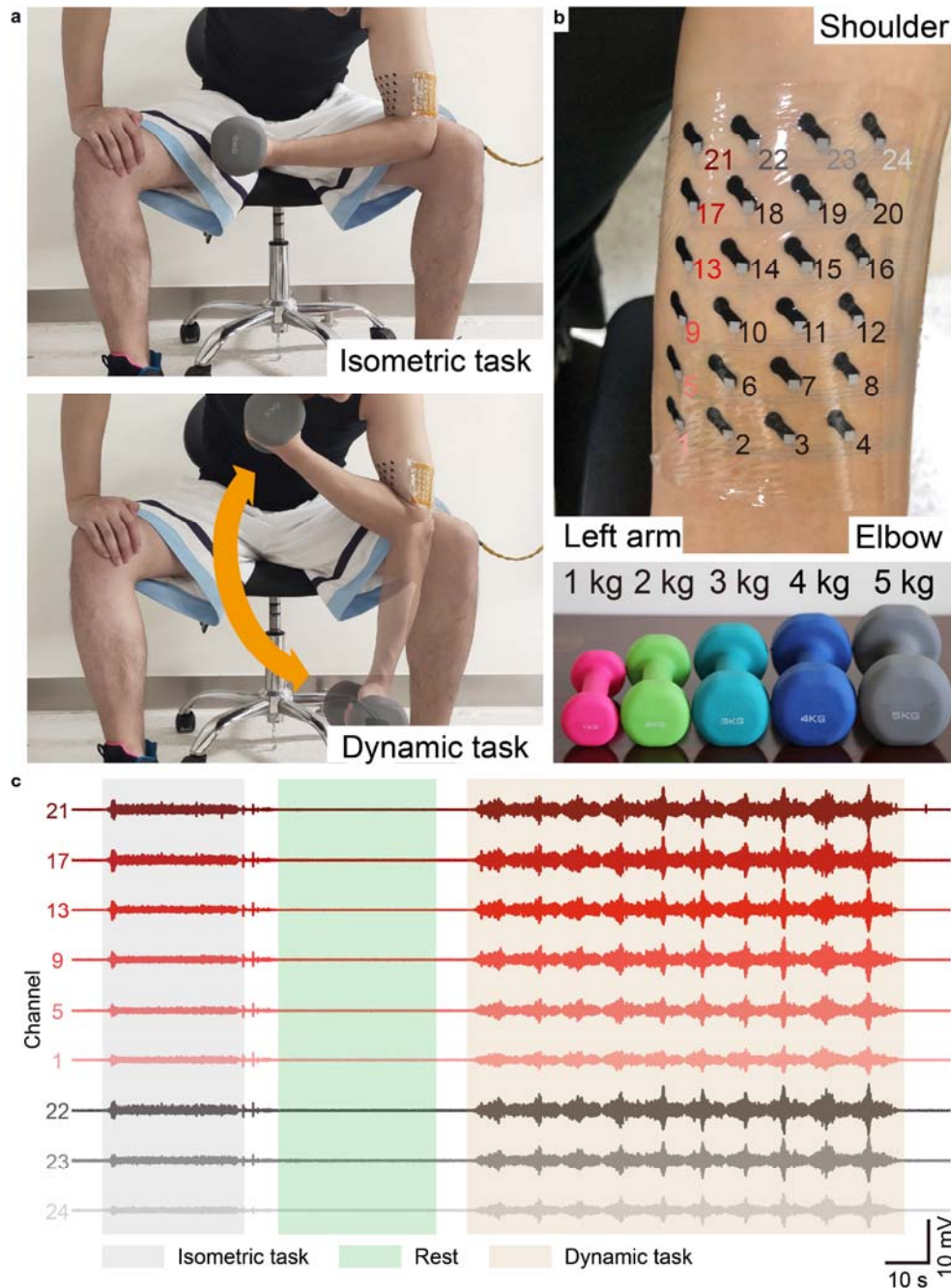


Figure 5.4.2 Experiment design for injury prevention. **a** Photographs of a session including isometric and dynamic tasks. **b** Photographs of channel sites of MEAP and different loads. **c** Three phases (isometric task, rest and dynamic task) in one session. sEMG signals were recorded from subject A during the session of 5 kg.

5.4.1 Muscle loading and fatigue of subject A

Before data analysis, it is necessary to provide an overview of the overall signal quality. For subject A, the results indicate that all channels successfully recorded sEMG signals during both isometric and dynamic tasks (Figure 5.4.3). Differences between each load, with higher sEMG amplitudes observed with heavier loads, can be distinguished due to the excellent SNR. Additionally, it can be observed that during the 30-second isometric tasks, some channels in the 5 kg session showed a noticeable increase in sEMG signal amplitude. However, this phenomenon was not as pronounced in sessions with lower loads. This increase in amplitude is likely due to muscle fatigue, which can result in higher sEMG signal amplitudes¹⁹⁹. The high-quality sEMG recording by MEAP contributes to the ability to observe such changes, confirming the feasibility of MEAP again.

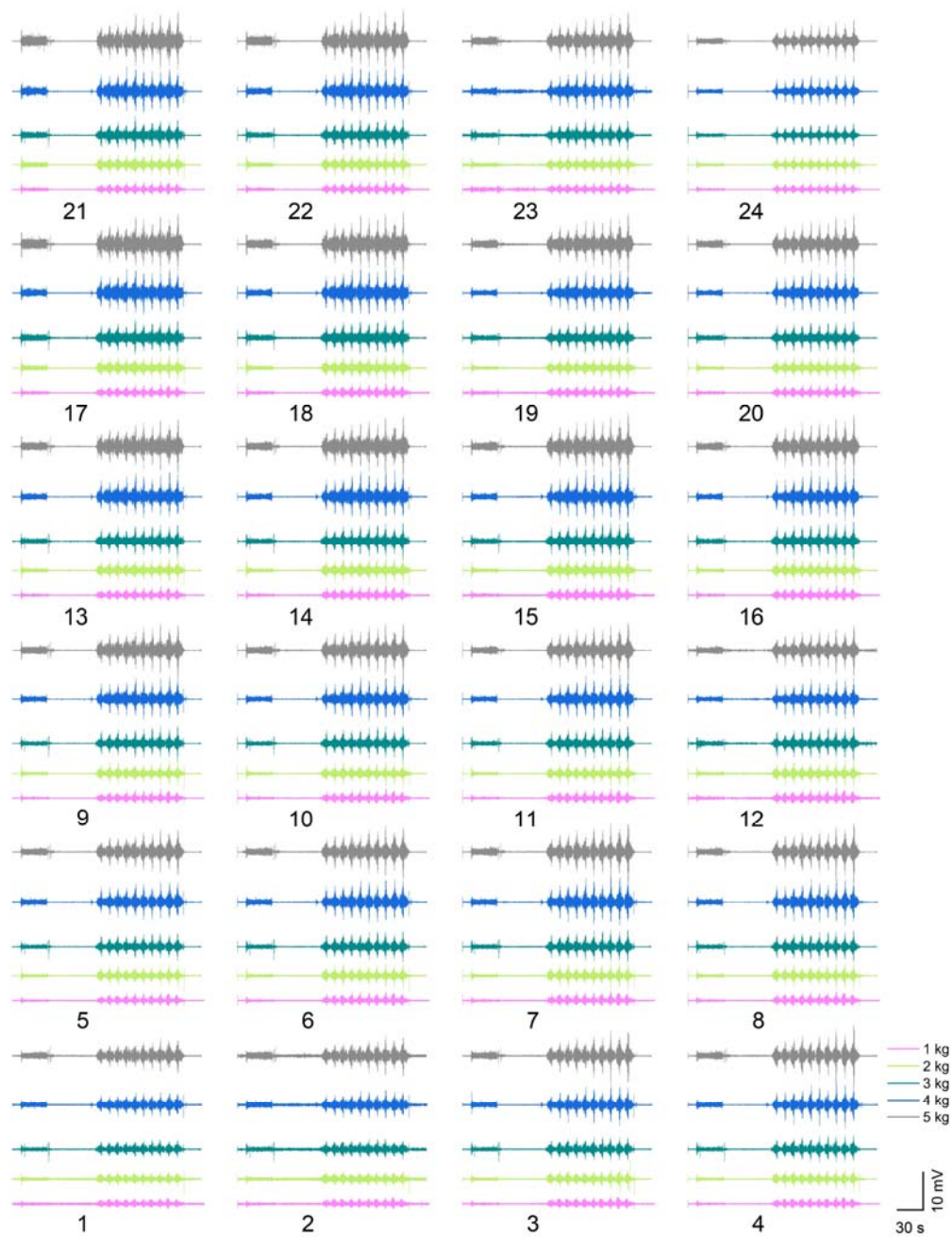


Figure 5.4.3 sEMG signals of biceps brachii of subject A with five different loads recorded by MEAP.

The sEMG signals contain multiplexed information and among them, the RMS, which directly reflects muscle activity, was the first parameter studied. The RMS values in isometric tasks across all channels in the first column for different sessions were summarized (Figure 5.4.4a). It is evident that

higher loads result in higher RMS values in the sEMG signals, demonstrating that MEAP successfully recorded muscle activity under varying loads. This observation opens up significant potential applications, such as using RMS values to estimate or infer muscle loads or force generation. These applications could be relevant in fields like prosthetics or human-machine interfaces, which will be discussed in Chapter 7. Another noteworthy finding is that within the same session, different channels exhibited varying RMS values. Channels 13, 17, and 21 consistently showed higher RMS values, with more significant differences between them, while channels 1, 5, and 9 consistently showed lower RMS values, with smaller differences between them. These two groups of channels corresponded to the muscle and tendon regions of the biceps brachii, respectively. This observation aligns with the spatial patterns of muscle activation discussed in Chapter 5.2.

For dynamic tasks, the highest RMS value during each biceps curl was recorded and compared (Figure 5.4.4b). The same pattern emerged, with higher loads resulting in higher RMS values. It is worth noting that in the high-load sessions (4 & 5 kg), RMS values exhibited a noticeable increase during the last few curls. This increase is indicative of muscle fatigue, which aligns with previous observations in sEMG signals²⁰⁰. These findings collectively demonstrate that MEAP can effectively detect muscle loading in both isometric and dynamic scenarios.

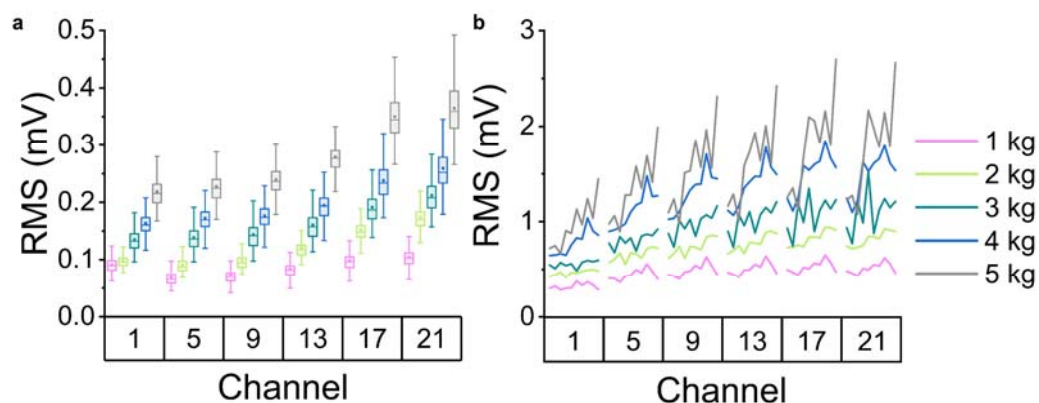


Figure 5.4.4 RMS values of sEMG signals of subject A. **a** RMS values recorded by selected channels in the isometric task ($n = 54$ RMS values per channel). **b** RMS values recorded by selected channels in the dynamic task. The box plots show the mean (centre square), median (centre line), the 25th to 75th percentiles (box) and the smallest and largest value that is ≤ 1.5 times the interquartile range (the limits of the lower and upper whiskers, respectively).

Furthermore, the study also delved into assessing muscle fatigue using MEAP. Aside from RMS, the median frequency is a common metric for detecting fatigue. A decrease in median frequency is considered a strong indicator of muscle fatigue, and the slope value of the linear fit of the median frequency is often used for assessment. The slope values were calculated for the isometric task across different sessions (Figure 5.4.5a). The results revealed that for low loads, the slope values were mostly positive, indicating no significant decrease in median frequency and suggesting that muscle fatigue was not evident. However, in high-load sessions (4 & 5 kg), the slope values from all channels were negative, signifying muscle fatigue. This finding provided a rough range for subject A to determine when he was likely to experience muscle fatigue for a specific task. Similarly, in dynamic tasks, the median frequency exhibited a noticeable decrease during the last few curls when loads exceeded 3 kg

(Figure 5.4.5b). The fatigue thresholds of subject A were determined to be 4 kg for the isometric task and 3 kg for the dynamic task. It is important to note that these thresholds may vary depending on task duration and experimental design, considering that the dynamic task followed the isometric task and lasted longer. These fatigue measures offer subjects a more objective way to gauge their exercise intensity rather than relying solely on subjective feelings.

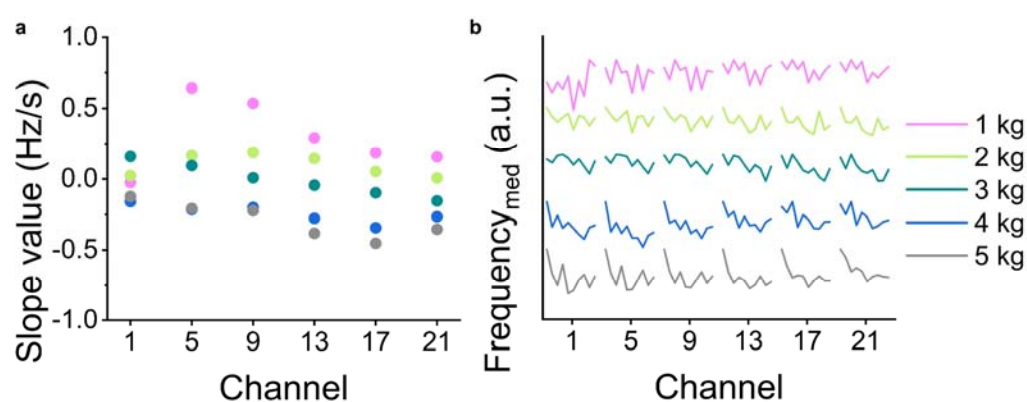


Figure 5.4.5 Median frequency details of sEMG signals recorded by MEAPs of subject A. a Linear fit slopes for median frequencies in the isometric task. **b** Changes of median frequencies in the dynamic task.

In addition to the selected channels, RMS and median frequency recordings from all channels in the 5 kg session were provided to demonstrate the reliability of MEAP across all channels (Figure 5.4.6). These recordings exhibited similar patterns to those observed earlier, such as the channel located closer to the muscle having higher RMS values. When it comes to fatigue measures, only higher loads resulted in negative slope values, indicating fatigue. These results illustrate that all channels in MEAPs yield consistent findings and conclusions regarding muscle condition. However, the precision or resolution of the results tends to be

highest in the specific column closest to the muscle region.

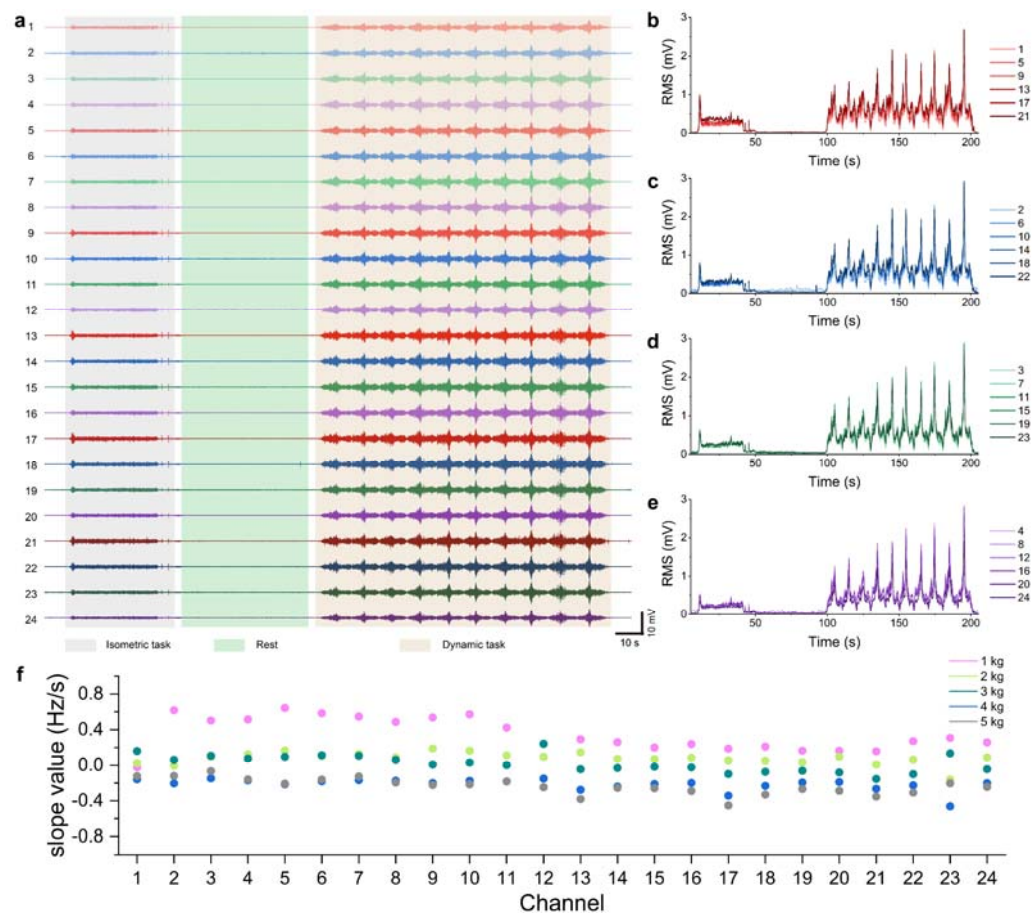


Figure 5.4.6 Summary of RMS and fatigue information of subject A. **a** sEMG signals recorded by all 24 channels with load of 5 kg. **b-e** RMS values of sEMG signals recorded by each column with load of 5 kg. **f** Slope values of the linear fitting of the sEMG median frequencies during the isometric task recorded by all 24 channels with different loads.

5.4.2 Location of muscle-tendon junction of subject A

Using the established rules from Chapter 5.3, determining tendon positions became a straightforward process, given the comparability of tasks. It was consistently observed that regardless of the load session, the mean frequency from channels located in the muscle region was consistently lower than that from channels in the tendon region (Figure 5.4.7a).

Relationships between mean frequency and tendon displacement under different loading conditions were identified. Notably, the displacements increased with higher loads because greater loads induced more contraction of the biceps, resulting in more tendon elongation compared to lower loads, even when the flexion angles remained the same across all isometric tasks. After performing repetitive tasks to reduce errors, the tendon displacement for each load session was determined, with mean values ranging from 3.74 to 4.50 cm (Figure 5.4.7b).

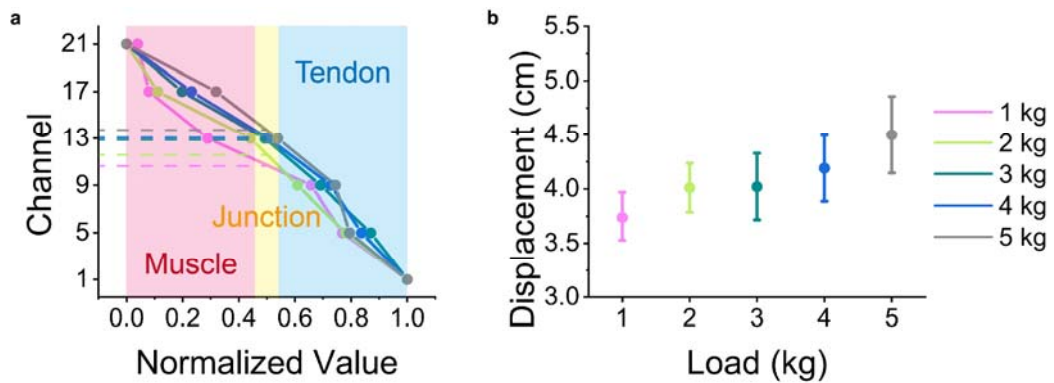


Figure 5.4.7 Muscle-tendon junction location of subject A in isometric task. **a** Plot of normalised value of mean frequencies among 6 channels. **b** Plot of tendon displacements ($n=3$ repetitive tasks for each measurement).

In the dynamic tasks, the mean frequencies of all channels in column 1 with a 5 kg load were normalized as a representative result, and the traces were smoothed to enhance clarity. It is evident that, apart from two channels at the two ends, the values of the channels in between increased during flexion, approaching the tendon range, and decreased with extension, for a total of ten cycles (Figure 5.4.8a). By employing the same determination strategy as in the isometric task, we successfully identified

the real-time movement of the muscle-tendon junction during the dynamic task. It was observed that during the initial curls, the tendon exhibited relatively stable movement. However, during the final few curls, the tendon displayed larger movements. It was speculated that this phenomenon is related to muscle fatigue. Considering that the biceps brachii must generate a similar force in each biceps curl to lift the dumbbell, the tendon may engage more as an elastic tissue to assist, especially when the muscle cannot produce the same force level due to fatigue.

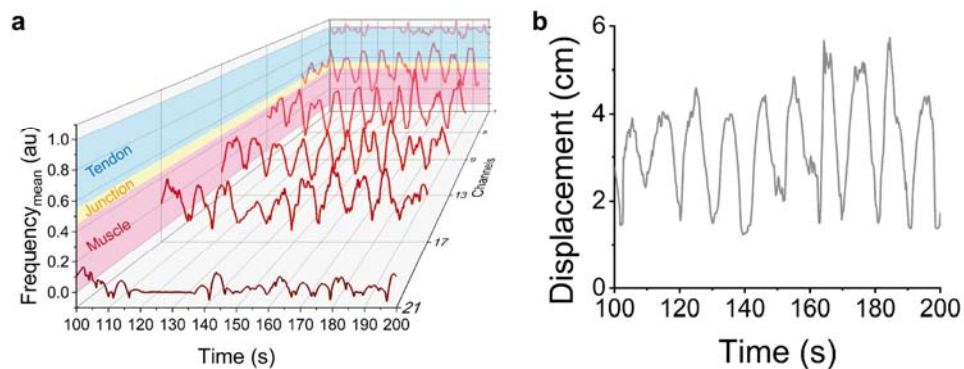


Figure 5.4.8 Muscle-tendon junction location of subject A in dynamic task. **a** Plot of normalised values of mean frequencies among 6 channels. **b** Plot of real-time monitoring of the tendon displacement in the dynamic task.

Further data analysis was conducted to explore the optimization of tendon range identification and statistical performance between different channels. For example, columns 1 and 2 exhibited the same trend in the ascending order of mean frequencies among channels. The rapid increase in mean frequencies in channels 1, 5, and 2, 6 during muscle extension was the primary reason we found the feasibility of mean frequency as a measure to identify the tendon range (Figure 5.4.9a, b). Although both columns 1 and 2 showed this trend, it is evident that column 1 displayed a larger

difference than column 2. Considering that column 1 is closest to the muscle (with the highest RMS), we ultimately decided to use the column with the highest RMS as the final column to identify the tendon location. In column 1, the majority of values of channel 21 were normalized to 0, and the majority of values of channel 1 were normalized to 1, while the values of channels 17, 13, 9, and 5 appeared in ascending order within the 0~1 range. In fact, the errors seemed to be less in column 1, as nearly all channel 21 values showed the lowest mean frequency values (Figure 5.4.9c). In contrast, in column 2, the range of channel 22 exhibited larger variability (Figure 5.4.9d). This observation may also be attributed to the anatomical shape of the muscle itself, specifically that channel 22 is positioned farther from the muscle belly.

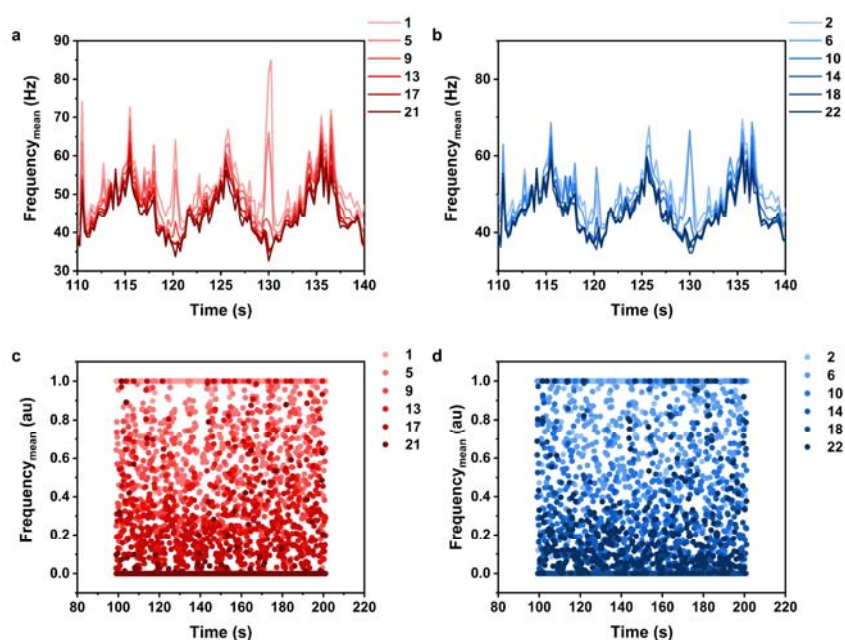


Figure 5.4.9 Mean frequencies of sEMG signals of subject A with load of 5 kg recorded by MEAP and their normalised values. a, b Mean frequencies of channels in 1st and 2nd column. Difference in mean frequencies was most obvious when the subject performed full extension during dynamic tasks **c, d** Normalised values of mean frequencies during dynamic tasks.

To explore the correlation between each channel, a scatter plot matrix with Pearson's r value was employed for assessment. In this matrix, each variable, represented by mean frequency from each channel in this case, is plotted against every other variable in the dataset, resulting in a grid of scatterplots. The Pearson's r value quantifies the strength and direction of the linear relationship between two variables, ranging from -1 (perfect negative correlation) to 1 (perfect positive correlation), with 0 indicating no linear correlation. This is a useful measure to assess the strength of correlations because higher absolute values of r indicate stronger correlations, providing a quantitative measure of the strength of the relationships.

In the isometric task, it was observed that every adjacent pair of channels had an r value over 0.9, indicating a strong correlation (Figure 5.4.10). This is natural because they are spatially close to each other and are more likely to be affected by the same region of the muscle. The r value decreased as the distance between channels increased. Two conclusions can be derived from this analysis: 1. Each TPP electrode showed similar and stable recording performances because high correlations could only be achieved when the electrode consistently recorded data; 2. The array design allowed MEAP to capture unique information from different areas of the muscle, as evidenced by the lower r values for more distant channels. These two rules not only demonstrate the reliability of TPP electrodes but also illustrate the wide range of applications for MEAP.

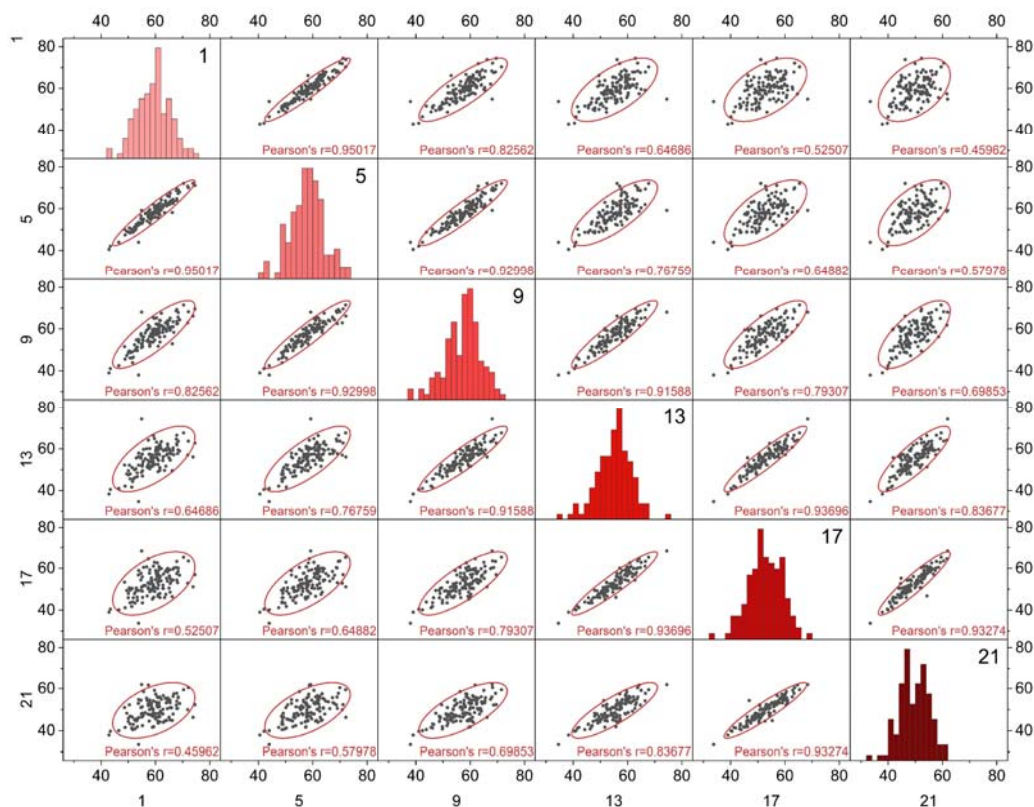


Figure 5.4.10 Scatter plot matrix of mean frequencies recorded in the 6 channels of column 1 of subject A during the isometric task.

Similar results were also observed in the dynamic task, and the two rules identified previously remain applicable (Figure 5.4.11). Another interesting phenomenon is that the r values between channels 1 and 5 are typically lower than those between channels 17 and 21, which corresponds to the correlation between the tendon region being lower than that of the muscle region. This difference is likely due to the mean frequency being primarily determined by sEMG signals from the muscle. Compared to the isometric task, the dynamic task exhibited higher variability in sEMG signal patterns. This increased variability was further amplified in the tendon region because the information recorded by the channels there was much less influenced by muscles. The unique behaviour of the tendon during dynamic

tasks may also contribute to the differences in r values between the tendon and muscle regions. Overall, these factors combine to explain the variations in correlation values between the tendon and muscle regions in dynamic tasks.

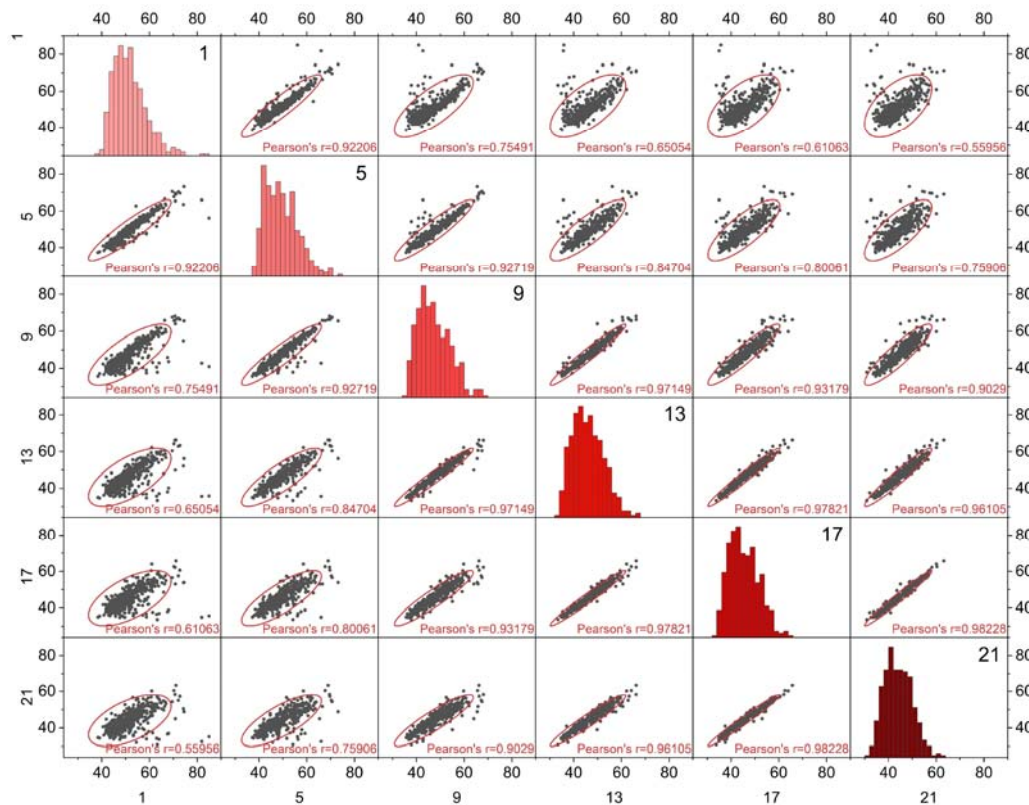


Figure 5.4.11 Scatter plot matrix of mean frequencies recorded in 6 channels of column 1 of subject A during the dynamic task.

Statistical analysis was conducted to examine the differences in mean frequencies recorded by each channel. Columns 1 and 2 were selected for comparison during the flexion by subject A (Figure 5.4.12). It was observed that in each column, when using the most proximal channels (channel 21 and 22) as controls, the distal channels exhibited significant differences. In such instances, muscle-tendon junctions should be longitudinally

distinguished between channel 17 and 13 (or channel 18 and 14). However, there was no noticeable difference between different load conditions, indicating that this measure may not be as precise as the normalized measure employed previously. Additionally, it was observed that some channels in column 2 did not show as significant differences as those in column 1. This reaffirms that the column closest to the muscle region, which is column 1 in this case, should be used for muscle-tendon junction location.

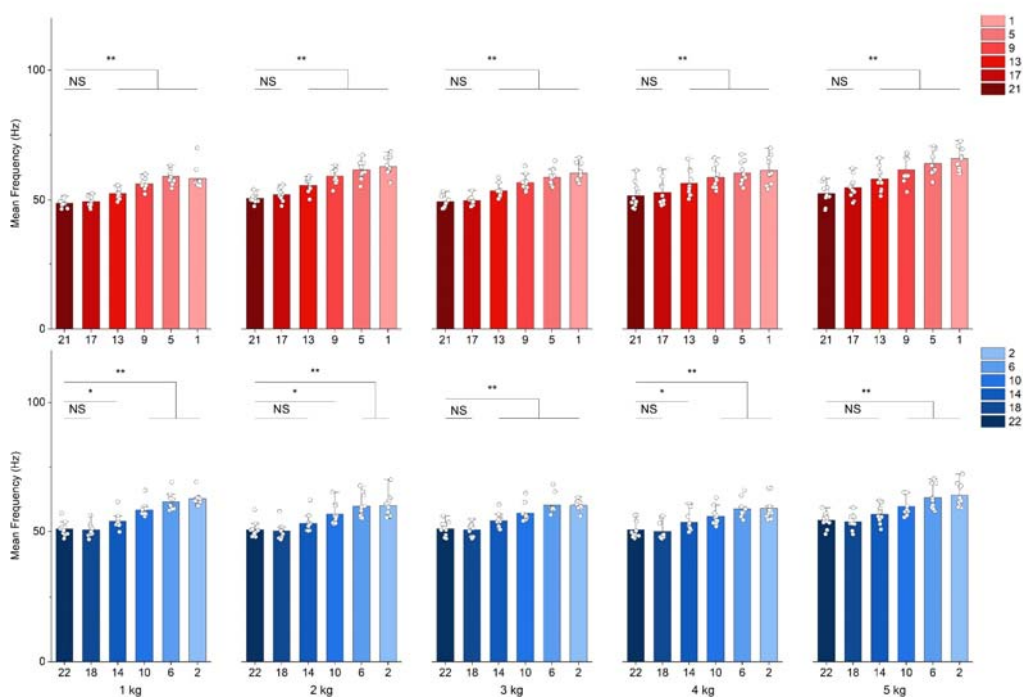


Figure 5.4.12 Statistical analysis of the differences in mean frequencies among different channels during full flexions by subject A. n=10 samples for each measurement. one-sided t test, *p < 0.05; **p < 0.01.

A similar comparison was conducted during the extension phase by subject A (Figure 5.4.13). Comparable conclusions were reached, albeit with a difference in position: In each column, when using the most proximal

channels (channel 21 and 22) as controls, the distal channels all exhibited significant differences. In such instances, muscle-tendon junctions should be longitudinally distinguished around channel 9 (or between channel 10 and 6), which are closer to the elbow compared to full flexions.

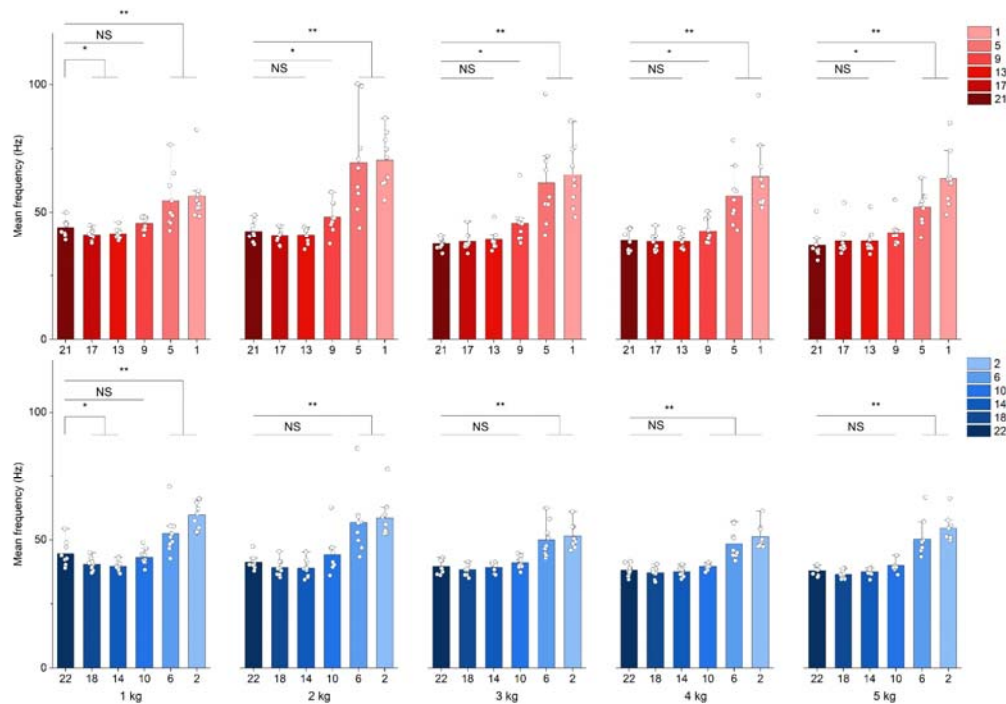


Figure 5.4.13 Statistical analysis of the differences in mean frequencies among different channels during full extensions by subject A. n=10 samples for each measurement. one-sided t test, *p < 0.05; **p < 0.01.

5.4.3 Muscle injury index

The results obtained in the previous two sections demonstrate that MEAP can provide quantitative measures such as RMS and median frequencies to help exercisers assess muscle loading and fatigue. It can also serve as a warning system, alerting exercisers to high tendon displacements during eccentric contractions to prevent injuries. To provide a more

comprehensive assessment of injury risk, we have combined RMS, fatigue slope values, and tendon displacement into a muscle injury index (Figure 5.4.14). Due to the distinct nature of isometric and dynamic tasks, the muscle injury index has been divided into two groups. RMS values were normalized based on the results obtained with a 1 kg load to create a universal frame for all exercisers. When a tendon experiences a strain of 8~10%, it is at a high risk of tearing^{123,201}. Consequently, this high-risk scenario is depicted as the red range in the muscle injury index. The other three ranges should be determined individually by exercisers under professional guidance. In the case of subject A, the loads were categorized as safe (< 3 kg), effective (3-5 kg), and vulnerable (>5 kg) based on the previous experiences of the subject.

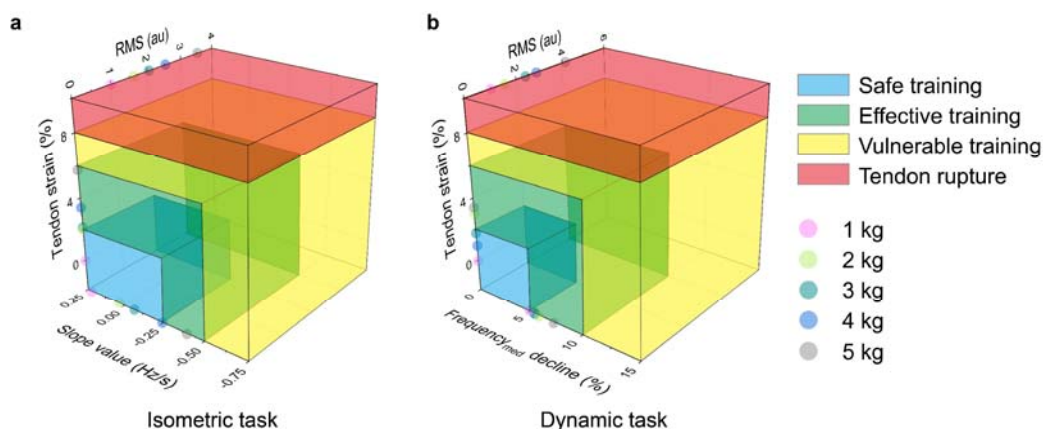


Figure 5.4.14 A visual representation of the potential for muscle injury index, generated based on the assessments made using the MEAP. The assessment is presented as a unified model using the measures obtained from Figure 5.4.3-5.4.13.

5.4.4 Statistics across different subjects

Following the successful completion of a customized injury prevention plan for subject A, it was crucial to confirm that MEAP had the ability to provide

similar evaluations for other individuals. In this context, the data was statistically analysed to ensure that each channel on the MEAP recorded distinct sEMG information from the muscle. It is important to note that RMS amplitudes can vary significantly among individuals even when performing the same task with the same recording conditions. To address this, all RMS data was normalized based on the respective highest values for comparison. Efforts were made to ensure that the MEAP was attached to comparable positions on each individual, as variations in attachment could lead to significant differences in results across subjects, particularly concerning muscle-tendon location.

Upon attaching the MEAP with channel 21 closest to the muscle region, consistent activation patterns were observed in the biceps muscle across five different subjects (Figure 5.4.15a). RMS values exhibited a decrease both along the longitudinal and horizontal directions. When using channel 21 as the control, all channels except 22 showed significant differences. The similarity observed between channels 21 and 22 might be attributed to errors in attachment or differences in individual sizes. While the structure and configuration of all MEAPs are consistent, individuals with larger biceps brachii may have two channels attached to the most activated region of the muscle, while those with smaller biceps brachii may have only one channel in that position. This underscores the importance of customized analysis for each subject due to individual variations.

Furthermore, it is worth noting that the variability of data increases as the distance between the recording channel and the control channel grows, as

indicated by the distributions (Figure 5.4.15b). This phenomenon can be primarily attributed to variations in muscle length among subjects. With the same IED, the channel on the distal end of the MEAP for subjects with smaller muscles may be farther from the muscle region than in subjects with larger muscles. These results affirm that each channel on the MEAP recorded distinct sEMG information from the muscle, demonstrating the consistent recording performance of MEAP across different individuals.

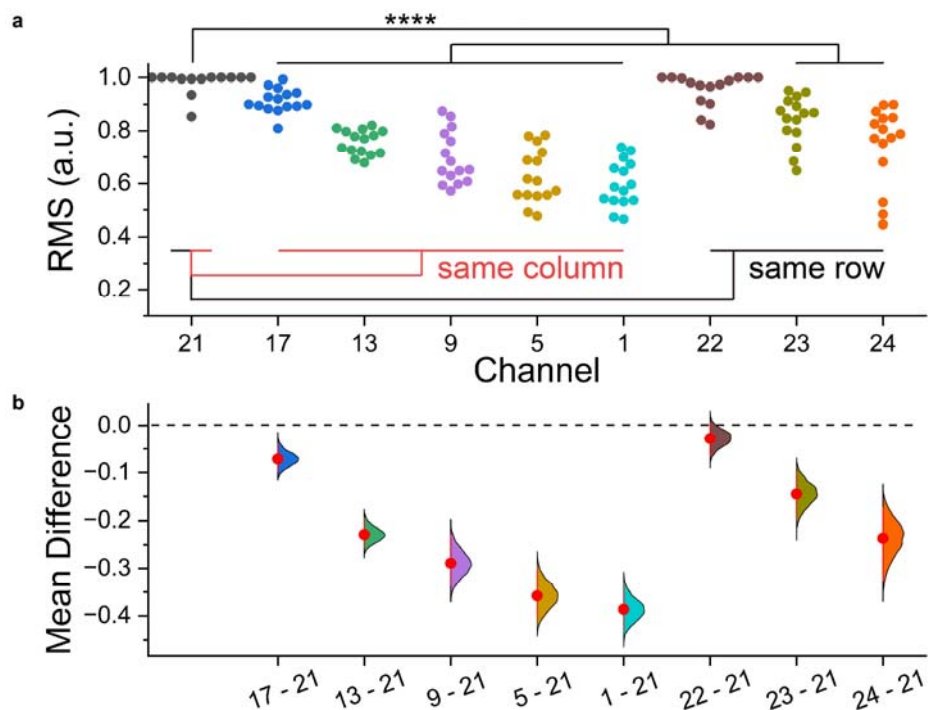


Figure 5.4.15 The Gardner-Altman of sEMG signals recorded by MEAP on different subjects. **a** The swarm plot of all RMS values of sEMG signals captured by MEAPs ($n=15$, 3 repeated isometric tasks performed by 5 subjects, different MEAPs used). The RMS values are normalised to their respective maximum values, and channel 21 (control) is compared with others. Significance was determined by one-side t test (* $P < 0.05$; ** $P < 0.01$; *** $P < 0.001$; **** $P < 0.0001$). **b** The mean difference plot of RMS values recorded by each channel, with mean presented as red dots, 0.95 confidence interval presented as red line, and Kernel Smooth used for distributions.

All results recorded from subjects B and C were summarized. Every rule

established previously in subject A was found to be applicable for subjects B and C as well. In the case of subject B, column 2 was selected as the one closest to the muscle region (Figure 5.4.16). The rapid increase in dynamic tasks exhibited a clear signal for muscle fatigue, which was also confirmed by median frequency results, indicating that subject B experienced muscle fatigue when the load exceeded 2 kg. The displacement of the tendon in the isometric task was also measured, ranging from 3.64 to 4.55 cm.

For subject C, column 2 was also selected as the one closest to the muscle region (Figure 5.4.17). The rapid increase in dynamic tasks revealed a clear signal for muscle fatigue, which was further confirmed by median frequency results, showing that subject C experienced muscle fatigue when the load exceeded 3 kg. The displacement of the tendon in the isometric task was also measured, ranging from 3.50 to 4.49 cm. Notably, the tendon displacement for 1 kg was greater than for 2 kg, which might be influenced by the inadequate accuracy or completeness of the task performed by subject C.

These results serve as clear evidence that MEAP successfully provided information about muscle loading, muscle fatigue, and tendon displacement for the other subjects, thus confirming the stable and reliable recording capability of MEAP across all individuals.

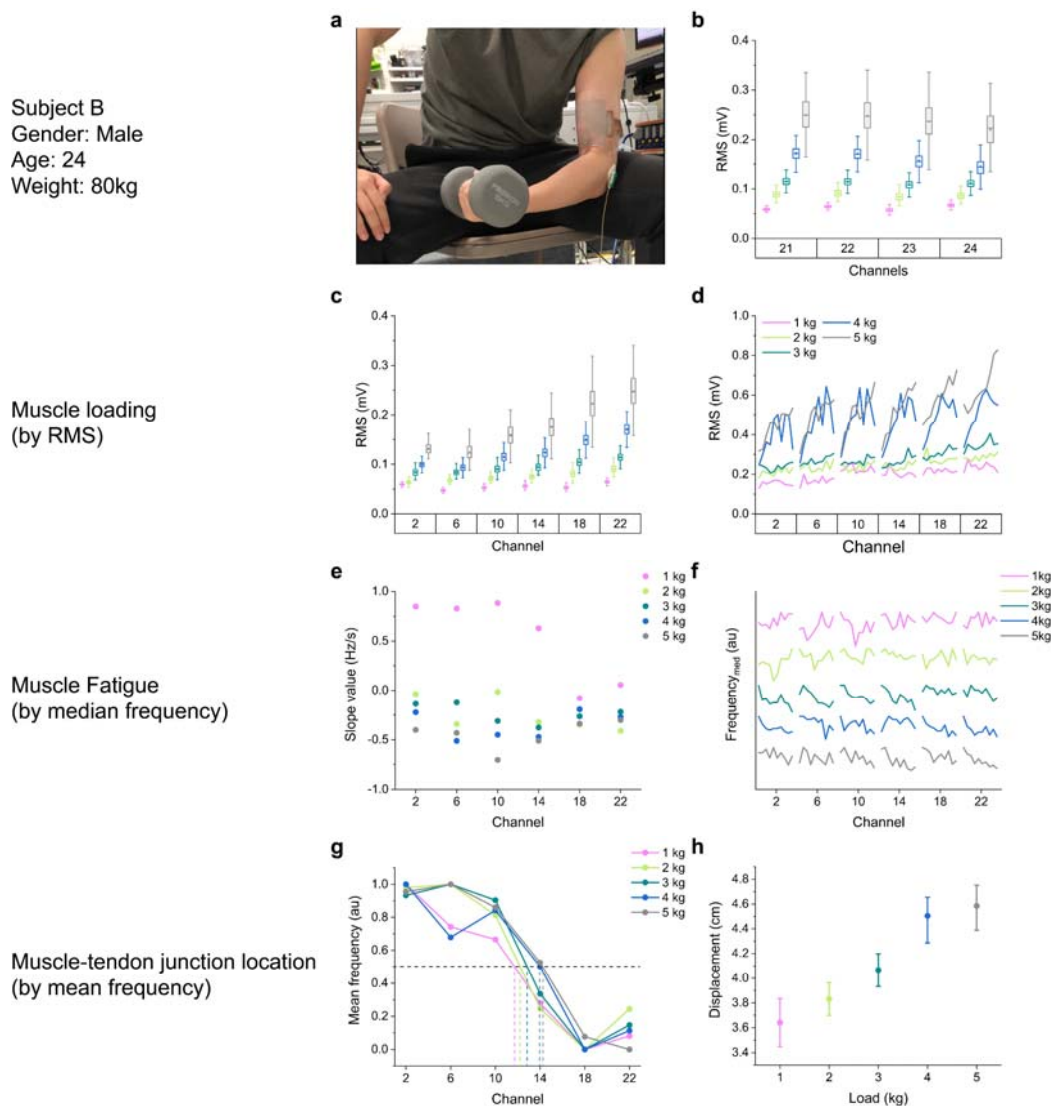


Figure 5.4.16 Results of muscle information recorded by MEAP of the task carried by subject B. **a** A photograph of subject B during the task. **b** RMS results of channels in the last row which is closest to the muscle belly of the biceps brachii. Channel 22 showed the highest RMS value, which therefore, made the second column be selected for identification of different muscle information. **c, d** RMS values of sEMG signals in isometric task and in dynamic task, respectively. **e, f** Median frequencies of sEMG signals in isometric task and in dynamic task, respectively. **g, h** Plots of normalised value of mean frequencies among 6 channels and tendon displacements in the isometric task.

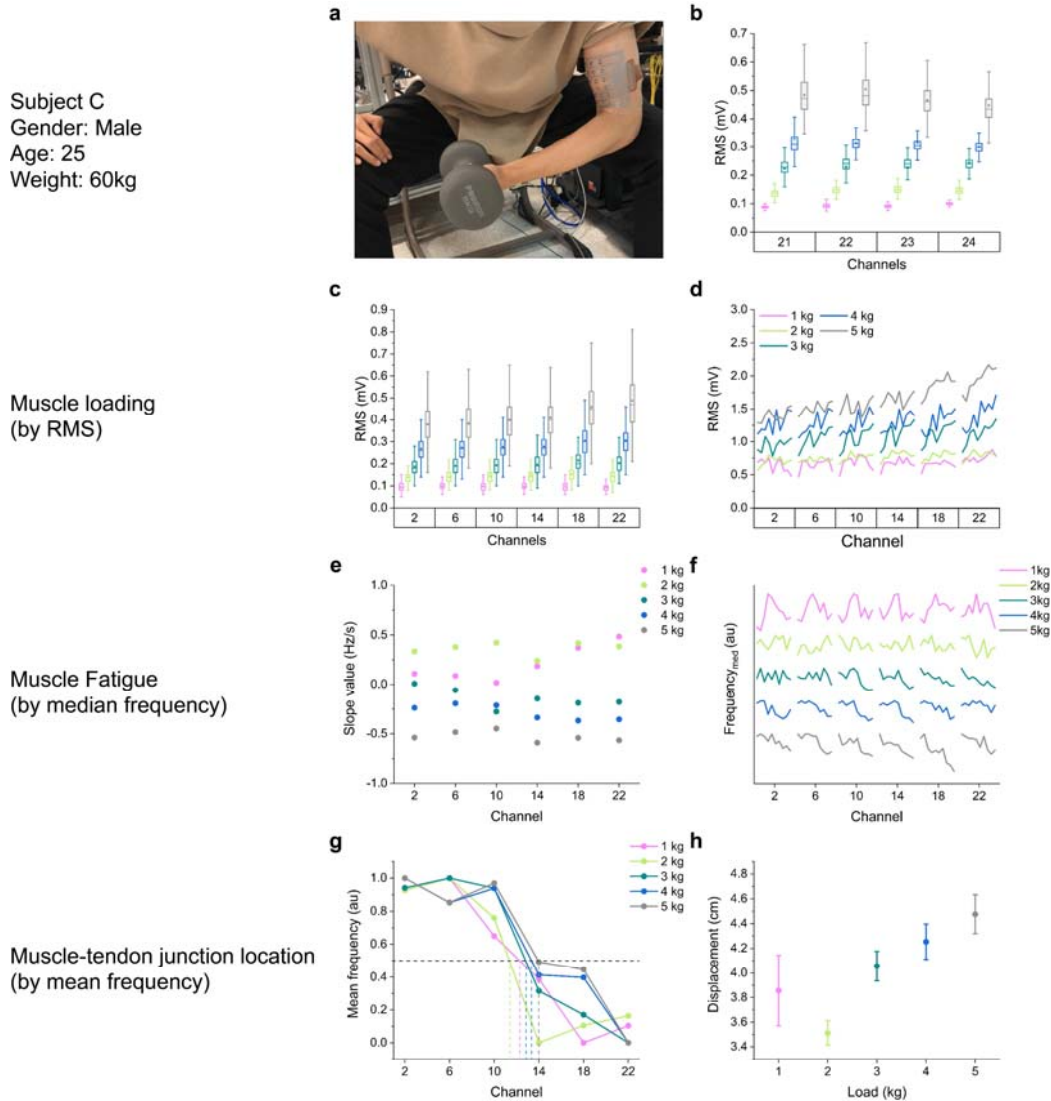


Figure 5.4.17 Results of muscle information recorded by MEAP of the task carried by subject C. a A photograph of subject C during the task. **b** RMS results of channels in the last row which is closest to the muscle belly of the biceps brachii. Channel 22 showed the highest RMS value, which therefore, made the second column be selected for identification of different muscle information. **c, d** RMS values of sEMG signals in isometric task and in dynamic task, respectively. **e, f** Median frequencies of sEMG signals in isometric task and in dynamic task, respectively. **g, h** Plots of normalised value of mean frequencies among 6 channels and tendon displacements in the isometric task.

5.5 Conclusions

By applying MEAPs to biceps brachii and abductor pollicis brevis, it has been demonstrated that MEAPs with high spatial and temporal resolution can accurately capture muscle recruitment and length changes during contractions. This capability has a wide range of applications, from clinical diagnostics and rehabilitation to sports performance analysis and human-machine interface development.

Additionally, by applying MEAPs to the biceps distal tendon and Achilles tendon, it has been shown that MEAP can monitor muscle-tendon junction locations in real-time during isometric and dynamic tasks, across different muscles. This capability is crucial for controlling tendon stretch within a safe range during exercise, reducing the risk of injury for exercisers.

Furthermore, based on the ability to obtain information about muscle loading, fatigue, and muscle-tendon junctions, MEAP can generate a muscle injury index for exercise guidance, improving training effectiveness and injury prevention. Its consistent recording performance across different subjects enhances its potential for future commercialization, making MEAP a valuable tool for promoting the widespread use of sEMG technology.

Chapter 6

Use of MEAP for electrodiagnostic

6.1 Introduction

Electrodiagnostic is a specialized medical field dedicated to assessing the electrical activity of muscles and nerves within the human body. These diagnostic tests are crucial for evaluating the health, integrity, and function of the neuromuscular system. Electrodiagnostic studies play a key role in diagnosing and monitoring various neurological and neuromuscular conditions.

The primary objective of an electrodiagnostic study is to localize the disorder. In most cases, the initial step in localization involves identifying the nature of the disorder, which can be categorized as neuropathic, myopathic, related to neuromuscular junction (NMJ) transmission, or associated with the central nervous system (CNS) (Figure 6.1.1). Once the disorder is localized, the differential diagnosis process becomes more focused, helping to narrow down the potential conditions.

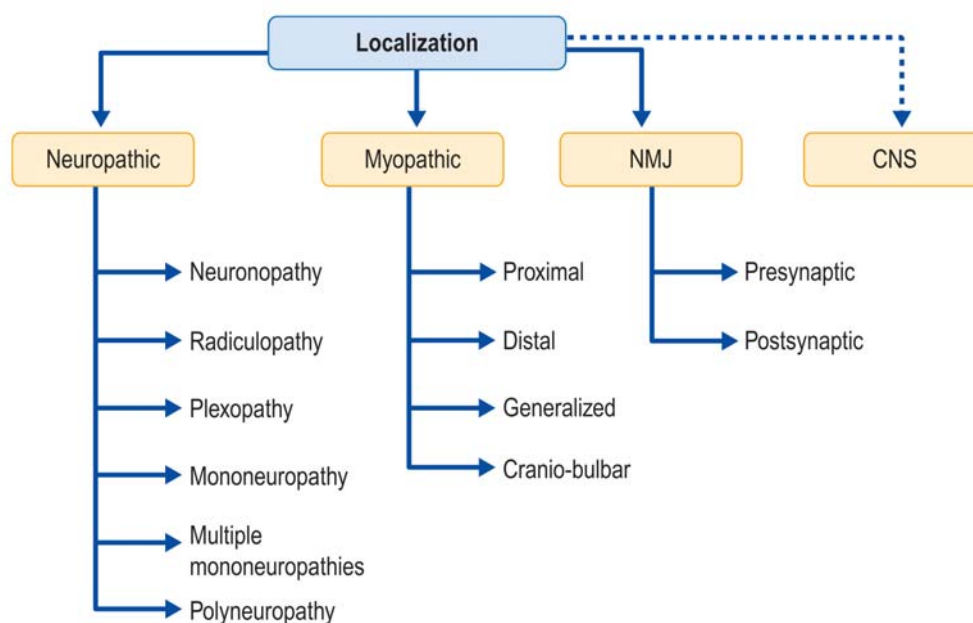


Figure 6.1.1 Possible localizations determined from the electrodiagnostic study. Adapted from *Electromyography and Neuromuscular Disorders. Electromyography and Neuromuscular Disorders: Clinical-Electrophysiologic Correlations: Third Edition* (Elsevier, 2013).

Electrodiagnostic studies require clinicians to meticulously attend to technical details while keeping the overall diagnostic objective in mind. As data is collected, real-time analysis becomes essential, allowing for necessary adjustments to narrow down potential conditions. This dynamic approach is crucial for accurate diagnosis. It is worth noting that once the patient leaves the clinic, diagnosis becomes impossible, as current instruments are designed for in-clinic use and are not suitable for long-term recording. As a result, the development of a tool capable of long-term wireless recording could represent a significant advancement in this field.

The two primary types of electrodiagnostic tests are needle EMG and nerve conduction studies (NCS). NCS measures the speed and strength of

electrical impulses along peripheral nerves, while needle EMG involves inserting fine needles into specific muscles to record and analyse their electrical activity both at rest and during contraction.

In the context of needle EMG, it serves as a powerful tool for examining the intricate activity within muscles, offering high-quality signal data. One of the pivotal steps in needle EMG is the analysis of motor unit action potentials (MUAPs). These MUAPs typically exhibit amplitudes below 2 mV, durations ranging from 10 to 5 ms, and consist of 3 to 4 phases²⁰². Notably, neuropathy, myopathy, disorders of NMJ or the CNS system display distinctive features within MUAPs, providing valuable insights for disorder localization.

For instance, it is common to employ needle EMG on thenar muscles, particularly the APB (Figure 6.1.2). APB is considered the most suitable median muscle for sampling distal to the carpal tunnel. The procedure involves the tangential insertion of a needle into the lateral thenar eminence, just lateral to the midpoint of the first metacarpal⁸. The patient is instructed to abduct the thumb with the arm and hand in a supinated position to activate the APB. Upon slight contraction, MUAPs become clearly observable. These MUAPs can be categorized and classified using specialized instrumentation, resulting in averaged final waveforms representing activities from different motor units. Parameters such as amplitude, duration, rise time, and rate can be analysed and compared with established standards to localize specific disorders.

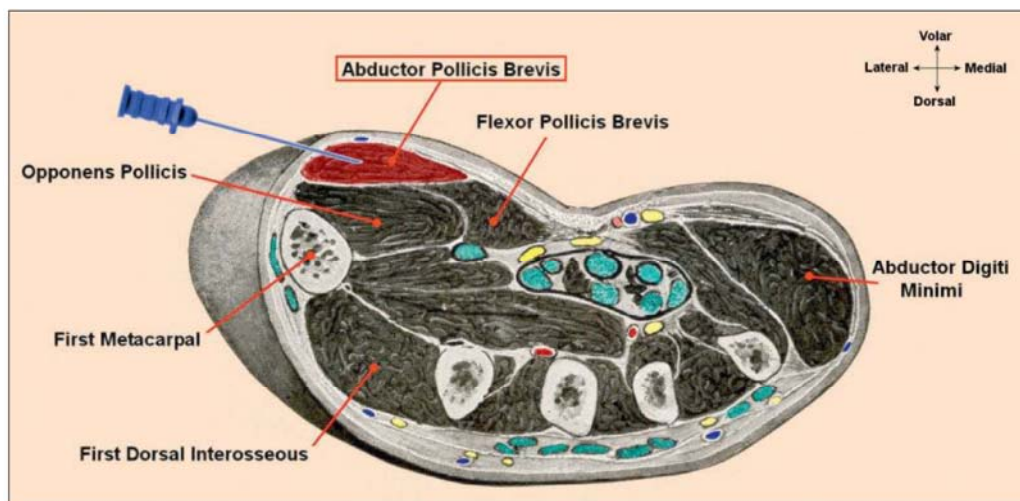


Figure 6.1.2 Cross-section anatomy and abductor pollicis brevis insertion point. Adapted from *Electromyography and Neuromuscular Disorders. Electromyography and Neuromuscular Disorders: Clinical-Electrophysiologic Correlations: Third Edition* (Elsevier, 2013).

However, it is worth noting that sampling the APB is usually perceived as more painful compared to other intrinsic hand muscles. In light of this, a non-invasive tool capable of replicating MUAP identification would significantly enhance patient comfort during diagnostic procedures. The MEAP shows promise in this regard because of its refined and high-quality recording capabilities, attributed to its high-density design and stretchable features. Moreover, considering the capability of MEAP for long-term recording, it opens up the possibility of conducting at-home diagnostic assessments. Therefore, my aim is to explore the potential of employing MEAP for electrodiagnostic purposes by recording EMG signals from APB and compare them with those recorded by needle electrode. Noted that MEAP with substrate of TPU is used in this section.

6.2 Comparison of EMG signals recorded by needle and MEAP

To demonstrate the feasibility of using MEAP for electrodiagnostics, the ability to capture MUAPs is crucial. To validate this, a clinician conducted the pilot tests that we describe here. Recordings were made from the APB using an MEAP while simultaneously recording with a standard needle EMG electrode (Figure 6.2.1). The 24-channel MEAP provided ample recording space to collect various MUAPs. Rows and columns were labelled with numbers and alphabets to provide precise location references. The needle electrode was consistently inserted between two adjacent MEAP channels, and bipolar recordings between these two channels were collected for comparison with the needle recordings. This ensured that the recording areas of both tools were as close as possible. The subject was instructed to make the slightest possible contraction of the APB to activate only one motor unit, facilitating a better comparison between the needle and MEAP recordings.

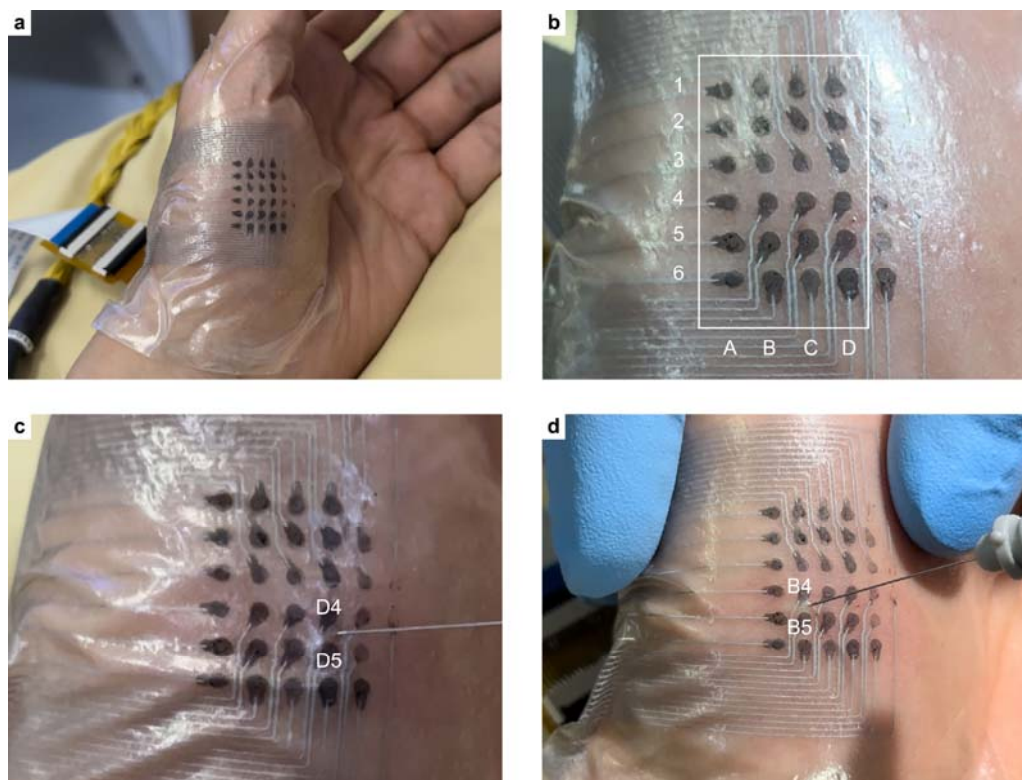


Figure 6.2.1 Recording configuration of MEAP and needle on APB. a Photograph of MEAP on APB. **b** The arrangement of the channels on MEAP. **c** Photograph of needle recording at D4-D5. **d** Photograph of needle recording at B4-B5.

6.2.1 Recording summary

Five trials were conducted at different locations on the APB muscle. The clinical diagnostic instrument used has an auto-sorting function that can differentiate signals from each motor unit and classify them accordingly. Three important parameters, namely rate, amplitude, and duration, were summarized in Table 6.2.1. It is evident that the amplitude of MUAPs recorded by MEAP was significantly smaller than those recorded by the needle electrode. This difference is expected because the amplitude depends on the distance between the recording area and the signal source. Compared to the inserted needle tip, MEAP records only from the surface

of the skin, resulting in a greater distance between the electrode and the signal source. This presents both advantages and disadvantages – it is non-invasive but may lose some information due to changes in MUAPs. However, for electrodiagnostics, amplitude serves as a reference, and the firing rate and duration hold greater significance for clinicians in localizing disorders. In this context, a comparison of the firing rates of the MUAPs recorded by both tools confirmed that their origin was from the same motor unit. Then, the durations of MUAPs recorded by the two tools were compared to explore potential similarities between them.

| Trial | Recording location | Motor unit | Rate (Hz) | | Amplitude (μV) | | Duration (ms) | |
|-------|--------------------|------------|-----------|------|-----------------------------|-------|---------------|--------------|
| | | | Needle | MEAP | Needle | MEAP | Needle | MEAP |
| 1 | D4-D5 | 1 | 10 | 10 | 1133.7 | 432.2 | 7.5 | 9.3 |
| | | 2 | 13 | 12 | 377.5 | 226.6 | 5.5 | 7.1 |
| | | 3 | 11 | 1 | 673.7 | 434.3 | 6.4 | 9.7 |
| 2 | D5-D6 | 1 | 13 | 2 | 432.6 | 355.9 | 5.9 | 6.1 |
| 3 | B4-B5 | 1 | 27 | 25 | 1199.1 | 132.6 | 5.3 | 4.7 |
| | | 2 | 12 | 23 | 832.4 | 92.8 | 5.2 | 4.9 |
| 4 | B4-B5 | 1 | 18 | 22 | 1163.8 | 89.3 | 5.0 | 3.7 |
| | | 2 | - | 8 | - | 102.6 | - | 5.8 |
| | | 3 | - | 6 | - | 147.0 | - | 5.3 |
| 5 | C2-C3 | 1 | 36 | 32 | 975.9 | 131.6 | 5.4 | 4.2 (6.3) |

Table 6.2.1 The summary of parameters of MUAPs recorded by needle and MEAP. The number in bracket in the last cell represents an alternative result proposed by the author.

6.2.2 Trial 1

The raster plot of firing rate provides strong evidence that the MUAPs

recorded by both tools originated from the same motor unit, with simultaneous bursts observed except for one instance marked by a red rectangle (Figure 6.2.2a). This sorting discrepancy is potentially the result of system error due to the noise present in the MEAP recording. This firing pattern consistency across different motor units further supports the confirmation of identical MUAPs. Upon comparing the shape of MUAPs, it was evident that the MUAPs recorded by MEAP exhibited a much smoother profile in contrast to those recorded by the needle electrode (Figure 6.2.2b). This phenomenon can be attributed to the subcutaneous fat layer acting as a filter, increasing the distance between the electrode and the source. Consequently, this low-pass filtering smooths the MUAP, resulting in a reduction in surface EMG amplitude.

Regarding the duration of MUAPs, the needle-recorded duration was approximately 7.5 ms, whereas the MEAP-recorded duration was approximately 9.3 ms. It is worth noting that the MEAP-recorded duration, particularly in the rising time portion, was longer. The influence of the skin should also be considered in the context of duration measurements. Additionally, it is important to acknowledge that MUAP duration measurements may involve some degree of error because they can currently only be determined by a clinician.

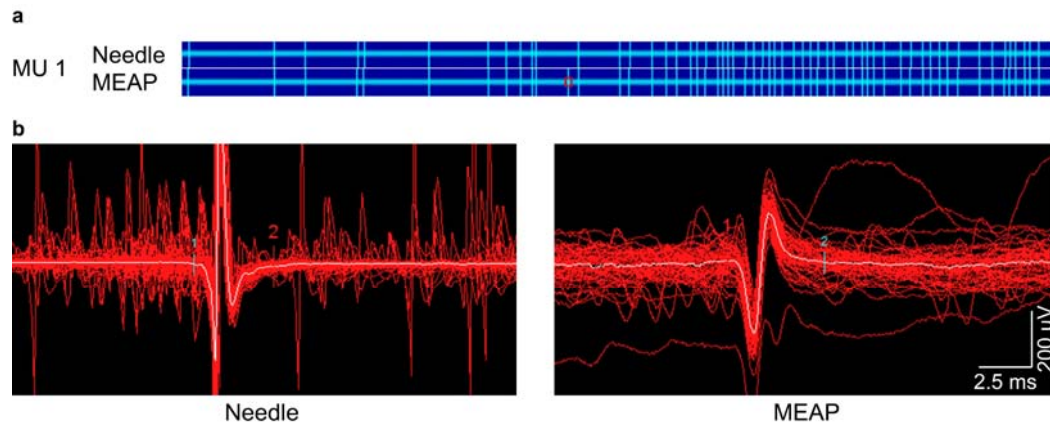


Figure 6.2.2 MUAP from motor unit 1 in trial 1. a Raster plot of firing of the MUAP. The red marker showed the only difference. **b** Averaged MUAP by needle and MEAP.

6.2.3 Trial 5

Another matching result is from trial 5. According to the raster plot, it can be observed that most of the firing patterns match, although there are some bursts missing in the raster plot recorded by MEAP (Figure 6.2.3a). This is possibly because of noise effects, which can lead to errors in the sorting function performed by the system. However, considering that most the bursts appeared at the same time, it is still evident that they originate from the same motor unit. This is the second instance in which MEAP has recorded the MUAP from the same motor unit as the needle. This indicates that MEAP has the capability to record single motor unit signals, similar to the needle electrode. Consequently, MEAP shows great potential for continued use in exploring non-invasive recording for clinical electrodiagnostics.

Regarding the duration of MUAPs, the duration recorded by the needle

electrode was approximately 5.4 ms, while the duration recorded by MEAP was approximately 4.2 ms. It is worth noting that the second duration determination was also conducted by the clinician, and the second marker might have been chosen differently by the author, possibly aligning more accurately with the negative peak (Figure 6.2.3b). In that case, the duration for MEAP should be around 6.3 ms. In this context, when comparing the duration of the MUAP recorded using the MEAP and the needle electrode in trials 1 and 5, it was observed that both recordings using the MEAP had a longer duration. Specifically, the duration was 1.24 times longer for trial 1 and 1.17 times longer for trial 5 when using the MEAP compared to the needle electrode.

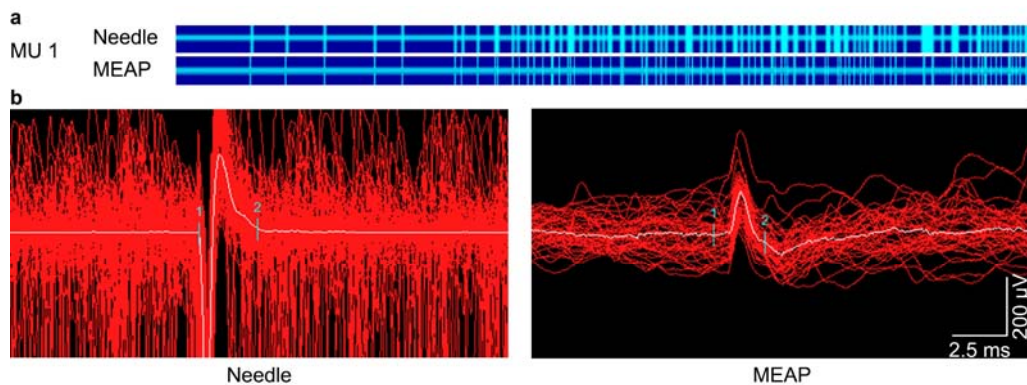


Figure 6.2.3 MUAP from motor unit 1 in trial 5. a Raster plot of firing of the MUAP. The red marker showed the only difference. **b** Averaged MUAP by needle and MEAP.

6.3 Conclusions

This pilot study demonstrated that MEAP successfully recorded single MUAPs from the same motor unit as the needle electrode. This finding strongly suggests that MEAP has the potential to further explore non-

invasive electrodiagnostic techniques. In terms of MUAP duration, a critical parameter for clinicians in the diagnostic process, MEAP recordings exhibited longer durations compared to the needle electrode, albeit with a similar ratio. This observation could serve as a valuable pattern for future investigations. While additional tests and trials are necessary to establish a robust and validated set of rules, this pilot study underscores the considerable promise of MEAP as a potential replacement for invasive needle electrodes in the future.

Chapter 7

General discussion

7.1 Material selection for developing dry electrode

When addressing the limitations of current Ag/AgCl sEMG electrodes, the first challenge is selecting the appropriate material for the new dry electrode. Conductivity is a fundamental requirement, limiting the choices to four main categories: metals, carbon materials, hydrogels, and conductive polymers. Regular metals, except for LM, lack stretchability unless specially structured, and achieving adhesiveness on metal surfaces is challenging due to their high surface energy. Carbon materials, like carbon nanotubes and graphene, have a high Young's modulus, making them unsuitable for bioelectronics¹⁴¹. Compared to them, LM offers unique properties such as easy shaping within various matrices, good stretchability when combined with elastomers, and the ability to form island topographies on the skin, enhancing adhesiveness when integrated with adhesive elastomers. However, liquid metal poses leakage issues when applied directly to the skin, making it less ideal for long-term electrophysiological recordings.

Conversely, the use of hydrogels and conductive polymers that can be tailored to specific requirements becomes a favourable strategy. These materials can be customized to provide specific functionalities based on different application scenarios. However, it is challenging to create a material that excels in every aspect. Enhancing one property may come at

the expense of another. For example, hydrogels contain a lot of water but dehydrate quickly, while making conductive polymers more stretchable often reduces their conductivity.

To address the durability issue of current Ag/AgCl gel electrodes, we decided to explore the use of conductive polymers and ultimately developed TPP electrodes. While TPP electrodes exhibited many satisfactory performances, the trade-off issue mentioned earlier was not fully resolved for TPP, as demonstrated in Chapter 3.2.2. This issue may be addressed in the future by tuning the formation of material or adjusting the microstructure to achieve desirable characteristics simultaneously.

In essence, selecting materials for dry sEMG electrodes presents a multidimensional challenge that goes beyond simple conductivity. It requires striking a delicate balance between mechanical properties, electrical performance, durability, and user comfort. It is necessary to consider the unique demands of their applications and prepare to manage trade-offs according to specific requirements. Establishing clear performance metrics tailored to the needs of sEMG applications can be helpful. These metrics may include parameters such as modulus of elasticity, impedance, adhesiveness, and baseline noise. Objective evaluation and comparison of different materials can be conducted based on these metrics.

7.2 Wireless recording for MEAP

While MEAP has demonstrated excellent performance in providing muscle and tendon information for injury prevention, the next crucial step is to upgrade the recording system to a wireless device. Carrying a bulky amplifier with a cable for MEAP connection is impractical for users. Although the development of a lightweight, portable, and high-SNR amplifier is beyond the scope of this thesis, there are still important issues to consider regarding the sEMG array. One key challenge is ensuring stable recording during potentially strenuous movements by exercisers. The stability here does not refer to the attachment of MEAP to the skin but rather concerns the phenomenon known as the "cable swing artifact." This artifact is an interference phenomenon caused by cable motion, often induced by mechanical vibrations. Cable swing artifacts can introduce significant noise into recorded signals, potentially providing misleading information thus impeding accurate signal analysis.

To mitigate this artifact, it is crucial to minimize the length of the cable transmitting analogue current to digital signals. This is because the cable swing artifact affect less when the analogue current is converted to digital as early as possible in the signal path. Even in wireless recording setups, cable swing artifacts can still occur since analogue current transmission is inherent in sEMG recording. Therefore, the focus should be on shortening the cables as much as possible.

When using MEAP, achieving this requires improved design for the LM circuit section. Additionally, the amplifier should be affixed to a part of the

body that experiences minimal movement to reduce the artifact. This may necessitate customized positioning for each specific muscle group. For instance, when recording arm muscles, place the amplifier near the elbow joint; when recording pectoralis, place the amplifier near the clavicle.

Another concern arises when multiple muscles need to be recorded simultaneously to analyse muscle synergy. In such cases, multiple MEAPs may be deployed, and they may not be located close to each other. Given the cable swing effect, it is advisable for each MEAP to have its dedicated amplifier. Multiple amplifiers pose higher requirements for wireless data transmission, especially considering that sEMG typically requires a sampling frequency of over 1000 Hz, and MEAPs have multiple channels.

Addressing these challenges related to front-end processing is essential to provide MEAP with a suitable platform for stable and high-quality sEMG signal acquisition in the future.

7.3 Minimizing the influence of skin deformation on MEAP recordings

It may raise concerns that the stretchable MEAP may not provide accurate tendon location due to the apparent variation in IED during skin deformation. However, it was found that the changing IEDs will not impact junction detection when employing the normalizing technique. Given that the junction should consistently be situated between two neighbouring electrode sites, a numerical value of 0.5 can be employed to determine

which two channels are involved. Consequently, the relative position of the muscle-tendon junction to the MEAP can always be ascertained, as long as the junction remains within the recording range of the MEAP. Regarding the absolute numerical value of tendon displacement, a thoroughly investigation of this issue and computational adjustments to minimize its impact have been provided below.

The IEDs between neighbouring channels at the muscle-tendon junction of the distal biceps tendon were measured when biceps brachii was in different states (Table 7.3.1).

| Flexion degree | IED ₂₁₋₁₇ (mm) | IED ₁₇₋₁₃ (mm) | IED ₁₃₋₉ (mm) | IED ₉₋₅ (mm) | IED ₅₋₁ (mm) |
|----------------|---------------------------|---------------------------|--------------------------|-------------------------|-------------------------|
| 30° | 15 mm | 15 mm | 15 mm | 15 mm | 15 mm |
| 0° | 15 mm | 15 mm | 16 mm | 18 mm | 18 mm |
| 110° | 15 mm | 15 mm | 14 mm | 13 mm | 12 mm |

Table 7.3.1 IED between adjacent channels when biceps brachii is relaxed, fully extended and fully flexed.

Since TPP electrodes are sticky and can adhere securely to the skin, the IED change is the same as skin deformation between two nearby electrodes. IEDs were evaluated in three distinct arm states: full extension (0°), full flexion (110°), and relax (30°). When the array was bonded to the skin during arm relaxation, the IEDs were all 15 mm. it was discovered that when the muscle is moving, the deformations of skin on the muscle part are not obvious.

For example, it is assumed the junction is right in the middle between channels 5 and 1 when the muscle is in full extension.

The calculated distance between junction and channel 21 is $D_{ce} = IED_{21-17}(30^\circ) + IED_{17-13}(30^\circ) + IED_{13-9}(30^\circ) + IED_{9-5}(30^\circ) + 1/2 IED_{5-1}(30^\circ)$;

the realistic distance between junction and channel 21 is $D_{re} = IED_{21-17}(0^\circ) + IED_{17-13}(0^\circ) + IED_{13-9}(0^\circ) + IED_{9-5}(0^\circ) + 1/2 IED_{5-1}(0^\circ)$.

When the junction is right in the middle between channel 13 and 17 when in full flexion,

the calculated distance between junction and channel 21 is $D_{cf} = IED_{21-17}(30^\circ) + 1/2 IED_{17-13}(30^\circ)$;

the realistic distance between junction and channel 21 is $D_{rf} = IED_{21-17}(110^\circ) + 1/2 IED_{17-13}(110^\circ)$.

Considering the absolute displacement D_a of channel 21 between flexion and extension in the space,

then the calculated displacement is $D_{ce} - D_{cf} + D_a = 1/2 IED_{17-13}(30^\circ) + IED_{13-9}(30^\circ) + IED_{9-5}(30^\circ) + 1/2 IED_{5-1}(30^\circ) + D_a$;

the realistic displacement is $D_{re} - D_{rf} + D_a = 1/2 IED_{17-13}(0^\circ) + IED_{13-9}(0^\circ) + IED_{9-5}(0^\circ) + 1/2 IED_{5-1}(0^\circ) + D_a$;

The reason we choose distance between junction and channel 21 instead of channel 1 is that we found $D_a(21) \approx 0$ mm, while $D_a(1) \approx 40$ mm.

Calculating from the muscle end can therefore reduce the effect of significant skin distortion.

Hence, the calculated displacement is 45 mm, while the actual displacement is 50.5 mm. The discrepancy is approximately 10%, which is considered acceptable. This impact of skin deformation is currently only observed in the case of biceps brachii. No significant skin deformation was

noted during flexion and extension for Achilles tendon identification; therefore, this influence is not a concern in that context.

Another factor affecting the impact of skin deformation is the body fat percentage of the individuals. In the case of Subject A, whose body fat percentage is approximately 20%, there were not many observed skin deformations. However, for individuals with body fat percentages of less than 15% or even 10%, skin deformation can lead to significant changes in IEDs and a greater risk of non-conformal electrodes detaching. In such cases, a stretchable electrode array becomes more valuable and relevant, especially when combined with a strain sensor on the patch. This integrated approach can monitor and mitigate the influence of skin deformation, ensuring more accurate and stable electrode performance. The use of multiple sensors in this manner can provide comprehensive and precise data for analysis.

7.4 Unlocking new frontiers in prosthetics and exoskeletons with MEAP

The deepest aspiration for amputees has always been the hope of regaining their lost limbs. While regenerative medicine has made remarkable progress, prosthetics remain a commonly adopted solution. However, these prosthetic devices, in their current state, offer only limited degrees of freedom (DoF). Consider hand prosthetics as an example; most available devices can merely perform basic gripping functions, offering users a single DoF. This limitation becomes evident when we think about

the intricate gestures our natural hands can execute. Clearly, these prosthetics are not fully equipped to meet the diverse and complex needs of their users.

One main reason for this is traditional prosthetic devices operate on mechanical force or strain sensors, typically controlled by other parts of the body, such as a pump in the armpit. To perform a basic grasping motion, users must use their arm to activate the pump. While this mechanism can adequately handle tasks suited for single-DoF prosthetics, it falls short when it comes to more complex, multi-DoF tasks. The limited control points restrict the execution of intricate hand movements, and users must rely on a cumbersome and often uncomfortable learning process.

In addition, the varied mechanisms used in different prosthetic devices further compound the learning curve. Some prosthetics require arm movements to operate, while others necessitate isometric contractions of the biceps for gripping. Adapting to these disparate control methods can be time-consuming and frustrating for users, who are essentially asked to issue commands to a different part of their body when they are trying to move their hand. This presents a considerable challenge in achieving seamless integration of prosthetics into daily lives of users.

Fortunately, using multi-channel sEMG as the driving mode for prosthetics can solve all issues above, since the movements of the hand and fingers are primarily governed by forearm muscles. For amputees who still possess forearms, a multi-channel sEMG array, exemplified by MEAP, has the ability to capture real-time muscle activity. Through advanced data

analysis techniques, including deep learning, these muscle activity patterns can be deciphered and utilized as input for prosthetic devices. The result is a significant expansion in the number of DoF that can be achieved. Moreover, the high-density sEMG recording offered by MEAP effectively captures individual muscle activities on the forearm without crosstalk, significantly enhancing gesture classification accuracy.

Another advantage of this approach lies in the fact that users issue commands to their forearm muscles directly when performing specific hand tasks. As a result, the extensive relearning process required by other prosthetic devices becomes unnecessary. This seamless transition empowers users to operate prosthetics without the burden of time-consuming adjustments, enabling them to regain a more natural sense of control.

To realize the sEMG driven mode for prosthetics, MEAP would be a preferable option. The muscle activity mapping demonstrated by MEAP, as outlined in Chapter 5.2, offers compelling evidence of its potential to comprehensively record muscle activity. Furthermore, by analysing median frequencies of individual muscles, MEAP can provide real-time muscle fatigue data to the prosthetic device, simulating muscle fatigue feedback. This innovation brings prosthetic control closer to the natural hand, making these devices more intuitive and responsive. In the near future, MEAP has the potential to become the leading input device for prosthetics due to its user comfort and high-density sEMG signal recording capabilities.

Beyond its potential in prosthetics, MEAP can also find exciting

applications in the realm of exoskeletons. As showcased in Chapter 5.4.1, MEAP can measure loads by analysing RMS of sEMG signals. When integrated into exoskeleton systems, this innovation can measure real-time muscle contraction levels, offering precise force assistance. By doing so, it optimizes task completion without the unnecessary expenditure of energy. This concept bears a resemblance to electronically power-assisted cycles and could significantly enhance task efficiency across various applications.

7.5 Advancing electrodiagnostic and electrophysiological research with MEAP

Aside from its non-invasiveness, MEAP possesses a notable advantage over needle recording due to its multichannel design. In the context of a single muscle, there are typically numerous motor units, numbering in the dozens or even hundreds. The capability to record multiple MUAPs separately offers substantial assistance to clinicians and neurophysiologists in gaining a deeper understanding of motor unit synergy. This emerging field holds the potential to unravel the fundamental mechanisms underlying muscle fibre function. In contrast, traditional needle electrodes have hindered progress in this area. The primary challenge lies in the extreme difficulty of concurrently recording different MUAPs with a single needle electrode.

To capture distinct MUAPs, the tip of the needle electrode must be precisely manoeuvred within the muscle to access various motor units. This intricate process demands the expertise of highly experienced clinicians or neurophysiologists to achieve both a high success rate and

minimal recording time. Even with skilled operators, the process often inflicts unbearable pain on subjects, frequently leading to interruptions in the recording process. Furthermore, this approach falls short of providing simultaneous recordings from all motor units within the muscle necessary for analysing motor unit synergy. The alternative of inserting multiple needles concurrently exacerbates subject discomfort, making research in this field exceedingly challenging. Some researchers have attempted to use sEMG electrodes to capture different MUAPs within the same channel and employ algorithms to differentiate them into distinct classifications. However, the results from this strategy are often contentious due to concerns surrounding their validity and accuracy.

In contrast, MEAP offers a compelling advantage for such research by eliminating subject discomfort entirely. With its high-density electrode array, MEAP evenly distributes recording sites across the target muscle area. This approach enables the simultaneous recording of multiple MUAPs from each channel, promising greater accuracy in MUAP decompositions compared to low-resolution electrodes. Consequently, we believe the potential of high-density sEMG electrode arrays, particularly MEAP, eclipse that of needle electrodes for future research.

However, the comparative tests between needle and MEAP in Chapter 6 have revealed a potential limitation in current recording systems or instruments. A critical observation is that no clinical recording system can facilitate multichannel recording to enable all MEAP channels to function simultaneously. This limitation stems from the fact that existing instruments

are primarily designed for needle electrodes, aligning with the previous statement that multi-needle recording is impractical in clinical settings. Consequently, the MEAP recording results presented in Chapter 6.2 are constrained to single-channel outputs, mirroring the capabilities of needle electrodes. Addressing these limitations necessitates efforts to develop compatible recording systems that can seamlessly integrate with high-density sEMG arrays like MEAP. Such endeavours are essential to ensure that every aspect of the recording process operates in harmony, ultimately yielding accurate and invaluable results.

In conclusion, MEAP offers a powerful tool for studying muscle physiology and motor unit interactions. Its multichannel, high-density recording capabilities provide an unparalleled advantage over traditional needle electrodes. While there are challenges in integrating MEAP with existing clinical recording systems, these challenges represent opportunities for innovation and collaboration in the field of electrophysiology. With continued research and development, MEAP holds the potential to reshape our understanding of muscle function and open new avenues for clinical applications.

Chapter 8

Conclusions

8.1 Concluding remarks

In a society increasingly focused on achieving and maintaining optimal physical health and fitness, the role of scientific exercise and injury prevention has become paramount. sEMG devices have emerged as a cornerstone in this pursuit, offering valuable insights into muscle activity and performance. However, existing commercial hydrogel sEMG electrodes come with their share of limitations, including short usage lifespans, inadequate conformability, and low-resolution recording capabilities. Additionally, while needle electrodes have traditionally been the gold standard in electrodiagnostic, there is a growing recognition of the potential and patient-friendliness of sEMG for future applications.

In response to these challenges and opportunities, this thesis introduces the concept of the MEAP, an adhesive, stretchable, biocompatible, and durable sEMG electrode array. MEAP leverages MPC and TPP for its circuitry and electrode components, ensuring flexibility and stretchability. This thesis provides a comprehensive exploration of the material formation, device fabrication, and the performance of MEAP across various sEMG applications.

Chapter 3 focuses on the development and characterization of TPP electrodes, a novel conductive polymer comprising PEDOT:PSS, PVA, and TA. These electrodes exhibit exceptional stretchability (with an elongation

at break of 188%) and adhesiveness (peeling force of 0.58 N/m). The chapter unravels the underlying mechanisms by examining the interactions between these components. Notably, the porous configurations within TPP films contribute to reduced cohesive energy and Young's modulus, enhancing compliance and stretchability. Long-term wear tests over ten days reveal sustained effectiveness and biocompatibility of the MEAP. Its adhesive properties enhance skin conformability, resulting in superior signal quality compared to traditional Ag/AgCl electrodes, especially in areas with skin folds and creases. These properties, combined with tunable viscosity through xanthan gum additions for improved patterning, lay the foundation for high-density electrode arrays and precise multi-channel sEMG recordings.

Chapter 4 explores the practical properties of MEAPs, emphasizing their repeatability and suitability for long-term wear. These characteristics are critical for ensuring user comfort, a central focus of MEAP development. The chapter highlights the challenges faced by commercial hydrogel electrodes and arrays in achieving consistent recording sites and conformability, issues resolved through the patternable LM circuitry employed in MEAP.

Chapter 5 presents diverse applications of MEAPs, showcasing their ability to provide precise muscle information and monitor muscle fatigue during activities like sports and training. The high-density sEMG electrode array of MEAP enables real-time monitoring of tendon displacement, aiding in the prevention of exercise-related injuries. Personal data analysis,

informed by MEAP recordings of loading, fatigue, and tendon displacement, empowers exercisers to train safely and efficiently, positioning MEAP as a valuable tool in the development of the sEMG field.

Chapter 6 serves as a pilot study on using sEMG arrays for electrodiagnostic purposes. The results demonstrate the capacity of MEAP to successfully record single MUAPs from the same motor unit as traditional needle electrodes. While differences in signal attributes such as amplitude, duration, and rise times are noted, their causes remain to be determined through further investigation. Understanding these differences may inform electrode optimization to enhance diagnostic accuracy. Nonetheless, this study strongly indicates the potential of MEAP for non-invasive electrodiagnostic techniques.

Chapter 7 delves into reflective discussions regarding experimental challenges encountered during the project and explores prospective applications of MEAPs. This chapter encapsulates the insights accumulated throughout the research journey, offering critical considerations and innovative possibilities arising from the development and utilization of MEAPs.

8.2 Future works

MEAP, with its remarkable attributes, holds immense promise in various sports and training environments, particularly for activities demanding explosive strength, such as sprinting and bodybuilding. In scenarios like weightlifting, where erectorspinae injuries are common and can disrupt

regular training, MEAP offers a distinct advantage. Unlike conventional sEMG electrodes that struggle to stay in place due to skin movement, MEAP provides a conformal attachment that can effectively monitor muscle activity and aid in injury prevention.

Furthermore, the versatility of MEAP is a key asset. Its sizes and designs can be easily adapted for different muscles or other electrophysiological recordings, including EEG and ECG. The high spatial resolution and extended working duration make MEAP a valuable tool in human-machine interfaces, such as prosthetics or virtual reality applications.

In the realm of clinical applications, the aim is to replace invasive needle electrodes with MEAP to enhance patient comfort. However, current MEAPs face challenges in distinguishing single motor unit signals from sEMG recordings due to limitations in backend algorithms, resulting in reduced efficiency and accuracy in selecting individual motor units. Consequently, the potential of MEAP in clinical diagnosis remains somewhat limited. Additionally, the reliance on cable connections in current MEAP designs restricts their application scenarios and overall simplicity. To overcome these limitations, one solution is to integrate MEAP with intelligent algorithms and wireless modules. This integration will not only enhance the utility of the device in clinical settings but also improve its portability for everyday use.

Looking ahead, we envision that MEAP has the potential for widespread commercialization, thanks to its cost-effectiveness and straightforward fabrication process. As a result, MEAP could serve as a versatile platform

for disease diagnosis, daily rehabilitation management, and scientific exercise, contributing significantly to advancements in healthcare and fitness.

References

1. Konrad, P. Noraxon: the ABC of EMG. *A practical introduction to kinesiological electromyography* 30–5 Preprint at http://www.noraxon.com/sdm_downloads/abc-of-emg (2005).
2. Gupta, A., Sayed, T., Garg, R. & Shreyam, R. Emg Signal Analysis of Healthy and Neuropathic Individuals. *IOP Conf Ser Mater Sci Eng* **225**, 012128 (2017).
3. Coorevits, P., Danneels, L., Cambier, D., Ramon, H. & Vanderstraeten, G. Assessment of the validity of the Biering-Sørensen test for measuring back muscle fatigue based on EMG median frequency characteristics of back and hip muscles. *Journal of Electromyography and Kinesiology* **18**, 997–1005 (2008).
4. Dugan, S. A. & Frontera, W. R. Muscle fatigue and muscle injury. *Phys Med Rehabil Clin N Am* **11**, 385–403 (2000).
5. Phinyomark, A., Thongpanja, S., Hu, H., Phukpattaranont, P. & Limsakul, C. The Usefulness of Mean and Median Frequencies in Electromyography Analysis. in *Computational Intelligence in Electromyography Analysis - A Perspective on Current Applications and Future Challenges* 195–220 (InTech, 2012). doi:10.5772/50639.
6. Knaflitz, M., Merletti, R. & De Luca, C. J. Inference of motor unit recruitment order in voluntary and electrically elicited contractions. <https://doi.org/10.1152/jappl.1990.68.4.1657> **68**, 1657–1667 (1990).
7. Preston, D. C. *Electromyography and Neuromuscular Disorders. Electromyography and Neuromuscular Disorders: Clinical-Electrophysiologic Correlations: Third Edition* (Elsevier, 2013). doi:10.1016/C2010-0-68780-3.
8. Preston, D. C. *Electromyography and Neuromuscular Disorders. Electromyography and Neuromuscular Disorders: Clinical-Electrophysiologic Correlations: Third Edition* (Elsevier, 2013). doi:10.1016/C2010-0-68780-3.
9. Bonner, F. J. & Devleschoward, A. B. AAEM minimonograph #45: The early development of electromyography. *Muscle Nerve* **18**, 825–833 (1995).
10. Licht S. *Electrodiagnosis and Electromyography, 3rd ed.* New Haven, CT. vols 1–23 (Elizabeth Licht Publisher, 1971).
11. Bakiya, A. & Kamalanand, K. Information analysis on electromyograms acquired using monopolar needle, concentric needle and surface electrodes. *2018 International Conference on Recent Trends in Electrical, Control and Communication (RTECC)* 240–244 (2019) doi:10.1109/RTECC.2018.8625631.
12. Guan, Y., Ding, Q., Liu, M., Niu, J. & Cui, L. Single-fiber EMG with concentric electrodes in lambert-eaton myasthenia. *Muscle Nerve* **56**, 253–257 (2017).

13. Z'graggen, W. J., Trautmann, J. P., Boërio, D. & Bostock, H. Muscle velocity recovery cycles: Comparison between surface and needle recordings. *Muscle Nerve* **53**, 205–208 (2016).
14. Ekstrom, R. A., Donatelli, R. A. & Soderberg, G. L. Surface electromyographic analysis of exercises for the trapezius and serratus anterior muscles. *Journal of Orthopaedic and Sports Physical Therapy* **33**, 247–258 (2003).
15. Rapeaux, A., Brunton, E., Nazarpour, K. & Constandinou, T. Recovery Dynamics of the High Frequency Alternating Current Nerve Block. *bioRxiv* 235135 (2017) doi:10.1101/235135.
16. Geng, W. *et al.* Gesture recognition by instantaneous surface EMG images. *Sci Rep* **6**, 6–13 (2016).
17. Merletti, R. & Muceli, S. Tutorial. Surface EMG detection in space and time: Best practices. *Journal of Electromyography and Kinesiology* **49**, 102363 (2019).
18. Larson, J. V. *et al.* Electrode characterization for use in a Regenerative Peripheral Nerve Interface. *International IEEE/EMBS Conference on Neural Engineering, NER* 629–632 (2013) doi:10.1109/NER.2013.6696013.
19. Yamagiwa, S., Sawahata, H., Ishida, M. & Kawano, T. Micro-electrode arrays for multi-channel motor unit EMG recording. *Proceedings of the IEEE International Conference on Micro Electro Mechanical Systems (MEMS)* 857–860 (2014) doi:10.1109/MEMSYS.2014.6765776.
20. Merletti, R., Botter, A., Troiano, A., Merlo, E. & Minetto, M. A. Technology and instrumentation for detection and conditioning of the surface electromyographic signal: State of the art. *Clinical Biomechanics* **24**, 122–134 (2009).
21. Loeb, G. E. & Gans, C. *Electromyography for experimentalists*. University of Chicago press (1987).
22. Neuman, M. The Biomedical Engineering Handbook. (1999) doi:10.1201/9781420049510.sec5.
23. Ferree, T. C., Luu, P., Russell, G. S. & Tucker, D. M. Scalp electrode impedance, infection risk, and EEG data quality. *Clinical Neurophysiology* **112**, 536–544 (2001).
24. Cui, X. & Martin, D. C. Electrochemical deposition and characterization of poly(3,4-ethylenedioxythiophene) on neural microelectrode arrays. **89**, 92–102 (2003).
25. Ludwig, K. A. *et al.* Poly(3,4-ethylenedioxythiophene) (PEDOT) polymer coatings facilitate smaller neural recording electrodes. *J Neural Eng* **8**, (2011).
26. Green, R. A. *et al.* Performance of conducting polymer electrodes for stimulating neuroprosthetics. *J Neural Eng* **10**, (2013).

27. Luo, S. C. *et al.* Poly(3,4-ethylenedioxythiophene) (PEDOT) nanobiointerfaces: Thin, ultrasmooth, and functionalized PEDOT films with in vitro and in vivo biocompatibility. *Langmuir* **24**, 8071–8077 (2008).
28. Chen, Y. *et al.* Poly(3,4-ethylenedioxythiophene) (PEDOT) as interface material for improving electrochemical performance of microneedles array-based dry electrode. *Sens Actuators B Chem* **188**, 747–756 (2013).
29. Lipomi, D. J. *et al.* Electronic properties of transparent conductive films of PEDOT:PSS on stretchable substrates. *Chemistry of Materials* **24**, 373–382 (2012).
30. Zanello, L. P., Zhao, B., Hu, H. & Haddon, R. C. Bone cell proliferation on carbon nanotubes. *Nano Lett* **6**, 562–567 (2006).
31. Pancrazio, J. J. Neural interfaces at the nanoscale. *Nanomedicine* **3**, 823–830 (2008).
32. Parker, R. A. *et al.* The use of a novel carbon nanotube coated microelectrode array for chronic intracortical recording and microstimulation. *Proceedings of the Annual International Conference of the IEEE Engineering in Medicine and Biology Society, EMBS* 791–794 (2012) doi:10.1109/EMBC.2012.6346050.
33. Wang, K., Fishman, H. A., Dai, H. & Harris, J. S. Neural stimulation with a carbon nanotube microelectrode array. *Nano Lett* **6**, 2043–2048 (2006).
34. Shirata, K. *et al.* Robust myoelectric signal detection based on stochastic resonance using multiple-surface-electrode array made of carbon nanotube composite paper. *Jpn J Appl Phys* **55**, (2016).
35. Duffy, D. C., McDonald, J. C., Schueller, O. J. A. & Whitesides, G. M. Rapid prototyping of microfluidic systems in poly(dimethylsiloxane). *Anal Chem* **70**, 4974–4984 (1998).
36. McDonald, J. C., Duffy, D. C., Anderson, J. R. & Chiu, D. T. Review General Fabrication of microfluidic systems in poly (dimethylsiloxane). *Electrophoresis* **21**, 27–40 (2000).
37. Jung, H. C. *et al.* CNT/PDMS composite flexible dry electrodes for long-term ECG monitoring. *IEEE Trans Biomed Eng* **59**, 1472–1479 (2012).
38. Lopes, P. A. *et al.* Soft Bioelectronic Stickers: Selection and Evaluation of Skin-Interfacing Electrodes. *Adv Healthc Mater* **8**, 1–11 (2019).
39. Jung, J. M. *et al.* Development of PDMS-based flexible dry type SEMG electrodes by micromachining technologies. *Appl Phys A Mater Sci Process* **116**, 1395–1401 (2014).
40. Tian, L. *et al.* Large-area MRI-compatible epidermal electronic interfaces for prosthetic control and cognitive monitoring. *Nat Biomed Eng* **3**, 194–205 (2019).
41. Tang, L. *et al.* Printable metal-polymer conductors for highly stretchable bio-devices. *iScience* **4**, 302–311 (2018).

42. Gabriel, C. *Compilation of the dielectric properties of body tissues at RF and microwave frequencies*. King's Coll London (United Kingdom) Dept of Physics. (1996).
43. Emily S. Kappenman and Steven J. Luck. The Effects of Electrode Impedance on Data Quality and Statistical Significance in ERP Recordings Emily. *Bone* **23**, 1–7 (2008).
44. Hewson, D. J., Hogrel, J. Y., Langeron, Y. & Duchêne, J. Evolution in impedance at the electrode-skin interface of two types of surface EMG electrodes during long-term recordings. *Journal of Electromyography and Kinesiology* **13**, 273–279 (2003).
45. Day, B. S. Important Factors in Surface EMG Measurement. *Measurement* 1–17 (2002).
46. Cogan, S. F. Neural Stimulation and Recording Electrodes. *Annu Rev Biomed Eng* **10**, 275–309 (2008).
47. Administration, U. S. F. and D. *FDA Backgrounder on Platinum in Silicone Breast Implants*. (2008).
48. Voskerician, G. *et al.* Biocompatibility and biofouling of MEMS drug delivery devices. *Biomaterials* **24**, 1959–1967 (2003).
49. Irimia-Vladu, M., Głowacki, E. D., Voss, G., Bauer, S. & Sariciftci, N. S. Green and biodegradable electronics. *Materials Today* **15**, 340–346 (2012).
50. Tang, L., Mou, L., Zhang, W. & Jiang, X. Large-Scale Fabrication of Highly Elastic Conductors on a Broad Range of Surfaces. *ACS Appl Mater Interfaces* **11**, 7138–7147 (2019).
51. Tang, L., Yang, S., Zhang, K. & Jiang, X. Skin Electronics from Biocompatible In Situ Welding Enabled By Intrinsically Sticky Conductors. *Advanced Science* **9**, 2202043 (2022).
52. Tan, P. *et al.* Solution-processable, soft, self-adhesive, and conductive polymer composites for soft electronics. *Nat Commun* **13**, 358 (2022).
53. Merletti, R., Farina, D. & Granata, A. Non-invasive assessment of motor unit properties with linear electrode arrays. *Electroencephalogr Clin Neurophysiol Suppl* **50**, 293–300 (1999).
54. Merletti, R. & Cerone, G. L. Tutorial. Surface EMG detection, conditioning and pre-processing: Best practices. *Journal of Electromyography and Kinesiology* **54**, 102440 (2020).
55. Dobloug, G. C., Svensson, J., Lundberg, I. E. & Holmqvist, M. Mortality in idiopathic inflammatory myopathy: Results from a Swedish nationwide population-based cohort study. *Ann Rheum Dis* **77**, 40–47 (2018).
56. Sarasola-Sanz, A. *et al.* A hybrid brain-machine interface based on EEG and EMG activity for the motor rehabilitation of stroke patients. *IEEE International Conference on Rehabilitation Robotics* 895–900 (2017) doi:10.1109/ICORR.2017.8009362.

57. NINDS. Idiopathic Inflammatory Myopathy Page. *NIH Publication* (2020).
58. Blijham, P. J., Hengstman, G. J. D., Ter Laak, H. J., Van Engelen, B. G. M. & Zwarts, M. J. Muscle-fiber conduction velocity and electromyography as diagnostic tools in patients with suspected inflammatory myopathy: A prospective study. *Muscle Nerve* **29**, 46–50 (2004).
59. Donnan, G., Fisher, M., Macleod, M. & Davis, S. Stroke. *The Lancet* **371**, 1612–1623 (2008).
60. Klein, C. S., Li, S., Hu, X. & Li, X. Editorial: Electromyography (EMG) Techniques for the Assessment and Rehabilitation of Motor Impairment Following Stroke. *Front Neurol* **9**, 1–3 (2018).
61. Cincotti, F. *et al.* EEG-based brain-computer interface to support post-stroke motor rehabilitation of the upper limb. *Proceedings of the Annual International Conference of the IEEE Engineering in Medicine and Biology Society, EMBS* 4112–4115 (2012) doi:10.1109/EMBC.2012.6346871.
62. NINDS. NINDS Multiple Sclerosis Information Page. *National Institute of Neurological Disorders and Stroke*. (2015).
63. Sarova - Pinhas, I., Achiron, A., Gilad, R. & Lampl, Y. Peripheral neuropathy in multiple sclerosis: a clinical and electrophysiologic study. *Acta Neurol Scand* **91**, 234–238 (1995).
64. NINDS. Myasthenia Gravis Fact Sheet. *NIH Publication* (2020).
65. Chiou-Tan, F. Y. *et al.* Literature review of the usefulness of repetitive nerve stimulation and single fiber EMG in the electrodiagnostic evaluation of patients with suspected myasthenia gravis or Lambert-Eaton myasthenic syndrome. *Muscle Nerve* **24**, 1239–1247 (2001).
66. NINDS. Parkinson's Disease Information Page. *NIH Publication* (2016).
67. Robichaud, J. A. *et al.* Variability of EMG patterns: A potential neurophysiological marker of Parkinson's disease? *Clinical Neurophysiology* **120**, 390–397 (2009).
68. Dayalu, P. & Albin, R. L. Huntington Disease: Pathogenesis and Treatment. *Neurol Clin* **33**, 101–114 (2015).
69. Siedenberg, R., Goodin, D. S. & Aminoff, M. J. Changes of forearm EMG and cerebral evoked potentials following sudden muscle stretch in patients with huntington's disease. *Muscle Nerve* **22**, 1557–1563 (1999).
70. Pandyan, A. D. *et al.* Spasticity: Clinical perceptions, neurological realities and meaningful measurement. *Disabil Rehabil* **27**, 2–6 (2005).
71. Albani, G. *et al.* Use of surface EMG for evaluation of upper limb spasticity during botulinum toxin therapy in stroke patients. *Funct Neurol* **25**, 103–107 (2010).
72. Wallace, D. M., Ross, B. H. & Thomas, C. K. Motor unit behavior during clonus. *J Appl Physiol* **99**, 2166–2172 (2005).

73. Mummidisetty, C. K., Bohórquez, J. & Thomas, C. K. Automatic analysis of EMG during clonus. *J Neurosci Methods* **204**, 35–43 (2012).
74. Hammer, G. D. & McPhee, S. J. Pathophysiology of disease: an introduction to clinical medicine (6th ed.). *New York: McGraw-Hill Medical* (2010).
75. Beniczky, S., Conradsen, I., Henning, O., Fabricius, M. & Wolf, P. Automated real-time detection of tonic-clonic seizures using a wearable EMG device. *Neurology* **90**, e428–e434 (2018).
76. Boulton, A. J. M. Management of Diabetic Peripheral Neuropathy. *CLINICAL DIABETES* **23**, 9–15 (2005).
77. Mete, T. *et al.* Comparison of efficiencies of michigan neuropathy screening instrument, neurothesiometer, and electromyography for diagnosis of diabetic neuropathy. *Int J Endocrinol* **2013**, (2013).
78. Liu, S., Reed, S. N., Higgins, M. J., Titus, M. S. & Kramer-Bottiglio, R. Oxide rupture-induced conductivity in liquid metal nanoparticles by laser and thermal sintering. *Nanoscale* **11**, 17615–17629 (2019).
79. Liao, J. & Majidi, C. Muscle-Inspired Linear Actuators by Electrochemical Oxidation of Liquid Metal Bridges. *Advanced Science* **9**, 2201963 (2022).
80. Lin, Z., Gao, C., Wang, D. & He, Q. Bubble-Propelled Janus Gallium/Zinc Micromotors for the Active Treatment of Bacterial Infections. *Angewandte Chemie International Edition* **60**, 8750–8754 (2021).
81. Hao, X. P. *et al.* Self-Shaping Soft Electronics Based on Patterned Hydrogel with Stencil-Printed Liquid Metal. *Adv Funct Mater* **31**, 2105481 (2021).
82. Park, Y. G., An, H. S., Kim, J. Y. & Park, J. U. High-resolution, reconfigurable printing of liquid metals with three-dimensional structures. *Sci Adv* **5**, (2019).
83. Lin, Y. *et al.* Vacuum filling of complex microchannels with liquid metal. *Lab Chip* **17**, 3043–3050 (2017).
84. Kim, M. gu, Brown, D. K. & Brand, O. Nanofabrication for all-soft and high-density electronic devices based on liquid metal. *Nature Communications* **2020 11:1** **11**, 1–11 (2020).
85. Guo, R. *et al.* One-Step Liquid Metal Transfer Printing: Toward Fabrication of Flexible Electronics on Wide Range of Substrates. *Adv Mater Technol* **3**, 1800265 (2018).
86. Khoshmanesh, K. *et al.* Liquid metal enabled microfluidics. *Lab Chip* **17**, 974–993 (2017).
87. Yu, H. *et al.* Laser-Generated Supranano Liquid Metal as Efficient Electron Mediator in Hybrid Perovskite Solar Cells. *Advanced Materials* **32**, 2001571 (2020).
88. Yu, F. *et al.* Ga-In liquid metal nanoparticles prepared by physical vapor

- deposition. *Progress in Natural Science: Materials International* **28**, 28–33 (2018).
89. Chen, S. & Liu, J. Spontaneous Dispersion and Large-Scale Deformation of Gallium-Based Liquid Metal Induced by Ferric Ions. *Journal of Physical Chemistry B* **123**, 2439–2447 (2019).
 90. Zhang, M. *et al.* Bio-Inspired Differential Capillary Migration of Aqueous Liquid Metal Ink for Rapid Fabrication of High-Precision Monolayer and Multilayer Circuits. *Adv Funct Mater* **33**, 2215050 (2023).
 91. Ding, L. *et al.* In Situ Deposition of Skin-Adhesive Liquid Metal Particles with Robust Wear Resistance for Epidermal Electronics. *Nano Lett* **22**, 4482–4490 (2022).
 92. Kim, S., Kim, S., Hong, K., Dickey, M. D. & Park, S. Liquid-Metal-Coated Magnetic Particles toward Writable, Nonwetttable, Stretchable Circuit Boards, and Directly Assembled Liquid Metal-Elastomer Conductors. *ACS Appl Mater Interfaces* **14**, 37110–37119 (2022).
 93. Markvicka, E. J., Bartlett, M. D., Huang, X. & Majidi, C. An autonomously electrically self-healing liquid metal–elastomer composite for robust soft-matter robotics and electronics. *Nature Materials* **2018 17:7** **17**, 618–624 (2018).
 94. Tang, L. *et al.* Metal-hygroscopic polymer conductors that can secrete solders for connections in stretchable devices. *Mater Horiz* **7**, 1186–1194 (2020).
 95. Pan, C. *et al.* Visually Imperceptible Liquid-Metal Circuits for Transparent, Stretchable Electronics with Direct Laser Writing. *Advanced Materials* **30**, 1706937 (2018).
 96. Niu, Y. *et al.* Thermal-Sinterable EGaIn Nanoparticle Inks for Highly Deformable Bioelectrode Arrays. *Adv Healthc Mater* **12**, (2023).
 97. Lee, W. *et al.* Universal assembly of liquid metal particles in polymers enables elastic printed circuit board. *Science (1979)* **378**, 637–641 (2022).
 98. Yuan, X. *et al.* Multifunctionally wearable monitoring with gelatin hydrogel electronics of liquid metals. *Mater Horiz* **9**, 961–972 (2022).
 99. Ma, Z. *et al.* Permeable superelastic liquid-metal fibre mat enables biocompatible and monolithic stretchable electronics. *Nature Materials* **2021 20:6** **20**, 859–868 (2021).
 100. Tang, L., Shang, J. & Jiang, X. Multilayered electronic transfer tattoo that can enable the crease amplification effect. *Sci Adv* **7**, eabe3778 (2021).
 101. Zhao, R. *et al.* Designable Electrical/Thermal Coordinated Dual-Regulation Based on Liquid Metal Shape Memory Polymer Foam for Smart Switch. *Advanced Science* **10**, 2205428 (2023).
 102. Cheng, J. *et al.* Wet - Adhesive Elastomer for Liquid Metal - Based Conformal Epidermal Electronics. *Adv Funct Mater* **32**, 2200444 (2022).

103. Dong, R. *et al.* Printed Stretchable Liquid Metal Electrode Arrays for In Vivo Neural Recording. *Small* **17**, 2006612 (2021).
104. Reis Carneiro, M., Majidi, C. & Tavakoli, M. Multi - Electrode Printed Bioelectronic Patches for Long - Term Electrophysiological Monitoring. *Adv Funct Mater* **32**, 2205956 (2022).
105. Li, Y. *et al.* A Highly Stretchable and Permeable Liquid Metal Micromesh Conductor by Physical Deposition for Epidermal Electronics. *ACS Appl Mater Interfaces* **14**, 13713–13721 (2022).
106. Zhong, L. *et al.* Stretchable Liquid Metal-Based Metal-Polymer Conductors for Fully Screen-Printed Biofuel Cells. *Anal Chem* **94**, 16738–16745 (2022).
107. Lee, W. *et al.* Universal assembly of liquid metal particles in polymers enables elastic printed circuit board. *Science (1979)* **378**, 637–641 (2022).
108. Kim, K. *et al.* Highly Sensitive and Wearable Liquid Metal - Based Pressure Sensor for Health Monitoring Applications: Integration of a 3D - Printed Microbump Array with the Microchannel. *Adv Healthc Mater* **8**, (2019).
109. Wang, Z., Volinsky, A. A. & Gallant, N. D. Crosslinking effect on polydimethylsiloxane elastic modulus measured by custom-built compression instrument. *J Appl Polym Sci* **131**, n/a-n/a (2014).
110. Kayser, L. V. & Lipomi, D. J. Stretchable conductive polymers and composites based on PEDOT and PEDOT:PSS. *Advanced Materials* **31**, 1806133 (2019).
111. Zhao, Y. *et al.* Ultra-conformal skin electrodes with synergistically enhanced conductivity for long-time and low-motion artifact epidermal electrophysiology. *Nat Commun* **12**, 1–12 (2021).
112. Zhang, L. *et al.* Fully organic compliant dry electrodes self-adhesive to skin for long-term motion-robust epidermal biopotential monitoring. *Nat Commun* **11**, 4683 (2020).
113. Li, P., Sun, K. & Ouyang, J. Stretchable and Conductive Polymer Films Prepared by Solution Blending. *ACS Appl Mater Interfaces* **7**, 18415–18423 (2015).
114. Liu, T. *et al.* Hydrogen - Bonded Polymer–Small Molecule Complexes with Tunable Mechanical Properties. *Macromol Rapid Commun* **39**, 1800050 (2018).
115. Lee, H., Dellatore, S. M., Miller, W. M. & Messersmith, P. B. Mussel-inspired surface chemistry for multifunctional coatings. *Science (1979)* **318**, 426–430 (2007).
116. Han, L. *et al.* Mussel-Inspired Adhesive and Tough Hydrogel Based on Nanoclay Confined Dopamine Polymerization. *ACS Nano* **11**, 2561–2574 (2017).
117. Kim, S., Saha, B., Boykin, J. & Chung, H. Gallol containing adhesive polymers. *Journal of Macromolecular Science, Part A* **59**, 625–645 (2022).

118. Oh, D. X., Kim, S., Lee, D. & Hwang, D. S. Tunicate-mimetic nanofibrous hydrogel adhesive with improved wet adhesion. *Acta Biomater* **20**, 104–112 (2015).
119. Yang, Q. *et al.* A bioinspired gallol-functionalized collagen as wet-tissue adhesive for biomedical applications. *Chemical Engineering Journal* **417**, 127962 (2021).
120. Lee, H., Scherer, N. F. & Messersmith, P. B. Single-molecule mechanics of mussel adhesion. *Proceedings of the National Academy of Sciences* **103**, 12999–13003 (2006).
121. Lee, D. *et al.* VATA: A Poly(vinyl alcohol)- And Tannic Acid-Based Nontoxic Underwater Adhesive. *ACS Appl Mater Interfaces* **12**, 20933–20941 (2020).
122. De Luca, C. J., Donald Gilmore, L., Kuznetsov, M. & Roy, S. H. Filtering the surface EMG signal: Movement artifact and baseline noise contamination. *J Biomech* **43**, 1573–1579 (2010).
123. Walton, C., Li, Z., Pennings, A., Agur, A. & Elmaraghy, A. A 3-dimensional anatomic study of the distal biceps tendon. *Orthop J Sports Med* **3**, 232596711558511 (2015).
124. Tankisi, H. *et al.* Standards of instrumentation of EMG. *Clinical Neurophysiology* **131**, 243–258 (2020).
125. Kabiri Ameri, S. *et al.* Graphene electronic tattoo sensors. *ACS Nano* **11**, 7634–7641 (2017).
126. Sun, Y. & Yu, X. B. Capacitive biopotential measurement for electrophysiological signal acquisition: a review. *IEEE Sens J* **16**, 2832–2853 (2016).
127. Lee, S. *et al.* Nanomesh pressure sensor for monitoring finger manipulation without sensory interference. *Science (1979)* **370**, 966–970 (2020).
128. Zhao, H. *et al.* Compliant 3D frameworks instrumented with strain sensors for characterization of millimeter-scale engineered muscle tissues. *Proc Natl Acad Sci U S A* **118**, e2100077118 (2021).
129. Oh, Y. S. *et al.* Battery-free, wireless soft sensors for continuous multi-site measurements of pressure and temperature from patients at risk for pressure injuries. *Nat Commun* **12**, 5008 (2021).
130. Song, E. *et al.* Miniaturized electromechanical devices for the characterization of the biomechanics of deep tissue. *Nat Biomed Eng* **5**, 759–771 (2021).
131. Yu, Y. *et al.* Biofuel-powered soft electronic skin with multiplexed and wireless sensing for human-machine interfaces. *Sci Robot* **5**, eaaz7946 (2020).
132. Moin, A. *et al.* A wearable biosensing system with in-sensor adaptive machine learning for hand gesture recognition. *Nat Electron* **4**, 54–63 (2021).

133. Ting, J. E. *et al.* Sensing and decoding the neural drive to paralyzed muscles during attempted movements of a person with tetraplegia using a sleeve array. *J Neurophysiol* **127**, 2104–2118 (2021).
134. Driscoll, N. *et al.* MXene-infused bioelectronic interfaces for multiscale electrophysiology and stimulation. *Sci Transl Med* **13**, eabf8629 (2021).
135. Wang, S. *et al.* Intrinsically stretchable electronics with ultrahigh deformability to monitor dynamically moving organs. *Sci Adv* **8**, eabl5511 (2022).
136. Wang, Y. *et al.* A highly stretchable, transparent, and conductive polymer. *Sci Adv* **3**, e1602076 (2017).
137. Yang, Y., Deng, H. & Fu, Q. Recent progress on PEDOT:PSS based polymer blends and composites for flexible electronics and thermoelectric devices. *Mater Chem Front* **4**, 3130–3152 (2020).
138. Donahue, M. J. *et al.* Tailoring PEDOT properties for applications in bioelectronics. *Materials Science and Engineering: R: Reports* **140**, 100546 (2020).
139. Romyen, N., Thongyai, S., Praserttham, P. & Sotzing, G. A. Enhancement of poly(3,4-ethylenedioxy thiophene)/poly(styrene sulfonate) properties by poly(vinyl alcohol) and doping agent as conductive nano-thin film for electronic application. *Journal of Materials Science: Materials in Electronics* **24**, 2897–2905 (2013).
140. Li, J. & Mooney, D. J. Designing hydrogels for controlled drug delivery. *Nat Rev Mater* **1**, 16071 (2016).
141. Liu, S., Rao, Y., Jang, H., Tan, P. & Lu, N. Strategies for body-conformable electronics. *Matter* **5**, 1104–1136 (2022).
142. Dierendonck, M. *et al.* Nanoporous hydrogen bonded polymeric microparticles: Facile and economic production of cross presentation promoting vaccine carriers. *Adv Funct Mater* **24**, 4634–4644 (2014).
143. Li, H. *et al.* Ternary Complex Coacervate of PEG/TA/Gelatin as Reinforced Bioadhesive for Skin Wound Repair. *ACS Appl Mater Interfaces* **14**, 18097–18109 (2022).
144. Li, G., Wang, S. & Duan, Y. Y. Towards gel-free electrodes: A systematic study of electrode-skin impedance. *Sens Actuators B Chem* **241**, 1244–1255 (2017).
145. Harati, A. & Jahanshahi, A. A reliable stretchable dry electrode for monitoring of EEG signals. *Sens Actuators A Phys* **326**, 112727 (2021).
146. Alban, M. V., Lee, H., Moon, H. & Yoo, S. Micromolding fabrication of biocompatible dry micro-pyramid array electrodes for wearable biopotential monitoring. *Flexible and Printed Electronics* **6**, 045008 (2021).
147. Jiang, Y. *et al.* Flexible and stretchable dry active electrodes with pdms and silver flakes for bio-potentials sensing systems. *IEEE Sens J* **21**, 12255–12268 (2021).

148. Yoon, S. *et al.* Highly stretchable metal-polymer hybrid conductors for wearable and self-cleaning sensors. *NPG Asia Mater* **13**, 4 (2021).
149. Yun, I. *et al.* Stable Bioelectric Signal Acquisition Using an Enlarged Surface-Area Flexible Skin Electrode. *ACS Appl Electron Mater* **3**, 1842–1851 (2021).
150. Li, Q. *et al.* Highly Thermal-Wet Comfortable and Conformal Silk-Based Electrodes for On-Skin Sensors with Sweat Tolerance. *ACS Nano* **15**, 9955–9966 (2021).
151. Tang, W. *et al.* Delamination-Resistant Imperceptible Bioelectrode for Robust Electrophysiological Signals Monitoring. *ACS Mater Lett* **3**, 1385–1393 (2021).
152. Won, Y. *et al.* Biocompatible, Transparent, and High-Areal-Coverage Kirigami PEDOT:PSS Electrodes for Electrooculography-Derived Human-Machine Interactions. *ACS Sens* **6**, 967–975 (2021).
153. Blau, R. *et al.* Intrinsically Stretchable Block Copolymer Based on PEDOT:PSS for Improved Performance in Bioelectronic Applications. *ACS Appl Mater Interfaces* **14**, 4823–4835 (2022).
154. Zhou, X. *et al.* Self-healing, stretchable, and highly adhesive hydrogels for epidermal patch electrodes. *Acta Biomater* **139**, 296–306 (2022).
155. Wang, S. *et al.* Self-adhesive, stretchable, biocompatible, and conductive nonvolatile eutectogels as wearable conformal strain and pressure sensors and biopotential electrodes for precise health monitoring. *ACS Appl Mater Interfaces* **13**, 20735–20745 (2021).
156. Cao, J. *et al.* Stretchable and Self-Adhesive PEDOT:PSS Blend with High Sweat Tolerance as Conformal Biopotential Dry Electrodes. *ACS Appl Mater Interfaces* **14**, 39159–39171 (2022).
157. Hazlett, R. L., Mcleod, D. R. & Hoehn-saric, R. Muscle tension in generalized anxiety disorder: Elevated muscle tonus or agitated movement? *Psychophysiology* **31**, 189–195 (1994).
158. Merletti, R. & Roy, S. Myoelectric and mechanical manifestations of muscle fatigue in voluntary contractions. *Journal of Orthopaedic and Sports Physical Therapy* **24**, 342–353 (1996).
159. de Gennes, P.-G., Brochard-Wyart, F. & Quéré, D. *Capillarity and Wetting Phenomena*. *Capillarity and Wetting Phenomena* (Springer New York, 2004). doi:10.1007/978-0-387-21656-0.
160. Pal, R. Effect of droplet size on the rheology of emulsions. *AIChE Journal* **42**, 3181–3190 (1996).
161. Shu, J. *et al.* Particle-based porous materials for the rapid and spontaneous diffusion of liquid metals. *ACS Appl Mater Interfaces* **12**, 11163–11170 (2020).
162. Li, F. *et al.* Magnetically- and electrically-controllable functional liquid metal droplets. *Adv Mater Technol* **4**, 1800694 (2019).

163. Yun, G. *et al.* Liquid metal-filled magnetorheological elastomer with positive piezoconductivity. *Nat Commun* **10**, 1300 (2019).
164. Vallem, V. *et al.* A soft variable - area electrical - double - layer energy harvester. *Advanced Materials* **33**, 2103142 (2021).
165. Lu, Y. *et al.* Mussel-inspired multifunctional integrated liquid metal-based magnetic suspensions with rheological, magnetic, electrical, and thermal reinforcement. *ACS Appl Mater Interfaces* **13**, 5256–5265 (2021).
166. Wang, H. *et al.* A liquid gripper based on phase transitional metallic ferrofluid. *Adv Funct Mater* **31**, 2100274 (2021).
167. Yuan, B., Sun, X., Wang, H. & Liu, J. Liquid metal bubbles. *Appl Mater Today* **24**, 101151 (2021).
168. Cole, T., Khoshmanesh, K. & Tang, S.-Y. Liquid metal enabled biodevices. *Advanced Intelligent Systems* **3**, 2000275 (2021).
169. Mayyas, M. *et al.* Gallium - based liquid metal reaction media for interfacial precipitation of bismuth nanomaterials with controlled phases and morphologies. *Adv Funct Mater* **32**, 2108673 (2022).
170. Mou, L. *et al.* Highly stretchable and biocompatible liquid metal - elastomer conductors for self - healing electronics. *Small* **16**, 2005336 (2020).
171. Ding, L. *et al.* A soft, conductive external stent inhibits intimal hyperplasia in vein grafts by electroporation and mechanical restriction. *ACS Nano* **14**, 16770–16780 (2020).
172. Cheng, S. *et al.* Electronic blood vessel. *Matter* **3**, 1664–1684 (2020).
173. Hang, C. *et al.* A soft and absorbable temporary epicardial pacing wire. *Advanced Materials* **33**, 2101447 (2021).
174. Zhong, B., Jiang, K., Wang, L. & Shen, G. Wearable Sweat Loss Measuring Devices: From the Role of Sweat Loss to Advanced Mechanisms and Designs. *Advanced Science* **9**, (2022).
175. Ribeiro, A. H. *et al.* Automatic diagnosis of the 12-lead ECG using a deep neural network. *Nat Commun* **11**, 1760 (2020).
176. Reaz, M. B. I., Hussain, M. S. & Mohd-Yasin, F. Techniques of EMG signal analysis: Detection, processing, classification and applications. *Biol Proced Online* **8**, 11–35 (2006).
177. Jang, H. *et al.* Graphene e-tattoos for unobstructive ambulatory electrodermal activity sensing on the palm enabled by heterogeneous serpentine ribbons. *Nat Commun* **13**, 6604 (2022).
178. S. Srinivasan, S. & M. Herr, H. A cutaneous mechanoneural interface for neuroprosthetic feedback. *Nat Biomed Eng* **6**, 731–740 (2022).
179. Farina, D. *et al.* Toward higher-performance bionic limbs for wider clinical use. *Nat Biomed Eng* **7**, 473–485 (2021).

180. Gu, G. *et al.* A soft neuroprosthetic hand providing simultaneous myoelectric control and tactile feedback. *Nat Biomed Eng* **7**, 589–598 (2021).
181. Bonizzato, M. & Martinez, M. An intracortical neuroprosthesis immediately alleviates walking deficits and improves recovery of leg control after spinal cord injury. *Sci Transl Med* **13**, eabb4422 (2021).
182. Vu, P. P. *et al.* A regenerative peripheral nerve interface allows real-time control of an artificial hand in upper limb amputees. *Sci Transl Med* **12**, eaay2857 (2020).
183. Choi, Y. S. *et al.* Stretchable, dynamic covalent polymers for soft, long-lived bioresorbable electronic stimulators designed to facilitate neuromuscular regeneration. *Nat Commun* **11**, 5990 (2020).
184. Miyamoto, R. G., Elser, F. & Millett, P. J. Distal biceps tendon injuries. *Journal of Bone and Joint Surgery* **92**, 2128–2138 (2010).
185. Mao, L. *et al.* Neurologic manifestations of hospitalized patients with coronavirus disease 2019 in Wuhan, China. *JAMA Neurol* **77**, 683 (2020).
186. Evans, W. J. *et al.* Metabolic changes following eccentric exercise in trained and untrained men. *J Appl Physiol* **61**, 1864–1868 (1986).
187. McCully, K. K. & Faulkner, J. A. Characteristics of lengthening contractions associated with injury to skeletal muscle fibers. *J Appl Physiol* **61**, 293–299 (1986).
188. McManus, L., De Vito, G. & Lowery, M. M. Analysis and biophysics of surface EMG for physiotherapists and kinesiologists: toward a common language with rehabilitation engineers. *Front Neurol* **11**, 576729 (2020).
189. Muceli, S. & Farina, D. Simultaneous and proportional estimation of hand kinematics from EMG during mirrored movements at multiple degrees-of-freedom. *IEEE Transactions on Neural Systems and Rehabilitation Engineering* **20**, 371–378 (2012).
190. Muceli, S., Falla, D. & Farina, D. Reorganization of muscle synergies during multidirectional reaching in the horizontal plane with experimental muscle pain. *J Neurophysiol* **111**, 1615–1630 (2014).
191. Merletti, R., Rainoldi, A. & Farina, D. Surface electromyography for noninvasive characterization of muscle. *Exerc Sport Sci Rev* **29**, 20–25 (2001).
192. Merletti, R., Farina, D. & Gazzoni, M. The linear electrode array: A useful tool with many applications. *Journal of Electromyography and Kinesiology* **13**, 37–47 (2003).
193. Merletti, R. *et al.* Multichannel surface EMG for the non-invasive assessment of the anal sphincter muscle. *Digestion* **69**, 112–122 (2004).
194. Sjøgaard, K., Christensen, H., Jensen, B. R., Finsen, L. & Sjøgaard, G. Motor control and kinetics during low level concentric and eccentric contractions in man. *Electroencephalography and Clinical*

- Neurophysiology/Electromyography and Motor Control* **101**, 453–460 (1996).
195. Madeleine, P., Bajaj, P., Sogaard, K. & Arendt-Nielsen, L. Mechanomyography and electromyography force relationships during concentric, isometric and eccentric contractions. *Journal of Electromyography and Kinesiology* **11**, 113–121 (2001).
 196. Mchugh, M. P., Tyler, T. F., Greenberg, S. C. & Gleim, G. W. Differences in activation patterns between eccentric and concentric quadriceps contractions. *J Sports Sci* **20**, 83–91 (2002).
 197. Dunlap, S. S., Aziz, M. A. & Ziermann, J. M. Anatomical variations of the deep head of Cruveilhier of the flexor pollicis brevis and its significance for the evolution of the precision grip. *PLoS One* **12**, e0187402 (2017).
 198. Ranavolo, A. *et al.* Surface electromyography for risk assessment in work activities designed using the “revised NIOSH lifting equation”. *Int J Ind Ergon* **68**, 34–45 (2018).
 199. Oliveira, A. de S. C. & Gonçalves, M. EMG amplitude and frequency parameters of muscular activity: Effect of resistance training based on electromyographic fatigue threshold. *Journal of Electromyography and Kinesiology* **19**, 295–303 (2009).
 200. Iridiastadi, H. & Nussbaum, M. A. Muscle fatigue and endurance during repetitive intermittent static efforts: development of prediction models. *Ergonomics* **49**, 344–360 (2006).
 201. Robi, K., Jakob, N., Matevz, K. & Matjaz, V. *The physiology of sports injuries and repair processes. Current Issues in Sports and Exercise Medicine These* (2013).
 202. Mills, K. R. The basics of electromyography. *J Neurol Neurosurg Psychiatry* **76 Suppl 2**, ii32-5 (2005).